Alma Mater Studiorum · Università di Bologna

SCUOLA DI INGEGNERIA

DIPARTIMENTO di INGEGNERIA DELL'ENERGIA ELETTRICA
E DELL'INFORMAZIONE "GUGLIELMO MARCONI" — DEI

CORSO DI LAUREA MAGISTRALE IN INGEGNERIA DELL'ENERGIA ELETTRICA

TESI DI LAUREA
in
Technological Management of Electrical Infrastructures

Effects of Cooling Lubricants on the Partial Discharge Inception Voltage of Hairpin Winding Interphase Insulation in EV Traction Motors

Relatore:
Chiar.mo Prof.
Andrea Cavallini

Candidato:
Davide Ramaschi

Correlatore:
Prof. Ing.
Paolo Seri

Anno Accademico 2025/2026
Sessione II

Il piacere più nobile è la
gioia della comprensione.

[Leonardo da Vinci]

Acknowledgements

I would first like to thank Prof. Cavallini for proposing a stimulating thesis topic and for the trust and autonomy he gave me throughout the work. His advice was often particularly effective in addressing the problems that arose during the project. I also thank him for the further trust placed in me and for the opportunity to continue working together in academia. I would also like to thank Prof. Seri for his valuable theoretical advice and, in particular, for helping me structure the work in a rigorous and methodical way. His contribution was important both in defining the scientific approach of the thesis and in guiding the analysis and interpretation of the results.

My thanks also go to Dario C., Simone S., Andrea R. and Fabrizio P. from LIMES lab for helping me become familiar with the laboratory, its equipment and its procedures, especially during the first months, and for making everyday laboratory life more relaxed and enjoyable, including the many lunches and breaks shared together. A special thanks goes to Jili, with whom I shared part of the experimental work.

Finally, I would like to thank my family for the constant support they have given me throughout my university years. Their trust and financial support allowed me to focus fully on my studies and pursue this path with the freedom and peace of mind needed to dedicate myself entirely to my studies. I am deeply grateful for everything they made possible along the way.

Abstract

The ongoing electrification of the transport sector is driving a continuous increase in the power and torque density of electrical machines – as torque density increases, thermal management becomes a critical challenge, since larger amounts of heat must be dissipated within increasingly confined volumes. Thus, conventional air-cooling solutions are often no longer sufficient, leading to the adoption of more effective cooling strategies based on dielectric oils, including configurations ranging from indirect cooling to full immersion systems. While dielectric oils provide significant thermal benefits and, generally, are not detrimental to insulation systems, their introduction can modify the dielectric environment surrounding the windings. As a result, electrical phenomena such as partial discharge inception may be affected by the presence of liquid phases and oil-derived vapours, potentially leading to changes in dielectric performance indicators such as the Partial Discharge Inception Voltage (PDIV).

This thesis focuses on the investigation of changes in partial discharge inception phenomena in oil-cooled electrical machines, with particular emphasis on comparing the effects of different dielectric cooling lubricants on PDIV. The experimental activity focuses on the comparison of different dielectric fluids under representative operating conditions, principally different temperatures, using specimens designed to reproduce the interphase insulation configuration of hairpin windings in the stator of a motor, particularly the interphase insulation of hairpin winding machines, and representative cooling conditions. Particular attention is devoted to assessing possible PDIV reductions with respect to conventional air-insulated conditions, especially in oil-wetted configurations where the coexistence of liquid and gaseous phases may facilitate partial discharge inception.

The primary objective is not only to quantify PDIV variations, but also to compare the relative performance of different dielectric oils. A further objective is to investigate the physical and chemical mechanisms responsible for the measured variations – to achieve this, a comprehensive physico-chemical characterization of the insulating fluids is carried out, with the aim of linking electrical behaviour to changes occurring within the oil during thermal exposure. Techniques such as Thermogravimetric Analysis (TGA) are used to study evaporation and degradation characteristics, while Fourier Transform Infrared Spectroscopy (FTIR) is employed to monitor changes in functional groups associated with thermal ageing and degradation. These analyses are made to to investigate whether changes in oil composition and volatility may be associated with vapour formation and the observed PDIV variations. The experimental results provide a better understanding of how different oil chemistries influence PDIV performance in realistic cooling conditions.

The final outcome of the thesis is a set of comparisons between dielectric fluids, supported by chemical evidence, providing insight into the interplay between oil composition, vapour formation, and partial discharge behaviour in oil-cooled electrical machines.

Sommario

L'elettrificazione del settore dei trasporti sta guidando un continuo aumento della densità di potenza e di coppia dei motori elettrici: all'aumentare della densità di coppia, la gestione termica diventa una sfida critica, poiché quantità di calore sempre maggiori devono essere dissipate all'interno di volumi sempre più contenuti. Pertanto, le tradizionali soluzioni di raffreddamento ad aria risultano spesso non più sufficienti, richiedendo dunque strategie di raffreddamento più efficaci basate su olio, sia con raffreddamento indiretto sia con sistemi a completa immersione. Sebbene gli oli dielettrici offrano notevoli benefici termici e, in generale, non siano dannosi per i sistemi di isolamento, il loro utilizzo può modificare l'ambiente circostante gli avvolgimenti. Di conseguenza, fenomeni elettrici quali l'innesco di scariche parziali possono essere influenzati dalla presenza di fasi liquide e di vapori derivati dall'olio, portando potenzialmente a variazioni degli indicatori di prestazione dielettrica, come la tensione d'innesco delle scariche parziali (PDIV – Partial Discharge Inception Voltage).

Il presente elaborato si concentra sull'indagine delle modifiche all'innesco delle scariche parziali nelle macchine elettriche raffreddate ad olio, con particolare attenzione al confronto dell'effetto di diversi oli isolanti sulla PDIV. L'attività sperimentale è focalizzata sulla comparazione di differenti oli dielettrici in diverse condizioni operative, principalmente a varie temperature, considerando campioni che mirano a replicare lo statore di un motore – in particolare l'isolamento fase-fase delle macchine con avvolgimenti hairpin – e le sue effettive condizioni di raffreddamento. Particolare attenzione viene dedicata alla valutazione di eventuali riduzioni della PDIV rispetto alle convenzionali condizioni di isolamento in aria, specialmente nelle configurazioni oil-wetted, dove la coesistenza di fasi liquide e gassose può facilitare l'insorgere di scariche parziali.

L'obiettivo non è soltanto quantificare le variazioni della PDIV, ma anche confrontare le prestazioni relative dei diversi oli dielettrici. Inoltre, uno scopo fondamentale di questo lavoro consiste nell'identificare i meccanismi fisico-chimici responsabili delle variazioni misurate; a tale scopo, viene effettuata una caratterizzazione chimico-fisica approfondita dei fluidi isolanti, con l'obiettivo di correlare il comportamento elettrico alle modificazioni che si verificano all'interno dell'olio durante l'esposizione termica. Tecniche quali l'analisi termogravimetrica (TGA) sono impiegate per studiare le caratteristiche di evaporazione e degradazione, mentre la spettroscopia infrarossa a trasformata di Fourier (FTIR) viene utilizzata per identificare le specie chimiche associate all'invecchiamento e alla decomposizione termica. Tali analisi sono destinate nello specifico a correlare le variazioni nella composizione e nella volatilità dell'olio con la presenza di vapori nelle regioni gassose e con il loro ruolo nella modifica dei processi di innesco delle scariche. I risultati che verranno ottenuti consentiranno una comprensione di come la differente chimica degli oli influenzi le prestazioni della PDIV in condizioni reali di raffreddamento.

Il risultato finale della tesi è il confronto tra fluidi dielettrici, supportati da evidenze chimiche, che offre una panoramica sulla complessa interazione tra composizione dell'olio, formazione di vapori e comportamento delle scariche parziali nelle macchine elettriche raffreddate ad olio.

Contents

Acknowledgements III

Abstract V

Sommario VII

List of Figures XVI

List of Tables XVII

Introduction 1

0.1 Global Climate Change Context . . . 1
0.1.1 The *Climate change* framework . . . 1
0.1.2 Global climate policy overview and future scenarios . . . 8
0.1.3 Sectoral emissions and the need for electrification . . . 16
0.2 Electrification of the transport sector and related challenges . . . 20
0.3 Objective of this work . . . 24
0.4 Thesis structure . . . 25

1 Theoretical background 27

1.1 Rationale of the work . . . 27
1.2 Electric rotating machines . . . 28
1.3 Types of stator winding construction & Insulation systems of motors . . . 30
1.4 Cooling systems of electric motors . . . 34
1.4.1 Thermal limits and loss mechanisms . . . 34
1.4.2 Transition from air cooling to liquid cooling . . . 35
1.4.3 Dielectric link: from oil direct cooling to Partial Discharge phenomena . . . 43
1.5 Partial Discharges (PD) theory and oil influence . . . 43
1.5.1 Main motor winding failure mechanisms & the critical role of partial discharges in motor's life . . . 43
1.5.2 Introduction to Partial Discharges theory . . . 45
1.5.3 PDIV as a function of temperature T . . . 52
1.6 Partial Discharge challenges in oil-cooled electric motors . . . 54

2 Materials and methods 57

2.1 Thermogravimetric analysis (TGA) . . . 57
2.1.1 Fundamental working principle . . . 57

2.1.2 Hardware architecture of a thermobalance . . . 59
2.1.3 Application of TGA for the analysis of oils . . . 60
2.1.4 *PerkinElmer* TGA 8000: description and setup . . . 61
2.2 Fourier Transform Infrared (FTIR) spectroscopy . . . 65
2.2.1 Working principle: theoretical fundamentals and the Michelson interferometer 65
2.2.2 *PerkinElmer* Spectrum Two . . . 67
2.2.3 FTIR analysis of oils . . . 68
2.3 Dielectric Cooling Lubricants . . . 73
2.3.1 Mineral and Ester-based oils: classification and generalities . . . 73
2.3.2 Properties of the investigated lubricants . . . 75
2.4 PD measurement setup and Omicron . . . 77
2.4.1 Test bay and its components . . . 79
2.4.2 Omicron MPD 800 Partial Discharge measurement system . . . 82
2.4.3 Omicron MPD Suite software . . . 84
2.5 Specimens and test cells . . . 89
2.5.1 Standard specimen configuration . . . 91
2.5.2 Pre-wetted specimen configuration . . . 92

3 Experimental results 93
3.1 TGA analysis results of the investigated oils . . . 93
3.2 FTIR spectral characterization of investigated oils . . . 96
3.3 Choice of the test temperatures . . . 99
3.4 Choice of the oils to be tested . . . 100
3.5 PDIV results under dielectric lubricant vapours exposure . . . 101
3.5.1 Dry specimens . . . 102
3.5.2 Wetted specimens . . . 104
3.6 PDIV vs. Temperature results, in air . . . 106

4 Discussion of results 109
4.1 Comparison between expected and experimental PDIV vs. temperature reduction 109
4.2 Comparative analysis of PDIV reduction for different oils . . . 110
4.2.1 FTIR spectroscopic indices . . . 110
4.2.2 FTIR-based interpretation of PDIV behaviour – no wetting . . . 113
4.2.3 Interpretation of PDIV behaviour, with samples pre-wetting . . . 121

Conclusion 123

Future developments 127
Characterization of oil vapours by Gas Chromatography . . . 127
Experimental determination of the Townsend ionization coefficient α . . . 128

A Demonstrations on climate model parameters 133
A.1 TCRE and airborne fractions . . . 133
A.2 Atmospheric CO_2 concentration . . . 137

B Experimental measured data 139

References 143

List of Figures

1 Temperature anomaly relative to the pre-industrial period (adapted from [26]) . 3
2 Annual world average concentration of atmospheric carbon dioxide CO_2 in the atmosphere (adapted from [27]) 4
3 Regional temperature scaling with CO_2 concentration [ppm] over 1850 to 2099 (adapted from [28]) 5
4 Annual CO_2 emissions from fossil fuels and industry for different countries (adapted from [26]) 7
5 Cumulated annual CO_2 emissions by world region Emissions from fossil fuels and industry (adapted from [26]) 7
6 Global annual greenhouse gases emissions and warming scenarios (adapted from [26] 10
7 CO_2 mitigation curves for 1.5 °C temperature anomaly target (adapted from [57]) 12
8 CO_2 mitigation curves for 2 °C temperature anomaly target (adapted from [57]) . 12
9 Global annual net CO_2 emissions pathways to limit global warming to 1.5 °C (adapted from [57]) 14
10 Illustration of the relationship between cumulative carbon dioxide emissions and global mean surface air temperature increase (adapted from [6]) 15
11 Global greenhouse gas emissions by sector, shown for year 2016 (adapted from [58]) 17
12 Comparison between *World* and *Europe* greenhouse gas emissions by sector from 1990 to 2020 (adapted from [60]) 18
13 Passenger transport demand by region under the Current Ambition scenario in years 2019 – 2050 in different world regions (adapted from [65]) 21
14 Transport sector CO_2 emissions by mode in the sustainable development scenario in the 2000-2030 years range (adapted from [72]) 22

1.1 Typical electric rotating machine types for traction applications, represented with an *exploded view*: (a) IPMSM, (b) IM, (c) SRM (adapted from [83]) 29
1.2 Hairpin winding technology (adapted from [95]) 31
1.3 Hairpin winding manufacturing process: (a) preformed hairpin conductor, (b) hairpin conductors inserted into the stator core slots, and (c) completed end-winding structure after the hairpin ends are twisted and welded (adapted from [80]) 31
1.4 Schemes of insulation subsystems for random-wound and form-wound windings machines, highlighting the T-T, P-G and P-P insulation subsystems (adapted from [84]) 33
1.5 Overview of the electrical insulation system components for a low voltage rotating machine (adapted from [84, 96]) 34

1.6 Comparison of heat transfer coefficients and maximum heat fluxes for different electric motor cooling methods (adapted from [98]) . . . 38
1.7 Maximum heat flux capability of different electric motor cooling methods as a function of motor torque and rotational speed (adapted from [98]) . . . 38
1.8 Finite-element temperature distribution of a synchronous reluctance motor equipped with a short water-path cooling jacket (SWJ) . . . 39
1.9 Direct stator oil cooling systems possibilities . . . 40
1.10 Direct oil-spray cooling configurations for hairpin end-windings: (a) axial injection from the end cover and (b) radial injection toward the end-winding region (adapted from [121]) . . . 40
1.11 Example of wetted stator cooling based on direct oil injection onto the hairpin end windings: the coolant directly wets the winding surface, forming an oil film and enabling direct heat removal from the conductors (adapted from [122]) . . . 41
1.12 Comparison of two in-slot liquid-cooling concepts for concentrated-winding electric machines . . . 42
1.13 Examples of hollow-conductor technology for direct oil cooling of electric machine stator windings. . . . 42
1.14 Iterative procedure for the numerical estimation of the partial discharge inception voltage based on the FEM electric-field distribution and the Schumann inception criterion . . . 51

2.1 Schematic of TGA equipment with the crucible at low position of the vertical heating furnace (adapted from [141]) . . . 60
2.2 Examples of different sample pans and crucibles commonly used for thermogravimetric analysis (adapted from [136]) . . . 60
2.3 Thermogravimetric analyzer used for the experimental characterization of the investigated dielectric cooling lubricants: PerkinElmer TGA 8000 model . . . 61
2.4 Close-up view of the TGA furnace and the balance suspension system in PerkinElmer TGA 8000, showing the sample holder connection inside the heated chamber (adapted from [137]) . . . 62
2.5 `Sample Info` tab of `Method Editor` window . . . 63
2.6 `Initial State` tab of `Method Editor` window . . . 64
2.7 `Program` tab of `Method Editor` window . . . 64
2.8 `View Program` tab of `Method Editor` window . . . 65
2.9 Schematic representation of a Michelson interferometer (adapted from [149])) . . . 67
2.10 FTIR spectrometer used for the chemical characterization of the investigated dielectric cooling lubricants: PerkinElmer Spectrum Two . . . 68
2.11 Close-up of the PerkinElmer Spectrum Two FTIR spectrometer, showing the sample measurement area (adapted from [150]) . . . 68
2.12 Indirect partial-discharge measurement circuit . . . 78
2.13 Equivalent circuit of the quadripole used in the partial discharge measurement system . . . 78

2.14 Laboratory oven used to heat the back-to-back specimens to the required test temperature . . . 79
2.15 Overall view of the high-voltage test setup . . . 80
2.16 PTFE-insulated feedthrough used to route the silicone-insulated high-voltage cables through the grounded metallic wall of the oven . . . 80
2.17 Close-up of the coupling capacitor and measuring impedance assembly used in the PD measurement circuit, with the high-voltage terminal at the top and the ground connection at the bottom . . . 81
2.18 High-voltage step-up transformer used to supply the test circuit during the partial-discharge measurements . . . 81
2.19 Omicron MPD 800 measurement unit and RBP1 battery pack used for PD measurements . . . 83
2.20 Measurement workstation used for the partial-discharge tests . . . 84
2.21 MCU2 control unit used in the MPD 800 partial-discharge measurement system . 85
2.22 Omicron MPD Suite 1.50 start page . . . 86
2.24 Omicron MPD Suite measurement interface showing the phase-resolved partial discharge (PRPD) display together with the time-domain PD signal and frequency-spectrum visualization . . . 86
2.23 Omicron MPD Suite system overview showing the detected MCU2 control unit and connected MPD 800 acquisition unit . . . 87
2.25 Omicron MPD Suite measurement interface in meter-display mode, showing the numerical and graphical representation of the acquired electrical quantities . . . 87
2.26 Main Omicron MPD Suite configuration panels used for the partial-discharge measurements . . . 88
2.27 Preparation of the twisted-pair specimen mounted on the test-cell lid . . . 90
2.28 Test container used for the partial-discharge measurements, showing the two insulated electrical feedthroughs . . . 91
2.29 Comparison of the same completed twisted-pair specimen under two initial surface conditions . . . 92

3.1 Thermogravimetric analysis (TGA) curves of the five investigated oils . . . 93
3.2 TGA curves of the investigated oils normalized with respect to the sample mass measured at 100 °C . . . 94
3.3 Derivative thermogravimetric (DTG) curves of the five investigated oils . . . 95
3.4 FTIR absorbance spectra of the investigated unaged oils, showing the comparison between the four mineral oils and the ester-based oil . . . 96
3.5 FTIR absorbance spectra of Castrol oil in new condition and after 1 h of thermal ageing at 145 °C and 180 °C . . . 98
3.6 FTIR absorbance spectra of Titan EG oil in new condition and after 1 h of thermal ageing at 145 °C and 180 °C . . . 98
3.7 FTIR absorbance spectra of ATF Ergoplus oil in new condition and after 1 h of thermal ageing at 145 °C and 180 °C . . . 99

3.8 FTIR absorbance spectra of Bizol oil in new condition and after 1 h of thermal ageing at 145 °C and 180 °C . . . 99
3.9 Normalized PDIV evolution as a function of temperature for the investigated oils, expressed in per-unit values with respect to the corresponding measurements in air at the same temperature . . . 103
3.10 Normalized PDIV measured in the presence of oil vapours with respect to the corresponding value in air, for the investigated lubricants and test temperatures, considering the measurements acquired at $t = 0$, namely immediately after reaching the target temperature . . . 104
3.11 Comparison between the normalized PDIV measured at $t = 0$ and after 1 h at the target temperature in the presence of oil vapours, with respect to the corresponding measurements in air . . . 104
3.12 Normalized PDIV as a function of temperature for the investigated oils, expressed with respect to the corresponding measurements in air, with preliminary wetting of the back-to-back specimens – logarithmic scale on the y-axis is utilized . . . 105
3.13 Enlarged view of the high-temperature region of fig. 3.12, shown with a linear y-axis to highlight the high-temperature differences among the investigated oils . 106
3.14 Comparison between the measured and predicted temperature dependence of the normalized PDIV for Castrol and Paryol oil samples . . . 107

4.1 FTIR absorbance spectra of Castrol and Titan EG oils – shaded regions identify the spectral intervals considered for the calculation of the FTIR indices . . . 119
4.2 Schematic of the experimental set-up of the Townsend discharge chamber (adapted from [193]) . . . 129
4.3 $\ln(I/I_0)$ as a function of electrode distance d for various reduced electric field values – solid lines show the linear fits used for the determination of α (adapted from [193]) . . . 130

A.1 The global carbon dioxide partitioning (atmospheric CO_2, land sink and ocean sink) averaged over the historical period 1900–2020 (adapted from [205]) . . . 137

List of Tables

1.1 Comparative rules of thumb for cooling type and heat transfer coefficients for electric motor cooling technologies (adapted from [98, 105, 112, 119]) 37

2.1 Main characteristics of fresh oils utilized in this thesis work (adapted from [174, 175, 176]) 76

3.1 Temperature initial data ranges used for selecting the proper test temperatures for PDIV tests of the investigated mineral oils 100

4.1 Percentage mass loss of the investigated dielectric cooling oils at the temperatures selected for the PD tests 114

4.2 Qualitative interpretation of the selected FTIR indicators, with corresponding chemical changes, possible volatile species, and potential relevance to PDIV . . . 118

4.3 Absolute values and relative variations of the FTIR indices evaluated for Castrol and Titan oils at different aging temperatures, together with the corresponding variation in PDIV. Relative/percentage variations of indices are calculated with respect to the value measured at 25 °C. 118

B.1 PDIV values measured for the investigated specimens in air and in the presence of Castrol oil. All voltage values are reported as $V_{peak}/\sqrt{2}$. 140

B.2 PDIV values measured for the investigated pre-wetted specimens in air and in the presence of Castrol oil under different thermal conditions. All voltage values are reported as $V_{peak}/\sqrt{2}$. 140

B.3 PDIV values measured for the investigated specimens in air and in the presence of Titan EG oil. All voltage values are reported as $V_{peak}/\sqrt{2}$ 141

B.4 PDIV values measured for the investigated pre-wetted specimens in air and in the presence of Titan EG oil under different thermal conditions. All voltage values are reported as $V_{peak}/\sqrt{2}$ 141

B.5 PDIV values measured for the investigated specimens in air and in the presence of Paryol oil. All voltage values are reported as $V_{peak}/\sqrt{2}$ 142

B.6 PDIV values measured for the investigated pre-wetted specimens in air and in the presence of Paroyl oil under different thermal conditions. All voltage values are reported as $V_{peak}/\sqrt{2}$ 142

Introduction

0.1 Global Climate Change Context

0.1.1 The *Climate change* framework

In recent decades, climate change has become one of the defining challenges of our era. On this point, according to the United Nations Framework Convention on Climate Change (UNFCCC) [1] it is possible to define:

> *«Climate change» means a change of climate which is attributed directly or indirectly to human activity that alters the composition of the global atmosphere and which is in addition to natural climate variability observed over comparable time periods.*

In this regard, the Secretary-General of the United Nations *António Guterres*, at the 2019 Abu Dhabi Climate Meeting delivered a critical warning [2, 3]:

> *"Climate change is the defining issue of our time, and we are at a defining moment."*
>
> — *António Guterres*

which serves not only as a critical warning but also underscores the absolute immediacy of immediate and coordinated actions. Though, faced with a lack of concrete progress from governments, during the opening of the 77$^{\text{th}}$ United Nations General Assembly on 20 September 2022 the Secretary-General stopped using polite diplomatic formulas and delivered a remarkably direct and sharp speech with sentences such as *«Our world is in peril – and paralysed»* and *«We are gridlocked in colossal global dysfunction»* [4, 5]. This shift in tone, from the strong warnings delivered in 2019 to the markedly harsher and more alarming language adopted in 2022, reflects the growing urgency and severity with which the climate crisis is now perceived at the international level – a sense of urgency that has yet to be matched by proper and concrete governmental action.

Yet these words from the Secretary-General resonate strongly, especially as we witness a series of devastating global events, making the effects of climate change increasingly evident worldwide: nowadays the damaging impacts of climate change affect almost every region of the world. As presented in [6, 7, 8], common extreme weather events and climate impacts on the world are:

- **Extreme heat**, namely a significant increase in the frequency, intensity, and duration of heatwaves across most land regions (an example is the recent record-shattering June 2026 heatwave, which saw France reaching its hottest day on record with a national average of 30.0 °C and local highs of 43.8 °C, alongside Germany and Czechia both eclipsing 41 °C and Switzerland which set a new June temperature record of 39 °C in the northern city of

Basel according to *Meteo-Suisse* [9]);

- **Intensified precipitation** with a rise in the frequency and amount of heavy rainfall leading to a higher risk of pluvial flooding;
- **Severe droughts**, namely the escalation of agricultural and ecological droughts as well as meteorological droughts (an example is the extreme 2022 drought in the Po Valley, when exceptionally low precipitation and persistent heatwaves brought the Po River to historically low levels across Northern Italy [10], a crisis that re-escalated sharply as record-breaking summer heat left the river dried up in the Cremonese area putting local agriculture at high risk [11], caused an alarming low-water emergency that panicked Torino [12], and even caused the ruins of Borgofranco – a hidden medieval toll station – to completely re-emerge from the receded riverbed near Pavia [13]);
- **Desertification and aridification**, namely the intensifying heat and atmospheric evaporative demand accelerate soil moisture loss and erosion;
- **Glacial retreat**, namely a rapid and widespread loss of glacier mass, leading to the disintegration of high-altitude ice reservoirs in the alpine region and accelerated mass loss of the polar ice masses in Greenland and Antarctica that, in turn, contributes directly to global sea-level rise.

Furthermore, the effects of climate change are not limited to the environment alone, but also represent a growing threat to human health worldwide[1]. Indeed, climate change leads to more deaths and illnesses during extreme heat events. The global warming-induced high temperatures make heart and lung diseases much worse because they put a massive strain on the cardiovascular system, increasing the risk of heart attacks and strokes. Additionally, heat worsens air quality by creating more ground-level ozone and smoke from wildfires, which harms the respiratory system.

In respect to the *Climate change* definition given in page 1, it is evident that widespread industrialization and human activities of the modern era have played a pivotal role in the current climate crisis. Indeed, as extensively discussed in [21, 22], humanity's impact on the global environment is now so profound that it rivals the great forces of nature[2], leading scientists to define our current era as the *Anthropocene*. This term, rooted in the Greek word for human, signifies that we have left the stable *Holocene* epoch as our activities have become a dominant geophysical force and can significantly affect planetary processes. Indeed, over the past century, the extensive use of energy resources, land-use changes[3], modern lifestyles, and current production and consumption patterns have significantly increased greenhouse gas emissions, which are identified as the main driver of recent warming (also [24] highlights the strong connection between global warming and human-generated greenhouse gas emissions). The aforementioned statements can be justified by looking at fig. 1, which represents the average temperature anomaly as well as the southern

[1] much more detail is provided in [14, 15, 16, 17, 18, 19, 20]

[2] in this context, the *great forces of nature* refers to the massive, slow-moving Earth systems and astronomical cycles that have controlled our planet's climate and environment for millions of years; before humans arrived, these were the only forces capable of changing the Earth on a global scale while nowadays, by saying that humanity now rivals them, it means humans are altering the planet faster than these natural systems do [23]

[3] land-use change refers to human-driven alteration of land cover, such as converting forests into agricultural land or expanding urban areas

and northern hemisphere temperature anomaly, and fig. 2, which represents the world average CO_2 concentration in the atmosphere along time. In particular, fig. 1 shows how global average temperatures, compared to a pre-industrial baseline, have markedly increased by around 1.3 °C, with even higher anomalies recorded in recent years (although this may appear modest in absolute terms, such a rapid temperature rise has substantial effects on climate and natural systems, as it was pointed out before with the list of weather events and climate impacts at page 1) – this warming has not been evenly distributed, as the northern hemisphere has experienced a stronger temperature increase than the southern hemisphere[4].

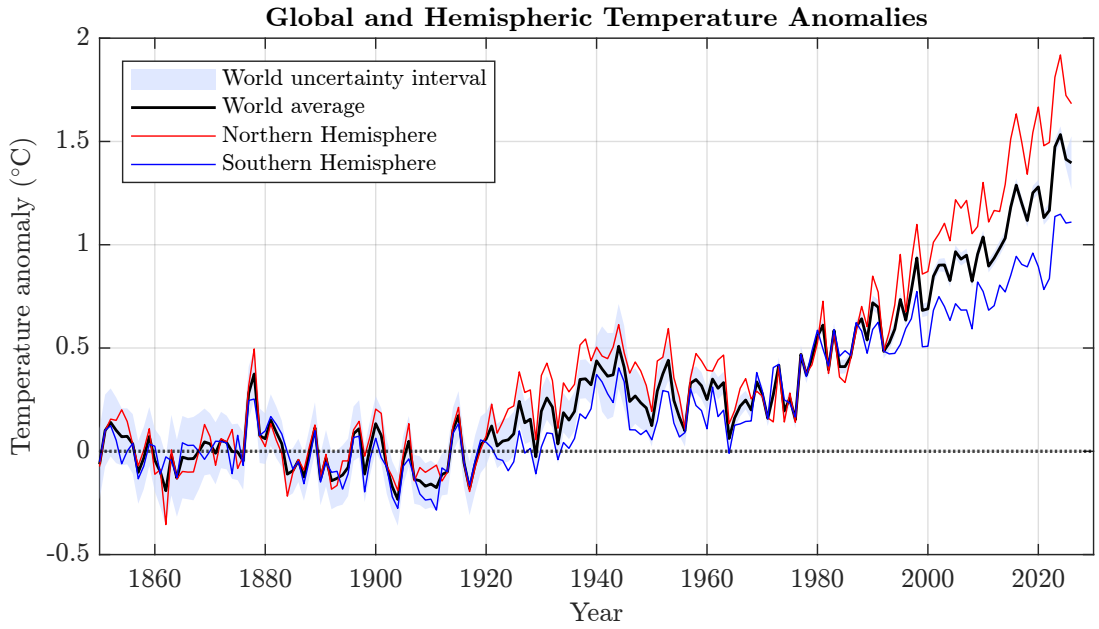


Figure 1. Temperature anomaly relative to the pre-industrial period – they're measured as the difference between the average land-sea surface temperature in a given year and the 1861-1890 mean; Upper and Lower boundaries of the so-called *World uncertainty interval* area represent the 95 % confidence interval (adapted from [26])

The still a bit unclear correlation between greenhouse gases emissions and global warming is better explained with fig. 3, which illustrates the regional temperature scaling with CO_2 concentration for two specific regions, Central Europe (CEU) and Central North America (CNA), from the year 1850 to 2099, namely combining historical data and projections based on the high-emissions "worst-case" scenario[5]. The temperatures shown in this figure are atmospheric temperatures, specifically the annual maximum daytime temperature TXx anomaly (solid lines) and the global mean temperature anomaly (dashed lines) – the different types of lines serve to distinguish between global trends and regional extremes as it was mentioned, but in particular

[4] since land surfaces respond more strongly to warming and cooling than oceans, land temperatures have increased by about 1.59 °C compared to 0.88 °C over oceans; this leads to stronger warming in the northern hemisphere, where land masses are more extensive, with even more pronounced increases at high latitudes exceeding 3 °C and in some cases 5 °C [25]

[5] to be more precise, the CO_2 concentrations and resulting temperatures in fig. 3 are calculated based on the *Representative Concentration Pathway 8.5* (RCP 8.5) scenario, which is characterized by having the largest greenhouse gas forcing and the least amount of mitigation activity among standard climate pathways; under this scenario, atmospheric CO_2 concentration increases from approximately 285 ppm in the pre-industrial era to roughly 936 ppm by the year 2099, and it has been studied that this consequently leads to the reported temperature increase [28]

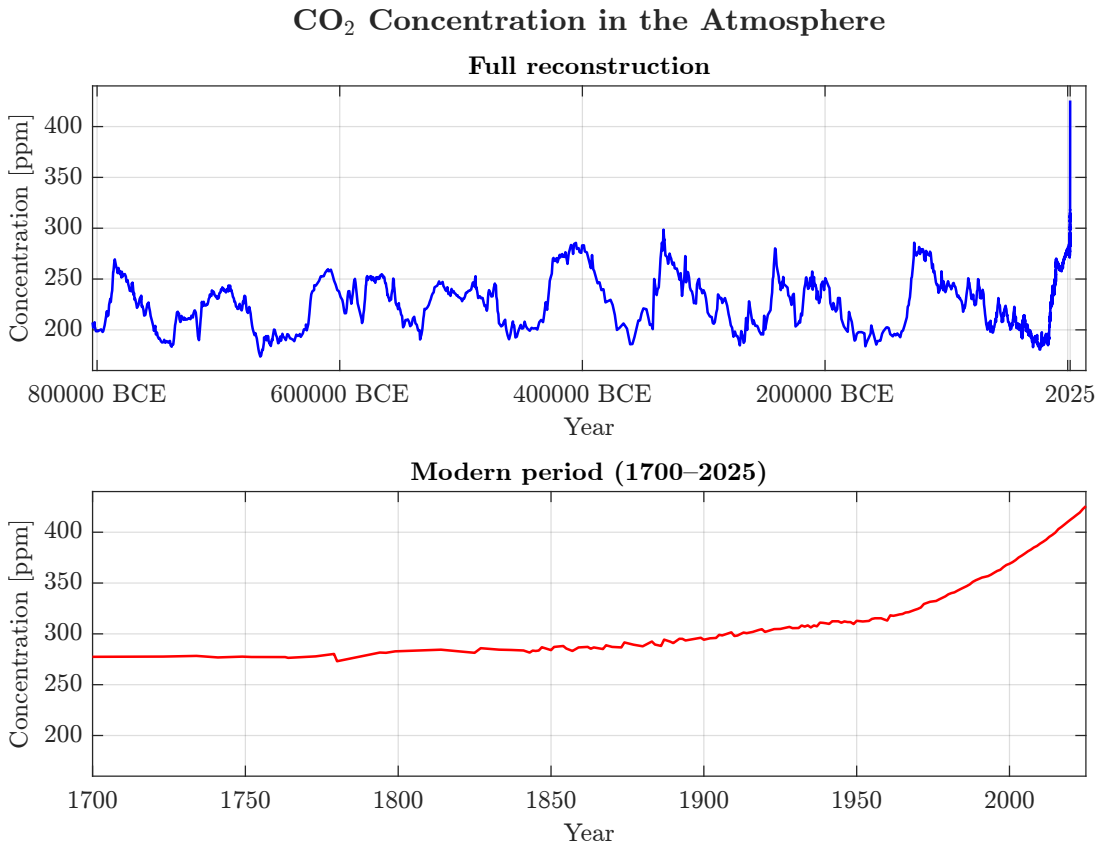


Figure 2. Annual world average concentration of atmospheric carbon dioxide CO_2 in the atmosphere, where long-term trends of concentration can be measured at high-resolution by means of preserved air samples from ice core studies (adapted from [27]) – similar trends can be observed also for N_2O and CH_4

more lines are reported for the two classes: the differences among these solid lines show how effective each strategy presented in [28] is at reducing regional extreme heat while the dashed lines represent the global mean temperature anomaly for those same experiments/strategy (namely, just like the solid lines, there is one dashed line for every experiment). Furthermore, global mean temperature includes the oceans, which warm more slowly than land. These graphs focus on land-only regional averages, which [28] note will experience a substantially higher magnitude of warming compared to the global target (this was already highlighted in a similar way with fig. 1 and with the numbers from [25]). Furthermore, these studies extend the understanding of the correlation between atmospheric CO_2 concentration and global warming by establishing a direct scaling relationship where temperature rise is treated as a proportional response to greenhouse gas forcing, namely it confirms from another point of view that temperature rise appears to be directly correlated to atmospheric CO_2 concentration.

In view of what has been mentioned, a correlation can be found between figs. 1 and 2. Throughout the timescale of the upper subplot of fig. 2, atmospheric CO_2 concentrations exhibited pronounced cyclic and natural variations linked to glacial and interglacial periods basically up to the modern age, which were mainly induced by variations in Earth's orbital configuration, known as *Milankovitch cycles* [29]. Nevertheless, atmospheric CO_2 levels remained below approximately 300 ppm during these cycles. This behaviour changed markedly with the onset of the *Industrial Revolution* and the consequent increase in anthropogenic CO_2 emissions,

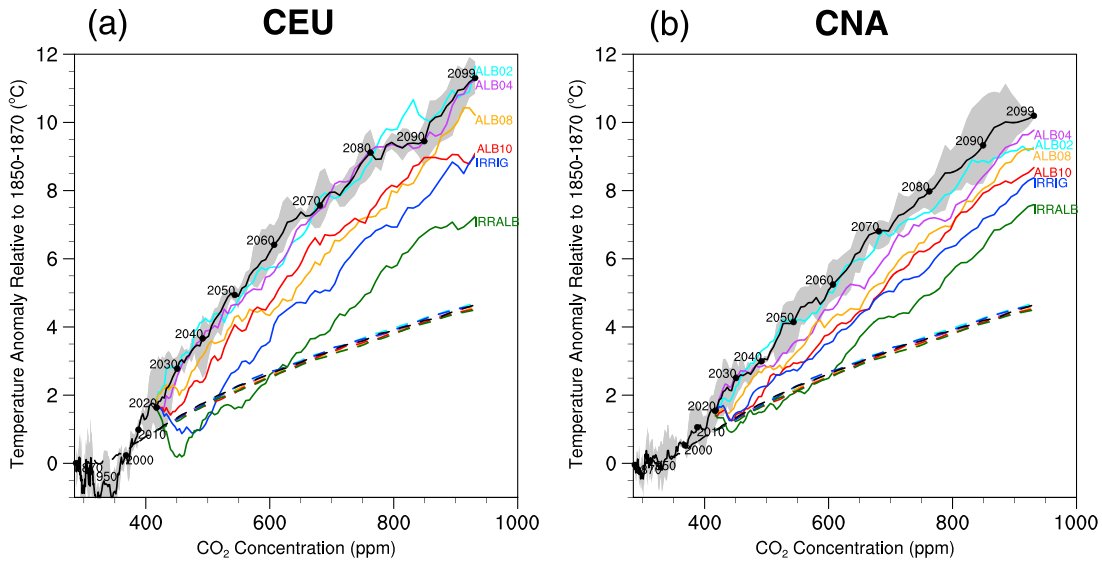


Figure 3. Regional temperature scaling with CO_2 concentration [ppm] over 1850 to 2099 (adapted from [28])

as shown in the lower subplot of fig. 2. Over the last few decades alone, atmospheric CO_2 concentrations have increased from roughly 270 ppm to more than 400 ppm at an unprecedented rate. Anyway, regarding the correlation between anthropogenic CO_2 emissions and climate change, for the sceptics these *Milankovitch cycles* cannot be regarded as the cause of current climate change for some key reasons [30]:

- *Milankovitch cycles* operate over tens of thousands to hundreds of thousands of years, whereas the current period of rapid warming has occurred over just decades and centuries;
- *NASA* satellite observations show that over the last 40 years, solar radiation has actually decreased slightly, meaning the Sun is not driving the current temperature increase;
- based on Earth's current orbital positions, the planet should naturally be in a long-term cooling trend that began 6000 years ago, rather than the warming we see today.

Thus, based on the data and evidence that have been presented, it is possible to conclude with high confidence that current global warming is primarily driven by human activities.

The relevance and the leading role of the greenhouse gases in the climate change context and the correlation shown between temperature anomaly and carbon dioxide concentration can be developed and explained also through the classical radiative explanation of the greenhouse effect, which is based on the fundamental energy balance maintained between incoming solar radiation and the outgoing terrestrial radiation emitted by our planet. A detailed treatment is proposed in [31] while hereafter only an intuitive explanation is reported. The Sun primarily radiates energy in a shortwave frequency range for which the atmosphere is almost transparent, allowing the majority of this light intensity to reach the Earth's surface. The Earth, behaving approximately as a black body, absorbs this solar energy and re-emits it as electromagnetic waves in the longwave infrared spectrum. Greenhouse gases possess an absorbing power in this specific infrared range, which makes the atmosphere partially opaque to the Earth's upward radiance. This process traps a significant portion of the infrared light emitted by the Earth before

it can escape into deep space, resulting in a "defect of radiance" in the spectrum seen from afar. This radiative transfer mechanism hence establishes a higher equilibrium temperature for the surface-atmosphere system than would exist if the atmosphere would be perfectly transparent. Consequently, when the concentration of greenhouse gases increases, the absorption coefficient of the air rises, enhancing the atmosphere's capacity to retain upward longwave radiation and leading to an increase in the global temperature, thereby contributing to the so-called *Global warming*.

The aforementioned *Greenhouse gases* are more rigorously defined as gases, both natural and human-made, that absorb and re-emit infrared radiation in the atmosphere with the unfortunate capability of trapping heat in the atmosphere [32]. The main greenhouse gases, associated with their relative percentage contribution for year 2022 reported between the square brackets (land-use change and forestryare emissions not accounted), are [32]:

- Carbon dioxide (**CO_2**) [79.7%]: it enters the atmosphere mainly through burning fossil fuels and solid waste;
- Methane (**CH_4dimmeli**) [11.1%]: it is emitted during the production and transport of fossil fuels but also from livestock and other agricultural practices as well as land use;
- Nitrous oxide (**N_2O**) [6.1%]: it is emitted mainly during agricultural, land use, and industrial activities;
- Fluorinated gases (**HFCs**, **PFCs**, **SF_6**, **NF_3**) [3.1%]: they are synthetic, powerful greenhouse gases that are emitted from a variety of household, commercial, and industrial applications and processes.

It's possible to observe how carbon dioxide represented the largest share of global greenhouse gas emissions, accounting for around three quarters of total emissions. These data should also be interpreted in light of the Global Warming Potential (GWP) over a 100-year time horizon (GWP_{100}) of greenhouse gases, which quantifies their warming effect relative to carbon dioxide[6] – in other words, the larger the GWP, the more that a given gas warms the Earth compared to carbon dioxide over that time period. As reported in [33], carbon dioxide by definition has a GWP of 1 regardless of the time period used because it is the gas being used as the reference; instead methane, for example, has a $GWP_{100} \approx 27 - 30$ while nitrous oxide has a $GWP_{100} \approx 273$. Consequently, on a per-unit-mass basis, these gases contribute far more strongly to global warming than carbon dioxide. Furthermore, in view of what has been just mentioned, in most emission charts the greenhouse gas emissions are often expressed in terms of carbon dioxide equivalent (**CO_2e**). This approach allows different greenhouse gases, each with different global warming potentials, to be standardized into a single measure with the result to have a common metric that makes it easier to compare the impact of different sectors or gases, since all are converted to their equivalent CO_2 impact.

The atmospheric CO_2 concentration data shown in fig. 2 should be considered alongside fig. 5, which presents annual cumulative CO_2 emissions from fossil fuel combustion and industry

[6] to be rigorous, [33] tells that *"the GWP, in particular* GWP_x*, is a measure of how much energy the emission of 1 ton of a gas will absorb over a given period of time (*x *years for instance), relative to the emission of 1 ton of carbon dioxide"*

by world region. The similarity between the two trends clearly demonstrates from another point of view the strong link between rising greenhouse gas concentrations and anthropogenic activities, especially those related to fossil fuel consumption. Global CO_2 emissions have continuously increased over time, reaching nearly 38.6 Gt in 2024 as shown in fig. 5. It is also worth noting that, if Europe and the United States accounted for more than 90 % of emissions during the most of the 20th century, the distribution of emissions has shifted significantly in recent decades: developing countries, particularly China but also other Asian countries, currently represent the largest share of global emissions.

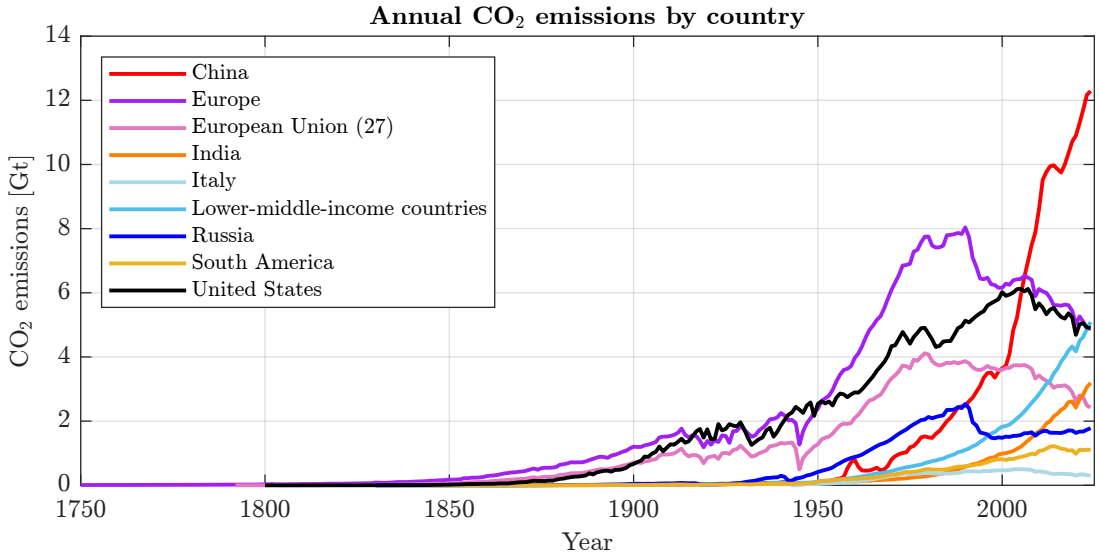


Figure 4. Annual CO_2 emissions from fossil fuels and industry for different countries; land-use change emissions are not included as well as emissions from international aviation and shipping are not included in the data for any individual country or region (adapted from [26])

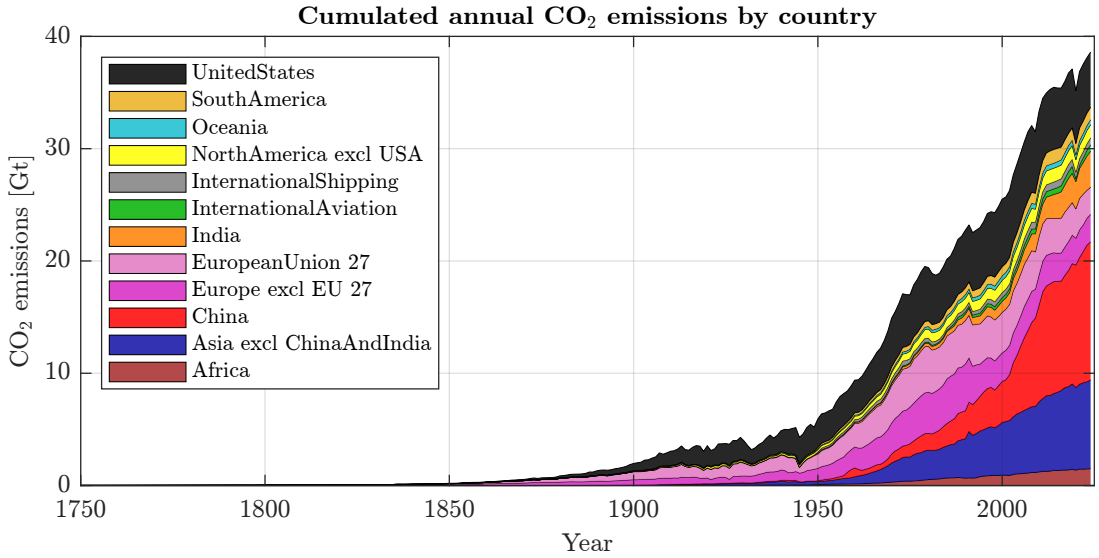


Figure 5. Cumulated annual CO_2 emissions by world region Emissions from fossil fuels and industry; land-use change emissions are not included and international aviation and shipping are accounted as separate entities (adapted from [26])

0.1.2 Global climate policy overview and future scenarios

As mentioned in the previous sections, climate change caused by human activities is widely recognized as one of the main challenges of the modern era. The continuous increase in greenhouse gas emissions is contributing, with very high likelihood, to the rise in global average temperature and leading to significant environmental, economic and social impacts. For this reason, governments and international organizations faced the need of an urgent action and thus have progressively introduced agreements and policies aimed at reducing emissions and supporting the transition toward more sustainable energy systems. The recognition of climate change as a global issue requiring urgent international action emerged gradually, mainly between the late 1980s and early 1990s, since during this period scientific evidence of anthropogenic global warming became increasingly robust. This lead in the first place to the establishment of the *Intergovernmental Panel on Climate Change* (IPCC) in 1988 with the goal to assess and synthesize climate science [34]. An overview of the key international climate milestones and the subsequent agreements and summits is provided below:

- **1992 – United Nations Framework Convention on Climate Change (UNFCCC)** [35]: the UNFCCC established the first global framework for international cooperation on climate change during the *Rio Earth Summit* in June 1992 by introducing climate change into the international political agenda, and in that place it was recognized the need to stabilize greenhouse gas concentrations in the atmosphere to avoid dangerous anthropogenic interference with the climate system and, furthermore, it was laid the foundation for the annual *Conferences of the Parties* (COPs) – from this point onward, climate change progressively evolved from a primarily scientific concern into a structured field of international policy, paving the way for subsequent agreements;
- **1997 – Kyoto Protocol** [36, 37]: it was the first legally binding international agreement on greenhouse gas emissions reduction, which entered into force on 16 February 2005 where industrialized countries committed to reducing, on average, emissions by at least 5 % below 1990 levels during the 2008–2012 period;
- **2015 – COP21 and the Paris Agreement** [38]: the adoption of the *Paris Agreement* during COP21 marked a major turning point in global climate governance because this agreement established the objective of limiting the increase in global average temperature to below 2 °C above pre-industrial levels, while pursuing efforts to limit warming to 1.5 °C (accordingly to subsequent scientific assessments, achieving the 1.5 °C target requires global greenhouse gas emissions to decrease by approximately 43 % by 2030 compared to 2019 levels and to reach net-zero CO_2 emissions around mid-century);
- **2019 – European Clean Energy Package (CEP)** [39]: in May 2019 the *European Union* introduced the *Clean Energy package for all Europeans* to support the energy transition through improvements in energy efficiency, renewable energy integration and electricity market reforms by also establishing targets for year 2030 such as including at least 32 % renewable energy penetration and a 32.5 % improvement in energy efficiency;
- **2019 – European Green Deal** [40] defined the European strategy for achieving climate neutrality by 2050: «*it aims to cut emissions by at least* 50 % *by 2030, rising towards* 55 %,

while legally binding the 2050 neutrality goal through the European Climate Law»;

- **2021 – COP26 Glasgow Climate Pact** [41, 42]: it reinforced the implementation of the Paris Agreement and highlighted the urgency of stronger short-term mitigation actions: it called for accelerated reductions in greenhouse gas emissions during the current decade, emphasizing that limiting global warming to 1.5 °C requires rapid and sustained emission cuts and the results were finalized with the so-called *Glasgow Climate Pact* which aims to limit the temperature anomaly to 1.5 °C;
- **2021 – EU Climate Law and "Fit for 55" package** [43, 44]: the European Union formally adopted the *European Climate Law*, making the 2050 climate neutrality target legally binding while, in parallel, the *"Fit for 55"* legislative package established the intermediate objective of reducing net greenhouse gas emissions by at least 55 % by 2030 compared to 1990 levels[7];
- **2023 – COP28 and the UAE Consensus** [45, 46]: it represented a significant political milestone because, for the first time, the final agreement explicitly recognized the need to transition away from fossil fuels in energy systems, but the *UAE Consensus* also promoted the objective of tripling global renewable energy capacity and doubling the average annual rate of energy efficiency improvements by 2030 in order to support the achievement of the *Paris Agreement* targets – according to the stocktake, global greenhouse gas emissions must be cut by 43% by 2030, compared to 2019, to limit warming to 1.5 °C even if member nations are not currently on track to achieve these targets though;
- **2024 – COP29 Baku Climate Conference** [47, 48]: it mainly focused on implementation strategies and climate finance mechanisms to support developing countries in mitigation and adaptation measures, such as developed countries committed to mobilizing $300 billion annually by 2035 to support developing nations, the rules for global carbon markets have been finalized, rendering emission trading mechanisms fully operational both between states and through a new centralized UN market, and the fund established to assist the most vulnerable nations affected by climate disasters has been fully institutionalized;
- **2025 – COP30 Belém Summit** [49, 50, 51]: it's the most recent COP summit which was held in Belém, on the edge of the Amazon rainforest, in November 2025 where one of the most significant outcomes was the commitment to triple funding for climate adaptation by 2035, with a focus on the most vulnerable countries – however, participating nations failed to agree on a roadmap for transitioning away from fossil fuels because of strong disagreements among countries since the final text approved by COP30 president André Corrêa do Lago did not include any explicit reference to fossil fuels, representing unfortunately a step back compared to previous COP agreements, and observers also expressed disappointment over the lack of stronger national climate plans given that the current commitments would lead to only about a 12 % reduction in global emissions which is far below the roughly 60 % reduction needed to keep the 1.5 °C warming limit still achievable.

[7] it's useful to clarify the relationship among the three mentioned initiatives: *European Green Deal* is the strategy (political direction, so a political roadmap or policy vision but not a law), while the *EU Climate Law* is the legally binding framework (legal backbone so, unlike the *Green Deal*, it's legally enforceable), and *Fit for 55* is the concrete legislative package to implement the 2030 target (set of laws that implement the *Climate Law* targets)

Following the previous overview of the major climate-policy milestones, fig. 6 provides an overview of historical greenhouse gas emissions and their projected evolution under different policy assumptions, translating the political ambitions discussed above into quantitative climate outcomes. At present, global greenhouse gases emissions are $\approx 54.5\,\text{Gt}\ CO_2e$ per year[8]. From this starting point, the figure compares a set of increasingly stringent mitigation scenarios. The "no climate policies" baseline illustrates a counterfactual trajectory in which emissions continue to rise throughout the century, leading to end-of-century warming of approximately $4.1 - 4.8\,°C$. The "current policies" pathway, which is based only on measures that are already implemented or legally adopted, slows the rate at which emissions increase relative to economic growth, but does not fully reverse the upward trend in global emissions and would lead to an estimated warming of about $2.5 - 2.9\,°C$ by 2100. A further improvement is observed under the "pledges & targets" scenario, which assumes full implementation of *Nationally Determined Contributions* (NDCs)[9] and long-term net-zero commitments announced by countries under the Paris framework. In this case, projected warming decreases to approximately $2.1\,°C$, but still does not reach the "well below $2\,°C$" ambition formalized at COP21. Finally, the figure illustrates the emission trajectories consistent with limiting warming to $2\,°C$ and $1.5\,°C$, as assessed by the Intergovernmental Panel on Climate Change in its *Special Report on Global Warming* of $1.5\,°C$ [54]: these pathways require a rapid and sustained decline in global emissions over the coming decades, reaching net-zero around mid-century for the $1.5\,°C$-consistent trajectory – the gap between current policies and the $1.5\,°C$ pathway highlights that global emissions would need to decline several times faster than the historical rate of reduction observed so far.

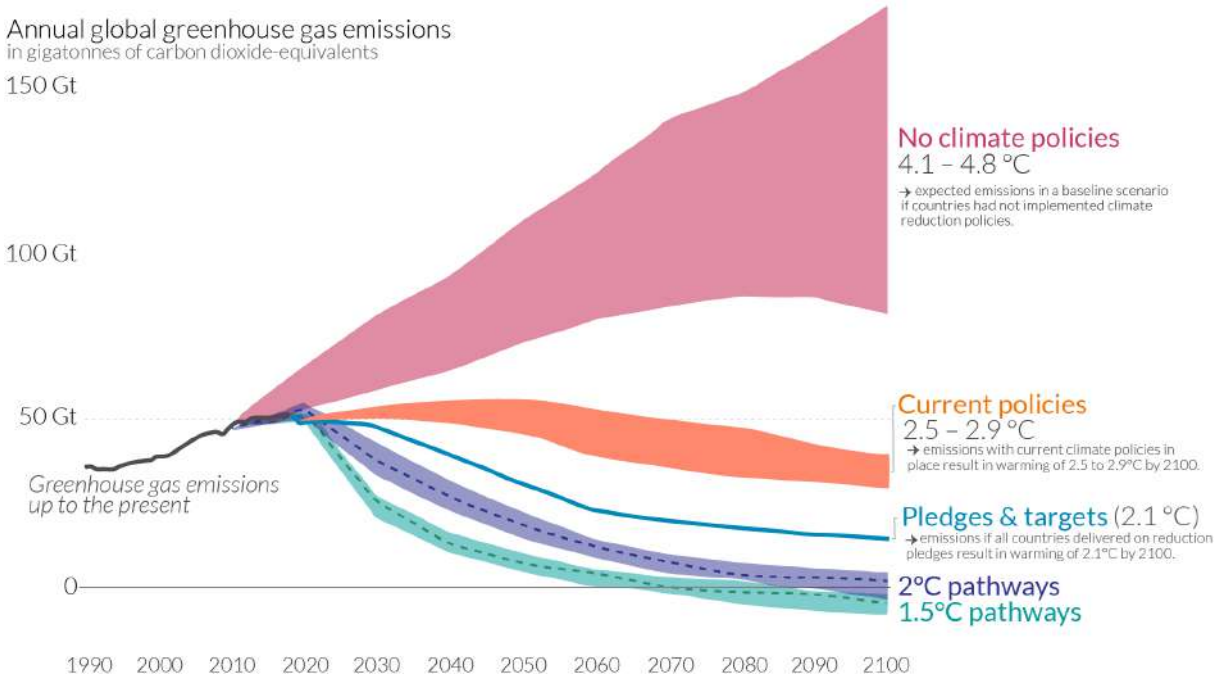


Figure 6. Global annual greenhouse gases emissions and warming scenarios (adapted from [26]) – the analysis refers to 2023 conditions

[8] this is data from [52] referred to year 2024, now including land use

[9] *Nationally Determined Contributions* (NDCs) are country-specific climate action plans detailing how each nation will reduce greenhouse gas emissions and adapt to climate impacts – they are the central pillar of the Paris Agreement, representing individual countries' pledges to help limit global warming [53]

To better understand the previous discussion on the required emission reductions, one can look at figs. 7 and 8 that are the so-called mitigation curves, which give a visual explanation of how fast global CO_2 emissions would need to fall to keep global warming below targets such as 1.5 °C or 2 °C. The mitigation curves are based on the concept of a carbon budget, namely the amount of CO_2 humanity can still emit while maintaining a certain probability of staying below a temperature threshold [6]. The two figures are connected to studies by *Michael Raupach* on cumulative emissions and warming (see [55, 56] for more), and are therefore sometimes referred to as Raupach curves. Figures 7 and 8 show time on the x-axis (from 1950 to 2100 in this case) and the annual global CO_2 emissions on the y-axis; furthermore, there is usually a historical emissions curve, which is rising until recent years, and several coloured curves showing hypothetical future pathways. Each future pathway simply answers this question: "If global emissions had peaked in year X, how quickly would emissions need to decline afterward to stay below 1.5 °C or 2 °C?" or, in other words, "Given a fixed remaining carbon budget, what annual emissions pathway is required if mitigation starts in a certain year?"[10]. For example, with reference to the case of fig. 7:

- if emissions had peaked around 2000, the world could have reduced emissions gradually, namely a mitigation rate in the order of 4 %/yr;
- if emissions had peaked in 2020, required reductions present monumental mitigation rates in the order of 10÷15 % annual reductions;
- if action is delayed further, the curves become almost vertical – for instance, constant emissions for 8 years starting from 2020 will use up the remaining carbon budget.

Instead, for the case of 2 °C temperature anomaly target represented in fig. 8, the decrease of the emissions must still decrease rapidly, although less sharply than in the 1.5 °C scenario (this is because, in year 2018 as reported in [54], the allowable carbon budget for the 1.5 °C temperature anomaly target is far smaller, namely 420 Gt CO_2 compared to 1170 Gt CO_2 for the 2 °C temperature anomaly target – still these are estimations with a certain likelihood). Indeed, with reference to the case of fig. 8:

- constant emissions for 10 years lead to a required mitigation rate of 10 %/yr;
- starting mitigation in 2020 would have required mitigation rate of 6 %/yr;
- starting mitigation in 2000 would have required mitigation rate of 2 %/yr.

It is important to emphasize that these data are somewhat dated, having last been updated on January 15, 2020 [57]. The curves therefore represent different starting dates for serious mitigation, under the constraint of the same total allowable cumulative emissions – the later mitigation starts the more of the budget has already been spent, the less room remains afterward, the faster emissions must decline later.

The aforementioned behaviour, namely the entire logic of the mitigation curves, comes from one of the most important findings in modern climate science: the atmosphere responds mainly to the total accumulated CO_2, not just emissions in a single year [55, 56] meaning that global

[10] these curves are reported both for past and future peaking years, where "past" and "future" are defined relative to 2019, the year in which the study was published

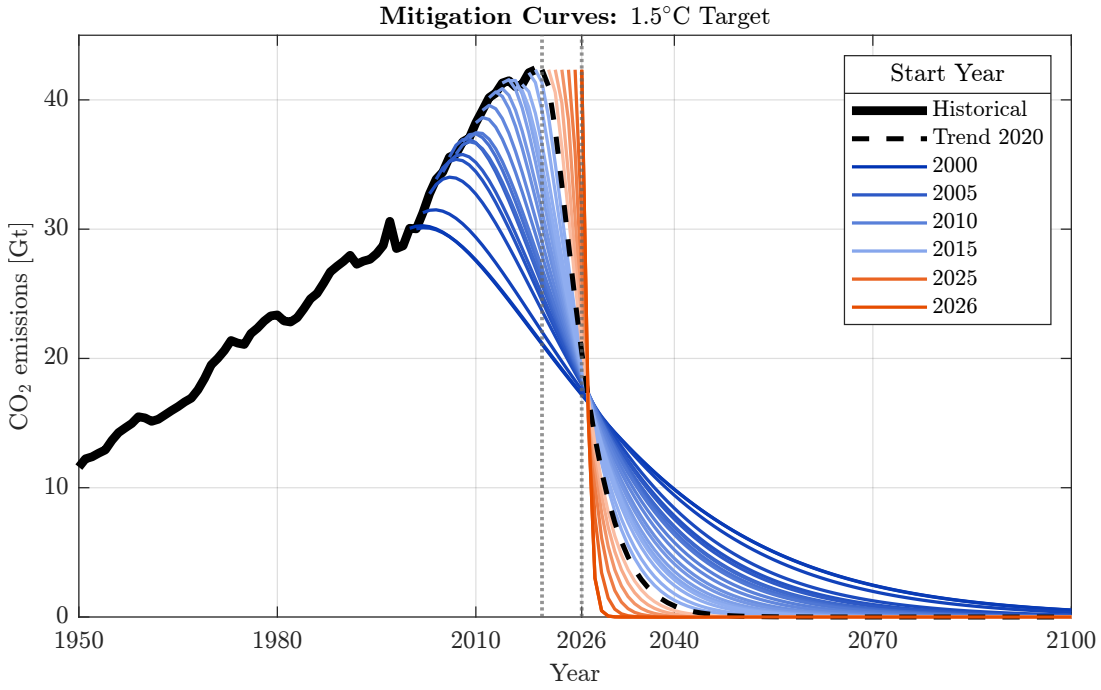


Figure 7. CO_2 mitigation curves for 1.5 °C temperature anomaly target (adapted from [57])

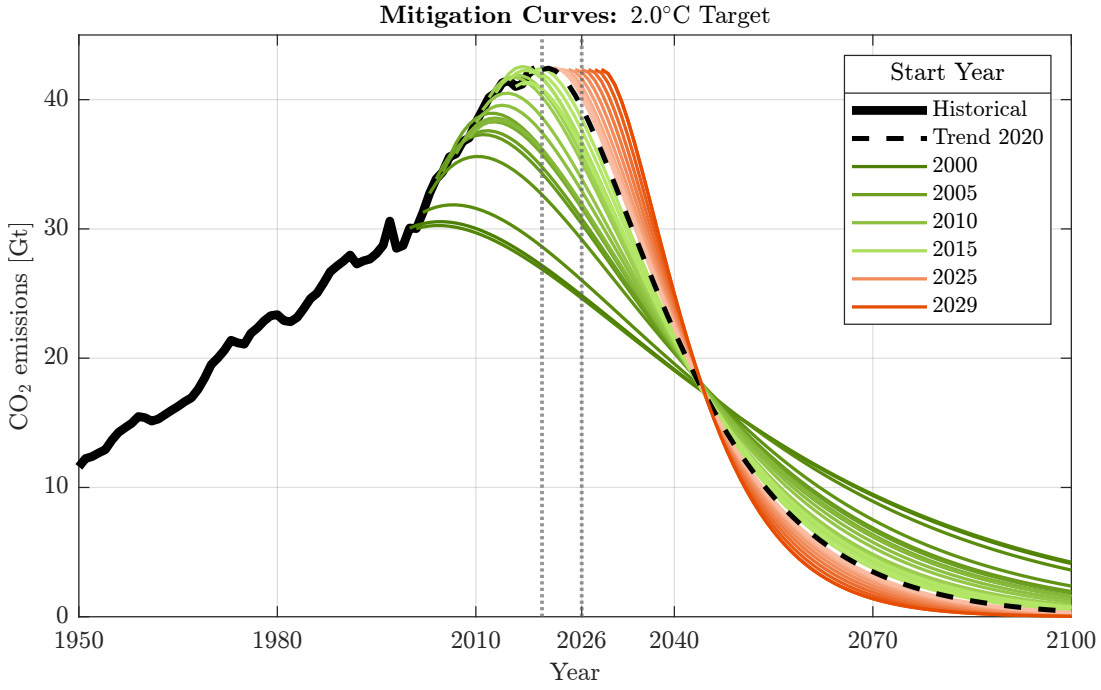


Figure 8. CO_2 mitigation curves for 2 °C temperature anomaly target (adapted from [57])

temperature increase is approximately proportional to cumulative CO_2 emissions[11]. Thus, with net positive emissions the atmospheric CO_2 continues increasing; consequently, global warming continues. This is why stabilizing emissions is not enough: global emissions must eventually decline toward net zero if we want to limit the temperature anomaly (this is another explanation

[11] this perfectly matches with the concept of carbon budget introduced with [6, 25], and it's often referred to as the carbon-budget framework

of the trends reported in fig. 6 as well as of the ones of figs. 7 and 8). Thus, every year of high emissions consumes more of the remaining carbon budget, leaving less room later which forces faster future reductions. Given that the aforementioned drastic reduction rates of CO_2 are nearly unfeasible for both temperature anomaly targets, the only way to stay within this budget is by generating substantial "negative" emissions, essentially removing CO_2 directly from the atmosphere in an active manner. Indeed, for instance as in figs. 7 and 8, "net negative emissions" would mean that some curves go below zero later in the century – this means that humanity would not only stop emitting CO_2 but would actively remove CO_2 from the atmosphere. Examples of negative-emission technologies include afforestation, BECCS (bioenergy with carbon capture and storage), direct air capture – however, [57] cautions that these technologies currently have significant limits. An example of how negative emissions can be managed is reported in fig. 9, which illustrates the same concept of figs. 7 and 8 but it implements the concept of negative CO_2 emissions. After the present day, which was year 2019 for the time in which the figure was built, the figure shows a family of possible mitigation pathways, namely the thin black trajectories. The area above zero, namely the brown region, represents future positive emissions whilst the area below zero, namely the green region, represents future negative emissions. Although the shapes of the different mitigation paths differ over time, they are all built so that their total net cumulative CO_2 emissions are approximately the same, hence leading to achieve approximately the same final warming level that is $\approx 1.5\,^{\circ}C$ in this example (this behaviour is again strictly linked to the carbon budget concept). Thus, one pathway may reduce emissions very rapidly, another may reduce them more slowly and rely more heavily on future negative emissions but, if the net area under the curve is similar, the expected long-term warming is also similar[12]. In other words, by following rapid mitigation pathways, less cumulative positive emissions occur and there is less need for future negative emissions and also lower overshoot risk, while instead with delayed mitigation pathways the emissions remain high longer, the positive-emission area becomes larger and stronger future negative emissions are required (this is the case of the black thick line).

To make a link with the currently active policies, it has been mentioned that the current policies pathway results in a partial decoupling of emissions growth which means that economies may become somewhat more efficient and emissions growth may slow but emissions are not decreasing fast enough. So, although the slope of emissions growth changes, the world still remains far above the mitigation curves compatible with $1.5\,^{\circ}C$. In other words, emissions are improving relative to a worst-case scenario, but not enough to stay within the remaining carbon budget. Figure 10[13] is conceptually connected to exactly the same physical principle behind the

[12] this is the reason why the carbon budget framework is so powerful: the precise timing and shape of the pathway matter for many reasons, such as the overshoot concept, but the dominant control on final warming is the total cumulative net CO_2 emitted; in other words, one of the most important aspects of this figure is that it shifts the focus away from a single year's emissions and toward the integral over time and, besides other possible downsides, this is why the area under the curve is what matters physically

[13] the thin black line represents observed historical global warming as a function of cumulative emissions from 1850 to 2019, and the accompanying purple shaded band and central line denote the estimated share of human-induced historical warming; the vertical purple bar highlights the assessed range of human-induced warming specifically for the 2010–2019 period. Instead, the coloured lines and shaded regions represent climate model projections across five *Shared Socioeconomic Pathways* (SSP1-1.9, SSP1-2.6, SSP2-4.5, SSP3-7.0, and SSP5-8.5) and the thick central lines show the median temperature estimates, while the matching coloured shading outlines the assessed "very likely" range of warming, accounting for all anthropogenic forcing agents; the thin coloured spaghetti lines

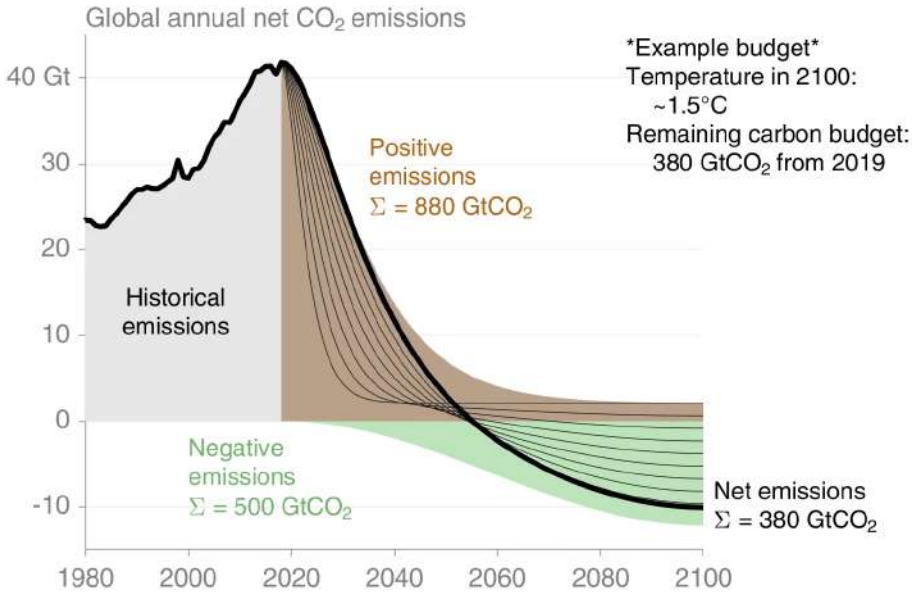


Figure 9. Global annual net CO_2 emissions pathways to limit global warming to 1.5 °C (adapted from [57]) – example starting from year 2019 combining different possible mitigation curves by exploiting the combination of both positive and negative emissions in order to match the remaining carbon budget so to keep the temperature anomaly precisely at 1.5 °C

mitigation curves reported in figs. 7 and 8 and to the dashed curves reported in fig. 3. Indeed, the common foundation is that global warming is approximately proportional to cumulative CO_2 emissions by means of an almost linear relation. This relationship is described by the so-called *Transient Climate Response to Cumulative* CO_2 *Emissions* (TCRE) – see section A.1 for more. In other words, the observation that can be drawn from figs. 3 and 10 is that global warming is approximately linear with cumulative emissions as well as with atmospheric concentration. Figures 3 and 10 are based on the same physics[14] and they are basically conveying the same message: indeed fig. 10 conveys that $\Delta T \propto$ cumulative CO_2 emissions, and this is basically the TCRE framework, while fig. 3 conveys that $\Delta T \propto$ atmospheric CO_2 concentration – the difference is mainly what variable is used on the x-axis but, since they are strictly linked (see section A.2 for more), then the the figures are describing different parts of the same causal chain. The result, which is particularly clear for fig. 10, can be hence formulated as:

$$\Delta T \approx \alpha \, Q_{\mathrm{E}} \tag{1}$$

where α is the TCRE and Q_{E} are the cumulative historical emissions. This near-linearity is extraordinarily important because it makes precisely the concept of carbon budgets possible. Basically indeed, as shown in fig. 10, stabilizing temperature requires yearly net CO_2 emissions to become zero because, as long as net CO_2 emissions are positive, then cumulative emissions continue increasing hence warming continues increasing. Instead, if yearly net CO_2 emissions suddenly become zero, the cumulative emissions stop increasing and so atmospheric CO_2 approximately

represent individual model simulations.

[14] anyway, besides the x-axis parameter that will be discussed later, one has to make a very important distinction: fig. 10 focuses on the global mean temperature anomaly while fig. 3 focuses on the regional maximum daytime temperatures anomalies with the solid lines and on the global mean temperature anomaly, but with reference to the worst-case scenario for what concerns the carbon dioxide emissions

stabilizes leading to the fact that global temperature approximately stabilizes[15]. Furthermore, to be more precise, if net zero **greenhouse gas** emissions are also reached and sustained[16], the global surface temperature is projected to gradually decline after an earlier peak. The last statement calls however for the *overshoot* concept: it occurs when the global surface temperature exceeds a specified target, such as 1.5°C, before being brought back down through sustained net negative emissions. However, such an overshoot may entail irreversible risks for fragile systems such as the extinction of animal species, the loss of unique ecosystems like coral reefs and Arctic sea-ice, and impacts from ice-sheet melt that could eventually cause several meters of sea-level rise over very long timescales [6].

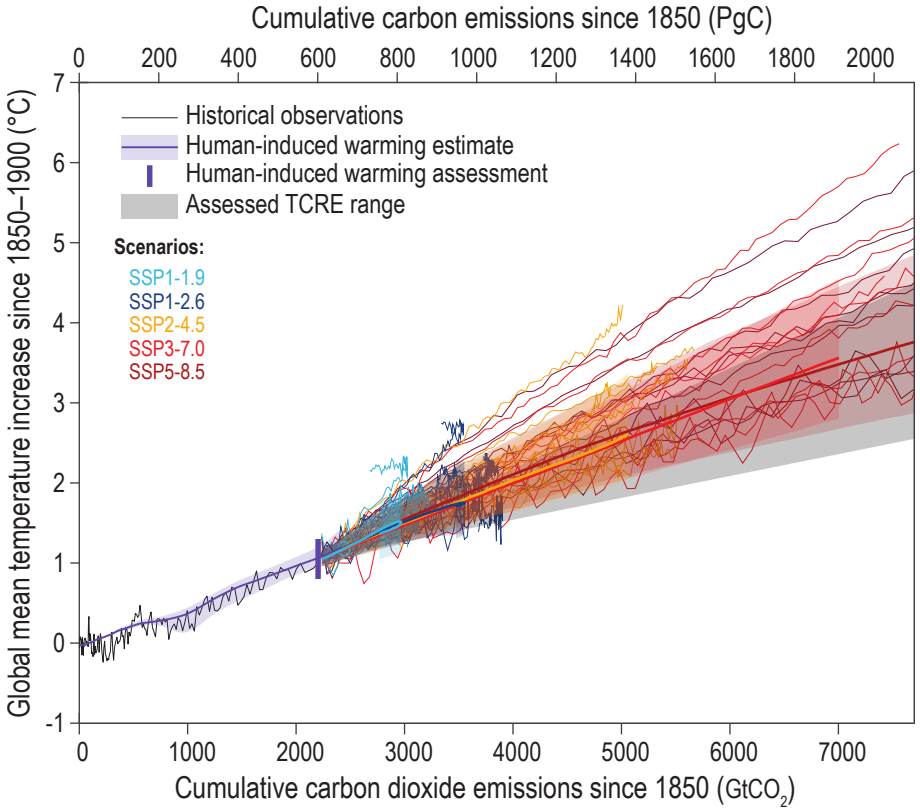


Figure 10. Illustration of the relationship between cumulative carbon dioxide emissions and global mean surface air temperature increase (adapted from [6])

As a conclusion for this section, one can state that the macroscopic data underscores that contemporary climate change is, with very high likelihood, a direct consequence of anthropogenic greenhouse gas accumulation. The robust, quasi-linear relationship between cumulative emissions and global warming – formalized by the Transient Climate Response to Cumulative CO_2 Emissions (TCRE) – demonstrates that stabilizing global temperatures strictly depends on achieving net-

[15] graphically, looking at fig. 10 or at fig. 4, we would stop at a certain x-axis position and hence, due to the existing linear relation between global temperature anomaly and CO_2 concentration, temperature would stop rising significantly – this consideration is also aligned with the carbon-budget framework

[16] it's indeed important to make the distinction between CO_2 and greenhouse gases net zero: indeed net zero greenhouse gas emissions take longer to achieve than net zero CO_2 because some non-CO_2 emissions, such as methane and nitrous oxide from agriculture, are considered "hard-to-abate" and cannot be fully eliminated with currently available technology – consequently, these residual non-CO_2 emissions must be balanced by net negative CO_2 emissions

zero emissions. Within this framework, the remaining carbon budget represents a non-negotiable physical constraint: any delay in mitigation rapidly erodes this threshold, locking in severe future warming or forcing a risky reliance on unproven carbon-removal technologies. Consequently, preventing dangerous overshoot requires moving beyond aggregate global targets. All this demands a granular, sector-by-sector analysis of emissions to effectively guide targeted decarbonization, technological innovation, and widespread electrification across the global economy.

0.1.3 Sectoral emissions and the need for electrification

Given the previous analyses, it is now necessary to investigate the possible pathways for achieving climate objectives, namely limiting global warming to 1.5 °C or 2 °C. In this context, since it has been mentioned that, with very high likelihood, the driver of the global warming are the greenhouse gas emissions, a useful starting point consists in analysing precisely the share of greenhouse gas emissions by sector, since this allows the identification of the activities responsible for the largest share of greenhouse gas emissions and, consequently, the sectors where mitigation actions are likely to be the most effective and technically meaningful[17]. Figure 11 allows to understand that there is a range of sectors and processes contribute to global emissions, which means there is no single or simple solution to tackle climate change and focusing on one single sector is insufficient. Precisely analysing fig. 11, which depicts the share global greenhouse gas emissions by economic sector for year 2016[18], it emerges that the largest contribution derives from energy-related activities, in particular energy use in buildings and industry as well as transportation – anyway, even within the energy sector, which accounts for almost three-quarters of emissions, there is no simple fix [58]. As shown in fig. 12, which reports slightly more updated data for year 2020 and with a slight different classifications of the sectors compared to fig. 11, out of a total of approximately 46.9 Gt CO_2e emitted worldwide in 2024, about 32.6 % was associated with electricity and heat generation, while transportation accounted for around 15.8 % of total emissions[19] – these sectors still rely heavily on fossil fuels, even though a transition toward renewables is underway, albeit at a pace that falls short of what is necessary.

[17] indeed, prioritizing interventions in highly emitting sectors is essential in order to maximize the impact of decarbonization strategies and accelerate the transition toward a low-carbon energy system

[18] at the time of writing of this document (≈ May 2026), this is the most recent picture available

[19] fig. 12 can be analysed in order to explain and understand the quite opposite overall trend in the magnitude of the emissions in time between the World and the Europe region between 1990 and 2020: the opposite trend mainly reflects the different pace of industrial development, energy transition, and climate policy implementation across world regions; at the global scale, the growth in emissions was largely driven by the rapid industrialization and economic expansion of emerging economies, accompanied by a substantial increase in energy demand (see [59] for more: it shows that energy use has increased dramatically since the Industrial Revolution in the late eighteenth century and, despite the growing deployment of low CO_2 energy sources, fossil fuels still dominate the global energy mix); furthermore, electricity generation, heavy industry, and transportation continued to rely predominantly on fossil fuels, leading to a steady rise in worldwide emissions; in particular, the electricity and heat sector remained the largest contributor to global greenhouse gas emissions, due to the extensive use of coal in rapidly developing economies; in contrast, Europe achieved a remarkable reduction in greenhouse gas emissions over the same period (a reduction of ≈ 34.5 % was observed); however, not all sectors contributed equally to this decline: for instance, transportation represented one of the most challenging sectors for European decarbonization since its emissions decreased much more slowly and, in some cases, even increased compared with 1990 levels because of the continuous growth in mobility demand; this explains why the electrification of transportation, together with the decarbonization of electricity generation, is currently considered one of the key strategies for achieving long-term climate targets; another relevant aspect concerns the partial relocation of energy-intensive industrial activities from Europe to other world regions: part of the apparent reduction in European territorial emissions is therefore linked to the outsourcing of carbon-intensive production processes, whose associated emissions are now generated abroad

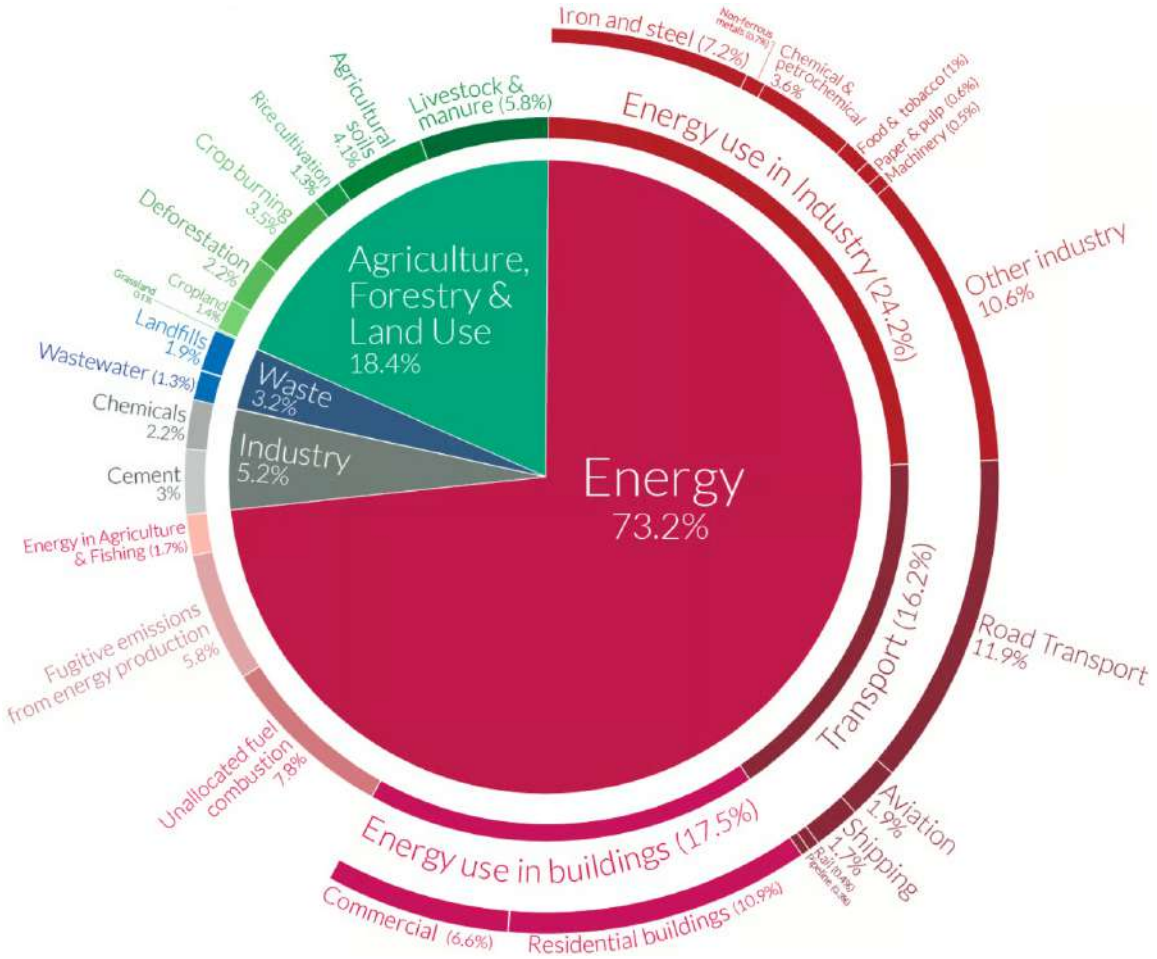


Figure 11. Global greenhouse gas emissions by sector, shown for year 2016 (adapted from [58])

Given the intrinsic differences among the sectors that are involved in the CO_2 emissions, and also what was introduced as partial explanation of fig. 12, the transition to a low-carbon future requires distinct strategies for different sectors. While the energy supply sector is expected to lead the way, "hard-to-abate" sectors like transportation face unique technological and structural barriers. In particular one can distinguish:

- **Energy Supply (Electricity)** [24]: decarbonizing the electricity sector is one of the fastest and most cost-effective ways to scale up mitigation, namely the energy supply sector is expected to reach net zero CO_2 emissions significantly earlier than others; this is mainly due to the cost-effectiveness because several low-emission technologies, such as solar and wind energy, have seen unit cost decreases of 85% and 55% respectively since 2010, and are now cheaper than fossil fuel-based electricity in many regions;
- **The "hard-to-abate" sectors (industry, transport, buildings)** [24]: these sectors generally reach net zero CO_2 emissions later than the energy sector, and their transitions are more complex because they rely on deep structural changes and the development of new technologies; for instance:
  - reducing industrial emissions requires coordinated action across entire value chains;

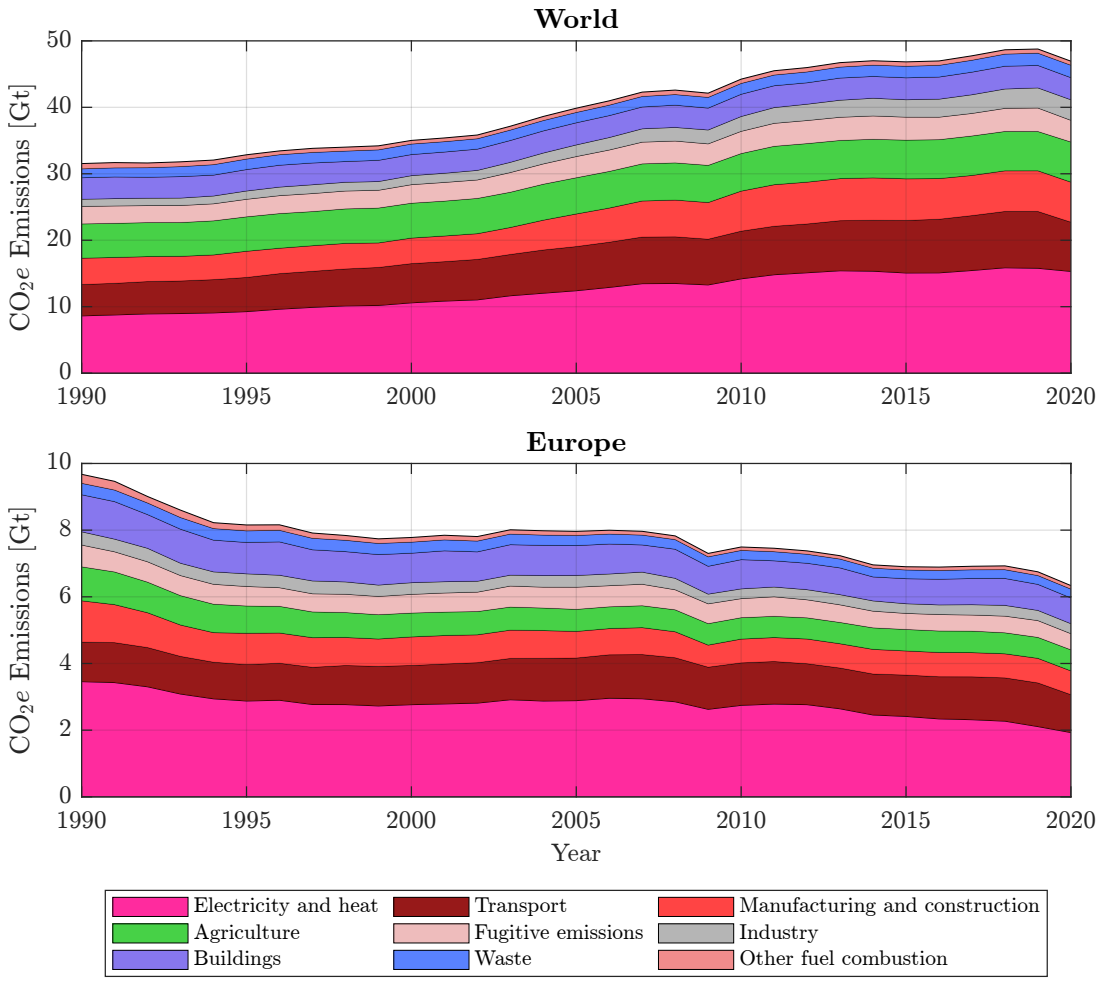


Figure 12. Comparison between *World* and *Europe* greenhouse gas emissions by sector from 1990 to 2020 measured in terms of carbon dioxide-equivalents; land-use change emissions are not included (adapted from [60])

- for the transport sector, the transition is led by electric vehicles for land-based transport, which have high potential to reduce emissions on a life-cycle basis, while for aviation and shipping, mitigation is more difficult because high energy-density fuels are required for long distances and the transition will likely depend on the usage of sustainable biofuels and low-emission hydrogen derivatives;
- for buildings the mitigation involves low-emission construction materials, highly efficient building envelopes, and the electrification of heating and cooling.

Nevertheless, as reported in [59], the continuous growth in global energy demand (and considering also that, while coal consumption is declining in several regions of the world, the use of oil and natural gas continues to expand rapidly) makes the transition from fossil fuels to low-carbon energy systems increasingly challenging. Thus, one of the major upcoming challenges is the development and deployment of low-carbon energy sources capable not only of satisfying the growing energy demand but also of progressively replacing fossil fuels within the global energy mix since their high polluting capability (recall in this regard the concept of carbon budget).

As presented in [61, 62], the primary drivers for the transition will be:

- renewable energy generation, such as solar and wind, which are enabled by the smart grids (indeed, a more electrified economy demands greater system flexibility to integrate high shares of variable renewables);
- advanced energy storage, which will be used to store energy from renewables production for later dispatch to meet peak load demand due to their intrinsic intermittency caused by weather and environmental conditions;
- electrification of heating and transport sector: indeed, the substitution of conventional internal combustion engine vehicles with electric alternatives can substantially reduce greenhouse gas emissions, particularly if the electricity is produced from low-carbon sources;
- alternative energy carriers, such as hydrogen and bioenergy for applications that are difficult to electrify, also referred to as "hard-to-abate" sectors;
- Carbon Capture Utilization and Storage (CCUS) which enables the capture of carbon dioxide generated by combustion or heavy industrial processes, namely to contribute reaching the emission goals and trying to match the carbon budget as a balance between positive and negative greenhouse gases emissions.

A promising solution amongst the previous ones to the problem is what is currently being seen nowadays: energy production is increasingly shifting toward renewable energy sources, as part of the broader transition to a sustainable and low-carbon economy. In particular, the acceleration of global electrification in several sectors, especially transportation one, is a central pillar of the clean energy transition required to reach net-zero emissions and this fact stems from its environmental and practical advantages over other forms of energy [20]. Specifically, the electrification contributes to decarbonization in two primary ways: first, the direct displacement of fossil fuels with low-carbon electrical alternatives and, second, efficiency gains since electric devices are often significantly more efficient than their combustion-based counterparts [20]. Yet one has to keep in mind some downsides of this revolution such as the intrinsic intermittency of renewables, increased pressure on electricity grids, dependence on critical minerals and environmental consequences of mining – still it's possible to work and possibly solve the aforementioned current shortcomings related to the power system weakness.

To detail the electric-based technologies that will likely constitute the low-carbon value chain, one can mention [20]:

- low-carbon electricity generation such as renewables production and nuclear power;
- in the energy storage sector, battery storage and Vehicle-to-Grid (V2G) technologies will become relevant;
- in the transport sector, Battery Electric Vehicles (BEVs), and Plug-in Hybrid Electric Vehicles (PHEVs) are expected to take over for the road sector, while for shipping and aviation sector some attempts are being made related to hybrid electric aircrafts and ships – this will be strictly related to advanced batteries based on specific chemistries such as Li-ion, Li-S and Li-air;
- direct electrification of heating and cooling, for instance by means of industrial heat pumps

and electric boilers as well as electric cooking.

Thus one can summarize by saying that the widespread electrification is a pillar of the net-zero transition, anchored by the energy sector's move toward low-cost renewables. However, the pace of change is limited by societal and physical inertia, which [57] likens to an "oil tanker" that *cannot turn on a dime*.

0.2 Electrification of the transport sector and related challenges

As highlighted in the previous section and as visible from fig. 12, transport is one of the largest contributors to global greenhouse-gas emissions since it accounts for $\approx 16\,\%$ of total global emissions, and it's also considered one of the strategic sectors for the electrification towards a low-carbon economy, though its feasibility varies significantly across different transport modes and it will require structural shifts in the modes used to move people and freight (indeed, while electricity is already prevalent in the buildings and industry sectors, the transport sector represents the largest proportional shift in energy use) [20].

Furthermore, [63, 64] make an important distinction: transport is repeatedly identified as a critical bottleneck for climate targets because electricity generation can decarbonize relatively fast with renewables, but transport currently still directly burns fossil fuels at the point of use; this is precisely the reason for which many transition frameworks distinguish between decarbonizing electricity supply and and electrifying final energy demand, where the second step requires exactly transport electrification and it's precisely the goal of the transport electrification.

In addition, something that complicates as well the decarbonization path of the transport sector is that transportation volumes are going to evolve in the future. Indeed, as population growth and rising incomes drive a continuous surge in global mobility, [65] projects that overall transport demand (measured in passenger-kilometers[20]) will continue rising significantly through 2050, which will further complicate efforts to reduce CO_2 emissions – under the current ambition scenario, passenger transport demand increases by about 79% compared to 2019, reaching roughly 110 trillion passenger-kilometres by 2050 [65]. Moreover, growth will be uneven across regions: the strongest increases are expected in emerging economies, while high-income regions show comparatively lower increases [65]. Figure fig. 13 describes precisely the passenger-kilometer outlook in the different world region[21], showing the aforementioned trends.

One of the reasons why transport is considered a strategic sector for direct electrification[22] is that it sits exactly at the intersection of the three main goals of the energy transition [64]:

- **decarbonization** [67] and **direct displacement of fossil fuels** [20]: indeed, as visible from figs. 11 and 12, the transport's is one of the few sectors where emissions have

[20] *passenger-kilometer* is a unit of transport measurement representing the carriage of one passenger over a distance of one kilometer – it is the standard metric used to calculate the actual distance travelled by passengers across various transit modes and it's essential for evaluating transport activity and emissions

[21] ENEA: East and Northeast Asia; LAC: Latin America and the Caribbean; MENA: Middle East and North Africa; SEA: Southeast Asia; SSA: Sub-Saharan Africa; SSWA: South and Southwest Asia; TAP: Transition economies and other Asia-Pacific countries; UCAN: United States, Canada, Australia and New Zealand [65]

[22] this is especially true for road transport and light vehicles, and in particular for EVs that are assumed to replace the traditional passenger cars [20, 66]

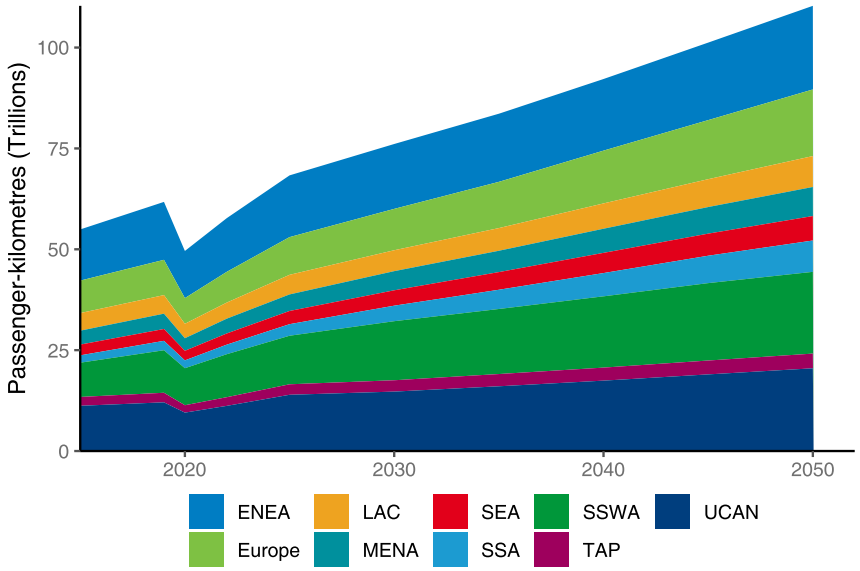


Figure 13. Passenger transport demand by region under the Current Ambition scenario in years 2019 – 2050 in different world regions (adapted from [65])

historically remained stubbornly high or even increased, especially in Europe and globally since 1990, but, as mentioned precisely with figs. 11 and 12, reducing transport emissions can substantially cut down the global emissions[23];

- **energy efficiency** represents one of the main advantages of vehicle electrification: indeed, EVs convert over 77 % of the electrical energy from the grid to power at the wheels whereas conventional gasoline vehicles only convert about 12÷30 % of the energy stored in gasoline to power at the wheels whilst the rest is converted in heat during the thermal cycle [68] – somehow electrification is not only about using cleaner energy but it is also about using far less energy for the same mobility service, namely it reduces primary energy needs;
- **energy security**: traditional transport depends overwhelmingly on imported oil for those countries which do not have their own, and this is particularly important in Europe and Italy, which are highly dependent on imported fossil fuels (energy security has become a major European priority since the Russian invasion of Ukraine, as shown by the recent *RePowerEU plan* presented by the European Commission) [66, 69].

Furthermore, unlike some "hard-to-abate" sectors, especially road transport already has technologically quite mature electric alternatives (instead, different means of transport still are facing some limitations and challenges). Focusing in particular on road electric vehicles, choice which will be justified in a while, their advantages have been demonstrated in many aspects, such as lower operational cost, improving public health (EVs reduce NO_x emissions and urban air pollution), acting as flexibility resource for renewable grids and interacting positively with renewable expansion through effective system integration [70]. To be fair, EVs have also some drawbacks compared to ICE vehicles [68]: they currently have a shorter driving range than most conventional vehicles although they are improving, and the recharge time is still fairly lengthy.

[23] anyway, as previously highlighted, this drop in emissions relies on the assumption that electricity generation itself is being decarbonized concurrently, being for instance entirely produced by renewables sources [20] – identifying the source of the electricity used to power electric vehicles remains one of the key issue in the decarbonization topic

Figure 14 illustrates the near-term trajectory of global CO_2 emissions across major transport modes from the year 2000 through a projected 2030 target window[24] [71]. The chart shows a steady increase in global transport emissions over the first two decades of the century, which was heavily underpinned by the expansion of two primary sub-sectors, namely passenger road vehicles and road freight vehicles. Post-2020, the Sustainable Development Scenario maps out a permanent inflection point: instead of rebounding along historical trends, total transport emissions begin a sustained downward trajectory, projected to fall below 7.5 Gt by 2030 [20], which represents the early decoupling of global mobility from fossil fuel consumption, driven primarily by the rapid commercial scale-up of electric vehicles and fuel-efficiency standards.

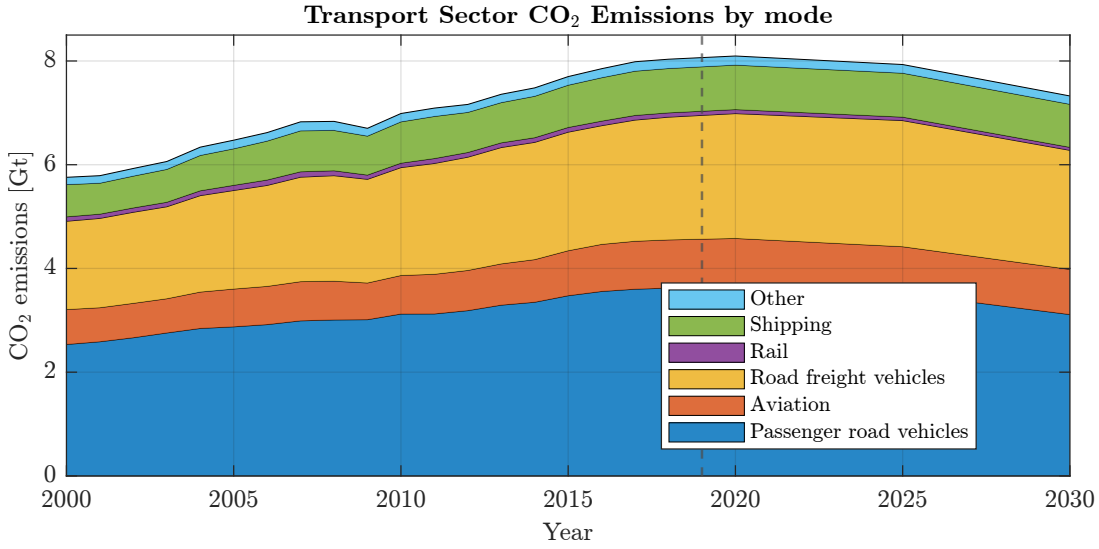


Figure 14. Transport sector CO_2 emissions by mode in the sustainable development scenario in the 2000-2030 years range (adapted from [72]) – data up to 2018 represent observed values while data from 2018 onward are projections (vertical dashed line represents precisely the 2018 threshold)

A more detailed analysis can identify the main sources of transport-related emissions, namely which transportation mode is contributing the most and/or and quantify the contribution of each transport mode. Indeed, in order to understand the mechanics of the decarbonization pathway, the transport sector must be evaluated by its component modes. In fig. 14 one can see different contributions in terms of emissions from different transportation segments [20, 71]:

- **Passenger road vehicles** account for 45.1% of transport emissions, which represents the single largest share of the transport carbon footprint: because it constitutes nearly half of the sector's emissions, it is the highest priority for short-to-medium-term climate policy;
- **Road freight vehicles**, such as highway heavy hauling trucks or box trucks, account for 29.4% of transport emissions, namely nearly a third of the sector's output;
- **Aviation** accounts for 11.6% of transport emissions by generating just under one billion tonnes of CO_2 annually (despite high public visibility, its raw emissions share is currently smaller than road freight);
- **International shipping** accounts for 10.6% of transport emissions, namely maritime

[24] for a slightly more updated data and broader forecast one can look at figure 3.16, page 154, of [20]

commerce generates a carbon footprint nearly identical to aviation, driven by the heavy fuel oil burned by global cargo fleets;

- **Rail and Pipelines** account for $\approx 3.2\,\%$ of transport emissions, where in particular rail travel is remarkably efficient since it contributes with a mere 1% of transport emissions due to widespread baseline electrification.

In general, the *Sustainable Development Scenario* (SDS)[25] highlights that different modes of transport will decarbonize at highly variable speeds – this difference is determined by asset operating lifetimes, the weight-to-power ratios required for propulsion, and the technological readiness of low-carbon alternatives. Concerning the data of fig. 14, one can notice that, as far as the whole world is concerned, the road transport is the dominant contributor to transport-related emissions, accounting for 74.5% of the total (road transports include the first two bullet points, namely *passenger road vehicles* and *road freight vehicles*). More in detail, the passenger travel deserves particular attention, since it makes up almost 50% of the total transportation emissions: thus, precisely for this reason, traditional passenger vehicle electrification is regarded as a key pathway towards the global sustainable energy transition [70, 75]. Indeed, studies like [76] have shown that electric vehicles generally exhibit lower life-cycle emissions than conventional fossil-fuel vehicles, even in regions where the electricity mix is not yet fully renewable – furthermore, the situation is expected to improve as the manufacturing processes improve as well as the power system energy supply becomes progressively less carbon-intensive. For these reasons, the combined decarbonization of the power sector and electrification of transportation, industry, and heating systems is considered a key strategy for achieving the long-term objectives established by international climate agreements, such as the ones described in section 0.1.2.

Thus, as shown in [20], it is forecast that, throughout the 2020s and 2030s, transitional technologies bridge the gap between conventional internal combustion engine models and full electric mobility regarding the privately owned passenger cars sector; hybrid electric car sales are projected to peak at roughly 15% of total car registrations in the early 2030s. As battery performance metrics improve, specifically regarding increased energy density, enhanced durability, and declining manufacturing costs, these intermediate hybrid powertrains will be entirely displaced by full battery electric vehicles (BEVs) by 2050 [20]. Eventually, despite some world regions may continue to sell conventional ICE vehicles into the 2060s, the global passenger car segment will approach zero emissions by 2070, at which point traditional battery EVs will comprise nearly 90% of the active passenger car fleet [20]. Regarding the "hard-to-abate" sectors, such as freight, shipping and aviation, they pose extreme engineering challenges, largely associated with the required energy density[26] [20, 71] – though, currently some projects also in this sector are being

[25] the SDS is a normative scenario introduced in 2017 which does not try to predict what will happen, but instead describes what would need to happen in the global energy system to achieve a set of sustainability goals simultaneously, namely it is essentially a pathway for transforming the global energy system – it was designed to achieve three major objectives together, that are the climate stabilization, universal energy access and cleaner air [73]; later on in 2020 the *Net Zero Emission* (NZE) scenario was introduced because the SDS was no longer considered ambitious enough for a 1.5 °C pathway, since the IEA explicitly states that the earlier SDS achieved many sustainability objectives, but attention increasingly shifted toward full net-zero emissions by 2050 – thus, the NZE is instead a modeled transition pathway developed by the IEA that specifies the evolution of the global energy system required to limit global warming to approximately 1.5°C, through rapid decarbonization, large-scale electrification, efficiency improvements, renewable deployment, and low-carbon technologies [74].

[26] indeed, the sheer size and weight of current lithium-ion battery configurations or bulky hydrogen tanks severely

examined: current examples include the *More Electric Aircraft* (MEA) or its evolutions towards *Hybrid Electric Aircraft* (HEA) or *All Electric Aircraft* (AEA) [77].

Having established the pivotal role of transport electrification in reducing greenhouse-gas emissions, attention must be shifted from the system-level benefits of electric mobility to the technical challenges introduced at the component level. In Battery Electric Vehicles (BEVs), the demand for increased vehicle range, reduced mass and compact powertrains is driving the development of traction motors with progressively higher power and torque densities [78, 79, 80, 81] – in other words, to maximize vehicle space and minimize weight, traction motors undergo an aggressive process of downsizing, which dramatically increases both their rated power and torque densities per unit of active mass. As a consequence, increasing electromagnetic and thermal loads must be managed within increasingly confined machine volumes, making thermal management one of the main constraints in traction-motor design [79, 80, 82]. Conventional air-cooling solutions may become insufficient under these operating conditions. More effective cooling architectures are therefore increasingly adopted in which dielectric lubricants are brought into close proximity to, or into direct contact with, the stator windings [80, 82]. Although these fluids provide significant thermal benefits and are generally selected to be compatible with the insulation system, their presence modifies the dielectric environment surrounding the winding conductors – this modification can be particularly relevant with respect to partial-discharge inception: indeed, in practical oil-cooled machines, the insulation system may not be surrounded by a homogeneous liquid phase; thus, oil-wetted surfaces, gaseous regions, bubbles and oil-derived vapours may coexist, especially at elevated operating temperatures due to oil partial vaporization. Since partial discharges preferentially initiate in gaseous regions subjected to sufficiently high electric fields, these multiphase conditions may alter the discharge-inception mechanisms and may even reduce the Partial Discharge Inception Voltage (PDIV) compared with conventional air-insulated conditions. Consequently, the possible deterioration of partial-discharge performance associated with dielectric cooling fluids, and particularly any resulting reduction in PDIV, must be carefully assessed. Evaluating this possible PDIV deterioration constitutes the main objective of this work.

0.3 Objective of this work

As just briefly introduced, the main objective of this work is to investigate how the presence of dielectric cooling lubricants influences the Partial Discharge Inception Voltage (PDIV) of the insulation system adopted in EV traction motors. In particular, the experimental activity is aimed at evaluating possible variations, and especially possible reductions, in PDIV with respect to conventional air-insulated conditions. For this purpose, PDIV measurements are carried out on specimens designed to reproduce representative insulation configurations of hairpin-winding stators, with particular attention to the interphase insulation between adjacent conductors. The comparison is performed under different dielectric environments: a first set of measurements is performed in air and is used as a reference condition, and then the same or equivalent specimens are tested in the presence of dielectric lubricants. The purpose of this comparison is to determine

restrict the operational range and cargo capacity of heavy vessels and aircraft [20, 71]

whether the presence of the liquid phase, the associated vapour phase, or their coexistence modifies the inception of partial discharges and leads to measurable changes in PDIV. Particular attention is also devoted to the effect of operating temperature, since temperature can significantly influence the physical state of the cooling fluid, including its evaporation and vapour formation which is largely dependent on temperature – to investigate the effect of temperature on the vaporization, TGA analysis and FTIR analysis at different temperatures were carried out on the oils. The experimental results are therefore analysed together with the physico-chemical characterization of the tested lubricants, with the aim of identifying possible correlations between their composition, volatility and the observed PDIV variations.

The final goal is to provide an experimental comparison among different dielectric cooling fluids, in order to determine firstly whether their presence modifies the partial-discharge inception behaviour of hairpin-winding interphase insulation with respect to pure air cooling condition and, secondly, to assess whether some fluids exhibit a more favourable PDIV performance than others under the investigated conditions.

0.4 Thesis structure

The present thesis work is structured as follows:

Chapter 1: Theoretical background introduces the insulation and cooling systems adopted in EV traction motors; the chapter also recalls the theoretical background of partial discharges and PDIV, discussing the influence of temperature, gaseous inclusions and oil-derived vapours on discharge-inception phenomena.

Chapter 2: Materials and methods describes the investigated dielectric lubricants, the specimens used to reproduce a simplified hairpin-winding interphase insulation configuration, and the experimental setups and procedures adopted for PDIV measurements; the physico-chemical characterization techniques employed to investigate the thermal behaviour and composition of the fluids, namely TGA and FTIR, are also presented along with a brief description of the corresponding instrumentation.

Chapter 3: Experimental results reports the results of the physico-chemical analyses and of the PDIV measurements performed under the investigated conditions: the chapter presents the comparison between the reference air condition and the tests carried out in the presence of the different dielectric fluids and their vapours, also considering the effect of temperature.

Chapter 4: Discussion of results discusses the experimental results by comparing the behaviour of the tested dielectric lubricants and evaluating their influence on PDIV; particular attention is devoted to possible PDIV reductions with respect to air, to the differences observed among the fluids, and to investigate possible correlations between their physico-chemical properties and partial-discharge inception behaviour.

Chapter 1

Theoretical background

1.1 Rationale of the work

The scope and rationale of this thesis work can be introduced by examining the individual elements contained in its title, where each one identifies a specific aspect of the problem that will be studied:

Effects of Cooling Lubricants on the Partial Discharge Inception Voltage of Hairpin-Winding Interphase Insulation in EV Traction Motors.

The title identifies four elements that define the theoretical and experimental framework of the work:

- **Cooling lubricants**: as already introduced, these fluids are being increasingly adopted in high-power-density electrical machines to improve heat removal from the active parts – although they are selected to provide adequate dielectric compatibility, their presence modifies the electrical environment surrounding the winding conductors and may influence partial discharge inception.
- **Partial Discharge Inception Voltage**: as it will be formally defined later in this chapter, the PDIV represents the voltage threshold at which partial-discharge activity becomes detectable – in this work, the PDIV of the considered sample is used as the main electrical indicator to assess the influence of different cooling lubricants and of the gaseous phases associated with them.
- **Hairpin-winding interphase insulation**: the investigated object is the insulation between conductors belonging to different phases in a hairpin-winding stator configuration – this region is particularly relevant because the close proximity of conductors at different electrical potentials may result in significant electric field thus a large voltage applied between two enamelled conductors which may not be fully potted or fully flooded with oil.
- **EV traction motors**: the application context is represented by the traction motors in the powertrain for electric vehicles which, as mentioned in the introduction, represents one of the most feasible solution in the decarbonization path – their increasing power and torque densities, compact dimensions and demanding operating temperatures encourage

and require the adoption of advanced direct-cooling solutions.

These four elements are closely interconnected and define the rationale for the theoretical topics introduced in the following sections of the chapter, as well as the guiding framework for the experimental activity developed in this thesis work.

1.2 Electric rotating machines

Before delving into the structure of electric motors insulation, it is useful to review the primary electric traction motors currently in use. The first concept to mention is that the selection of an electric machine topology for traction applications must meet demanding requirements, such as delivering high torque at low rotational speeds to ensure effective vehicle launch and hill-climbing capability, as well as providing a wide constant-power operating region at high speeds. Industrial and academic research mainly focuses on the following major technologies, also presented in fig. 1.1 [83, 84, 85]:

- **Interior Permanent Magnet Synchronous Machines (IPMSM)** – fig. 1.1 (a). These machines currently represent the most mature and widely adopted technology in the automotive market: here the magnets are embedded within the rotor structure, and this makes it possible to exploit not only the synchronous/electromagnetic torque, but also an additional reluctance torque component produced by the geometric saliency of the rotor. IPMSMs provide very high torque density and excellent efficiency; however they require rare-earth-based magnets and, in addition, exposure to high temperatures creates a serious risk of thermal demagnetisation of the magnet itself[1].

- **Surface Permanent Magnet Synchronous Machines (SPMSM)** [86, 87, 88]. In this configuration the permanent magnets are affixed directly onto the outer periphery of the rotor core. This layout simplifies the mechanical assembly of the rotor and produces a highly sinusoidal air-gap flux density, which minimizes cogging torque. However, when contrasted with IPMSMs for traction applications, SPMSMs present several severe limitations such as the absence of saliency[2] and absence of reluctance torque while, conversely, IPMSMs embed magnets within the rotor iron and create a significant asymmetry which introduces a substantial reluctance torque component that significantly increases the machine's overall torque density; other disadvantages are the highly constrained field-weakening capability[3], and also at high rotational speeds the surface-mounted magnets are subjected to immense centrifugal forces trying to fling them off the rotor.

- **Induction Machines (IM)** – fig. 1.1 (b). They provide a highly robust and economically competitive solution and have historically been successfully adopted by some of the pioneers of the electric vehicle industry; although induction machines eliminate dependence on rare-earth materials, they generally have a lower power factor and lower efficiency at low

[1] though this is a feature that unites all the electric motor that features permanent magnets on the rotor circuit, and not only the IPMSM motors

[2] indeed, given that the permanent magnets are positioned on the rotor surface and behave magnetically like air, the magnetic path is uniform regardless of rotor position and, as a consequence, produces no reluctance torque

[3] indeed, due to the lack of saliency, in order to operate the machine above its base speed a strong demagnetizing d-axis stator current must be continuously injected to oppose the permanent magnet flux

speeds than IPMSMs; their main thermal limitation is related to rotor Joule losses in the copper or aluminium conductors and, since the heat is generated on the rotating rotor, it is inherently difficult to remove, imposing significant limitations on the continuous torque density that can be delivered.

- **Switched Reluctance Machines (SRM)** – fig. 1.1 (c). They are characterised by an extremely robust, simple and cost-effective structure, with salient poles on both the stator and the rotor; the rotor contains neither permanent magnets nor windings and consists entirely of shaped magnetic laminations, hence the torque is generated by the tendency of the rotor to move towards the position of minimum magnetic reluctance (basically they produce all their torque via reluctance torque mechanism); thus, the strong dependence of torque on the rotor position produces high torque ripple and severe radial vibrations in the stator.

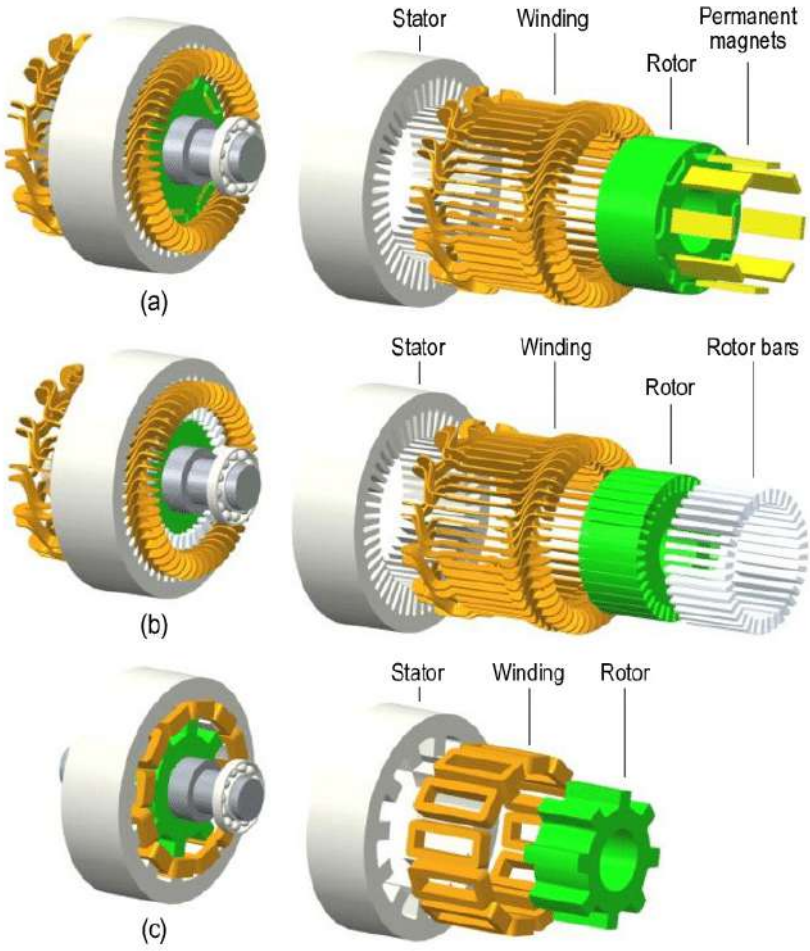


Figure 1.1. Typical electric rotating machine types for traction applications, represented with an *exploded view*: (a) IPMSM, (b) IM, (c) SRM (adapted from [83])

1.3 Types of stator winding construction & Insulation systems of motors

Regardless of the electrical-machine typology and the stator winding architecture, the stator typically comprises three fundamental material systems: the electrical conductors forming the winding, the laminated ferromagnetic core, and the Electrical Insulation System (EIS). The conductors and the magnetic core have active electromagnetic functions: currents flowing through the stator winding generate the magnetomotive force required to establish the rotating magnetic field, whereas the core provides a low-reluctance path that guides and concentrates the resulting magnetic flux. By contrast, the primary function of the EIS is electrical separation: it prevents short circuits between adjacent turns, different phases, and the winding and grounded stator core, while trying to occupy the smallest possible fraction of the slot volume [89]. However, the EIS should not be regarded as performing a purely electrical function since it also contributes to the mechanical fixation of the winding, reducing conductor movement and vibration under electromagnetic forces [90]. Moreover, EIS influences heat transfer between the winding, stator core, housing, and cooling medium – as it will be described, impregnation materials can improve the thermal contact between conductors and the core by filling air gaps [90]. The EIS also provides protection against moisture, dust, lubricants, chemicals, and other environmental contaminants that could otherwise accelerate dielectric degradation.

The insulation systems installed inside an electrical machine always and exclusively concern the windings; therefore, it is necessary to examine their main configurations [85]. The operational regime of an electrical machine is dictated by the interplay between its structural design, namely its overall geometry and winding configuration, and the profiles of the applied voltages and currents – evidently, the stator rotating-field windings represent the most stressed insulation subsystems, as they are subjected to the highest voltage amplitudes and elevated operating temperatures, historically making the stator winding the most susceptible component to electrical and thermal failures [85]. To cope with this challenge, designers primarily choose between three main stator winding architectures [84, 85, 91, 92, 93, 94]:

- **Random-wound windings**. They are manufactured using insulated copper conductors with a circular cross-section, called magnet wires, that are inserted into the stator slots without a precisely ordered arrangement; because of this random geometry, conductors that are physically close to each other may belong to electrically distant turns of the coil, such as the first and last turns; as a result, the thin enamel insulation may be exposed to very high potential differences and may create severe localized electrical stress – this makes them highly vulnerable to inter-turn insulation breakdown and partial discharges under modern high-frequency inverter duty.
- **Hairpin form-wound windings**. They are based on the rigid insertion of preformed rectangular copper bars shaped like hairpins that are welded at the end turns (an example is shown in fig. 1.2, and the manufacturing process is described in fig. 1.3), allowing to maximise the slot fill factor (up to 70%) and reducing the overall motor dimensions; hence, this technology has emerged as a leading solution for high-power-density traction motors, or leaving additional space for more effective cooling channels; furthermore, their fixed

and ordered arrangement provides deterministic control over the turn-to-turn voltage, eliminating large voltage differences between adjacent conductors; the main disadvantage is their susceptibility to significant high-frequency AC losses caused by skin and proximity effects, which are mainly associated with the large cross-sectional area of the conductors.

- **Litz-wire windings**. It consists of several thin, individually insulated strands twisted according to precise geometric patterns, which are designed to ensure that each strand experiences approximately the same exposure to the magnetic field, namely the specific arrangement ensures that each strand spends an equal proportion of its length on the outer boundary of the conductor, dramatically suppressing skin and proximity effect losses, hence they are widely used at high frequencies); while Litz wires provide exceptional mechanical flexibility and excellent high-frequency performance, they generally do not maximize the slot-fill factor, they have high manufacturing costs and terminal connection is hard.

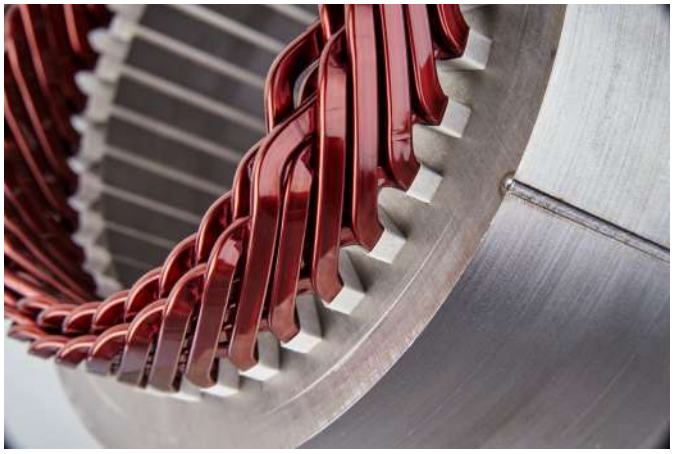


Figure 1.2. Hairpin winding technology (adapted from [95])

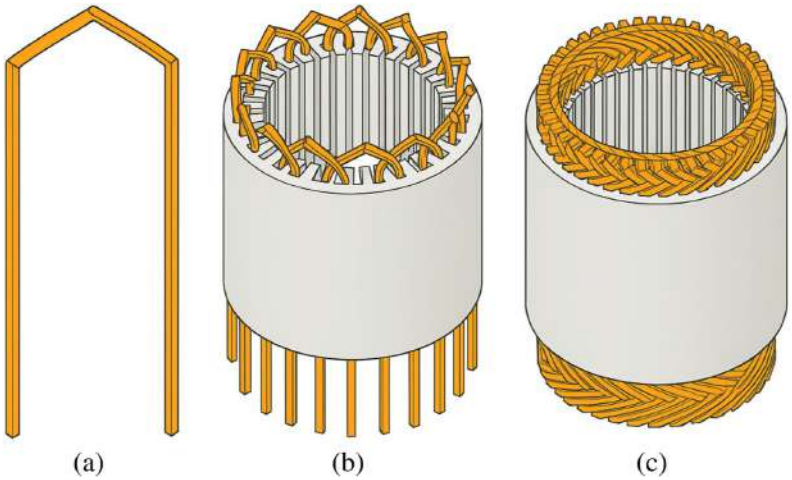


Figure 1.3. Hairpin winding manufacturing process: (a) preformed hairpin conductor, (b) hairpin conductors inserted into the stator core slots, and (c) completed end-winding structure after the hairpin ends are twisted and welded (adapted from [80])

Although the insulation does not directly contribute to electromagnetic energy conversion and torque production, namely it doesn't have an explicit active electromagnetic function, its condition

strongly determines the reliability and service lifetime of the stator winding: indeed, insulation degradation[4] can ultimately result into failures such as turn-to-turn, phase-to-phase, or phase-to-ground short circuits. The EIS is therefore widely regarded as one of the principal lifetime-limiting and reliability-critical subsystems of an electrical machine – Its importance becomes even greater in compact, high-power-density, inverter-fed traction motors, where elevated temperatures, steep-front voltage impulses, partial discharges, mechanical vibration, and aggressive cooling media may impose severe combined stresses on the winding insulation [84, 85].

Low-voltage electrical machines, which are defined as those machines typically rated at 1000 V or below, typically employ a less complex EIS than their medium- and high-voltage counterparts [96]. As illustrated in fig. 1.5, this system comprises a diverse array of materials, including magnet wires, flexible laminates, coated materials, structural elements, and impregnation resins or varnishes [96]. Functionally and structurally, to safely manage the aforementioned stresses across the machine's required operating envelope, these components are broadly classified into three primary categories: magnet-wire insulation, ground/slot insulation, and phase insulation – they are described hereafter and they are represented in fig. 1.4 [78, 84, 85, 92, 93, 96]:

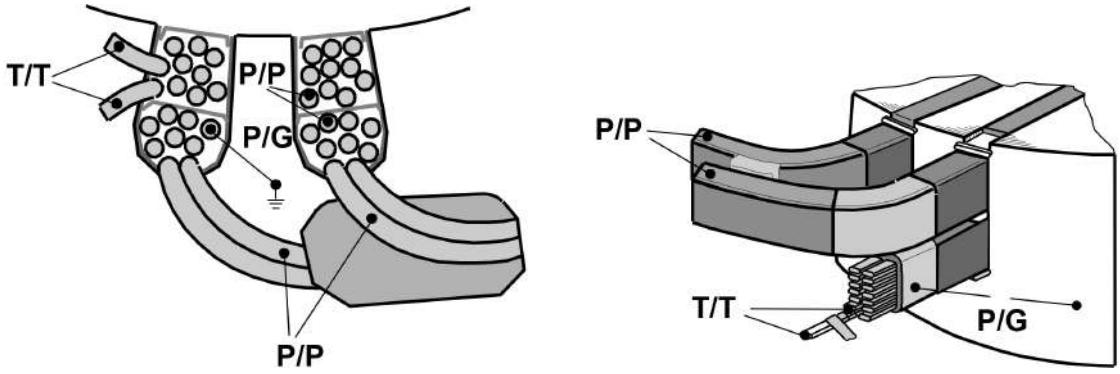
- **Turn-to-Turn (T-T) Insulation Subsystem**. It serves as the first dielectric barrier, withstanding the voltage difference appearing between individual turns within a slot. For transport traction motors, turn insulation consists of a thin polymeric enamel coated directly onto the copper or aluminium conductors, and it can feature different materials and architectures[5]; its thickness is standardized into insulation grades (typically Grades 1, 2, and 3 [85]). The design of the T-T subsystem is especially critical in machines fed by modern wide-bandgap converters since they generate extremely fast $\mathrm{d}v/\mathrm{d}t$ switching transients with very short rise times, and this creates a highly non-uniform voltage distribution along the stator winding, forcing a substantial portion of the transient jump voltage to drop across the very first coil and its initial turns.
- **The Phase-to-Ground (P-G) Subsystem**. It isolates the high-potential copper winding from the grounded stator frame and steel laminations, and its failure can thus trigger a catastrophic ground fault – in low-voltage machines this groundwall isolation is primarily established by lining the stator slots with a flexible protective sheet known as a slot liner; an emerging alternative to sheet slot liners is direct electrostatic powder coatings, which are applied directly to the slots of the core pack, successfully eliminating material interfaces, improving thermal heat transfer and reducing the likelihood of slot-edge voids.
- **The Phase-to-Phase (P-P) Subsystem**. It isolates different phase windings from each other: indeed, since different phases operate under higher line-to-line voltage differences than adjacent turns of the same phase, this boundary experiences severe electrical stress; hence, phase isolation is ensured by inserting slot separators between the winding layers

[4] the insulation degradation can be generally ascribed to the exposure to combined Thermal, Electrical, Ambient, and Mechanical (TEAM) stresses during service: they can be called with the acronym TEAM because, rather than acting independently, these stresses operate under a coupled framework, where it is possible even that the degradation from one stress intensifies sensitivity to another [78, 92]

[5] ad instance, instead of a single layer, a dual-layer architecture can be used: a polyester-imide (PEI) base-coat provides high thermal stability and dielectric strength, while a polyamide-imide (PAI) over-coat ensures superior mechanical abrasion resistance, adhesion, and chemical durability

inside the slots; in the highly vulnerable end-winding region, namely where the coils exit the core, phase separators made of the same high-dielectric flexible papers and films are structurally placed between the phase coil noses.

- **Secondary Insulation System (Impregnation and Casting)**. To consolidate the stator windings, a secondary insulation barrier in the form of a liquid impregnating resin or varnish is introduced and cured – examples of primary chemistries are epoxy-based resins and varnishes, which are applied via trickle, dipping, or Vacuum Pressure Impregnation (VPI); furthermore, this insulation is not inserted only for the purpose precisely of electrically insulating the different conductors of the stator windings but, because these resins have a heat-exchange coefficient approximately ten times higher than that of air, the heat dissipation pathway is greatly optimized. Impregnation also prevents the delamination of wire enamel by mechanically gluing the conductors to withstand electromagnetic vibrations, it drastically suppresses partial discharges by eliminating gaseous cavities[6] and it prevents other chemical ingress and contact with the "naked" conductors.



(a) Random-wound winding **(b)** Form-wound winding

Figure 1.4. Schemes of insulation subsystems for random-wound and form-wound windings machines, highlighting the T-T, P-G and P-P insulation subsystems (adapted from [84])

As mentioned, in fig. 1.1 one can see the exploded view of the three main kinds of motors. After this recall about the winding architectures and insulation systems, one can eventually focus on the structure that's mainly currently adopted in the industry: as presented in [83], in the context of modern electric vehicle (EV) traction applications the Interior Permanent Magnet Synchronous Motor (IPMSM) is by far the most common and widely utilized kind of motor[7]. Furthermore, it's pretty common in these technical solutions to use bar-wound windings[8] [83] – such marriage between IPMSM rotors and hairpin stator windings in modern EV powertrains is driven by some key physical synergies [83, 85, 97]:

[6] however one has to mention that inadequate or defective impregnation may itself lead to the formation of voids, cracks, or local discontinuities within the insulating system, which can act as highly favourable sites for partial discharge inception

[7] notice that [83] does not feature and describe SPMSM motor, and this is because the mechanical and electromagnetic limitations of SPMSMs, such as magnet retention sleeves expanding the air gap and poor field-weakening performance, make them less suitable for the highly dynamic and high-speed requirements of EV drivetrains

[8] bar-wound windings is the industrial and patent-mature name for hairpin windings: instead of using conventional stranded round wires, this configuration uses pre-formed rectangular copper bars inserted into the stator slots

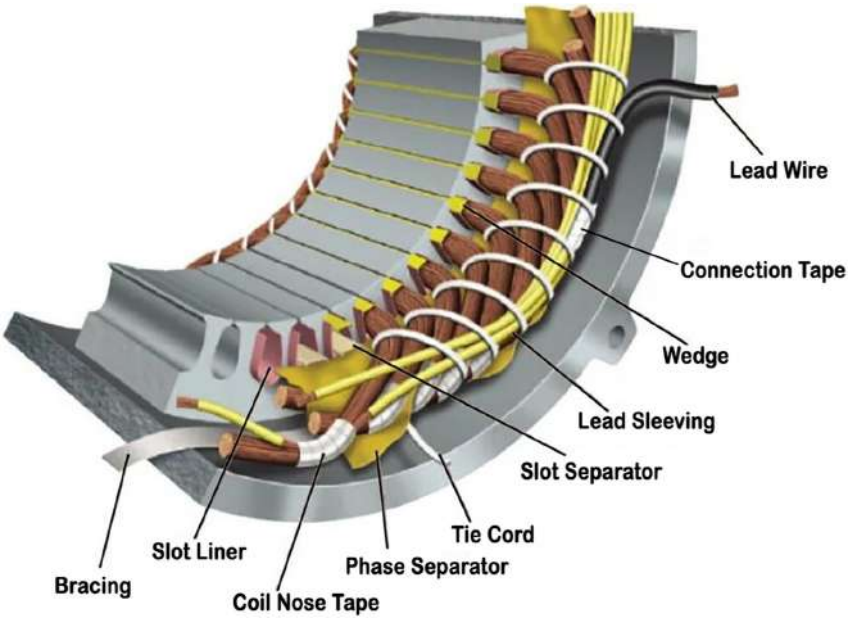


Figure 1.5. Overview of the electrical insulation system components for a low voltage rotating machine (adapted from [84, 96])

- **Maximization of power density**: hairpin windings increase the stator slot fill factor to over 70% and, when paired with an IPMSM, which inherently possesses the highest power and torque density, the resulting motor is incredibly compact thus satisfying the strict volume limitations under the vehicle's hood.
- **Critical thermal management**: permanent magnets in an IPMSM are highly sensitive to temperature, and hairpin windings feature flat, rectangular surfaces that offer much lower thermal resistance to the stator core and lend themselves perfectly to direct cooling hence allowing for a superior heat dissipation of the rotor.

Thus, this is all to say that, given the industry tendencies and EV market requirements, it's worthwhile taking the hairpin-wound stator winding as a reference case study in this thesis.

1.4 Cooling systems of electric motors

The material in this section is based on what is presented in [81, 98, 99, 100, 101, 102, 103, 104, 105, 106, 107, 108, 109, 110, 111, 112, 113, 114, 115, 116, 117, 118]. For full details and proofs, one should refer to the original source.

1.4.1 Thermal limits and loss mechanisms

In modern battery electric vehicles and hybrid electric vehicles, the electric motor is the core traction component responsible for energy conversion.To achieve high power density and lightweight traction systems, automotive manufacturers must maximize the torque and power densities; this trend toward miniaturization and higher operating speeds has consequently drastically increased the volumetric heat loss density inside traction motors, and this creates an extreme thermal challenge. The primary heat sources within an electric machine are:

- **Joule/copper losses** P_{Cu}: they are generated by the stator armature currents flowing through the windings; they can be formulated as:

$$P_{\mathrm{Cu}}(T) = 3I_{\mathrm{rms}}^2 R_{\mathrm{DC}}(T) \cdot k_{\mathrm{AC}}(f) \tag{1.1}$$

  where I_{rms} represents the phase root-mean-square current, R_{DC} is the temperature-dependent direct-current resistance of the windings[9], and $k_{\mathrm{AC}}(f)$ is an equivalent AC loss factor that captures and models the high-frequency skin and proximity effects in solid copper conductors[10].

- **Iron/core losses** P_{iron}: they are hysteresis and eddy current losses occurring within the stator and rotor silicon steel laminations due to high-frequency magnetic flux variations; they are traditionally decomposed into hysteresis and eddy current components:

$$P_{\mathrm{iron}} = P_{\mathrm{hysteresis}} + P_{\mathrm{eddy}} = k_{\mathrm{h}} f B_{\mathrm{max}}^2 + k_{\mathrm{e}} f^2 B_{\mathrm{max}}^2 \tag{1.2}$$

  where k_{h} and k_{e} are the hysteresis and eddy current loss coefficients of the core material, f is the electrical frequency, and B_{max} is the peak magnetic flux density.

- **Mechanical and Stray losses**: they are mainly windage losses in the rotor air gap, frictional losses in bearings and seals, and also high-frequency eddy current losses in permanent magnets must be accounted for.

Thus, as a conclusion, these losses are mainly concentrated almost entirely in the active parts of the stator and the rotor: indeed stator copper losses and core iron losses constituting approximately 95% of the total thermal load of the machine. If these generated losses are not evacuated efficiently, they lead to excessive operating temperatures[11] that compromise motor reliability and safety in two ways: firstly insulation degradation, namely the traditional organic insulation materials degrade rapidly at temperatures exceeding their limits thus risking dielectric breakdown, partial discharges and phase-to-phase short circuits, and secondly magnet demagnetization, namely in Permanent Magnet Synchronous Motors (PMSMs) the high operating temperatures within the rotor can cause irreversible thermal demagnetization of rare-earth permanent magnets, permanently reducing the motor's peak torque capacity and efficiency. Thus, advanced thermal management is not merely a reliability safeguard, but an enabling technology that directly determines the continuously exploitable torque and power density of electrified powertrains.

1.4.2 Transition from air cooling to liquid cooling

Historically, industrial motors and low-power traction motors (typically under 50 kW) relied on natural convection or forced air cooling. Indeed, air-cooled systems are highly cost-effective and

[9] since the electrical resistivity of copper increases linearly with temperature, the DC resistance should be continuously updated according to the thermal state of the machine, namely it is $R_{\mathrm{DC}}(T) = R_{\mathrm{DC}}(T_0)[1+\alpha(T-T_0)]$ where α is the temperature coefficient of the resistivity of the conductor material

[10] indeed, in high-frequency, high-performance inverter-fed motors, AC copper losses are exacerbated by skin and proximity effects in solid copper conductors, particularly in modern hairpin winding topologies

[11] to go deeper, if these losses are not rapidly dissipated the concentrated thermal energy causes a rapid localized temperature rise which leads to the formation of severe localized hotspots, typically located in the stator slot centers and the end-windings which pose a direct threat to the motor's integrity

mechanically robust because they do not require auxiliary components; however, air cooling is fundamentally limited by the poor thermal conductivity, low density, and low specific heat capacity of air. To scale the motor power density, operating current densities must exceed $10 - 15\,\mathrm{A/mm^2}$ and, at these levels, the low convective coefficients of forced air, reported in table 1.1, fail to remove the severe heat flux generated within the confined stator slots, which causes the slot winding temperatures to climb rapidly beyond the thermal limits. Therefore, a transition to a high-capacity liquid cooling system is mandatory for high-performance automotive traction applications. To quantitatively describe the phenomenon, the convective heat dissipation rate Q from any solid surface to a surrounding fluid is fundamentally governed by Newton's Law of cooling:

$$Q = hA(T - T_\mathrm{c}) \tag{1.3}$$

where h is the convective heat transfer coefficient, A is the active heat-dissipating surface area, T is the solid surface temperature and T_c is the bulk temperature of the cooling fluid. The absolute physical limitation of a given cooling technology can be defined by its Maximum Heat Flux (MHF) capacity, which represents the highest heat flux that can be handled before the winding temperature reaches the safety threshold of the insulation material:

$$\mathrm{MHF} = h_\mathrm{max} \cdot \Delta T_\mathrm{max} = h_\mathrm{max} \cdot (T_\mathrm{limit} - T_\mathrm{c,min}) \tag{1.4}$$

where T_limit is the maximum allowable continuous working temperature of the selected insulation class and $T_\mathrm{c,min}$ is the minimum inlet temperature of the coolant. One can here precisely see that the maximum heat that can be removed is mainly dependent on the heat transfer coefficient, which basically takes into account the fluid's physical properties, the flow conditions and the surface geometry of the interface – thus, to improve the heat removal one has to improve h.

One can now consider that the selection of the motor cooling technology is strictly linked to its targeted current density J and the convective heat transfer coefficient h of the cooling medium, as summarized in the rules of thumb shown in table 1.1 as well as in fig. 1.7. In particular, the heat transfer coefficients of air-based cooling methods are mathematically constrained by the poor thermophysical properties of air, yielding precisely to extremely low heat transfer coefficients and limits the stator current density to a modest range; while forced air convection improves the heat transfer coefficient, it remains entirely inadequate to manage the massive heat fluxes generated in modern automotive powertrains[12]. Thus, for high-power-density EV traction applications requiring current densities well above $15 - 30\mathrm{A/mm^2}$, conventional air cooling is completely obsolete, making liquid-based cooling systems a mandatory design requirement.

[12] furthermore, forced air systems require open frame designs to circulate the air, exposing the active windings to external dirt, moisture, and chemical debris, which significantly reduces the motor's operational lifespan

Table 1.1. Comparative rules of thumb for cooling type and heat transfer coefficients for electric motor cooling technologies (adapted from [98, 105, 112, 119])

Cooling Type	**Current density (max. range)** [A/mm^2]	**Heat transfer coefficient** [W/(m^2 · K)]	**Cooling efficiency**	**System complexity**
Natural air convection	1.5–25	5–10	Low	Simple
Forced air convection	5–12	10–300	Medium	Medium
Housing water-jacket	10–30	50–20000	High	Complex
Slot water channel	12-33	–	Very high	Complex
Hollow conductors	15-50	–	Very high	Very complex
Spray, jet, dripping oil	15-30	200–25000	Very high	Complex
Oil flooded stator	15-90	–	Very high	Very complex

Figure 1.6 compares the heat-transfer capability of different cooling technologies used in electrical machines[13] (they will be described later on): natural and forced air convection occupy the left region of the diagram, corresponding to comparatively low heat-transfer coefficients and heat-flux capability (while direct air cooling is higher but still limited compared with liquid-based approaches), whilst liquid convection extends the achievable cooling performance, while more advanced liquid-based techniques such as microchannels, jet impingement and spray cooling occupy regions associated with much higher heat-transfer coefficients and heat fluxes. Furthermore, the relatively large dispersion visible in fig. 1.6 is also meaningful: spray cooling has the largest dispersion among the compared methods, which the authors attribute to its strong sensitivity to parameters such as liquid flow rate, motor geometry, nozzle configuration and operating conditions. Yet one has to notice that the numerical values reported in fig. 1.6 are more conservative compared to the one reported in table 1.1.

Figure 1.7 is useful as a general heat-transfer argument: it shows that, as the heat flux to be removed increases, progressively more effective cooling techniques are required. Precisely looking at fig. 1.7, the three-dimensional scatter plot represents the heat flux generated by electric motors as a function of rotor speed and torque; the horizontal axes are therefore motor operating variables, while the vertical axis gives the heat flux generated at the end winding, and the coloured horizontal planes represent the approximate maximum heat flux that can be handled by the different cooling technologies. This makes the physical meaning very intuitive: as torque and/or speed increase, the operating points can move toward higher heat-flux values, while each cooling technique has an upper thermal capability. The authors of fig. 1.7 use it specifically as a cooling-method applicability map, and their criterion is straightforward: the MHF of the selected cooling method must exceed the heat flux generated by the motor.

[13] to be rigorous, the paper explicitly proposes heat transfer coefficient and maximum heat flux (MHF) as quantitative indicators for comparing electric-motor cooling methods, and it has to be noted that the motor heat flux is strongly related to rotor speed, torque, and motor dimensions

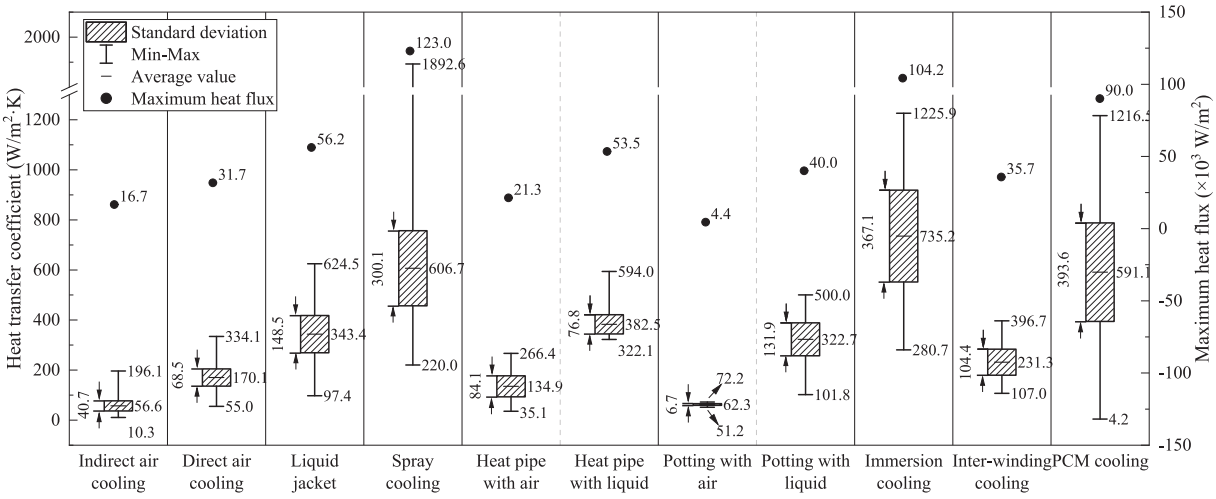


Figure 1.6. Comparison of heat transfer coefficients and maximum heat fluxes for different electric motor cooling methods (adapted from [98])

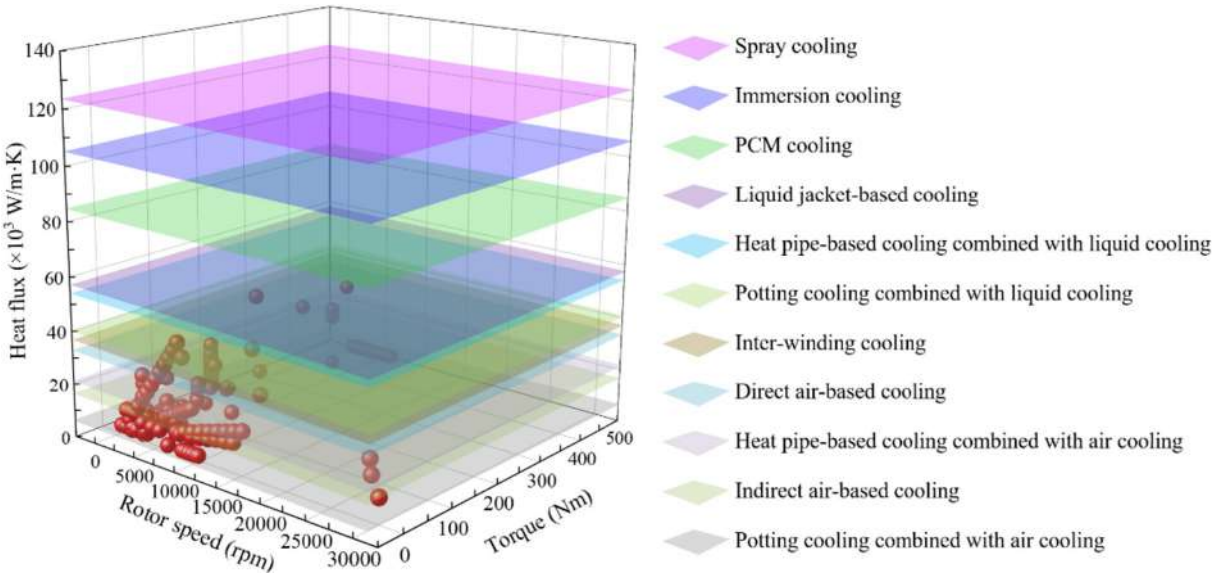


Figure 1.7. Maximum heat flux capability of different electric motor cooling methods as a function of motor torque and rotational speed (adapted from [98])

Now it's worthwhile describing briefly the various cooling techniques that have just been introduced. The transition to liquid cooling has historically been dominated by Housing Water Jackets, which utilize a circulated mixture of ethylene glycol and water – an example is presented in fig. 1.8. However, ordinary water-based coolants are electrically conductive[14] and highly corrosive, which strictly prevents it from coming into direct contact with the live copper conductors or lamination cores. Consequently, water-cooled systems are inherently indirect, meaning that the coolant is confined to serpentine, helical, or spiral channels carved into the aluminium motor housing, completely isolated from the stator slots. This indirect arrangement hence creates a

[14] this is the main reason for which it's not possible to use water with direct cooling: indeed water-glycol mixtures possess high electrical conductivity and cannot directly wet current-carrying components under high voltage due to the immediate risk of phase-to-phase short-circuits and catastrophic insulation breakdown

long and highly resistive thermal conduction path:

Copper Winding → Impregnation Varnish → Slot Liner Insulation → Stator Teeth

or, more precisely, the thermal energy generated in the winding copper must cross a series of high thermal resistances before reaching the external fluid jacket:

$$R_{\text{th,total}} = R_{\text{enamel}} + R_{\text{impregnation}} + R_{\text{liner}} + R_{\text{iron}} + R_{\text{conv}} \tag{1.5}$$

where R_{enamel} is the resistance of the primary wire insulation, $R_{\text{impregnation}}$ is the resistance of the slot-filling resin, R_{liner} is the slot liner thermal barrier, R_{iron} is the stator core conduction path, and $R_{\text{conv}} = 1/(h \cdot A_{\text{jacket}})$ is the convective boundary resistance. Among these, the slot liners and the contact resistance at the stator-to-housing shrink-fit interface constitute severe thermal barriers. As a result, the water jacket fails to efficiently cool the end-windings and is completely insulated from the rotor by the air gap, which acts as a thermal barrier – this thus leaves critical hotspot regions, such as the slot centers and the end-windings, at elevated temperatures during heavy transient overloads.

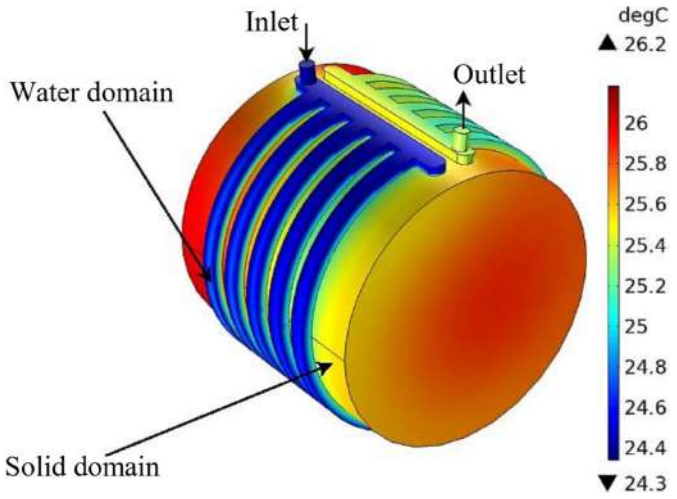


Figure 1.8. Finite-element temperature distribution of a synchronous reluctance motor equipped with a short water-path cooling jacket (SWJ); the water-cooling channels surrounding the motor constitute the fluid domain, while the motor and jacket structure form the solid domain: coolant enters through the inlet and flows through the circumferential channels toward the outlet, progressively absorbing heat from the motor, and the colour map illustrates the resulting temperature field and highlights the temperature increase of the coolant along the flow path as heat is transferred from the solid motor components to the circulating water (adapted from [120])

To overcome these conduction limitations, Direct Oil Cooling has emerged as the state-of-the-art solution. Synthetic lubrication oils, such as Automatic Transmission Fluid (ATF) or synthetic polyalphaolefins (PAO), are non-conductive with favourable thermal properties and have high dielectric strength, thus allowing advanced direct cooling arrangements – these electrical properties allow the cooling fluid to be brought into direct physical contact with the primary heat sources: by wetting the bare stator end-windings, the stator core, and even flowing inside the stator slots, oil cooling bypasses the high-resistance thermal path, eliminating contact interfaces and slot liner barriers. Although oil has a lower specific heat and a higher viscosity

compared to water, its ability to achieve direct heat exchange yields significantly higher effective cooling capacity, removing localized hot spots and maintaining a highly uniform temperature profile. Direct oil cooling can be classified into four distinct physical architectures, which are reported in fig. 1.9.

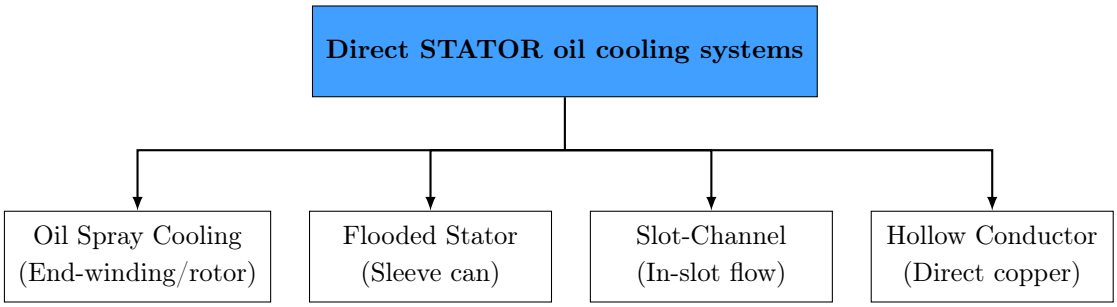


Figure 1.9. Direct stator oil cooling systems possibilities

It is possible to give a more complete description of the cooling techniques presented in fig. 1.9:

1. **Oil spray cooling** (see fig. 1.10): oil is pressurized by an external pump and forced through tiny orifices or nozzles to atomize into fine droplets or direct liquid jets aimed at the hot end-windings and rotor surfaces; this technique is is highly attractive because it focuses the coolant directly onto the machine's critical hot spots, thus providing excellent localized heat removal exactly where the copper overhang is exposed, while maintaining a very low fluid inventory (up to 90% coolant volume reduction compared to flooded systems). Fluid dynamics trade-offs are present: the behavior of the sprayed oil is heavily temperature-dependent and, as the oil warms up, its viscosity drops dramatically and this promotes the formation of a thinner, more uniform oil film on the winding surfaces, enhancing the local heat transfer coefficient; however, low viscosity also increases oil splashing and, furthermore, as rotor speed increases, windage forces can deflect the droplets.

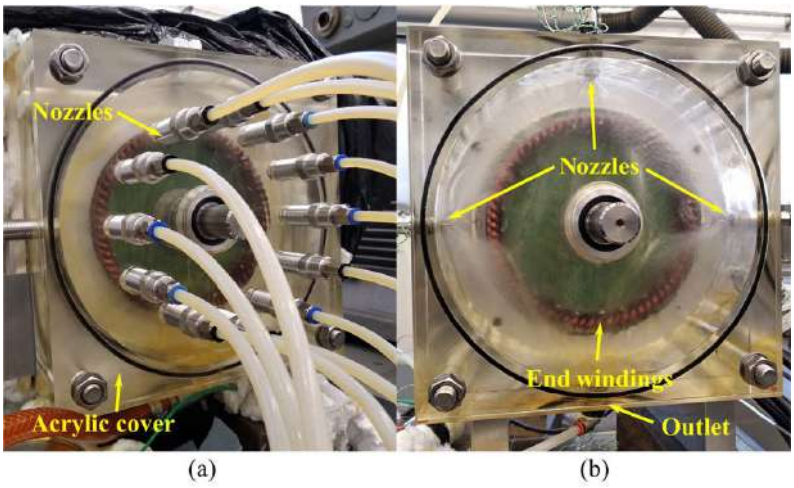


Figure 1.10. Direct oil-spray cooling configurations for hairpin end-windings: (a) axial injection from the end cover and (b) radial injection toward the end-winding region (adapted from [121])

2. **Wetted/flooded stator cooling** (see fig. 1.11): here the entire stator chamber is completely flooded with dielectric oil, ensuring that the winding slots, teeth, yoke and end-

windings are fully submerged – this guarantees the absolute maximum contact area between the coolant and the copper conductors, removing the possibility of localized hot spots even under extreme transient overloads. To prevent high-viscosity oil from flooding the rotor chamber, which would cause massive, unacceptable hydrodynamic drag and shear losses at high rotor speeds, a thin and electrically insulating sleeve is placed, which splits the motor into a "wet" stator chamber and a "dry" rotor chamber. The flooded stator provides unmatched thermal performance, enabling steady-state operating current densities $> 40\,\mathrm{A/mm^2}$ while, however, the mechanical challenges are severe. The air gap sleeve must be perfectly sealed and its presence increases the magnetic air gap length, which can degrade the motor's power factor and electromagnetic torque.

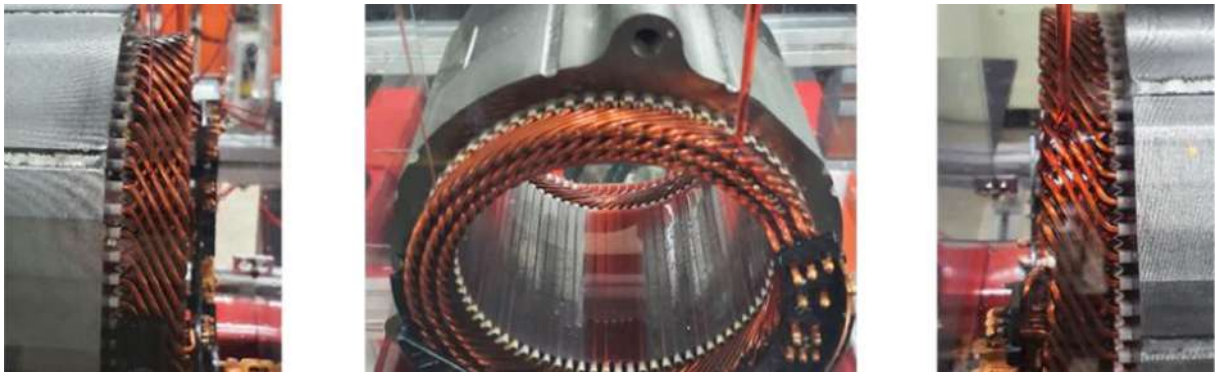
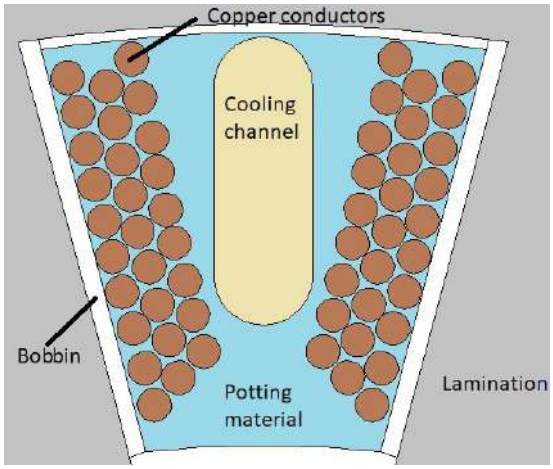
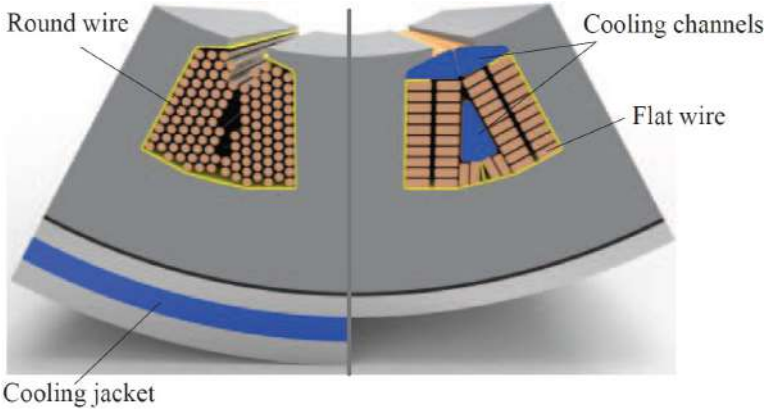


Figure 1.11. Example of wetted stator cooling based on direct oil injection onto the hairpin end windings: the coolant directly wets the winding surface, forming an oil film and enabling direct heat removal from the conductors (adapted from [122])

3. **Slot-channel/In-slot oil cooling** (see fig. 1.12): this system targets the active length of the stator windings directly within the slots, which typically acts as a severe thermal bottleneck that end-winding spray systems cannot address; in this architecture, axial oil ducts or cooling channels are placed directly within the stator slots: these channels run parallel and adjacent to the insulated conductors, and the cooling oil is pumped axially through these channels, absorbing heat directly from the slot copper. Recalling the indirect cooling technique, one can here recognise that, by bringing the convective fluid inside the slots, the conduction path through the stator teeth and lamination is bypassed – however, because the oil is physically separated from the bare copper by a required electrical insulation layer (the conductor's enamel and slot liner), a small thermal barrier remains.
4. **Hollow conductor direct cooling** (see fig. 1.13): it is considered the ultimate thermal management strategy and it involves fabricating the stator hairpin conductors with an internal, longitudinal flow channel and, in this manner, the dielectric cooling oil is then circulated directly through the core of the copper conductors themselves.



(a) Oil-based in-slot cooling with cooling channel formed within the potted winding region (adapted from [123])



(b) Indirect in-slot cooling using insulated liquid-cooling channels integrated in stator slot (adapted from [124])

Figure 1.12. Comparison of two in-slot liquid-cooling concepts for concentrated-winding electric machines



(a) Cross section of the hollow conductors showing the central channel for direct oil cooling (adapted from [121])



(b) BAE Systems Hybridrive TB08 electric traction motor (230kW) with stator hollow conductors (adapted from [125])

Figure 1.13. Examples of hollow-conductor technology for direct oil cooling of electric machine stator windings.

1.4.3 Dielectric link: from oil direct cooling to Partial Discharge phenomena

While the transition to direct in-slot oil cooling and pressurized spray systems effectively resolves the thermal bottleneck of highly downsized traction motors, it simultaneously introduces a quite critical reliability concern at the system level. Indeed, routing a dielectric coolant directly through the stator slots, like in the in-slot cooling or in the flooded stator cooling cases, or spraying it onto the end-windings, places the fluid in a region characterized by extreme and highly repetitive electrical stress, driven by the steep voltage rise times $\mathrm{d}v/\mathrm{d}t$ and high switching frequencies of modern inverter supplies [79, 82, 126]. Under these rapid transient voltage surges, the localized electric field strength in the narrow stator clearances can easily exceed the dielectric breakdown threshold of the gaseous or multiphase medium surrounding the conductors [79].

Crucially, the introduction of the liquid coolant does not act as a simple dielectric shield; instead, it can degrade the overall insulation performance. Indeed, at high operating temperatures, depending on the cooling system that is adopted, the dielectric oil can partially evaporate, creating an unstable local environment where liquid oil phases, ambient air, and volatile oil-derived vapours coexist. This complex, temperature-dependent multiphase mixture significantly alters precisely the local environment; specifically, the presence of volatile vapours can dramatically trigger partial discharges (PD) at voltage levels well below those measured in pure air at the same temperature, leading to a severe and unexpected reduction in the Partial Discharge Inception Voltage (PDIV). This electric-field-induced ionization not only attacks the solid enamel insulation via chemical and physical bombardment, but can also initiate a self-accelerating degradation loop within the coolant itself[15] [79].

Hence, understanding how different chemical compositions of cooling lubricants affect the PDIV under specific thermal and electrical stresses, and trying to identify the physical mechanisms linking oil volatility, temperature and partial discharge inception, is therefore of paramount importance. This is the central multi-physical challenge that the experimental and analytical work of this thesis tries to adress.

1.5 Partial Discharges (PD) theory and oil influence

1.5.1 Main motor winding failure mechanisms & the critical role of partial discharges in motor's life

The material in this subsection is based on what is presented in [84, 85]. For full details and proofs, refer to the original source.

In low-voltage electrical machines, the stator winding is historically the most vulnerable component to in-service failures and it represents the primary bottleneck for the reliability and lifetime of motors under 10 kW, which are typical in transport electrification. Under normal service conditions, this degradation occurs progressively due to the combined action of Thermal,

[15] as shown by recent experimental investigations, the high-voltage pulse trains trigger localized PD activity that breaks the covalent bonds of the hydrocarbon chains (ad instance in polyalphaolefin oils), generating free radicals, increasing oil acidity, and producing highly volatile dissolved gases, and this chemical decomposition products further degrade the liquid's dielectric strength and accelerate the ageing of both the fluid and solid insulation [79]

Electrical, Ambient, and Mechanical (TEAM) stresses. The main routes to insulation failure are:

- **Thermal deterioration**: this is the most common cause of motor faults, particularly in air-cooled machines; when the motor hotspot temperature exceeds the limits of its insulation class, progressive thermal oxidation occurs which then leads to cracked or peeling magnet wire films and a severe drop in insulation resistance which can eventually cause turn-to-turn short circuits.
- **Inadequate resin impregnation**: it was mentioned that secondary insulation through resin impregnation is essential to fill the empty spaces inside the stator slots, and if this is done in an inadequate manner it can leave air-filled micro-cavities within the winding; in addition, the lack of mechanical packing allows the wires to vibrate under electromagnetic forces, causing abrasive enamel wear; moreover, poor impregnation impedes heat dissipation.
- **Contamination**: the exposure to environmental factors such as dust, dirt, moisture, and oil can produce a conductive layer on the exposed end-windings, which facilitates surface currents known as electrical tracking which erodes the polymer over time, eventually sparking phase-to-phase or phase-to-ground short circuits.
- **Converter-induced over-stresses**: the transition to modern fast-switching wide-bandgap converters exposes motor windings to extremely high electrical stresses, in particular exceptionally fast voltage rise times, which aggravate phenomena like *Voltage reflection and Overshoots*, and *Uneven voltage distribution* namely a major portion of the voltage drop is concentrated across the very first turns of the winding, thus highly stressing the turn-to-turn insulation.

However, the Partial Discharge phenomenon hasn't been mentioned yet; as it will be described more in detail in the next section, a partial discharge is a localized electrical discharge that only partially bridges the insulation between conductors. In low-voltage machines, these discharges occur typically in air-filled cavities, namely micro-cavities, left by incomplete impregnation or at the boundaries between different dielectric materials under high electric fields. Internal voids caused by incomplete impregnation represent only one of the possible locations in which PD activity can develop: indeed, in hairpin windings, small inter-conductor gaps may remain between adjacent enamelled conductors, particularly when these regions are not completely encapsulated by a solid insulating material. These regions constitute precisely low-density dielectric paths that may be occupied by air and, in the case of direct oil cooling, may also be influenced by lubricant vapours or direct liquid wetting. When the local electric field across this low-density medium becomes sufficiently high, partial discharges may therefore occur even in the absence of an impregnation defect or delamination. This condition is particularly relevant for the interphase insulation configuration considered in this thesis, where the electrical stress is concentrated across a narrow gap separating two enamelled hairpin conductors.

Focusing on the prevention and detection of PDs is one of the most critical task for ensuring the reliability of modern inverter-fed transportation motors due to the following reasons: *Vulnerability of organic materials*, which are employed precisely in low-voltage electric motors, *Rapid chemical erosion* due to the continuous bombardment of high-energy electrons which cause ions breaks the chemical covalent bonds of the polymer chains which results in the local erosion of the polymer

and finally forming carbonized paths which lead to an immediate short circuit, and eventually the most worrying one is the *Extremely short lifetimes under PD* since empirical research shows that standard organic turn-to-turn insulation subjected to continuous PD activity under inverter waveforms fails rapidly (often in a matter of minutes or even seconds).

Thus, regard to the goal of this thesis work, one can consider the *Inception Voltage* as the *Lifetime boundary*: indeed, in a multi-stress environment, once the combination of aging degradation, voltage overshoots, and environmental conditions causes the Partial Discharge Inception Voltage (PDIV) to drop below the operating voltage, PD activity begins and the remaining lifetime of the motor is reduced to minutes, as just mentioned. In this context, the introduction of direct oil cooling adds a further environmental variable that cannot be neglected. When the cooling lubricant is brought into direct contact with, or in close proximity to, the winding insulation, the dielectric environment surrounding the conductors is no longer necessarily represented by dry air alone. At elevated operating temperatures, the lubricant can partially volatilize, introducing oil-derived vapours into the gaseous regions between adjacent conductors; depending on the cooling configuration, the insulation surfaces may also become directly wetted by the liquid lubricant. Consequently, the physical and chemical properties of the dielectric medium in which a discharge may develop are modified, potentially changing the ionization processes governing discharge inception and therefore the resulting PDIV. Therefore, in any case, finding the PDIV at the reference operating conditions of a given machine is the primary and absolute prerequisite for designing highly reliable electrical drives.

In this thesis work, the goal is to assess the negative effect on the PDIV performance index that the oil cooling of the motor can have.

1.5.2 Introduction to Partial Discharges theory

The material in this subsection is based on what is presented in [84, 85, 127, 128, 129, 130, 131, 132]. For full details and proofs, refer to the original source.

It is firstly crucial to establish a clear physical distinction between complete electrical breakdown and partial discharges (PD):

- a complete electrical breakdown is a disruptive discharge that completely bridges the insulation between conductors/electrodes, causing a temporary or permanent loss of dielectric strength, a massive surge in current and immediate catastrophic failure of the electrical apparatus and its EIS;
- instead, according to international standard `IEC 60270`, a partial discharge is defined as:

  > «*Localized electrical discharge that only partially bridges the insulation between conductors and which can or cannot occur adjacent to a conductor*»

  and, although PD events do not cause immediate short-circuits, their persistent activity leads to degradation of the surrounding organic dielectric materials (such as enamels and resins), eventually initiating electrical treeing and culminating in complete breakdown.

In the design and qualification of electrical insulation systems, two parameters are conventionally used to characterize PD activity and it's important to give them a proper definition,

even if they have been already intuitively introduced:

- **Partial Discharge Inception Voltage (PDIV)**: *Lowest voltage at which partial discharges are initiated in the test arrangement when the voltage applied to the test object is gradually increased from a lower value at which no such discharges are observed*;
- **Partial Discharge Extinction Voltage (PDEV)**: *Voltage at which partial discharges are extinguished in the test arrangement when the voltage applied to the test object is gradually decreased from a higher value at which such discharges are observed*; due to space charge deposition on the dielectric surfaces, also known as the memory effect, the PDEV is typically lower than the PDIV.

The physical phenomena governing electrical breakdown in gases serve as the bedrock for understanding PDs. Generally, discharges occur when free charge carriers, namely electrons, are accelerated by an external electric field to energies high enough to cause impact ionization of neutral gas molecules. First one should recall the **Townsend mechanism**, which is developed for uniform electric fields between bare parallel-plate electrodes. It describes a primary electron avalanche process: the process begins with a single initial electron somehow generated which, driven by the electric field E, travels a distance x towards the anode undergoing some collisions; if electron's kinetic energy exceeds the ionization potential of the gas molecules, the collision is inelastic and results in impact ionization, freeing a secondary electron and leaving a slow-moving positive ion behind. This continuous multiplication of charge carriers is mathematically represented using Townsend's first ionization coefficient α, which represents the average number of ionizing impact events produced by an electron per unit length in the direction of the electric field. The growth of the electron population $n(x)$ along the gap spacing x can be described by the first-order differential equation, which has also an immediate solution:

$$\frac{dn(x)}{dx} = \alpha \cdot n(x) \quad \Longrightarrow \quad n(x) = n_0 \cdot e^{\alpha x} \tag{1.6}$$

where n_0 is the number of starting electrons. In attaching/electronegative gases, one must also account for the attachment process which is characterized by the attachment coefficient η (similarly to α, η represents the average number of electron attachment events per unit drift length). To account for this, the effective ionization coefficient α_{eff} is introduced:

$$\alpha_{\text{eff}} = \alpha - \eta \tag{1.7}$$

thus, net electron growth can only occur when $\alpha_{\text{eff}} > 0$. Typically the ionization coefficient is normalized to the pressure, namely α/p, and is a function of the reduced electric field E/p. It's possible to express it as:

$$\alpha = A \cdot p \cdot \exp\left(-\frac{B}{E/p}\right) \tag{1.8}$$

where A and B are experimental constants dependent on the gas composition, and typical values can be found in literature for each gas. To sustain the discharge without an external source of primary electrons, a feedback mechanism must be active: in Townsend regime, this feedback is

provided by positive ions returning to the cathode and bombarding its surface, extracting new electrons with an emission probability designated as Townsend's secondary electron emission coefficient γ. The total current $i(d)$ flowing through a gap of length d under these feedback conditions is given by:

$$i(d) = i_0 \frac{\exp(\alpha \cdot d)}{1 - \gamma \left[\exp(\alpha \cdot d) - 1\right]} \tag{1.9}$$

where i_0 is the initial current associated with the primary electrons entering the avalanche process. The condition for self-sustaining breakdown occurs when the denominator of the current equation approaches zero, leading to mathematically infinite current, namely:

$$\gamma \left[\exp(\alpha \cdot d) - 1\right] = 1 \quad \Longrightarrow \quad \alpha \cdot d = \ln\left(1 + \frac{1}{\gamma}\right) \tag{1.10}$$

By substituting the empirical expression of $\alpha(E)$ into this self-sustaining criterion, one obtains the Paschen's law, which mainly states that the breakdown voltage V_{B} in a uniform field is a function of the product of gas pressure p and gap distance d:

$$V_{\mathrm{B}} = \frac{B \cdot p \cdot d}{\ln\left(\frac{A \cdot p \cdot d}{\ln(1+1/\gamma)}\right)} \tag{1.11}$$

While the Townsend mechanism explains breakdown in short gaps, it fails when the gap distance exceeds a few centimeters or when high overvoltages are applied. Under these conditions, the breakdown occurs much faster than the time required for positive ions to drift back to the cathode to initiate secondary avalanches. This rapid transition is explained by the **streamer mechanism**: it considers that the space charge generated by a single primary electron avalanche distorts the local electric field and, as the avalanche moves toward the anode, fast electrons accumulate at its head, while slow-moving positive ions lag behind in the tail, creating a localized electric dipole. The space charge generates a radial electric field E_{r} which opposes the external applied field E_0 inside the avalanche body but significantly reinforces it at the immediate front and tail. According to Meek's criterion, the transition from an avalanche to a self-propagating streamer channel occurs when this localized radial space-charge field E_{r} becomes comparable to the external background field E_0, namely $E_{\mathrm{r}} \approx E_0$. At this threshold, the field distortion is sufficient to trigger intense photoionization: excited molecules in the lower-field core of the avalanche relax, emitting high-energy photons that ionize surrounding neutral gas molecules in the reinforced field regions. This creates a cascade of secondary avalanches that quickly merge, forming a highly conductive plasma channel, which is precisely the streamer. The threshold for this transition is conventionally expressed as a critical number of electrons N_{c} in the primary avalanche head:

$$N_{\mathrm{c}} = e^{\alpha d} = 10^8 \quad \Longrightarrow \quad \ln(N_{\mathrm{c}}) = \alpha \cdot d = k \approx 18.4 \tag{1.12}$$

However, moving towards the partial discharges phenomenon, one must recognise the inadequacy of Paschen's law for insulated electrodes, such the one which are represented by two

adjacent hairpin enamelled conductors. This completely changes the boundary conditions of the gaseous breakdown:

- **Absence of cathode electron emission**: Paschen's law relies strictly on secondary electron emission γ via positive ion bombardment of a bare metallic cathode; however, when the cathode is covered by an organic insulator, this feedback loop is almost suppressed because the work function of typical insulating polymers (around 9 eV) is far higher than that of copper (around 4.5 eV).
- **Field non-uniformity**: the twisted-pair geometry or the hairpin winding geometry of stator windings creates highly non-uniform electric fields in the sub-millimetric air gaps between adjacent wires.

Consequently, Paschen's law cannot be directly used to predict the PDIV of enamelled wires and it must be replaced by single-avalanche streamer inception criteria. So, one has to consider the following situation: partial discharges generally take place in gaseous voids, delaminations, or interfaces within the insulation system where the dielectric constant is lower than that of the surrounding solid, hence leading to local electric field enhancement condition. When a discharge is triggered, it behaves as a cold plasma: electrons travel extremely fast to the temporary positive dielectric barrier, while positive ions drift slowly to the negative boundary. These charges become trapped on the dielectric surfaces, generating an internal charge field E_{q} that opposes the external applied field E_0, hence leading to an overall internal field:

$$E_{\mathrm{internal}} = f \cdot E_0 - E_{\mathrm{q}} \tag{1.13}$$

where f is the field enhancement factor of the cavity, which depends on the geometry of the cavity itself as well as on the permittivity of the solid insulation surrounding the void. The discharge is rapidly quenched when the internal field drops below a residual field E_{res} which is the minimum field required to sustain the plasma:

$$E_{\mathrm{internal}} = E_{\mathrm{res}} \quad \Longrightarrow \quad f \cdot E_0 - E_{\mathrm{q}} = E_{\mathrm{res}} \tag{1.14}$$

This charge deposition creates a short-term memory effect. When the external AC voltage reverses polarity, the deposited charges now reinforce the local field, causing subsequent discharges to trigger at a much lower applied voltage – this physical mechanism explains why PDEV is lower than PDIV. Anyway, physical characteristics of PD pulses depend heavily on the dimensions of the cavity or air gap. One can foresee two main kinds of discharges:

- **Townsend-like PD**: in extremely narrow air gaps, typically below 5 μm, the avalanche cannot grow large enough to distort the field and initiate a streamer; hence, the discharge remains a slow, low-magnitude, sub-critical Townsend-like avalanche with a rise time of up to 60 ns, a pulse width up to 900 ns, and a current below 1 mA; these pulses have low frequency content and are extremely difficult to detect.
- **Streamer-like PD**: in larger gaps, the avalanche transitions into a highly energetic streamer; these pulses have rise times in the range of 1 ns to 8 ns, generating high-frequency electromagnetic radiation in the GHz range that can be much more easily detected.

To predict the PDIV in non-uniform, dielectric-bounded gaseous gaps, the **Schumann streamer inception criterion** is utilized. It states that a primary electron avalanche transitions into a self-propagating streamer when the integration of the effective ionization coefficient α_{eff} along the most stressed E-field line of length d reaches a critical dimensionless threshold k[16]:

$$\int_0^d \alpha_{\text{eff}}(E(x)) \cdot dx = k \tag{1.15}$$

where x is the coordinate along the field line and $E(x)$ is the E-field distribution, typically computed using Finite Element Method (FEM) software for the given geometrical configuration. Yet, even if it was mentioned that it is $k = \ln(N_c)$, one has to discuss the actual value to assign to k. In classical macroscopic spark breakdown between bare metals, Raether's criterion assumes $k \approx 18$. However, for sub-millimetric gaps and dielectric cavities typical of electrical machine insulation, the feedback from secondary cathode emission is absent. Under these conditions, experimental validation has shown that a much smaller critical avalanche size is sufficient to trigger a self-sustaining discharge. It is widely established in PD literature that the critical integration constant is $k = 9$, which corresponds to a critical number of electrons of:

$$N_c = e^k = e^9 \approx 8100 \text{ electrons} \tag{1.16}$$

This formulation has been successfully applied to model the PDIV of enameled wires. By assuming a parabolic approximation for the effective ionization coefficient in air near the ionization threshold, namely 2.5 kV/(mm bar), which is proven to be a good approximation:

$$\frac{\alpha_{\text{eff}}}{p} = C\left(\frac{E}{p} - \left(\frac{E}{p}\right)^{\text{cr}}\right)^2 \tag{1.17}$$

and integrating it over a spherical cavity of diameter $2r$, the inception field E_{inc} within the cavity can be analytically derived as:

$$E_{\text{inc}} = 2.5 \cdot p\left(1 + \frac{18.34}{\sqrt{p \cdot r_{\mu m}}}\right) \tag{1.18}$$

where p is the pressure in bar, and $r_{\mu\text{m}}$ is the cavity radius in micrometers.

However, at this point one has to link all these concepts which have been introduced. In particular, how does a different gas changes the discharge inception? A gas with poorer dielectric properties (such as oxygen compared with nitrogen, or air compared with hydrogen) is generally characterized by molecules with a lower ionization potential. For example, oxygen requires a lower ionization energy than nitrogen (approximately 12 eV versus 15.6 eV). This is reflected at both the microscopic and macroscopic levels as follows:

- **Increase in** α: for the same reduced electric field E/p, electrons accelerated by the electric field over their mean free path have a higher probability of acquiring sufficient energy to ionize gas molecules through inelastic collisions; consequently, the first Townsend ionization

[16] notice that, conceptually, k is the same type of quantity of $k = \ln(N_c)$ that was found in eq. (1.12) for the streamer breakdown criterion

coefficient α becomes higher (considering eqs. (1.8) and (1.17), the influence of the gas is seen respectively in constants A, B and in constants C and in the parameter $(E/p)^{\text{cr}}$);

- **Reduction in the inception field (E_{inc})**: recalling Schumann's criterion, namely eq. (1.15), if the effective ionization coefficient α_{eff} is intrinsically higher because of the poorer dielectric properties of the gas, the integral along the electric field line reaches the critical constant k at a lower local electric field E_{inc};
- **Reduction in partial discharge inception voltage**: since a lower electric field is required to initiate the critical electron avalanche, thus a lower externally applied voltage is sufficient to reach the partial discharge inception condition within the gaseous gap.

Schumann's condition is a local criterion based on the electric field distribution along an electric field line, whereas PDIV is a global parameter expressed as a voltage. The transition from the field-based inception criterion to the corresponding inception voltage can be achieved through an iterative numerical algorithm (see fig. 1.14 for a more schematic representation):

1. **Electrostatic simulation at a reference voltage**: the geometry of the system is modelled and the electric field is solved using FEM softwares such as COMSOL by applying an arbitrary reference voltage V_0, thereby obtaining the spatial distribution of the reference electric field $E_0(x, y)$;
2. **Linear scaling of the electric field**: Since the electrostatic problem remains linear prior to discharge inception, the electric field $E(x, y)$ corresponding to any other applied voltage V is directly proportional to the reference field like $E(x, y) = \frac{V}{V_0} E_0(x, y)$;
3. **Integration along the electric field lines**: individual electric field lines connecting the electrodes are extracted from the FEM model, including those extending through the enamel insulation and the gaseous region; for a generic trial voltage V, the effective ionization coefficient α_{eff}, previously determined as a function of the reduced electric field using Boltzmann-equation solvers such as BOLSIG+, is integrated along each field line i[17]:

$$I_i(V) = \int_0^{x_c} \alpha_{\text{eff}}(E_i(s))\, ds \tag{1.19}$$

4. **Iterative solution**: the algorithm progressively increases the applied voltage V until Schumann's condition, namely $I_i(V) = k_i$.

[17] the dimensionless quantity I_i is the value of the ionization integral evaluated along the i^{th} electric field line

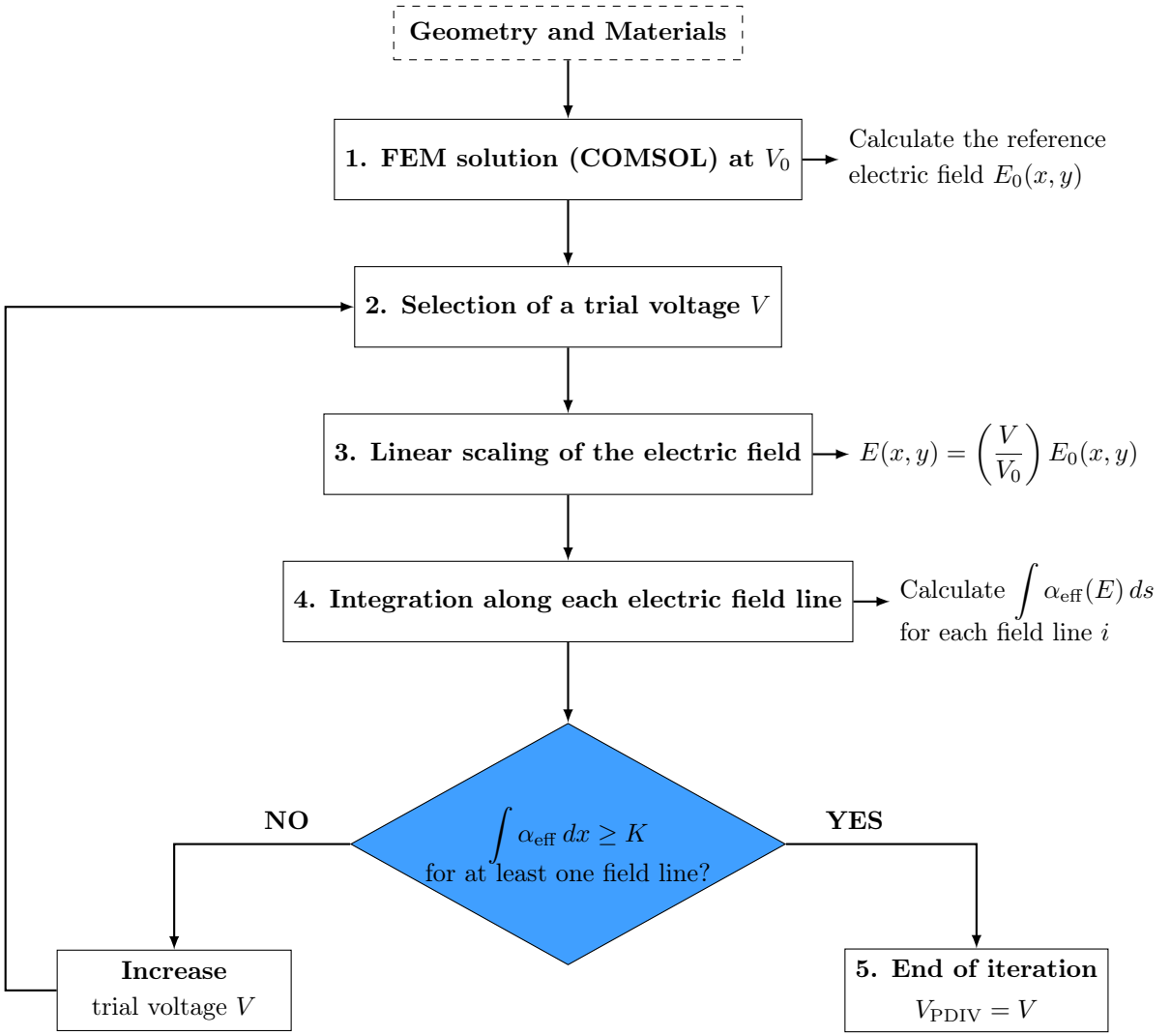


Figure 1.14. Iterative procedure for the numerical estimation of the partial discharge inception voltage based on the FEM electric-field distribution and the Schumann inception criterion

Something that must be accounted for is the *Stochastic nature of PD inception and time lag*. Indeed, while the deterministic Schumann criterion defines the absolute physical limit of gaseous stability, real-world PD measurements reveal significant stochastic behaviour. Precisely, for a partial discharge to occur, two conditions must be satisfied simultaneously:

- the local electric field must exceed the physical inception threshold $E \geq E_{\text{inc}}$;
- a starting or seed electron must be present within the active volume to initiate the avalanche.

Given that the generation of a starting electron is a random process, there is precisely a stochastic time lag between the moment the voltage exceeds the theoretical inception value and the moment the discharge actually triggers. Consequently, the experimentally measured PDIV is always a random variable that statistically exceeds the true deterministic PDIV, especially under fast voltage rise times where the voltage sweeps past the threshold before a seed electron is made available. One theory which is useful in this regard is the so-called **volume-time theory** – it's not reported and explained here for the sake of brevity.

In conclusion, the inception of partial discharges in electrical machine insulation is a highly complex phenomenon that transitions from fundamental gaseous ionization physics to non-uniform, dielectric-bounded electrostatic interactions. By combining the deterministic Schumann criterion, which must be applied with $k = 9$, with the probabilistic Volume-Time theory, researchers and design engineers can successfully calculate both the physical limits of insulation stability and the statistical distribution of PDIV under standard and reduced pressures, ensuring reliable motor operation across modern transportation – yet, for doing this it is necessary to have a very deep knowledge of both the geometry of the system and the chemical structure of the environment in which the PD will develop.

1.5.3 PDIV as a function of temperature T

Regardless of the geometry configuration of this particular thesis work, which will be defined in the following, there is the common phenomenon for which, when the low-density insulating media is air, the PDIV decreases as the temperature increases – this is mainly explained by the reduction of gas number density and the consequent more effective development of an electron avalanche[18]. To prove this, one can start from the Paschen's law[19], where we want to highlight the temperature dependence of the Townsend coefficients $A(T)$ and $B(T)$ and how this dependence propagates directly into the Paschen's law equation [84, 133, 134]. This law can be written as[20]:

$$V_{\mathrm{PDIV}}(T) = \frac{B(T)\, p\, d}{\ln(A(T)\, p\, d) - \ln\left(\ln\left(1 + 1/\gamma_{\mathrm{se}}\right)\right)} \tag{1.20}$$

where p and d are respectively the pressure and the distance of the gap, and γ_{se} is the effective secondary electron emission coefficient of the cathode. As it can be noticed in the previous equation, $A = A(T)$ and $B = B(T)$ coefficients are not proper constants but they precisely depend on the temperature T. From Townsend avalanche theory, it can be written:

$$A(T) = \frac{\varepsilon_i \sigma}{k_B T} \tag{1.21}$$

$$B(T) = \frac{\sigma}{k_B T} \tag{1.22}$$

[18] this interpretation is valid within the range in which the reduction in gas density increases the mean free path of electrons sufficiently to allow them to gain more energy between successive collisions; however, a further decrease in density does not indefinitely favour ionization since, when the gas becomes too rarefied, the collision frequency decreases to such an extent that, although electrons travel longer distances between collisions, the number of ionizing collisions occurring along the discharge path is reduced; consequently, the overall effectiveness of avalanche multiplication decreases

[19] although Paschen's law was originally formulated to describe the breakdown voltage of a gaseous gap between bare metallic electrodes under a uniform E-field, it can still be adopted here as a useful theoretical reference for the interpretation of PDIV; indeed this side note comes from the fact that the inception of a partial discharge and the complete breakdown described by the classical Paschen law are conceptually distinct phenomena, as already described; nevertheless, both phenomena rely on the same fundamental gas-ionization mechanisms; in the absence of a general closed-form analytical expression capable of describing the PDIV for the actual non-uniform geometries and insulated-electrode configurations considered in this work, the Paschen formulation therefore provides a convenient first-order framework to capture the influence of temperature on discharge inception; yet, the formula and its result should not be interpreted as an exact prediction of the experimental PDIV, but rather as a physically motivated reference model that allows the temperature dependence of gaseous discharge inception to be discussed on a consistent theoretical basis

[20] notice that eq. (1.20) is formally equivalent to eq. (1.11)

where the Townsend ionization coefficients are scaled as $A(T) \propto 1/T$ and $B(T) \propto 1/T$, which is conceptually and mathematically equivalent to the **classical Dunbar temperature correction** of Paschen's law[21]. Thus, by considering the values of the two coefficients A and B at a reference temperature T_0, it's possible to write eqs. (1.21) and (1.22) precisely for the temperature T_0 and for a generic temperature T. By making their ratio, one gets:

$$A(T) = A_0 \frac{T_0}{T} \tag{1.23}$$

$$B(T) = B_0 \frac{T_0}{T} \tag{1.24}$$

where precisely $A_0 = A(T_0)$ and $B_0 = B(T_0)$ are the values of the coefficients at the reference temperature T_0. By replacing eqs. (1.23) and (1.24) into eq. (1.20), one obtains a more explicit expression for the PDIV as a function of temperature:

$$V_{\mathrm{PDIV}}(T) = \frac{B_0 \frac{T_0}{T}\, p\, d}{\ln\left(A_0 \frac{T_0}{T}\, p\, d\right) - \ln\left(\ln\left(1 + 1/\gamma_{\mathrm{se}}\right)\right)} \tag{1.25}$$

Now, by defining the dimensionless product $X = A_0\, p\, d$ and the constant $C = \ln\left(\ln\left(1 + 1/\gamma_{se}\right)\right)$ then the ratio of PDIV at the two temperatures T and T_0 is:

$$\frac{V_{\mathrm{PDIV}}(T)}{V_{\mathrm{PDIV}}(T_0)} = \frac{T_0}{T} \frac{\ln(X) - C}{\ln\left(X \frac{T_0}{T}\right) - C} \tag{1.26}$$

It's possible to make a numerical estimation of the PDIV ratio at a temperature chosen as reference, just to make an example. By assuming a typical secondary-electron-emission coefficient $\gamma_{se} \approx 10^{-4}$, then one gets:

$$C = \ln\left(\ln\left(1 + 10^4\right)\right) \approx \ln(9.21) \approx 2.22 \tag{1.27}$$

By letting be $T_0 = 298\,\mathrm{K}$ ($25\,^\circ\mathrm{C}$) and $T = 453\,\mathrm{K}$ ($180\,^\circ\mathrm{C}$), the temperature ratio is:

$$\frac{T_0}{T} = \frac{298}{453} \approx 0.658 \tag{1.28}$$

Considering the following indicative parameters $A_0 \approx 12\,\mathrm{Pa}^{-1}\,\mathrm{m}^{-1}$, $p = 1\,\mathrm{atm} = 101\,235\,\mathrm{Pa}$ and $d \approx 1 \times 10^{-4}\,\mathrm{m}$, one gets:

$$X \approx 120 \quad \Longrightarrow \quad \ln(X) \approx 4.8 \tag{1.29}$$

$$\ln\left(X \frac{T_0}{T}\right) = \ln(120 \times 0.658) \approx 4.36 \tag{1.30}$$

[21] indeed in this case we accounted for the variation of the two constants $A(T)$ and $B(T)$ with the temperature, while the proper Dunbar correction would define fixed/reference values for the constants A and B but would define an equivalent pressure as $p_{\mathrm{eq}} = p_0 \frac{T_0}{T}$, and the result is mathematically the same – indeed, reiterating the concept, the Dunbar correction is formulated by defining an equivalent pressure p_{eq} that scales the ambient pressure p to represent the reduction in gas density N in an open system where gas is free to expand under constant pressure

By eventually evaluating eq. (1.26), one gets:

$$\frac{V_{\mathrm{PDIV}}(180\,^{\circ}\mathrm{C})}{V_{\mathrm{PDIV}}(25\,^{\circ}\mathrm{C})} = 0.658 \times \frac{4.8 - 2.22}{4.36 - 2.22} \approx 0.79 \tag{1.31}$$

which is basically a $\sim 21\%$ decrease in respect to the one at ambient temperature.

Alternatively to the Dunbar temperature correction of Paschen's law, one can introduce also the **Peek's temperature correction**, which is the primary alternative historical correction found in literature [133, 134]. Unlike Dunbar's approach, which corrects the gas density both inside and outside the logarithm, Peek's correction is empirical and scales the overall breakdown voltage directly with the gas density ratio:

$$V_{\mathrm{PDIV}}(T) = V_{\mathrm{PDIV}}(T_0) \cdot \frac{T_0}{T} \quad \Longrightarrow \quad \frac{V_{\mathrm{PDIV}}(T)}{V_{\mathrm{PDIV}}(T_0)} = \frac{T_0}{T} \tag{1.32}$$

thus the ratio of PDIV at temperature T to that at the reference temperature T_0 is much simpler. For instance, considering the same temperatures as before, one can compute the Peek's ratio:

$$\frac{V_{\mathrm{PDIV}}(T)}{V_{\mathrm{PDIV}}(T_0)} = \frac{T_0}{T} = \frac{298\,\mathrm{K}}{453\,\mathrm{K}} \approx 0.658 \tag{1.33}$$

which is basically a $\sim 34.2\%$ decrease in respect to the ambient temperature. Yet, as it will be discussed in chapters 3 and 4, Peek's correction is the worst estimation of the actual variation of the PDIV in respect to temperature.

1.6 Partial Discharge challenges in oil-cooled electric motors

The physical mechanism behind the experimentally found drop in PDIV upon oil volatilization can be qualitatively interpreted by combining the framework of Paschen's law with molecular ionization physics. Under normal conditions, the gas phase in the insulation cavity consists of air (primarily N_2 and O_2), whose relatively high ionization energies contribute to the electrical strength of air (15.6 eV for N_2 and 12.1 eV for O_2). The breakdown voltage V_{b} of a gas gap is mathematically defined by Paschen's law as a function of the pressure p and the gap distance d through the aforementioned eq. (1.11). When thermal degradation or localized electrical discharge causes part of the oil to volatilize, the vapour-phase composition of the low-density dielectric space is altered. The volatile compounds, specifically alkenes, aldehydes, ketones, and organic acids, which will be introduced and explained better in section 2.2.3, influence this system through some distinct physical mechanisms:

1. **Modification of electron–molecule collision kinetics and cross-sections**: due to their larger molecular sizes compared to diatomic N_2 and O_2, volatile organic compounds possess significantly larger collision cross-sections and this increases the probability of electron-molecule collisions within the gas gap, altering the Townsend ionization coefficient α (potentially increasing it under the relevant field conditions and thereby contributing to a reduction in PDIV, as explained with fig. 1.14);
2. **Introduction of species with lower ionization energies (low IP)**: the presence of

particular volatile organic compounds, polar carbonyl oxygen atoms and delocalized π-electrons[22] drastically reduces the effective ionization potential of the gas mixture compared to those of the main constituents of air; indeed, representative aldehydes, ketones, and alkenes exhibit ionization energies approximately in the $9.7 - 10.9\,\text{eV}$ range, compared with approximately $12.1,\text{eV}$ for O_2 and $15.6\,\text{eV}$ for N_2, thus introducing ionization channels that become energetically accessible to electrons at lower kinetic energies than those required for ionization of the main constituents of air.

Consequently, as these volatile chemical species accumulate in the vapour phase, the effective Paschen curve of the gas gap shifts downward. Electrons easily initiate avalanches at much lower voltage stresses, leading to severe pre-breakdown dynamics, high-energy partial discharges, and a dramatic drop in the PDIV.

[22] a delocalized π-electron is an electron belonging to a π-bond that is not confined between only two specific atoms, but whose electron density is spread over several adjacent atoms; in practice, instead of thinking of the π-electrons as belonging exclusively to the given bond, quantum mechanically the adjacent orbitals interact and form molecular orbitals extending over the entire conjugated region

Chapter 2

Materials and methods

2.1 Thermogravimetric analysis (TGA)

The material in this section is based on what is presented in [135, 136, 137, 138, 139, 140]. For full details and proofs, one should refer to the original source.

2.1.1 Fundamental working principle

Thermogravimetric Analysis (TGA) is a quantitative analytical technique within thermal analysis which is very important in materials characterization. At its thermodynamic core, TGA continuously monitors and records the absolute or percentage the change in mass (either weight loss or weight gain) of a sample as a function of temperature or time. The specimen is subjected to a strictly controlled, user-programmed temperature profile within a defined gaseous atmosphere. By establishing a link between temperature and mass change, TGA enables a quantification of thermal stability, material composition and decomposition kinetics. Mathematically, the proper thermogravimetric response can be expressed as a continuous function of time t under isothermal conditions:

$$m = f(t) \quad \text{(under isothermal conditions)} \tag{2.1}$$

or as a function of temperature T during non-isothermal (dynamic heating or cooling) programs:

$$m = f(T) \quad \text{(non-isothermal or dynamic thermal conditions)} \tag{2.2}$$

In proper experimental setups, the mass m is typically normalized and plotted as weight percent relative to the initial mass m_0 on the ordinate axis, while the abscissa displays either elapsed time (t, in minutes or seconds) or sample temperature (T, in °C or K).

The fundamental principle underlying TGA is straightforward: as a material undergoes thermal treatment, it experiences physical or chemical transitions that lead to either a mass loss or a mass gain. In particular, we can distinguish the two:

- **Mass loss processes**: they are typical endothermic or pyrolytic events, such as the evaporation of absorbed moisture or residual solvents, the volatilization of low-molecular-weight

additives, chemical decomposition (for instance, thermal cracking of polymer backbones), desorptions, and chemical reductions in reducing atmospheres;

- **Mass gain processes**: they are typically chemical reactions between the sample and a reactive purge gas, such as the oxidation of metals or carbonaceous materials in an air/oxygen environment, or the absorption of gaseous species onto the material's surface.

An important aspect in the interpretation of thermogravimetric measurements is that TGA curves should not be regarded as thermodynamic equilibrium curves, but rather as the experimental manifestation of kinetically controlled processes[1]. Thermodynamics determines indeed whether a given transformation is energetically favourable in a given condition, whereas kinetics determines the rate at which such a transformation actually takes place under the imposed experimental conditions[2]. Consequently, a material may in principle undergo a certain transformation at a given temperature, while the corresponding reaction rate may be too low to produce a measurable mass variation within the time scale of the experiment – as the temperature increases, the reaction rate generally rises and the associated mass change becomes progressively detectable. It's possible to give a mathematical description of this concept – the kinetics of a thermal decomposition process can be expressed in terms of the fractional conversion α as:

$$\frac{d\alpha}{dt} = k(T)f(\alpha) \tag{2.3}$$

where α represents the extent of conversion[3], $f(\alpha)$ describes the dependence of the reaction rate on the reaction progress and therefore reflects the assumed reaction mechanism, and $k(T)$ is the temperature-dependent kinetic rate constant[4]. Due to the exponential dependence of $k(T)$ on temperature, relatively small increases in temperature may result in a significant increase in reaction rate. Thus, the temperature at which a noticeable mass loss appears in a TGA curve does not necessarily correspond to a unique thermodynamic decomposition temperature, but rather to the temperature at which the process becomes sufficiently rapid to be observed under the adopted experimental conditions. This aspect and all these considerations are particularly relevant in non-isothermal TGA experiments, in which the sample temperature is continuously varied according to a prescribed heating program. For a linear heating ramp, the heating rate

[1] one has to mention that "thermodynamic equilibrium curve" means a curve that would represent the state the material reaches after being given sufficient time to attain equilibrium at each temperature while "experimental manifestation of kinetically controlled processes" means that the TGA curve shows how fast physical or chemical transformations actually occur under the specific experimental conditions rather than simply indicating whether those transformations are thermodynamically possible

[2] to explain better the concept that have been mentioned, thermodynamics answers questions like "is this transformation energetically favourable at a given temperature and pressure? What is the equilibrium state?" and, for a chemical transformation, this is related to quantities such as Gibbs free energy; kinetics instead answers to questions like "How fast does the transformation occur?" because a process can be thermodynamically favourable but kinetically extremely slow because it must overcome an activation-energy barrier

[3] the fractional conversion α is a dimensionless quantity that tells how far a mass-loss process has progressed, and a common definition is $\alpha = \frac{m_0 - m_t}{m_0 - m_f}$ where m_0 is the mass before the considered process starts, m_t is the mass at a given time or temperature, and m_f is the final mass after that process is complete

[4] it can be for instance the well-known Arrhenius equation $k(T) = A\exp\left(-\frac{E_a}{RT}\right)$, where A is the pre-exponential factor, E_a is the apparent activation energy, R is the universal gas constant, and T is the absolute temperature

can be defined as:

$$\beta = \frac{dT}{dt} \tag{2.4}$$

and the kinetic equation can therefore be rewritten as:

$$\frac{d\alpha}{dT} = \frac{1}{\beta} k(T) f(\alpha) = \frac{A}{\beta} \exp\left(-\frac{E_a}{RT}\right) f(\alpha) \tag{2.5}$$

This formulation explicitly shows that the experimentally observed conversion as a function of temperature depends not only on the intrinsic kinetic parameters of the material, but also on the applied heating rate β: at a higher heating rate the sample spends less time within each temperature interval and the reaction has less time to proceed; as a result, an equivalent degree of conversion is generally reached at a higher temperature, producing an apparent shift of mass-loss transitions and decomposition peaks toward higher temperatures; conversely, lower heating rates provide more time for thermally activated processes to develop and can therefore lead to the observation of mass changes at lower temperatures. For such reason, characteristic temperatures obtained from TGA, such as the onset temperature or the temperature associated with a given percentage of mass loss, should not be interpreted as absolute material constants. Therefore, when TGA is used to assess the thermal stability of a material, the resulting temperature limits should always be interpreted within the specific experimental conditions under which they were obtained.

2.1.2 Hardware architecture of a thermobalance

The laboratory instrument used to execute these measurements is known as a thermobalance or a Thermogravimetric Analyzer. A high-performance thermobalance is primarily composed of three integrated systems:

1. **The precision microbalance**: it's the core quantitative transducer of the system, capable of continuously recording minute changes in sample mass relative to the initial mass with typically microgram-level sensitivity – modern TGAs frequently operate on the null-balance principle. A common physical balance configuration is the so-called Hangdown pan (see fig. 2.2 for some pans types): the sample pan is suspended below the balance mechanism via a thin hangdown wire (for instance, this mechanism can be found in the PerkinElmer TGA 8000 or traditional thermobalances – see for instance fig. 2.1 for a schematic representation and fig. 2.4 for an actual realization); this vertical suspension takes natural advantage of gravity, enabling high precision and reproducibility.

2. **The programmable furnace**: it surrounds the sample area and is regulated by a programmed temperature controller; it must be capable of precise heating and cooling ramps, as well as maintaining stable isothermal steps.

3. **Atmosphere control and gas management**: this module controls the composition of the vapour phase surrounding the sample crucible, typically regulated by Mass Flow Controllers (MFCs). Carrier gases are divided into two main categories:

    - **Inert purge gases** (for instance, Nitrogen, Helium, Argon): they are used to

study non-oxidative thermal decomposition, allowing the sample to strictly react to temperature without chemical combustion;

- **Reactive purge gases** (for instance, Air, Oxygen): they are used to study the oxidative stability of materials, carbon burn-off, or active oxidation kinetics

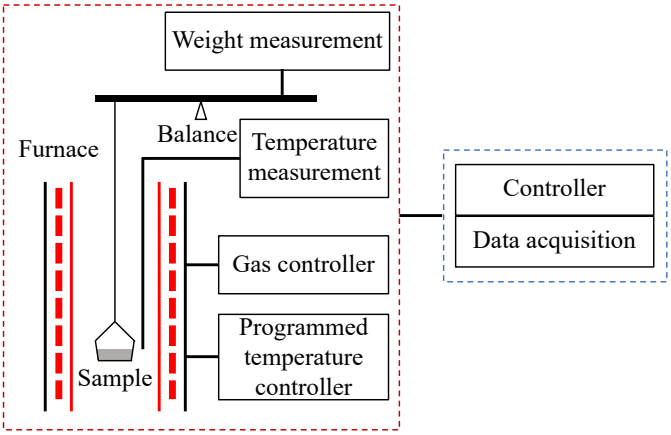


Figure 2.1. Schematic of TGA equipment with the crucible at low position of the vertical heating furnace (adapted from [141])

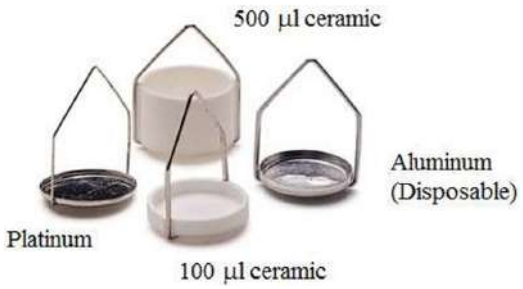


Figure 2.2. Examples of different sample pans and crucibles commonly used for thermogravimetric analysis (adapted from [136])

2.1.3 Application of TGA for the analysis of oils

Thermogravimetric analysis is widely used for the thermal characterization of oils and lubricants, as it provides direct information on their mass-loss behavior as a function of temperature. This is particularly relevant for lubricants, which are complex mixtures containing components with different volatilities and thermal stabilities. When an oil sample is progressively heated, the measured mass loss may result from the evaporation of volatile or semi-volatile fractions and, at sufficiently high temperatures, from the onset of thermal degradation of the lubricant. Under an inert atmosphere, TGA therefore provides a useful indication of the temperature ranges over which the oil remains comparatively stable and those in which significant volatilization or decomposition occurs. The corresponding derivative thermogravimetric curve (DTG) can additionally be used to identify the temperature regions in which the mass-loss rate becomes more pronounced.

In the present study, TGA is employed primarily to support the selection of the temperatures used for the electrical experiments, in particular PDIV measurements, on dielectric cooling

lubricants – this allows the influence of the dielectric cooling lubricants decomposition products on the electrical behaviour of the hairpin-winding interphase insulation to be investigated under controlled thermal conditions while minimizing the contribution of severe lubricant degradation. More in detail, since the investigated oils are exposed to elevated temperatures during the PDIV tests, which are chosen in a manner to be representative of the actual working condition of the motor, it is important to verify that the selected experimental conditions do not produce substantial thermal degradation of the lubricant but yet they release in the atmosphere those particles and molecules which are expected to lower the PDIV of the stator winding. For this reason, the thermogravimetric curves are used to determine a temperature range in which the cumulative mass loss remains limited but still present. In particular, a maximum mass-loss criterion of 0.8% is adopted in this work as a practical reference for identifying suitable test temperatures. This approach does not imply that the oil remains completely unchanged below this threshold, since limited evaporation of the most volatile fractions may still occur, but it rather provides a consistent criterion for avoiding temperature regions associated with substantial mass loss and thermal decomposition.

2.1.4 *PerkinElmer* TGA 8000: description and setup

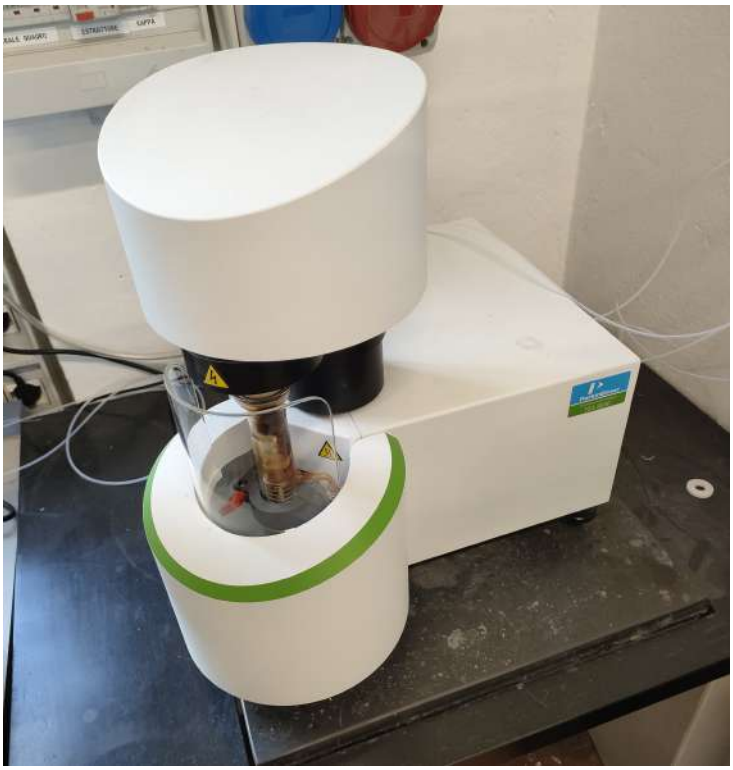


Figure 2.3. Thermogravimetric analyzer used for the experimental characterization of the investigated dielectric cooling lubricants: PerkinElmer TGA 8000 model

The main features of the *PerkinElmer* TGA 8000 equipment, which picture is reported in fig. 2.3, are described below:

- **Hangdown balance configuration**: TGA 8000 adopts a bottom-loading or hangdown configuration, namely the sample pan is suspended below the microbalance by means of

a suspension wire; this geometry improves measurement stability and helps reduce the influence of convective currents generated by the temperature gradients within the furnace, therefore contributing to good reproducibility of the experimental measurements.

- **Microbalance specifications and performance**: the instrument is equipped with a highly sensitive microbalance, characterized by a precision of 0.001% and a maximum capacity of 1300 mg, allowing high accuracy mass detection; the standard furnace operates over a temperature range extending from sub-ambient temperatures up to 1200 °C, allowing both the early volatilization of lighter oil components and the thermal decomposition of heavier residues to be investigated.
- **Software control and automation**: temperature control, heating programs, and data acquisition were managed using the proprietary *PerkinElmer Pyris* software.



Figure 2.4. Close-up view of the TGA furnace and the balance suspension system in PerkinElmer TGA 8000, showing the sample holder connection inside the heated chamber (adapted from [137])

As partially mentioned in the previous sections, the goal is to test the behaviour of the oils in inert atmosphere in order not to trigger and to minimize oxidative reactions and isolate the mass-loss behaviour associated primarily with volatilization and thermally induced degradation of the lubricants. Thus, it's important now to describe the setup of the TGA test that has been run for these work; one has to use *PerkinElmer Pyris* software and go to look into the `Method Editor` window, where some tabs are present:

- `Sample Info` (see fig. 2.5): in this tab one has simply to name the sample that has to be tested and the directory where the results will be located;
- `Initial State` (see fig. 2.6): in this tab one has firstly to set the initial temperature value of the test, and then most importantly one has to set the gas which will constitute the environment during the heating phase (in this case it has been selected to be only nitrogen but one can also use dry air, or even try different and more complex patterns with a mixture or with a switch between air and nitrogen);
- `Program` (see fig. 2.7): this is one of the most important tabs because here one has to set the temperature-time profile that will be followed in the test; in this case it has been used:
  - a first fast linear heating up to 80 °C at a 10 °C/min;

- from 80 °C to 350 °C a slower linear heating at a 5 °C/min rate is chosen in order to analyse quite properly the mass changes due to ongoing reactions;
- in the middle of the previous heating phase, a constant temperature step at 100 °C for 5 min was used in order to let all the water content go away;
- then, a linear fast heating from 350 °C up to 650 °C at a 10 °C/min rate is used to heat up the pan (the higher rate is used also thinking that all the proper thermal reactions have already vanished);
- eventually, a constant temperature step at 650 °C for 30 min is used basically thermally clean the pan from possible residues;

In the bottom part one can also see the temperature-time chart that was actually implemented during the tests;

- `View Program` (see fig. 2.8): in this last tab one can basically see a recap of the gas selection and of the temperature program that were defined in 2nd and 3rd tabs.

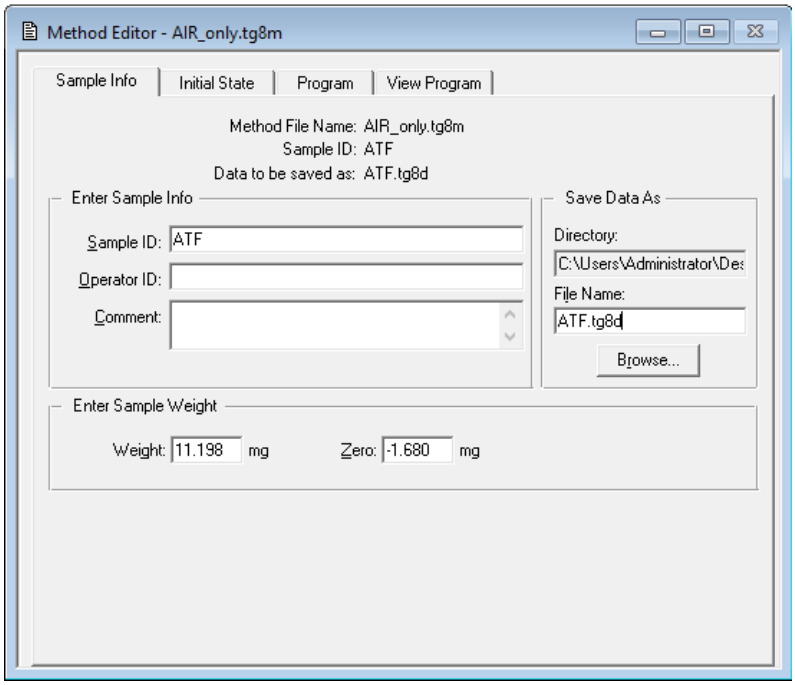


Figure 2.5. `Sample Info` tab of `Method Editor` window

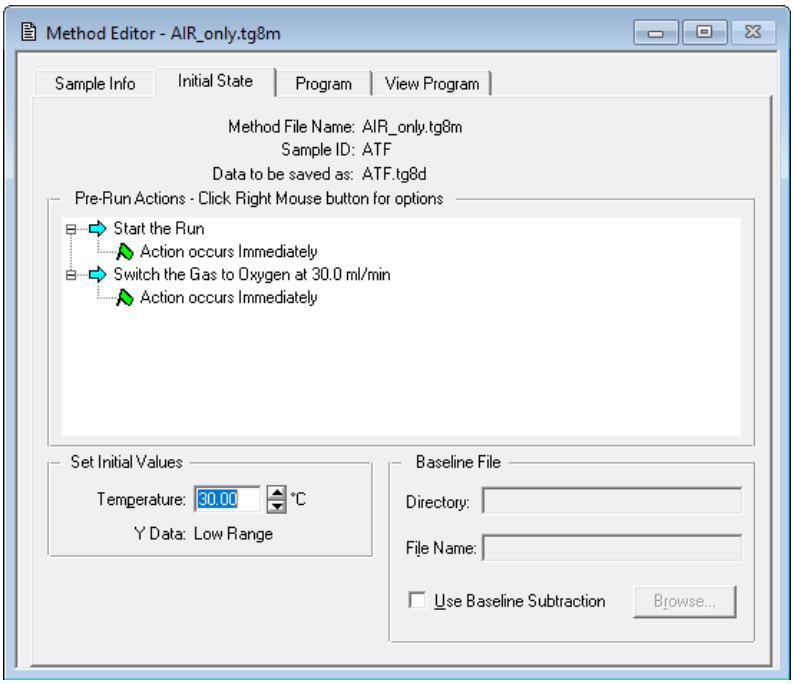


Figure 2.6. `Initial State` tab of `Method Editor` window

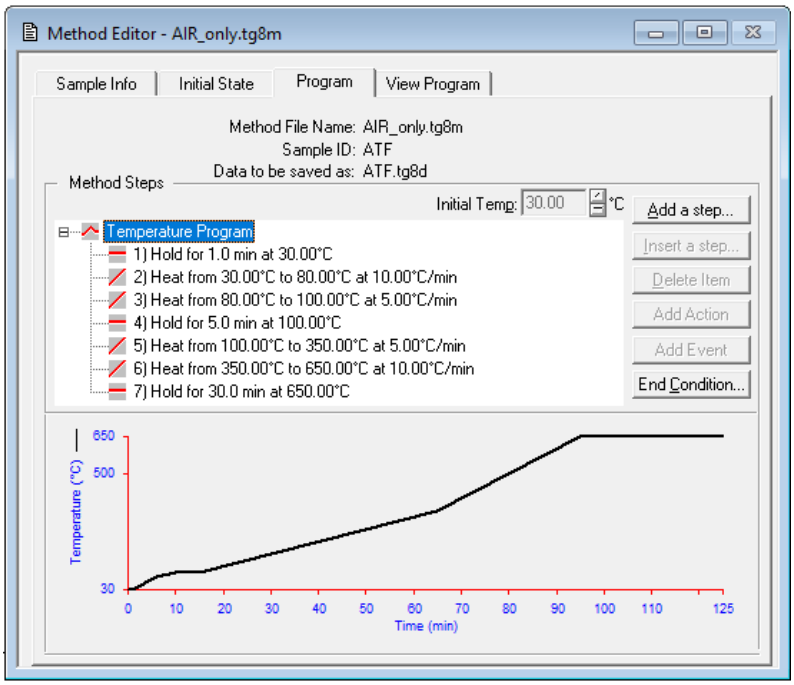


Figure 2.7. `Program` tab of `Method Editor` window

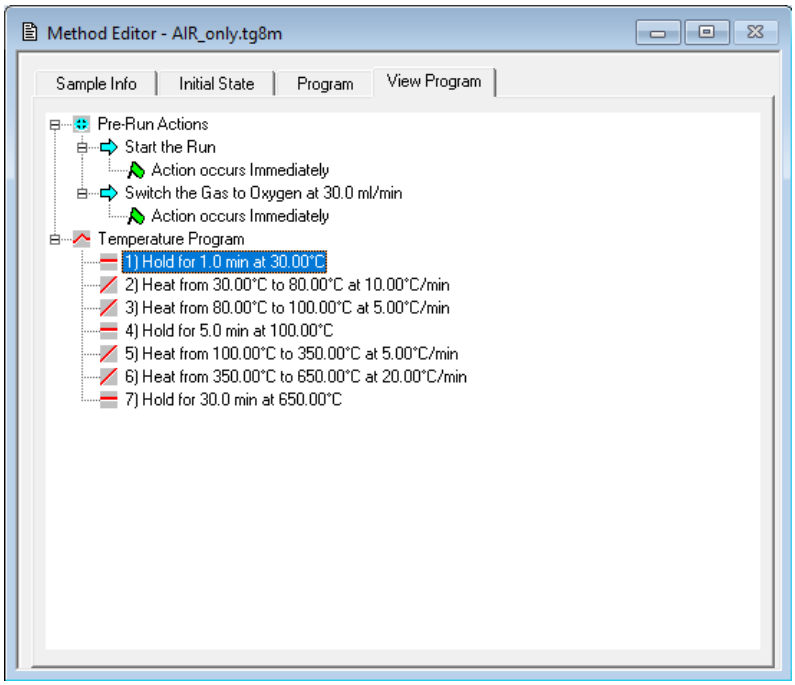


Figure 2.8. `View Program` tab of `Method Editor` window

Once the `Method` has been set, one has to prepare the sample to be tested in the pan. Before the sample preparation, one has to perform the so-called taring the balance, namely put the empty pan on the balance and enforce the zero mass of the balance itself. Then, once the zero has been done, even if the rated maximum mass of the sample in the pan is 1300 mg, PerkinElmer professionals suggest to put no more than $10 - 15$ mg. Thus, with a syringe, we put around 10 mg and then, with the lateral buttons present in the main window of the *Pyris* software, one has to make the mass measurement – indeed the TGA analysis is strictly linked to the mass variation overtime, hence this passage is very important. Eventually, everything is ready to perform the TGA analysis: the setup is concluded, the analysis can be run and one can obtain the results that will be presented and discussed in chapter 3.

2.2 Fourier Transform Infrared (FTIR) spectroscopy

The material in this section is based on what is presented in [142, 143, 144, 145, 146, 147, 148]. For full details and proofs, one should refer to the original source.

2.2.1 Working principle: theoretical fundamentals and the Michelson interferometer

Infrared spectroscopy (IR) is the study of how electromagnetic radiation in the infrared region interacts with matter. The infrared region of the spectrum lies broadly between the visible and microwave regions, but the portion of greatest practical utility to chemists is the mid-infrared region, spanning from $4000\,\mathrm{cm}^{-1}$ to $400\,\mathrm{cm}^{-1}$, which corresponds to wavelengths from $2.5\,\mu$m to $25\,\mu$m. When a sample is exposed to infrared radiation, the molecules absorb specific frequencies of light that match their natural vibrational frequencies; the absorption of this energy causes

the chemical bonds within the material to undergo a transition to a higher vibrational state, increasing their vibrational amplitude. These molecular vibrations are classified into two primary modes:

- **Stretching vibrations**: a rhythmical movement back and forth along the bond axis, altering the interatomic distance and thus the length of the bond along this axis;
- **Bending vibrations**: a movement that changes the angle between chemical bonds while keeping bond length constant.

Crucially, a molecular vibration is only active in the infrared spectrum if it induces a change in the net dipole moment of the molecule[5]. The oscillating electric field of the incoming infrared photons couples with the changing charge distribution accompanying the vibration, allowing energy transfer to occur[6]. Chemical structural fragments, known as functional groups, tend to absorb infrared light within characteristic wavenumber ranges, regardless of the structure of the rest of the molecule. Consequently, the resulting plot of intensity versus wavenumber[7], known as an infrared spectrum, serves as a unique molecular fingerprint.

If older dispersive spectrometers resolved spectra slowly by scanning successive narrow frequency intervals, instead the modern Fourier-Transform Infrared (FTIR) spectroscopy overcomes this limitation by measuring all infrared frequencies simultaneously. This result is achieved using an optical device called the Michelson interferometer, which consists of some optical components (for a schematic representation, one can look at fig. 2.9):

- **Radiation source**: it can be a laser source or a broadband infrared source;
- **Beam splitter**: it's typically made of a thin coating of germanium sandwiched between two pieces of potassium bromide substrate, and it's designed to transmit half of the incoming light and reflect the other half;
- **Fixed mirror**: it rebounds the reflected portion of the beam back to the beam splitter along a constant optical path;
- **Moving mirror**: it rebounds the transmitted portion of the beam back to the beam splitter, translating continuously over a short distance thereby continuously varying the optical path length of that beam;
- **Recombination path**: as the moving mirror shifts, it introduces an optical path difference between the two split beams and, when they recombine at the beam splitter, they interfere with one another; depending on the position of the moving mirror, this interference is either constructive, when the beams are in phase, or destructive, when the beams are out of phase thus cancelling each other; the resulting combined beam, which carries this complex interference pattern, passes through the sample compartment and strikes the detector;

[5] in other words, for a vibration to appear as an absorption band in an IR spectrum, the vibration must make the molecule's dipole moment change with time

[6] this second sentence explains why the changing dipole moment matters physically: the electromagnetic radiation consists of oscillating electric and magnetic fields, and for IR spectroscopy, the important interaction is mainly between the radiation's oscillating electric field and the molecule's oscillating dipole moment

[7] here "intensity" is a generic term for how strongly the sample absorbs (or transmits) infrared radiation at each wavenumber; what is actually plotted on the y-axis depends on how the FTIR spectrum is presented, but most commonly one will encounter transmittance or absorbance

- **Detector or observation plane**: in fig. 2.9 this is represented by the screen, where the resulting interference pattern, or interferogram, is observed; the detector records a time-domain signal called an interferogram, which plots detector response (light intensity) against the optical path difference – this interferogram contains encoded intensity information for all infrared wavelengths simultaneously; to extract a usable spectrum, namely intensity versus wavenumber, a computer applies the mathematical operation of Fourier Transform which converts the raw time-domain interferogram into the frequency-domain spectrum.

Notice that, during analysis, a background spectrum is first measured without a sample to capture the contributions of the instrument and the atmospheric environment (such as water vapour and CO_2 gas) – this passage can be somehow thought and intended as a calibration procedure for the instrument. A sample single-beam spectrum is then acquired with the sample in place. The sample spectrum is eventually mathematically ratioed against the background spectrum, yielding a clean transmittance or absorbance spectrum that is free from instrumental and atmospheric artifacts.

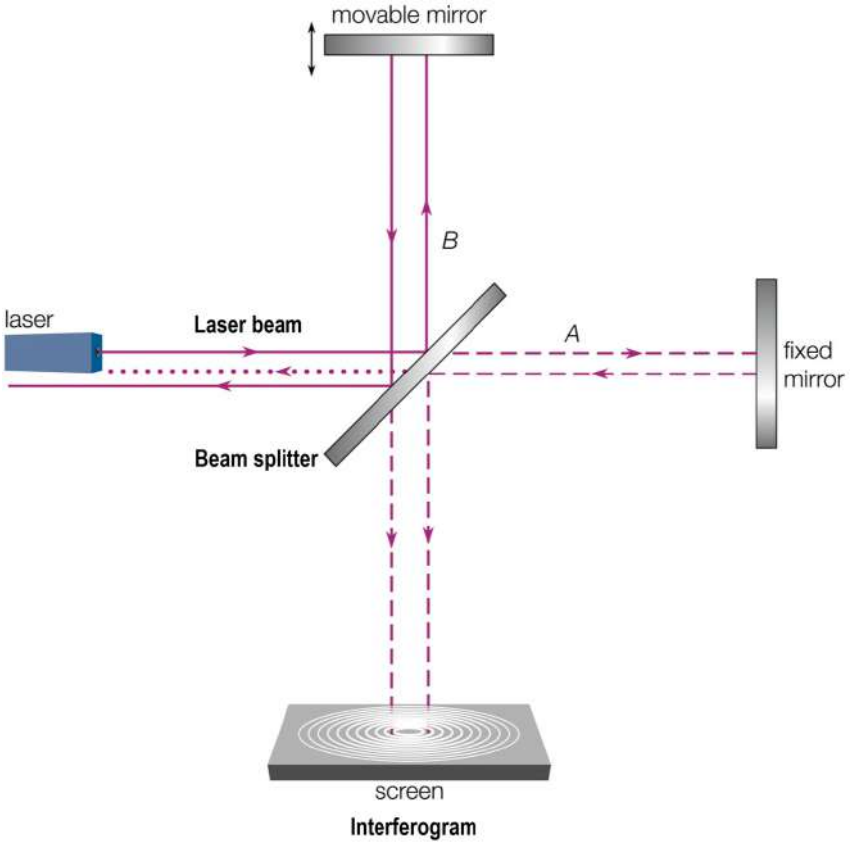


Figure 2.9. Schematic representation of a Michelson interferometer (adapted from [149]))

2.2.2 *PerkinElmer* Spectrum Two

The PerkinElmer Spectrum Two FTIR spectrometer, which is the machine which has been used for performing the analyses of this thesis, is a portable platform optimized for both laboratory use and field applications. From an optical specifications standpoint, the system provides an optimized spectral range of $8300-350\,\mathrm{cm}^{-1}$ when equipped with the proprietary KBr beamsplitter.

The instrument features a standard spectral resolution of $0.5\,\mathrm{cm}^{-1}$, a wavenumber accuracy better than $0.01\,\mathrm{cm}^{-1}$ at $3000\,\mathrm{cm}^{-1}$. At the core of the optical system there is the *Dynascan* interferometer, a rotary Michelson interferometer based on a pair of fixed mirrors. One can see a picture of the actual machine in fig. 2.10, while in fig. 2.11 one can see in the very center of the grey area the measurement area where one has to put the sample to be tested[8].



Figure 2.10. FTIR spectrometer used for the chemical characterization of the investigated dielectric cooling lubricants: PerkinElmer Spectrum Two



Figure 2.11. Close-up of the PerkinElmer Spectrum Two FTIR spectrometer, showing the sample measurement area (adapted from [150])

2.2.3 FTIR analysis of oils

The material in this subsection is based on what is presented in [151, 152, 153, 154, 155, 156, 157, 158, 159, 160, 161, 162, 163, 164]. For full details, one should refer to the original source.

[8] for solid samples, one has to use the so-called ATR pressure arm which is attached to the upper part of the machine in fig. 2.11, while instead if the sample to be tested is precisely oil then one has just to pour very few droplets of oil on the very central part of the measurement area where the sensor is located

FTIR is an exceptional and widely accepted technique for the analysis of oils and lubricants: indeed, liquid oil samples are highly suited for infrared spectroscopy, and their chemical characteristics can be analysed qualitatively and quantitatively. In this context, one can mention *Key Spectral Markers*, sometimes also called diagnostic bands or characteristic absorption peaks: they are specific wavenumbers (namely, basically cm^{-1} values) where chemical functional groups absorb infrared radiation. In other words, infrared absorbance spectrum that comes out from the FTIR analysis serves as a unique molecular "fingerprint," mapping the vibrational frequencies of the chemical bonds present within the fluid. Notice, however, that not all of these absorption bands necessarily originate from the oil's original chemical structure; some may also be associated with new chemical species formed through reactions occurring during operation, particularly as a consequence of thermal and oxidative ageing. In particular, the convention that is considered is the following one:

- light blue indicates the response of the proper oil constituents;
- during operational service, insulating and lubricating oils undergo precisely extensive oxidative and thermal deterioration; this process involves a complex series of chemical reactions, which are indicated with green[9].

Any FTIR spectrum of oil thus contains several diagnostic functional group absorptions:

- **Vegetable Oil Thermal Aging Dynamics**: when natural vegetable oils undergo prolonged heating at elevated temperatures, a clear chemical structural alteration is observed. In particular, a **Decline at** $3008\,\mathrm{cm}^{-1}$ is observed: there is a progressive decrease in the intensity of the cis double bond (=C-H stretching) band at this wavelength, and this decline is directly linked to the destruction of the cis double bonds during thermal oxidation;
- **Aliphatic hydrocarbon chains** (C-H stretching and bending), where the hydrocarbon backbone of mineral base oils (which are one of the main constituents), paraffinic structures, naphthenic molecules, and the long-chain fatty acids of natural/synthetic esters are defined by highly prominent aliphatic absorption bands:
  - **Asymmetric and Symmetric stretching of Methyl ($-CH_3$) and Methylene ($-CH_2-$) groups** ($\sim 2952-2954\,\mathrm{cm}^{-1}$, $\sim 2920-2922\,\mathrm{cm}^{-1}$, and $\sim 2851-2854\,\mathrm{cm}^{-1}$ and $\sim 2870\,\mathrm{cm}^{-1}$): these peaks represent the fundamental aliphatic C-H stretching vibrations typical of alkanes and the long-chain hydrocarbon base oils;

    Under severe thermal stress or localized electrical discharge, homolytic cleavage[10] of the saturated carbon-carbon (C-C) and carbon-hydrogen (C-H) bonds occurs; this thermal and electrical cracking causes a progressive decline in the main methylene stretching peaks ($2921, 2853\,\mathrm{cm}^{-1}$) and the scission of these chains releases volatile gases such as light alkanes and highly reactive alkenes/olefins; consequently, they alter the vapour-phase composition of the insulating cavity: while light, saturated

[9] however this doesn't imply that every green band is exclusively an ageing product; indeed, a given spectral region can already contain a weak contribution in the fresh oil and then increase, decrease or anyway change during ageing

[10] homolytic cleavage, or homolysis, is the equal splitting of a covalent bond where each bonded atom takes one of the two shared electrons

alkanes have a moderate effect, the generated alkenes have exceptionally low Ionization Potentials (IP of $8.0 - 10.0\,\text{eV}$) compared to air ($12 +$ eV), thus the presence of these highly reactive, easily ionizable molecules lowers the dielectric breakdown strength of the vapour, accelerating streamer inception and possibly reducing the PDIV.

- **Deformation and Bending vibrations** ($\sim 1454 - 1465\,\text{cm}^{-1}$ and $\sim 1369 - 1377\,\text{cm}^{-1}$): the band centered around $1454 - 1465\,\text{cm}^{-1}$ is assigned to the C-H asymmetric bending/scissoring of methylene and methyl groups; the peak around $1376 - 1377\,\text{cm}^{-1}$ corresponds to C-H symmetric bending/deformation of methyl groups (though in some insulating mineral oil literature, this band has also been associated with O-H alcohol bending);

  During advanced thermal ageing, a decrease in the intensity of the $1460\,\text{cm}^{-1}$ bending peak is observed and this indicates a progressive loss of the original saturated methylene structure; under extreme stress, this scission leads to the volatilization of light organic compounds: this is the precursor to the formation of volatile alkenes and light oxygenated species which possibly, due to their low IP, increases the local electronic ionization coefficient α thereby lowering the PDIV.

- **Skeletal Rocking vibrations** ($\sim 721 - 722\,\text{cm}^{-1}$): this sharp absorption band corresponds to the in-plane rocking of long-chain methylene groups, specifically indicating the presence of four or more consecutive CH_2 groups in a row; during the thermal oxidation of vegetable oils the peak at $722\,\text{cm}^{-1}$ undergoes a noticeable decrease in intensity, and this decline is directly linked to the structural destruction of the long fatty acid chains and the loss of cis double bonds.

- **Ester and Carbonyl markers**: unlike mineral oils, which consist strictly of paraffinic, naphthenic, and aromatic hydrocarbons, ester-based fluids are characterized by strong polar ester linkages. In particular:

  - **Ester Carbonyl stretching (C=O)** ($\sim 1740 - 1744\,\text{cm}^{-1}$): this extremely intense, sharp peak is the primary diagnostic marker for the ester carbonyl group of triglycerides or synthetic fatty acid esters;

    Triglyceride hydrolysis and synthetic ester thermal degradation break the ester structures into highly volatile fragments, releasing volatile light alcohols, volatile esters, and light organic acids; while the high molecular weight liquid esters possess excellent dielectric strength, their volatile decomposition products are highly polar and have elevated dipole moments; when they evaporate, they accumulate in bubbles or gas pockets which facilitate gas-phase space charge polarization and lower the dielectric breakdown voltage; additionally, volatile esters and alcohols possess lower ionization energies than air, thus reducing the PDIV.

  - **Conjugate C=C and Aromatic Core Fingerprints** ($\sim 1450 - 1463\,\text{cm}^{-1}$): in highly aged transformer mineral oils, which have undergone intense localized thermal stress, a prominent peak emerges at $1463\,\text{cm}^{-1}$ representing an increase in the concentration of conjugated C=C double bonds and aromatic contents; these compounds

are produced via the dehydrogenation of cyclo-alkanes, and this dehydrogenation releases hydrogen gas H_2 and low-molecular-weight volatile aromatic compounds; this alters the breakdown characteristics: hydrogen gas has a high mobility, while volatile aromatics possess very low ionization potentials due to their delocalized π-electron aromatic rings, and the evaporation of these species into the gas phase possibly lowers the PDIV of the insulating gaseous medium.

- **Ester C–O–C stretching** ($\sim 1230 - 1158\,\mathrm{cm}^{-1}$): strong stretching vibrations of the ester C-O-C group occur in this region, with primary diagnostic peaks typically centered around $1237\,\mathrm{cm}^{-1}$ and $1159 - 1160\,\mathrm{cm}^{-1}$; in synthetic base oils, this region undergoes noticeable alterations when the temperature overcomes 180 °C, indicating the onset of thermal cracking; in natural esters, the peak at $1237\,\mathrm{cm}^{-1}$ is used to track the degradation of the ester backbone.
- **Alcohols (-C-OH Stretching)** ($\sim 1070 - 1078\,\mathrm{cm}^{-1}$): the peak corresponds to the -C-OH stretching vibration of secondary and primary alcohols, and it emerges in used gear oils at $1078\,\mathrm{cm}^{-1}$ as a consequence of advanced thermal oxidation; the degradation of hydrocarbons generates polar volatile alcohols that readily volatilize under high operational temperatures: they possess high dipole moments and lower ionization potentials than nitrogen and oxygen.

- **Industrial and drivetrain fluid degradation profiles**: in gear lubricants and Automatic Transmission Fluids (ATF), FTIR spectroscopy is utilized to track specific industrial degradation modes. They are mainly:
  - **Soot accumulation** ($\sim 2000\,\mathrm{cm}^{-1}$): carbon black and particulate soot are detected via a baseline rise centered around precisely $2000\,\mathrm{cm}^{-1}$, and high soot levels drastically accelerate abrasive wear in sliding contacts.
  - **Nitration** ($\sim 1630\,\mathrm{cm}^{-1}$): represents the undesirable chemical reaction of the lubricating base oil with nitrogen oxides (NO_x) generated under high thermal and load stresses; severe nitration indicates advanced thermal degradation, which can lead to the volatilization of highly polar nitrogenous compounds whose introduction into the gas phase dramatically enhances the ionization coefficient of the vapour and, because of their strong electron-attracting groups and polar nature, they distort the local electric field, facilitating the initiation of corona discharges at lower voltage levels.
  - **Sulfation** ($\sim 1150\,\mathrm{cm}^{-1}$): sulfate by-products, arising from the oxidation of sulfur compounds within the base oil or antioxidant/antiwear additives, form a broad band at $1150\,\mathrm{cm}^{-1}$; in particular, strong C-O stretching vibrations characteristic of ester compounds appear at $\sim 1158 - 1170\,\mathrm{cm}^{-1}$ and, in mineral oils, the peak at $1150\,\mathrm{cm}^{-1}$ is assigned to sulfation, which represents sulfate by-products resulting from the thermal oxidation of sulfur compounds within the base oil.

    In synthetic esters, drastic, sudden changes in the peaks at $1170\,\mathrm{cm}^{-1}$ and $1150\,\mathrm{cm}^{-1}$ are observed when temperature passes from 140 °C to 180 °C, and this indicates that thermal degradation of the ester linkages accelerates exponentially; the thermal

scission releases volatile light alcohols and volatile ethers, and this dramatically lowers the dielectric strength of the vapour, and these molecules undergo ionization at lower electric fields due to their lower IP and polar bonds.

- **ZDDP additive depletion** ($\sim 960\,\mathrm{cm}^{-1}$): zinc dialkyldithiophosphate (ZDDP), a critical antiwear and anticorrosion additive, exhibits characteristic peaks around $960\,\mathrm{cm}^{-1}$; additive degradation is mapped by the progressive decline of this peak, exposing gear teeth and bearings to direct metal-to-metal contact; in particular, during the thermal oxidation, the peak in the $(947 - 1016\,\mathrm{cm}^{-1}$ range decreases dramatically, and this indicates the rapid consumption and depletion of ZDDP as it reacts with peroxy radicals to prevent oil oxidation; the ZDDP depletion and thermal decomposition release volatile phosphorus and sulfur by-products, alongside volatile alkenes: this removes the primary defense against oxidation.
- **Water and Glycol contamination** ($\sim 3400\,\mathrm{cm}^{-1}$ and $880 - 800\,\mathrm{cm}^{-1}$): coolant leaks introduce water and ethylene glycol; moisture generates a broad O-H stretching band at $3400\,\mathrm{cm}^{-1}$, while glycol is detected at $880\,\mathrm{cm}^{-1}$ and $800\,\mathrm{cm}^{-1}$; glycol contamination dramatically accelerates oil ageing, sludging and viscosity increases.

- **Carbonyl sub-zone partitioning (zone A vs. zone B)**: to monitor thermal oxidation and distinguish it from other contamination issues, FTIR methodology partitions the C=O carbonyl absorption region $\sim 1820 - 1650\,\mathrm{cm}^{-1}$ into two critical sub-zones. They are:
  - **Zone A** ($\sim 1725 - 1650\,\mathrm{cm}^{-1}$): it is dedicated to the assessment of thermal oxidation and degradation; thermal stress results in a prominent increase in absorbance within Zone A, driven by the generation of highly polar carboxylic acids, ketones, and aldehydes; carboxylic acids and ketones exhibit highly characteristic carbon-oxygen double bond (C=O) stretching and hydroxyl (O-H) vibrations in this range; this degradation is tracked by the emergence of a carboxylic acid carbonyl band at $1710 - 1711\,\mathrm{cm}^{-1}$, which often appears as a broadening or shoulder on the main $1735\,\mathrm{cm}^{-1}$ ester peak;

    The decomposition of the hydroperoxides and the subsequent cracking of oxidized hydrocarbon chains release a suite of highly oxygenated volatiles, which represent the most critical threat to gas-phase dielectric insulation: aldehydes and ketones possess low Ionization Potentials (IP of $9 - 10.8\,\mathrm{eV}$) and their polar molecular structures and elevated dipole moments make them highly susceptible to electric field polarization; in the vapour phase these volatile compounds undergo rapid electron impact ionization, accelerating the initiation of electrical discharge streamers, thus possibly drastically decrease the PDIV in the gas/vapour phase.
  - **Zone B** ($\sim 1770 - 1725\,\mathrm{cm}^{-1}$): it corresponds to esters, and in diesel engines the fuel dilution can be detected by monitoring the growth of a sharp methyl ester peak at approximately $1745\,\mathrm{cm}^{-1}$.

- **Unsaturation markers**: unsaturated fatty acids, containing cis double bonds, exhibit distinct spectral features. In particular:

- **Cis =C-H Stretching vibration** ($\sim 3004 - 3008\,\mathrm{cm}^{-1}$): represents the C-H stretching of a cis-configured double bond, directly reflecting the unsaturation degree of the fatty acid chains.
- **C=C Stretching vibration** ($\sim 1654 - 1658\,\mathrm{cm}^{-1}$): it is a weak-to-moderate band corresponding to carbon-carbon double bonds; during the thermal oxidation of natural vegetable oils, a progressive increase in the peak at $1654 - 1655\,\mathrm{cm}^{-1}$ is observed, and this peak is directly attributed to the formation of conjugated cis-allylic double bonds and secondary oxidation products; the thermal cracking associated with the formation of these double bonds leads to the cleavage of alkyl chains, releasing volatile light alkenes/olefins: they represent an extremely severe hazard to dielectric strength since the π-electrons in the carbon-carbon double bond (C=C) are much less tightly bound to the atomic nuclei than the σ-electrons in saturated alkanes; consequently, alkenes have exceptionally low IsP of $8.0 - 10.0\,\mathrm{eV}$ and, when these volatile alkenes evaporate into the vapour space of the insulation cell, they require significantly less energy to be ionized under the local electric field, thus reducing PDIV to extremely low thresholds.

One has to mention that, even if this is not the main focus of this thesis work, industry relies heavily on FTIR to monitor engine oils, lubricants, and fuels: indeed, by tracking the changes in the carbonyl region (indicating oxidation and nitration), the depletion of additives and the accumulation of contaminants like water or soot, operators can assess oil degradation and engine wear [143, 165].

2.3 Dielectric Cooling Lubricants

The material in this section is based on what is presented in [166, 167, 168, 169, 170, 171]. For full details, one should refer to the original source.

2.3.1 Mineral and Ester-based oils: classification and generalities

As a first thing, one can consider the chemical structure and synthesis methods of the two main families of oils: *Mineral* oils and *Ester* oils, which are further divided into *natural* and *synthetic* esters. **Mineral oils** have been the dominant liquid insulation in power transformers for over a century and have also found widespread use also in other electrical equipment where they can provide insulating, cooling and lubricating functions. Physically, they are obtained through the refining and distillation of crude fossil petroleum. Chemically, mineral oils are non-polar or weakly polar, organic hydrocarbon compounds, which are conventionally categorized into four primary hydrocarbon groups depending on their carbon bond configurations: paraffinic, naphthenic, aromatic, and olefines[11]:

- **Paraffinic hydrocarbons** consist of straight or branched saturated carbon chains; if paraffinic oils possess reasonable chemical stability, they suffer from a major drawback: a high wax content, which significantly elevates their pour point[12] – this characteristic makes

[11] even if some concepts and considerations are referred to the transformer machine, they are obviously valid in general for any other machine

[12] the pour point of a liquid, most commonly petroleum products such as lubricating oils, is the lowest temperature

them highly inadmissible for high-voltage equipment operating in colder climates, as they freeze rapidly and halt oil circulation;

- **Naphthenic hydrocarbons (cycloalkanes)** feature saturated ring structures; naphthenic-based oils are highly preferred for power transformer applications due to their much lower viscosity at low temperatures and an advantageous pour point; furthermore, although naphthenic oils oxidize more easily than paraffinic ones, their oxidation byproducts take the form of soluble sludge rather than insoluble precipitates – this prevents the clogging of cooling ducts and helps maintain efficient heat dissipation;
- **Aromatic and Olefinic** compounds contain unsaturated carbon rings and double carbon-carbon bonds, respectively; aromatics provide some natural gas-absorbing properties under electrical stress but are highly susceptible to oxidation, whereas olefins are highly reactive and generally minimized during the refining process to ensure thermal stability.

Under operating conditions, the primary ageing pathway for mineral oils is a free radical chain reaction of oxidation: molecular bonds break down, generating carbon dioxide, carbon monoxide, and highly reactive peroxides that form free radicals – this degradation yields acidic byproducts and soluble sludges that degrade both the oil's dielectric strength and the solid paper insulation. Moreover, mineral oils present critical environmental and safety risks: they are non-biodegradable, non-renewable, and highly flammable due to their relatively low flash points (typically between $100 - 170\,^{\circ}\mathrm{C}$).

Natural esters, also commonly called vegetable oils, are bio-sourced liquids extracted from the seeds of food crops such as soybean, rapeseed sunflower and coconut. Chemically, natural esters consist of triglycerides naturally synthesized by the esterification of glycerol (a tri-alcohol) with three saturated or unsaturated fatty acid chains; saturated fatty acids have only single carbon-carbon bonds and pack together tightly, causing them to solidify at room temperature while, conversely, unsaturated fatty acids contain one or more double carbon-carbon (C=C) bonds, which introduce bends and kinks in the molecular chain which act as active sites that lower the crystallization temperature but make the oil highly susceptible to oxidation. To overcome viscosity and pour point limitations, crude vegetable oils can undergo chemical transesterification which is a process where triglycerides react with an alcohol (typically methanol) in the presence of a base catalyst to separate glycerol, producing Fatty Acid Methyl Esters (FAME). The other branch is the one of **Synthetic Esters**, which are manufactured through an industrial esterification process that directly reacts a synthesized polyol (an alcohol containing multiple hydroxyl groups, such as pentaerythritol) with carboxylic acids – saturated organic chains are highly preferred in this synthesis because they do not contain the weak double bonds that compromise chemical stability.

Under standard quasi-uniform field testing conditions, unused mineral oils and esters exhibit comparable and highly satisfactory AC breakdown voltages (AC-BDV); however, the behaviour of these liquids diverges significantly in the presence of water. Mineral oil has low moisture tolerance given that its AC-BDV drops precipitously when water content exceeds roughly 20 ppm; in contrast, the AC-BDV of ester liquids is highly resistant to moisture (indeed, the polar

at which the liquid continues to flow or pour when cooled under specified test conditions [172]

ester linkages in both natural and synthetic esters create hydrogen bonds with water molecules, allowing them to dissolve up to 30 times more water than mineral oil – a significant drop in the AC-BDV of synthetic esters is only observed at high water concentrations of $\approx 600\,\text{ppm}$).

Another difference, which can be considered as major dielectric advantage especially in transformers, of ester liquids over mineral oils is their higher relative permittivity[13]: **mineral oils** have $\varepsilon_r \approx 2.1-2.5$ whereas **esters** have $\varepsilon_r \approx 3.1-3.3$. Furthermore, mineral oil has excellent basic dielectric properties, characterized by a very low dissipation factor ($\tan\delta$) and extremely high DC resistivity; instead, due to their polar structure and a higher concentration of mobile ions, esters naturally exhibit a higher dissipation factor and lower resistivity. Other differences that can be listed are the ones related to the rheological parameters. The primary physical limitation of esters is their high viscosity, which affects heat transfer within the transformer; indeed, the viscosity values are $\approx 11-13$ cSt at $40°\text{C}$ for **mineral oils** and $\approx 26-41$ cSt at $40\,°\text{C}$ for **esters**. According to convective heat transfer principles, highly viscous fluids flow more slowly and are characterized by a lower Reynolds number, which limits their flow pattern to the laminar regime. Consequently, the convective heat transfer coefficient h of esters is lower, making them less efficient cooling mediums than mineral oil. Regarding fire safety, namely flash and fire points[14], mineral oil is highly flammable, with a low flash point of approximately $140-165°\text{C}$ and a fire point of approximately $170-185°\text{C}$. Conversely, natural esters exhibit an exceptionally high flash point $> 300°\text{C}$ and fire point $350-360°\text{C}$; synthetic esters similarly exceed a flash point of $250°\text{C}$ and a fire point of $300°\text{C}$.

2.3.2 Properties of the investigated lubricants

The experimental campaign of this thesis work was carried out using initially five different lubricating fluids, later restricted to three. The investigated products include four mineral-oil-based lubricants, namely BIZOL Protect ATF D-6, Fuchs TITAN ATF D-6, Lubra ATF Ergoplus and Castrol BOT BEV G5, together with Fratelli Parodi Tras 24, which is based on a synthetic ester. The main available physicochemical properties of the investigated fluids are summarized in table 2.1 – where specific values were not publicly available from the corresponding technical documentation, the related entries were left unspecified. These parameters provide a concise characterization of the fluids employed during the experimental activity.

[13] higher ester-oil permittivity is advantageous because it provides better permittivity matching with the solid insulation, resulting in a more uniform electric-field distribution and lower electrical stress in the liquid phase and at solid–liquid interfaces; indeed it's simple to prove that $\frac{E_{\text{oil}}}{E_{\text{paper}}} = \frac{\varepsilon_{\text{paper}}}{\varepsilon_{\text{oil}}}$

[14] the flash point is the lowest temperature where a liquid gives off enough vapour to flash a brief flame, but it stops burning when the fire away is taken away; the fire point is a slightly higher temperature where the vapour keeps burning for at least five seconds after the fire is removed [173]

Table 2.1. Main characteristics of fresh oils utilized in this thesis work (adapted from [174, 175, 176])

Make	**Bizol**	**Fuchs**	**Lubra**	**Castrol**	**Fratelli Parodi**
Characteristics	**Protect ATF D-6**	**Titan ATF D-6**	**ATF Ergoplus**	**BOT BEV G5**	**Tras 24 – Paryol**
Chemical nature	Mineral (HC) Hydrocracked	Mineral	Mineral	Synthetic derived from mineral	Synthetic ester
Colour, visual	Red	Red	Red	Amber/light colored	Bright and clear
Density @ 15 °C (kg/m^3)	840	846	–	–	950-1000
Viscosity @ 40 °C (cSt), DIN 51562-1	25.5	29.8	–	–	29
Viscosity @ 100 °C (cSt), DIN 51562-1	5.5	6	–	–	4.4 – 5.4
Viscosity index (min), DIN ISO 2909	129	151	–	–	–
Flammability (°C), DIN ISO 2592	216	206	–	–	$\geq$ 310
Pour point (°C), DIN ISO 3016	−50	−54	–	–	−50
Breakdown voltage (kV)	–	–	–	–	$\geq$ 45
Specifications	–	–	–	–	IEC61099

2.4 PD measurement setup and Omicron

To analyse the electrical phenomena associated with partial discharges, a simplified capacitive representation known as the "abc" model is conventionally used [177]. This model represents the physical dielectric and the defect cavity as a network of three lumped capacitances. Since this concept is quite broadly known, it is here omitted for the sake of brevity. Given that, physically, a partial discharge involves a rapid displacement of charges inside the void collapsing the local electric field inside the cavity to zero, in the "abc" model, this is approximated by a short-circuit in the capacitance associated to the defect, thus resulting in a sudden charge redistribution [177]. Because the generator branch acts as an open circuit during these high-speed transient events due to its series inductance, the total charge inside the EUT boundary remains conserved; to re-establish electrostatic equilibrium and balance Kirchhoff's Voltage Law, one has to introduce the concept of *Apparent charge*, which is the actual charge which can be measured by external instruments which can be proven to be significantly smaller than the actual charge of the discharge [177]. Yet in the case of this thesis work, the aim is just to evaluate the PDIV thus the calibration of the measurement instrument is not needed.

In the experiments that have been carried out for this thesis work, the *Indirect measurement circuit* configuration has been implemented (see fig. 2.12). In detail, to measure high-frequency PD currents, an external coupling capacitor C_k is connected in parallel with the EUT, providing a low-impedance path to close the high-frequency current loop. The fraction of the apparent charge forced to flow through the coupling capacitor loop q_k is determined by:

$$q_\mathrm{k} = \frac{C_\mathrm{k}}{C_\mathrm{a} + C_\mathrm{k}} \cdot q_\mathrm{app} = \frac{1}{1 + C_\mathrm{a}/C_\mathrm{k}} \cdot q_\mathrm{app} \tag{2.6}$$

hence it indicates that a larger coupling capacitance C_k compared to the EUT capacitance C_a yields a higher measurement sensitivity. In particular in the case of the indirect circuit, the measuring impedance is inserted in series with the coupling capacitor C_k. The indirect circuit is generally preferred because it is more practical and safer for high-voltage testing; unlike the direct configuration, it does not require the EUT to be isolated from ground, which is often impossible for large equipment such as transformers and generators, and it also protects the measuring instrumentation from the full fault current in the event of insulation breakdown[15]. Its main drawback is a somewhat lower theoretical sensitivity, since the total discharge current does not flow directly through Z_m; in addition, the indirect configuration reverses the polarity of the measured PD pulses and can introduce ambiguity in PRPD pattern interpretation.

Another very important component of the circuit is the quadrupole, which is a passive four-terminal network connected in series with the coupling capacitor C_k. Its primary function is to act as a signal separator, decoupling the high-voltage power-frequency AC component ($50-60\,\mathrm{Hz}$) from the high-frequency PD current pulses (kHz to MHz range). Indeed, to reconstruct the PRPD patterns needed for diagnostic visual analysis, the detector requires two separate inputs from the quadrupole: the *high-frequency PD signal* and a *synchronized low-frequency AC reference signal*. The internal passive circuitry of the quadrupole is designed to provide these dual outputs

[15] yet this is not the case of the here presented thesis work given that the samples to be tested are just a kind of representation of the stator of a motor and they are not part of an operating/running motor

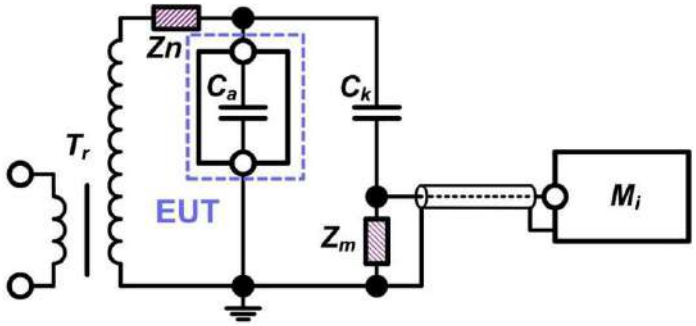


Figure 2.12. Indirect partial-discharge measurement circuit, including the high-voltage transformer T_r, test object (EUT), coupling capacitor C_k, measuring impedance Z_m and measuring instrument M_i (adapted from [177])

through a specialized RLC filter network:

- **High-frequency PD path**: the partial discharge current pulses contain extremely high frequency components; the quadrupole presents a resistive measuring impedance R_M in parallel with the main branch; high-frequency current signals pass through this resistive path with minimal attenuation, generating high-frequency voltage pulses that are routed directly to the PD detection channel.
- **Low-frequency synchronization path**: to synchronize the detected PD pulses with the phase of the applied AC voltage, a capacitive voltage divider is formed between the external coupling capacitor C_k (typically in the range of 1 nF, which is also our case as it can be seen from fig. 2.17) and a much larger internal capacitor C_M in the microfarad range; this divider scales down the high-voltage AC signal to typically few volts (in our case there is a 1 : 1000 transformation ratio, as visible from fig. 2.17); to prevent high-frequency PD current pulses from entering and distorting the synchronization channel, a blocking inductance L_M is placed in series with the sync output: at high frequencies, L_M acts as an open circuit, forcing the PD transients to flow exclusively through the resistive PD path, while at 50 Hz its impedance is negligible.

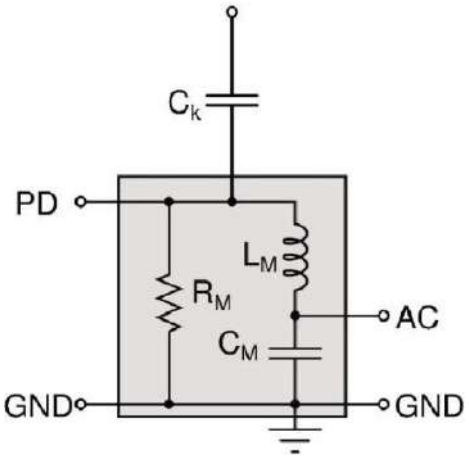


Figure 2.13. Equivalent circuit of the quadripole used in the partial discharge measurement system, showing the coupling capacitor C_k, internal measuring components R_M, L_M and C_M as well as the PD, AC synchronization and ground terminals. (adapted from [177])

2.4.1 Test bay and its components

The theoretical indirect measurement circuit described above was physically implemented through the laboratory setup shown in fig. 2.15 – even if it is a little bit clumsy, the correspondence between the theoretical circuit elements and their physical implementation can be identified[16]. As also visible in the upper part of fig. 2.15, the test bench was located beneath an extraction hood, used to remove the vapours and fumes generated during the heating of the dielectric oils present in the samples employed in the measurements. The high-voltage supply was provided by the step-up transformer shown in fig. 2.18, while the coupling capacitor and measuring-impedance assembly, visible in fig. 2.17, constituted the measurement branch corresponding to C_{k} and Z_{m} of the indirect circuit. The EUT, represented by the back-to-back insulated conductor specimens which will be described later, was instead placed inside the laboratory oven shown in fig. 2.14, allowing the PDIV measurements to be performed at a given temperature. Since the oven enclosure is metallic and grounded, the high-voltage connection to the specimens was routed through the oven wall by means of the PTFE-insulated feedthrough shown in fig. 2.16 – this arrangement ensured adequate electrical insulation between the energized conductor and the grounded metallic enclosure while allowing the specimens to remain connected to the external high-voltage circuit during heating and testing and trying to avoid as much as possible undesired PDs. The entire test bench was installed inside a dedicated interlocked high-voltage test room, surrounded by a metallic shielding structure; the access to the test area was controlled by a safety interlock connected to the room entrance: opening the access door automatically disabled the high-voltage supply and removed the energization of the DUT, thereby safeguarding the operator also during specimen positioning and connection changes.



Figure 2.14. Laboratory oven used to heat the back-to-back specimens to the required test temperature

[16] to be extremely clear, in this configuration the transformer energizes the specimen, whereas the coupling-capacitor branch provides the low-impedance high-frequency return path required for detecting the current pulses associated with partial-discharge activity

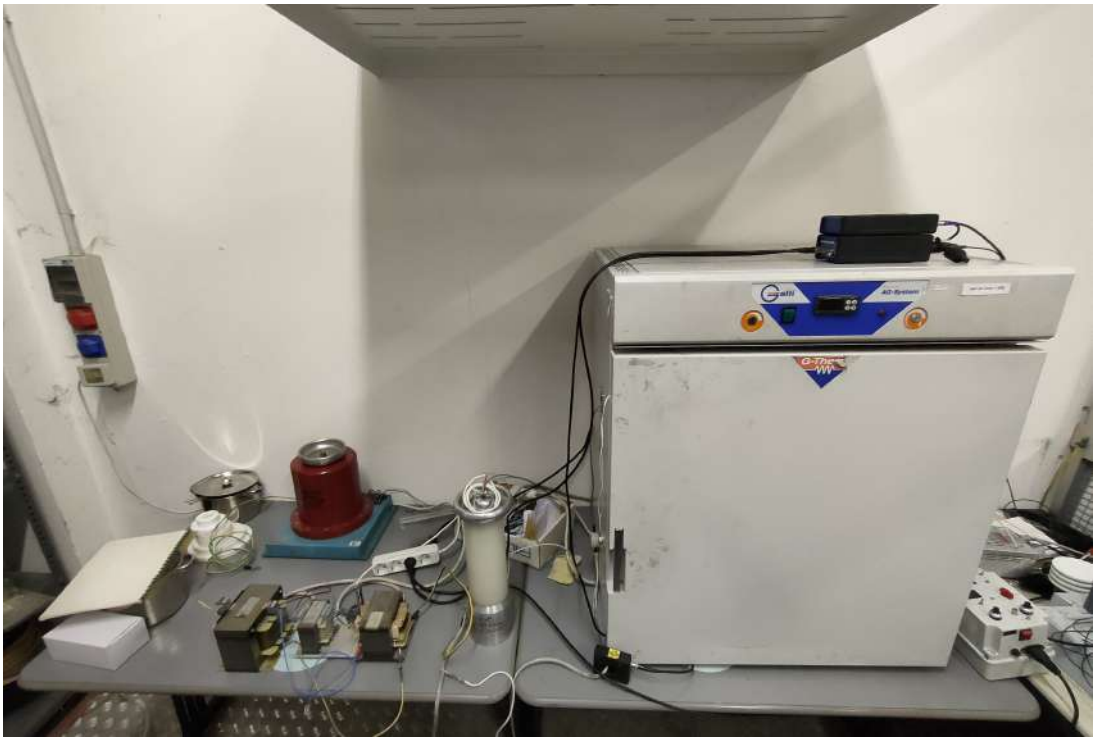


Figure 2.15. Overall view of the high-voltage test setup, showing the laboratory oven on the right and the main components of the PD measurement circuit on the left, including the step-up transformer and coupling capacitor/measuring impedance assembly



Figure 2.16. PTFE-insulated feedthrough used to route the silicone-insulated high-voltage cables through the grounded metallic wall of the oven



Figure 2.17. Close-up of the coupling capacitor and measuring impedance assembly used in the PD measurement circuit, with the high-voltage terminal at the top and the ground connection at the bottom



Figure 2.18. High-voltage step-up transformer used to supply the test circuit during the partial-discharge measurements

2.4.2 Omicron MPD 800 Partial Discharge measurement system

The material in this subsection is based on what is presented in [178, 179, 165, 180, 181]. For full details and complete description of the system, one should refer to the original source.

The *Omicron MPD 800* partial discharge measurement and analysis system represents the latest technological evolution of *Omicron electronics* company, incorporating over twenty years of field and laboratory engineering experience. This device is engineered to detect, localize, and assess the insulation defects that generate partial discharges in the insulation system across a variety of primary assets. The system operates strictly in accordance with international testing regulations – under AC voltage testing, the MPD 800 performs standard-compliant measurements according to the `IEC 60270` and `IEEE C.57.113` standards.

An innovation that is included in the MPD 800 is the fiber-optic internal connection, compared to other systems which use the traditional copper-wired systems. A primary physical challenge in partial discharge detection is indeed isolating minuscule transient currents from massive background electromagnetic interference while operating in close proximity to high-voltage test setups; traditional PD measurement systems rely on coaxial copper cabling to transmit analog signals from the high-voltage coupling quadripole to the monitoring instrument, but this architecture exhibits several fundamental engineering limitations that are resolved by the MPD 800's distributed fiber-optic network. This can be seen as providing different advantages in the measurement system:

- **Galvanic isolation and safety**: traditional coaxial cables physically link the high-voltage testing bay directly to the operator's control desk (see fig. 2.20), but this link represents a severe safety hazard in case of electrical flashover or insulation breakdown; in contrast, the MPD 800 digitizes the raw analog PD signals directly at the measurement point in the high-voltage area and this digitized data is subsequently transmitted via fiber-optic links to the MCU2 control unit (see fig. 2.21), which converts the optical signals back into USB electrical communication for the operator's PC; this design guarantees absolute galvanic isolation, separating the dangerous high-voltage workspace from the low-voltage control workspace and ensuring complete operator safety.
- **Electromagnetic shielding and ground loop elimination**: in standard testing setups long coaxial cables act as high-frequency radio-frequency (RF) antennas, picking up background noise which overlays and corrupts the PD signal; furthermore, routing multiple coaxial cables to a central unit establishes ground loops, introducing mains-borne noise and ground current interference. The MPD 800's fiber-optic cables are completely immune to electromagnetic fields, eliminating high-frequency coupling into the transmission line – by replacing long copper cables with optical fibers and utilizing rechargeable battery packs (RBP1) to power the acquisition units, ground loops are entirely prevented, resulting in a drastically lower system noise floor.
- **Decoupling from mains noise via battery power**: grid-connected test instruments are vulnerable to high-frequency transients, voltage fluctuations, and harmonics propagated through the local power supply; the MPD 800 acquisition units and their associated coupling devices are instead designed to operate on-site using the RBP1 rechargeable battery packs

(see fig. 2.19): running on battery power completely decouples the measurement digitizers from the local power grid, suppressing mains-borne noise and ensuring the highest signal-to-noise ratio in electrically polluted environments.



(a) Front view of the MPD 800 measurement unit powered by the RBP1 rechargeable battery pack, with the fiber-optic connection used for data transmission



(b) Rear view of the MPD 800 measurement unit showing the BNC connections for the PD signal and the AC synchronization/reference signal

Figure 2.19. Omicron MPD 800 measurement unit and RBP1 battery pack used for PD measurements

The MPD 800 partial discharge diagnostic platform consists of a modular suite of hardware units, external coupling devices, and high-frequency sensors that are combined depending on the testing requirements. Hereafter they are briefly described:

- **MPD 800 acquisition unit**: the core of the system is the MPD 800 acquisition unit, a dual-channel digital measurement device; the analog PD input impedance is $50\,\Omega$ ($\pm 20\%$) and the frequency range of the PD input spans from $6-35\,\text{MHz}$ with the internal quadripole enabled and from $0-35\,\text{MHz}$ when bypassed; the AC synchronization input operates from $0.01\,\text{Hz}-10\,\text{kHz}$ with an input impedance of $4.5\,\Omega$ ($\pm 20\%$).
- **MCU2 multi-device control unit**: it functions as the central interface controller between the PC running the MPD Suite software and the distributed acquisition network, namely it converts incoming optical data streams from the fiber-optic network into standard high-speed USB electrical signals. Furthermore, MCU2 devices, an integrated GPS receiver and external GPS antenna port, allow the MCU2 to synchronize its internal system clock to the atomic clocks of GPS satellites – this achieves clock synchronization across multiple independent laptops, enabling to merge datasets recorded simultaneously at different geographical locations (for instance, opposite terminations of a long power cable).

- **RBP1 rechargeable battery pack**: to maintain the galvanic safety isolation and decouple the acquisition hardware from power grids, the RBP1 battery pack is utilized; a single RBP1 powers an MPD 800 unit for up to 14 hours at room temperature, but up to five RBP1 units can be connected in cascade to power long-term monitoring setups.
- **Measuring impedances, coupling capacitors, external sensors**: the external coupling and sensing devices used in an MPD 800 measurement are not fixed, but are selected according to the electrical asset, the expected PD signal, and the adopted test circuit; in the conventional measurement configurations, the resulting PD and synchronization/reference signals are ultimately fed to the dedicated BNC inputs of the MPD 800 acquisition unit.

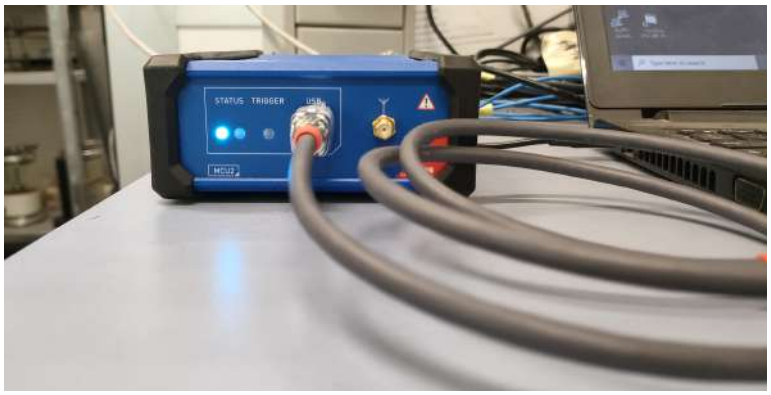


Figure 2.20. Measurement workstation used for the partial-discharge tests: the setup includes the control laptop and the MCU2 receiving/control unit of the MPD 800 system, while the variable autotransformer (Variac) visible on the right-hand side is used to manually regulate the voltage supplied to the high-voltage test equipment through its adjustment knob

2.4.3 Omicron MPD Suite software

The Omicron MPD Suite software represents the control, analysis, and visualization framework of the MPD system. The software architecture is divided into two primary execution windows:

- When launching the MPD Suite, the operator is presented with the **Start Page**, which acts as the system gateway (see fig. 2.22); it provides the following functional sections such as *Start Measurement* and *Workflow - Cable Factory Testing* in the upper part, and *User Profiles Area* in the bottom part; eventually, on the right side one has other sections and other additional areas.
- Then the operator, by selecting one among the various *User profiles*, can access to the **Main Measurement Window** which is split into distinct functional zones separated by adjustable splitters (see figs. 2.23 to 2.25):
  - **Upper diagram view**: it displays the primary real-time plots, including the PRPD, H(Q), Ellipse, PD/DC, Meters, and System Overview;



(a) Front view of the MCU2 control unit used in the MPD 800 partial-discharge measurement system



(b) Top view of the MCU2 control unit connected to the laptop via USB cable and to the fiber-optic communication cables

Figure 2.21. MCU2 control unit used in the MPD 800 partial-discharge measurement system

- **Control panel**: it's collapsible panel on the right side containing settings tabs: *Setup & Calibration*, *PRPD & AC*, *Assessment*, *Reporting*, *Exporting*, *Record/Replay* and few others;
- **Lower diagram view**: it displays secondary diagnostic plots, such as the *Assessment* view, *Scope* view, *3PARD*[17], *3FREQ*[18], *FFT* and few others.

[17] in multi-phase systems, PD pulses from a defect on one phase capacitively couple to the adjacent phases, appearing as simultaneous signals across all three measurement points; 3PARD isolates these cross-coupled signals by performing synchronous multi-channel measurements on all three phases: when a pulse is detected simultaneously on all three channels, its amplitude relations are plotted as a vector sum on a star diagram with three axes arranged at 120° angles and, because the coupling coefficient from the defect to the sensors is constant, pulses from a specific defect location form a tight, colored cluster on the 3PARD star plot; by drawing selection rectangles around these clusters, the operator can perform 3PARD back-transformation which displays only the PD events belonging to the selected defect cluster, greying out the residual coupled noise in the background

[18] for single-phase measurements where multi-phase coupling is unavailable, the 3FREQ technique is used; this single-channel method characterizes PD sources by their high-frequency spectral signature; the MPD 800 utilizes three digital bandpass filters running in parallel on a single channel: the main filter (f_{m}) and two auxiliary filters ($f_{\mathrm{Aux\ I}}$, $f_{\mathrm{Aux\ II}}$), each detected pulse is measured simultaneously on all three bands; the ratio of the three charge amplitudes is plotted on a 3FREQ star diagram and, like 3PARD, this separates distinct insulation defects into separate clusters based on their frequency components, allowing single-channel back-transformation and noise isolation

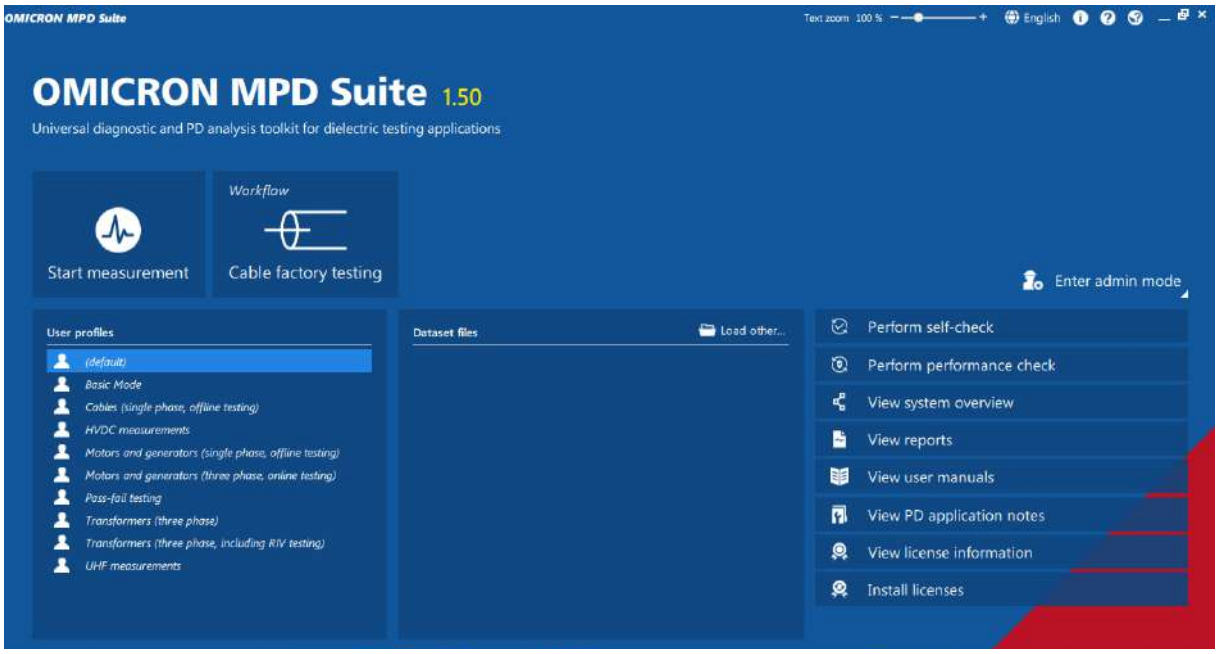


Figure 2.22. Omicron MPD Suite 1.50 start page

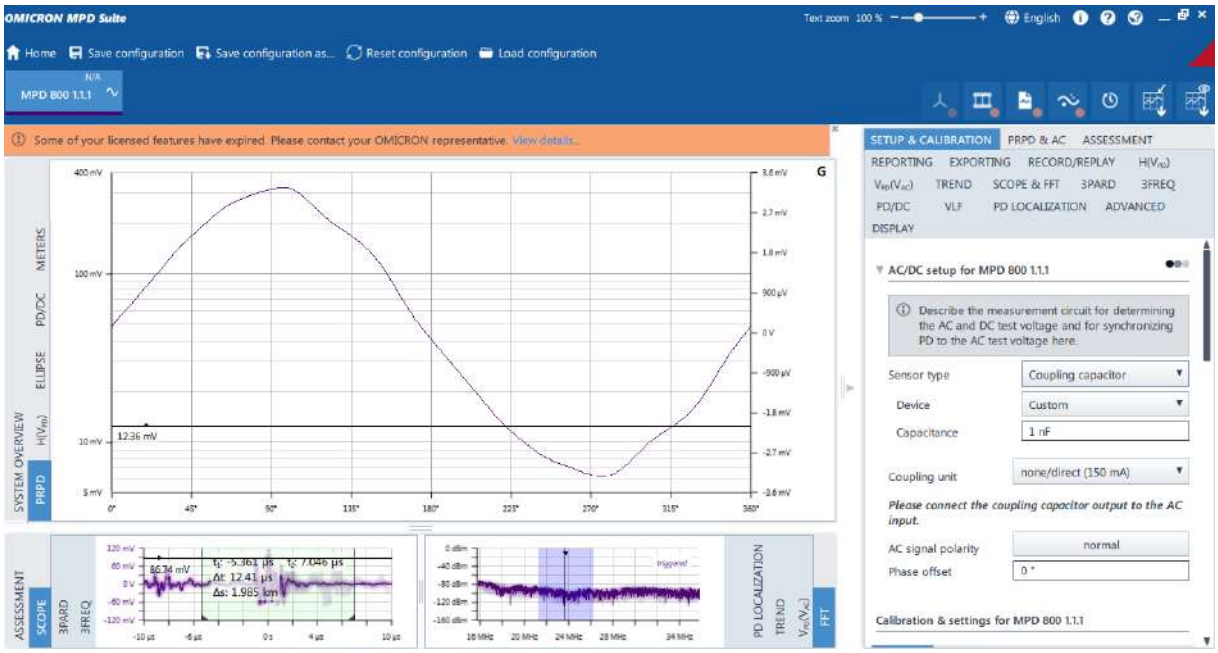


Figure 2.24. Omicron MPD Suite measurement interface showing the phase-resolved partial discharge (PRPD) display together with the time-domain PD signal and frequency-spectrum visualization

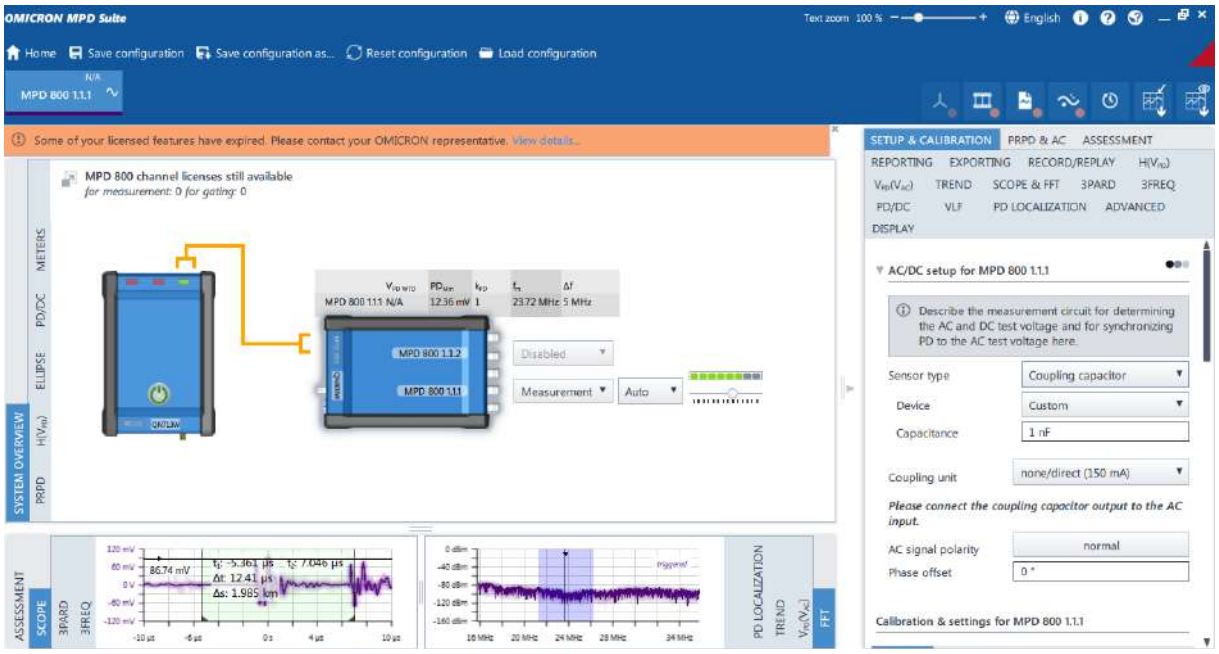


Figure 2.23. Omicron MPD Suite system overview showing the detected MCU2 control unit and connected MPD 800 acquisition unit

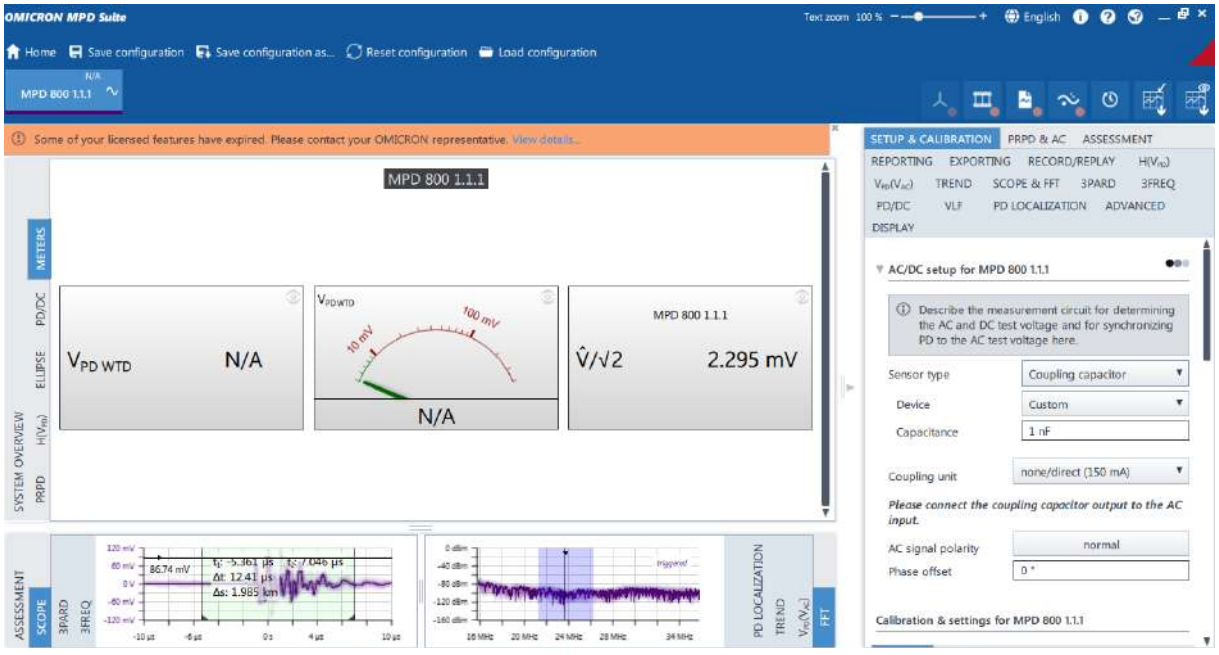
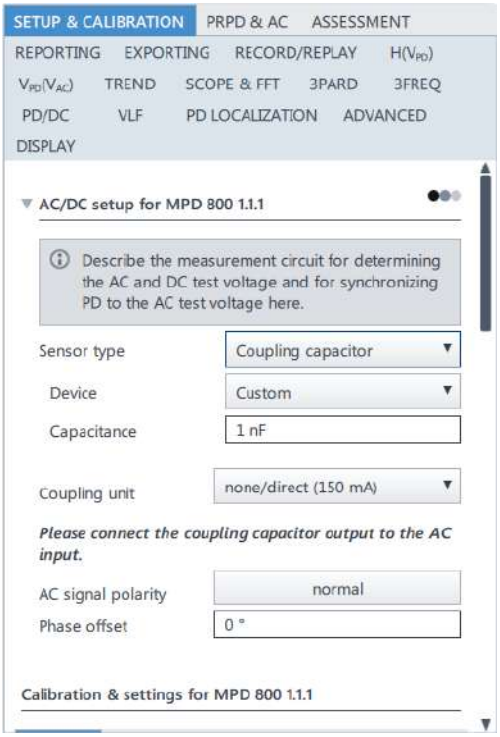


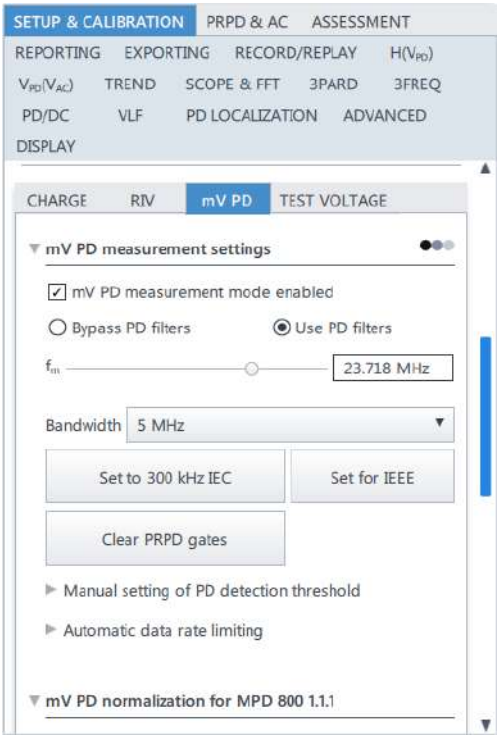
Figure 2.25. Omicron MPD Suite measurement interface in meter-display mode, showing the numerical and graphical representation of the acquired electrical quantities

Now it's possible to briefly describe what one can find in the *Setup & Calibration* control panel tab. One can look at the four subfigures of fig. 2.26;

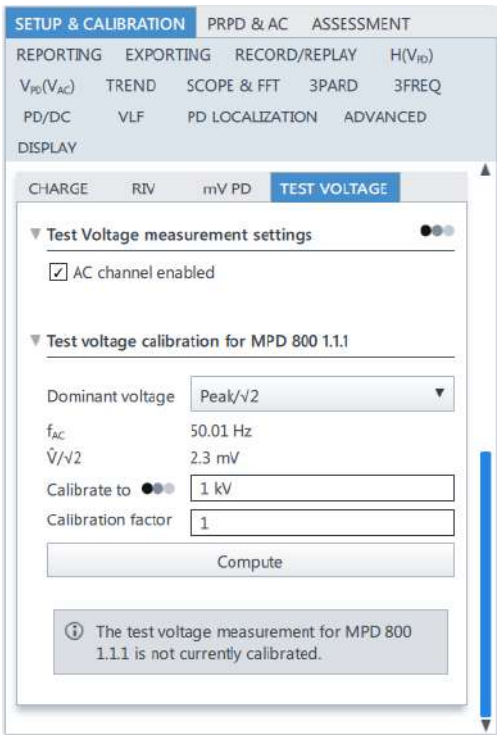
- The MPD Suite allows modeling the electrical circuit connected to each channel group; in the *AC/DC Setup* expander, the operator defines the Sensor type (direct/custom, Coupling Capacitor, HFCT, VT, Rogowski coil, TEV sensor, or HV resistor) – see fig. 2.26a.



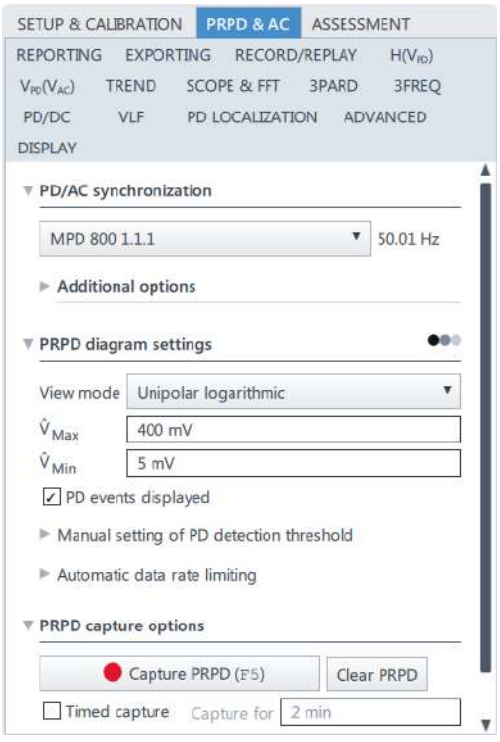
(a) AC/DC measurement setup panel used to define the sensor, coupling configuration, capacitance, signal polarity, and phase offset for the connected MPD 800 channel



(b) Partial-discharge measurement settings used to configure the PD acquisition mode, measurement center frequency, and acquisition bandwidth



(c) Test-voltage measurement and calibration panel used to enable the AC reference channel and define the voltage scaling and calibration parameters



(d) PRPD and AC synchronization settings used to select the synchronization source and configure the PRPD diagram, display limits, and acquisition options

Figure 2.26. Main Omicron MPD Suite configuration panels used for the partial-discharge measurements

- To ensure standard-compliant charge evaluations in picocoulombs (pC), a loop calibration must be performed by means of an external calibrator; if calibration is not possible or maybe not even desired, like in this thesis work where the objective is only to measure the PDIV, one can set the measurement on *mV PD* – see fig. 2.26b.
- The DSP core of the MPD 800 allows the operator to adjust the bandpass filter characteristics to maximize the SNR; in the Frequency-Domain integration the raw high-frequency current is filtered using a digital bandpass filter with a configurable center frequency f_m up to 35 MHz (or 62.5 MHz for MPD 800 – to be rigorous, this is the Nyquist/maximum selectable digital center frequency, given that the MPD 800 samples the PD signal at 125 MSa/s) and bandwidth Δf ranging from 30 kHz to 20 MHz – see fig. 2.26b.
- The PRPD is the primary diagnostic view; it plots individual PD pulses as a statistical aggregate over many AC cycles, where the horizontal axis represents the phase angle of the high-voltage test voltage (0° to 360°) while the vertical axis displays the apparent charge (Q) or PD voltage (V_{PD}); the colour of each point indicates the pulse recurrence density. The PRPD displays different scaling and polarity configurations, or *view modes*: Unipolar Linear or Unipolar Logarithmic, which disregards the polarity of the pulses by plotting absolute values, and Bipolar Linear or Bipolar Logarithmic, which displays positive and negative pulses in separate upper and lower halves of the diagram (they are are valuable for identifying the relationship between pulse polarity and the derivative of the AC test voltage) – see fig. 2.26d.

2.5 Specimens and test cells

The experimental specimens and test cells were specifically designed to investigate the influence of dielectric cooling lubricants on the partial discharge inception voltage (PDIV) of an insulation arrangement representative of the interphase region of a hairpin-winding electric motor. The adopted configuration was therefore conceived to reproduce, in a simplified and controllable manner, the electrical interaction between two adjacent insulated rectangular conductors while allowing the surrounding gaseous environment to be modified through the introduction and heating of different lubricating oils.

The specimens were manufactured from two sections of enamel-insulated rectangular copper conductor, having dimensions of 1×3 mm and provided with a 80 μm polyamide-imide (PAI) coating layer. The two conductors were arranged in a back-to-back (B2B) configuration so as to reproduce the arrangement that may occur between adjacent hairpin conductors belonging to different phases of an electrical-machine winding. A controlled separation between the two conductors was introduced in the central active region of the specimen: one of the two conductors was first locally wrapped with five layers of Kapton tape, which acted as an insulating spacer; after positioning the two conductors against one another, an additional external wrapping was applied around the pair in order to keep the conductors mechanically packed together – the resulting spacer thickness, measured using a thickness gauge, was approximately $150 - 200\,\mu$m. In this way, a small and reproducible-as-practically-possible inter-conductor region was obtained, representing the location in which partial-discharge activity was expected.

Each specimen was manually manufactured without the use of a dedicated forming jig or mould; consequently, small variations in conductor positioning, curvature, mutual alignment and local gap geometry could not be completely eliminated from one specimen to another. Such variability must be considered when interpreting the experimental results, since the local electric-field distribution and therefore the absolute PDIV can be strongly influenced by geometrical differences. Thus, the results presented are primarily evaluated in normalized or per-unit terms, rather than by assigning an absolute significance to the PDIV measured on an individual specimen.



(a) Intermediate assembly stage **(b)** Completed specimen ready for testing

Figure 2.27. Preparation of the twisted-pair specimen mounted on the test-cell lid

The subsequent preparation steps of the B2B specimen are illustrated in fig. 2.27. The conductors were electrically connected to the test-cell terminals through the two internal metallic clamps. These clamps could be tightened by means of screws, ensuring both mechanical retention and electrical continuity between the specimen and the external high-voltage connections. In particular, the test cells consisted of cylindrical stainless-steel containers closed by a metallic lid, as shown in fig. 2.28 – four totally equal test cells were used, thus allowing to perform four different measurements of the same experimental condition in order to perform a sort of statistical campaign of the phenomenon; they were numbered on the top of the lid in order to being able to distinguish them from the outside. Two ceramic feedthroughs were installed in the lid, with an approximate center-to-center separation of 35 mm, allowing the two terminals of the B2B specimen to be brought outside the sealed container while maintaining adequate electrical insulation. On the external side of the lid, the terminals were accessible for connection to the high-voltage measurement circuit, for example through crocodile clips, whereas on the inner side the corresponding screw-operated clamps were used to secure the two ends of the specimen.

For experiments involving the lubricating oils, 50 g of oil were introduced into the bottom of each stainless-steel container, with the quantity determined using a laboratory balance. The

container was then closed with the specimen suspended above the bulk liquid. The assembled test cell was subsequently placed inside the laboratory oven and heated to the required test temperature. A thermocouple was positioned in contact with the bottom region of the container in order to monitor the temperature reached by the oil[19]. As the oil temperature increased, evaporation of its more volatile constituents progressively modified the gaseous atmosphere surrounding the specimen. The resulting environment can therefore be regarded precisely as an air-oil-vapor mixture whose composition depends on the oil formulation, temperature, and thermal exposure conditions.



(a) Top view of the test container **(b)** Side view of the test container

Figure 2.28. Test container used for the partial-discharge measurements, showing the two insulated electrical feedthroughs

2.5.1 Standard specimen configuration

In the first experimental configuration, the B2B specimen was installed inside the test cell without intentionally applying oil directly to its surface. The specimen was therefore initially dry, while the selected lubricant was present only at the bottom of the stainless-steel container. This configuration was adopted to isolate, as far as experimentally possible, the influence of the modification of the gaseous environment produced by oil evaporation. For each investigated temperature, a reference PDIV measurement was first performed under air conditions; the corresponding experiment was then repeated at the same nominal temperature after introducing the selected oil into the test container. During heating, the volatile fraction of the lubricant evaporated and mixed with the air already present in the test cell, thereby changing the physicochemical properties of the low-density medium surrounding the insulation system. The comparison was consequently performed between the PDIV obtained in air and that obtained in the presence of an air–oil-vapor atmosphere at the same temperature. Maintaining the temperature as the comparison parameter was essential, since the PDIV itself is temperature

[19] indeed, the liquid oil represents one of the components with the largest thermal inertia within the test cell; therefore, monitoring its temperature provided a practical indication that the complete system had approached the desired thermal condition before the electrical measurements were performed

dependent even in air. The purpose of this procedure was therefore to distinguish the additional effect associated with the presence of lubricant vapours from the PDIV variation that would result simply from increasing the temperature.

2.5.2 Pre-wetted specimen configuration

A second experimental configuration was introduced to investigate a different initial condition of the insulation system. In this case, before closing the test cell, the completed B2B specimen was deliberately pre-wetted with a syringe with 5 ml of the same lubricant subsequently placed at the bottom of the container. The difference between the two configurations is illustrated in fig. 2.29: in fig. 2.29a the completed specimen is shown before the application of oil while fig. 2.29b shows the same specimen after pre-wetting with the test lubricant. Apart from this initial surface condition, the same general thermal and electrical test procedure was maintained. The test cell contained 50 g of the corresponding oil at its bottom, was closed and placed in the oven, and was heated until the prescribed test temperature was reached.



(a) Completed twisted-pair specimen before oil application

(b) Same twisted-pair specimen after pre-wetting with the test oil

Figure 2.29. Comparison of the same completed twisted-pair specimen under two initial surface conditions

The purpose of this second configuration was to distinguish between two potentially different effects of the lubricant: indeed, in the standard configuration, the specimen initially remained dry and the lubricant primarily affected the insulation environment through the progressive formation of an air–oil-vapour mixture during heating while, instead, in the pre-wetted configuration the lubricant was already present directly on the surface of the enamelled conductors and in the region surrounding the inter-conductor gap before the beginning of the test. The latter condition therefore allowed the influence of direct oil contact with the specimen surface to be assessed in addition to the modification of the surrounding gaseous atmosphere caused by evaporation. Thus, PDIV measurements obtained under the pre-wetted condition could then be compared with those obtained using the initially dry specimen configuration, providing an additional indication of the role played by direct lubricant–insulation interaction in the observed partial discharge behaviour.

Chapter 3

Experimental results

3.1 TGA analysis results of the investigated oils

The thermogravimetric behaviour of the five investigated oils is reported in figs. 3.1 to 3.3.

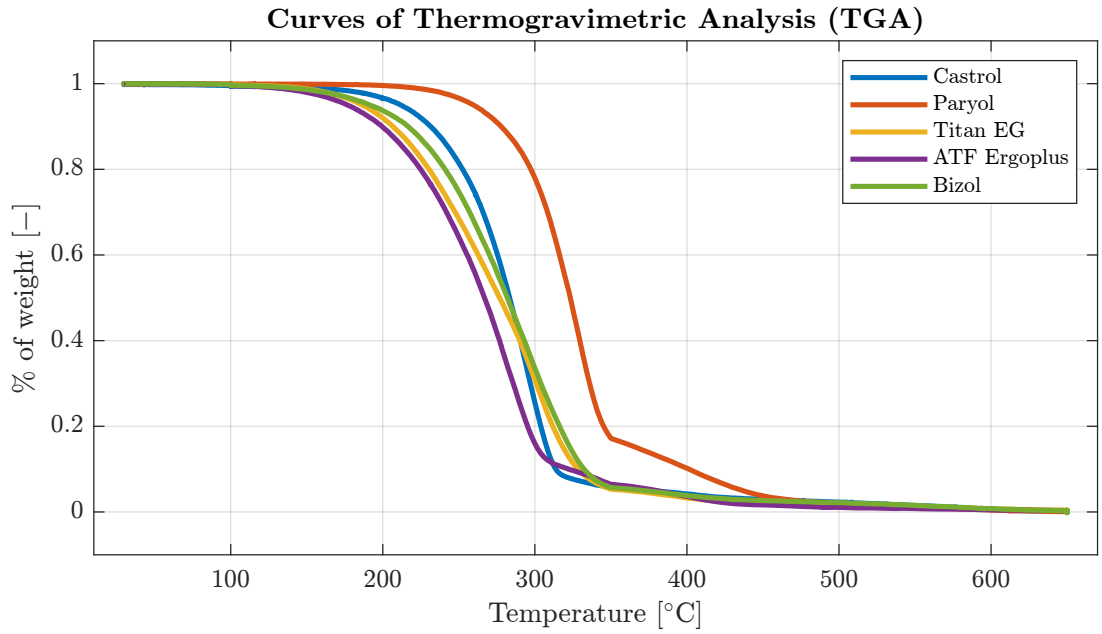
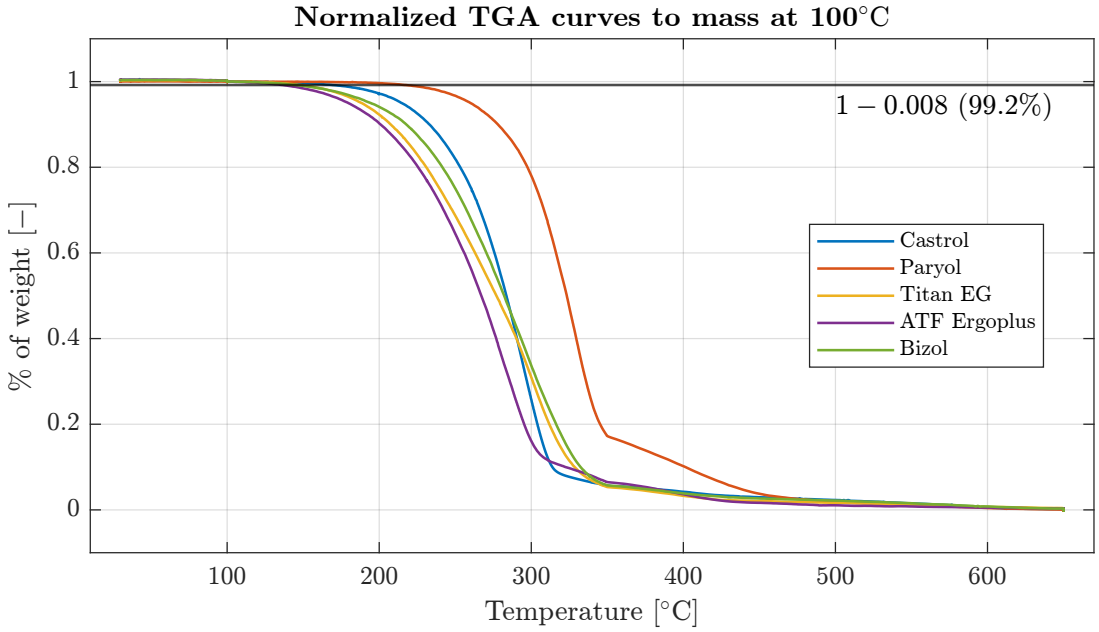


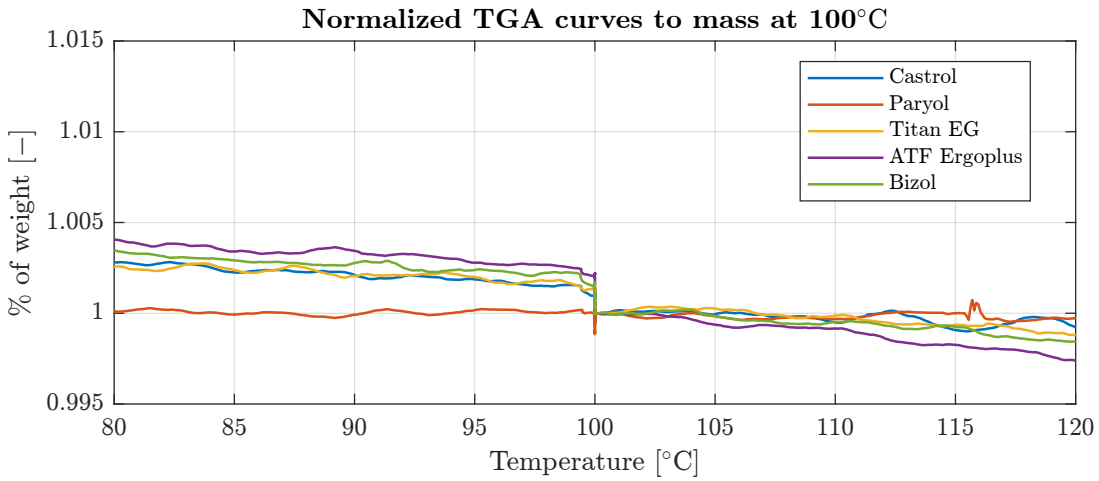
Figure 3.1. Thermogravimetric analysis (TGA) curves of the five investigated oils, expressed as the remaining mass fraction normalized with respect to the initial sample mass at 30 °C

Figure 3.1 shows the TGA curves, expressing the instantaneous sample mass as a fraction of the initial mass measured at 30 °C so to compare in relative terms the mass evolution of oil samples having different initial mass. For all the investigated fluids, the normalized mass remains close to unity throughout the initial temperature range, followed by a pronounced decrease at higher temperatures. Most of the mass loss occurs approximately within the 200−350 °C interval, although the onset, slope and temperature range of the main mass-loss region differ among the investigated oils. In particular, Paryol exhibits the most clearly shifted mass-loss profile towards higher temperatures, with its major decrease occurring at temperatures higher than those observed for the other fluids. Castrol, Titan EG, ATF Ergoplus and Bizol instead show

more closely grouped profiles, although differences in both the onset and progression of their mass loss can still be observed. Above the main mass-loss region, only a small residual mass fraction remains, which progressively approaches zero as the temperature is further increased.



(a) Normalized TGA curves of the investigated oils over the complete temperature range



(b) Detail of the normalized TGA curves around the 100 °C moisture-removal step

Figure 3.2. TGA curves of the investigated oils normalized with respect to the sample mass measured at 100 °C, after the 5-min isothermal step introduced to reduce the contribution of residual moisture; the horizontal line indicates a remaining mass fraction of 0.992, corresponding to a mass loss of 0.8 % relative to the normalization point

Figure 3.2a reports instead the same thermogravimetric measurements after normalization with respect to the mass recorded at 100 °C: during the experimental procedure, the samples were maintained at this temperature for 5 min before continuing the temperature ramp (recall the temperature profile shown in fig. 2.7) – the isothermal step was introduced to reduce the contribution associated with residual moisture before analysing the subsequent thermal behaviour of the oils. Consequently, the mass measured after this conditioning step was taken

as the reference value $m_{100\,^\circ\mathrm{C}}$, and the curves were calculated as $m(T)/m_{100\,^\circ\mathrm{C}}$ – this second normalization possibility facilitates the comparison of the mass loss occurring after the moisture-removal step, namely considering the high temperature behaviour of the oil netted of the possible moisture contribution. Maintaining the samples at 100 °C for 5 min allows most of the residual moisture to be removed before the subsequent temperature ramp, thereby reducing its contribution to the measured mass loss and enabling a more representative evaluation of the oil thermal degradation and volatilization behaviour without accounting for the moisture contribution. The release of this residual moisture is evident from fig. 3.2b (one can for instance observe that ATF Ergoplus is the oil with the largest water content, whereas the Paryol ester apparently is very stable, namely it doesn't lose any water content), but it is also visible in the corresponding DTG curves around 100 °C, where a narrow and pronounced pulse appears as a consequence of the rapid mass variation occurring during the isothermal conditioning step.

Figure 3.3 presents the derivative thermogravimetric (DTG) curves obtained from the corresponding TGA: if a TGA curve describes the amount of mass remaining at each temperature, the DTG curve represents instead the rate at which this mass changes with temperature.

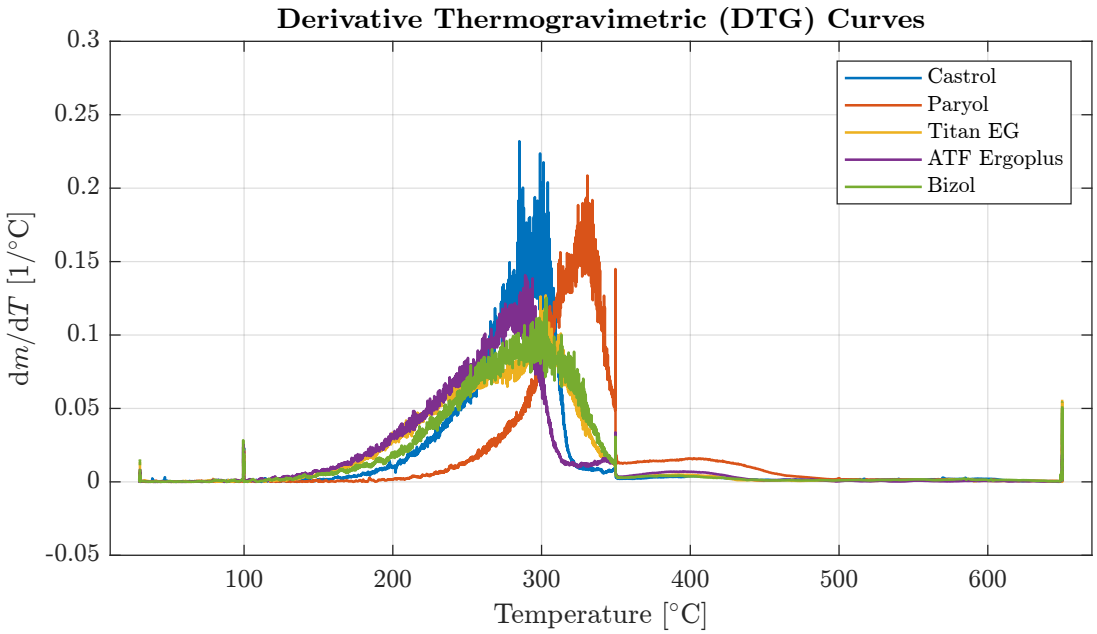


Figure 3.3. Derivative thermogravimetric (DTG) curves of the five investigated oils, showing the rate of mass loss as a function of temperature; the main peaks identify the temperature regions in which the most pronounced mass-loss processes occur – for simplicity, the absolute value is represented

When the mass-loss rate is represented as $-\mathrm{d}m/\mathrm{d}T$, a larger positive DTG value therefore corresponds to a more rapid reduction of sample mass – the maxima of the DTG curves identify the temperature regions in which the most intense mass-loss processes take place, and allow differences that are less immediately visible from the original TGA curves to be highlighted. As visible, all five fluids exhibit a principal DTG region approximately between $250 - 350\,^\circ\mathrm{C}$, consistently with the steep mass reduction observed in the corresponding TGA curves. Castrol, Titan EG, ATF Ergoplus and Bizol show partially overlapping broad mass-loss-rate distributions, with their highest rates concentrated around the upper part of the 200 °C range and approximately 300 °C (yet the ATF Ergoplus is the oil with the poorest performance in this regard, since it

decomposes at lower temperatures); Paryol again exhibits a distinct behaviour, with its principal DTG maximum shifted towards higher temperatures, at $\approx 330\,^{\circ}\mathrm{C}$. After the main peaks, the DTG values decrease substantially, although smaller secondary contributions can be observed at higher temperatures. In possible comparisons, it should also be noted that at $350\,^{\circ}\mathrm{C}$ there is the shift from $\beta = 5\,^{\circ}\mathrm{C/min}$ to $\beta = 10\,^{\circ}\mathrm{C/min}$.

3.2 FTIR spectral characterization of investigated oils

The FTIR spectra obtained for the investigated oils are presented in figs. 3.4 to 3.8 – in particular, fig. 3.4 provides a preliminary comparison among the oils in their unaged condition, whereas figs. 3.5 to 3.8 compare the spectra of each mineral oil before and after thermal ageing[1]. The comparison of the unaged oils in fig. 3.4 highlights a clear distinction between the investigated oil families: the four mineral oils exhibit broadly comparable spectral profiles and substantial overlap over large portions of the investigated wavenumber range whilst the ester-based oil presents a markedly different FTIR spectrum, consistent with its different chemical nature. A feature that can be observed in the Paryol spectrum is the absorption band located around 3400 cm^{-1}: this spectral region is typically associated with the stretching vibration of O–H bonds and can therefore be attributed to the presence of a small amount of absorbed moisture within the oil; the broader character of the band is also consistent with hydrogen-bonded water molecules dispersed in the liquid phase.

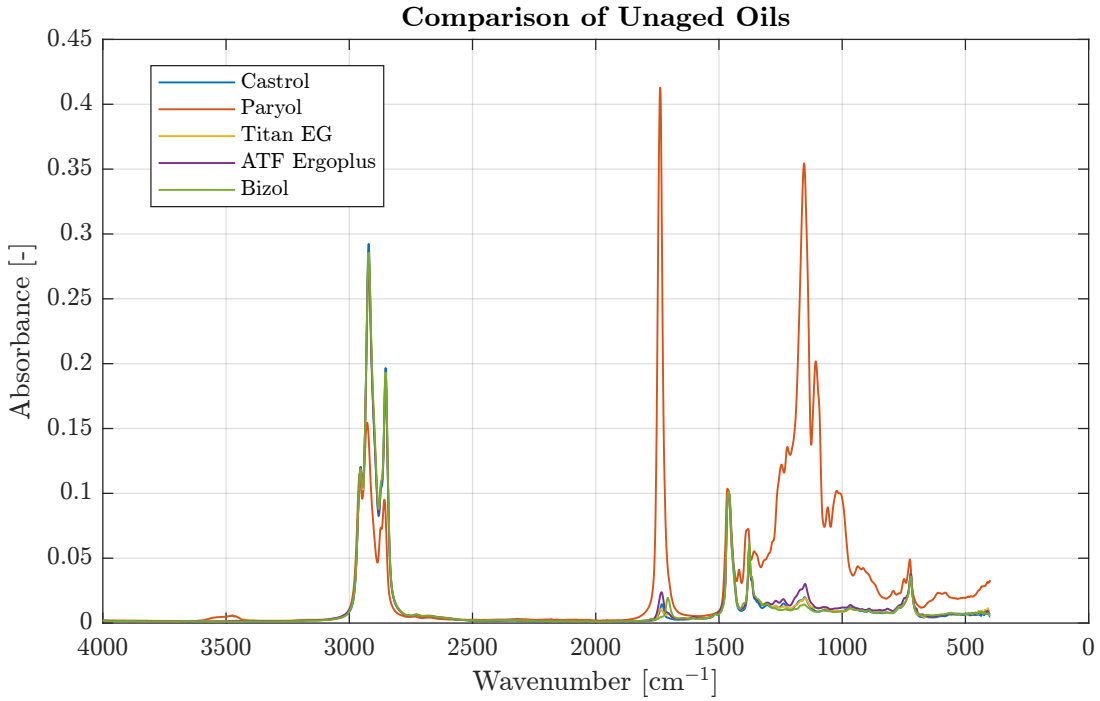


Figure 3.4. FTIR absorbance spectra of the investigated unaged oils, showing the comparison between the four mineral oils and the ester-based oil

As can be observed from figs. 3.5 to 3.8, namely in the absorbance spectra for aged mineral

[1] notice that the aged spectrum of the ester Paryol oil is not reported, since even after thermal exposure at $215\,^{\circ}\mathrm{C}$, corresponding to the temperature at which a mass loss of approximately 0.8 % was observed, only very limited differences were detected with respect to the unaged spectrum.

oils under different temperature conditions, a first comment is that the spectra obtained for the same oil under the three investigated conditions remain largely overlapped, indicating that the relatively short thermal exposure produces only limited modifications that can be identified at this stage from the overall spectral shape. A more detailed assessment of the individual absorption bands and of the differences associated with thermal ageing is provided in chapter 4[2]. The two ageing temperatures, 145 °C and 180 °C, correspond to the lower and upper temperatures considered in the experimental investigation. In figs. 3.5 to 3.8 a colour convention was adopted: the spectrum of the fresh oil is represented in blue, the spectrum after ageing at 145 °C in green, and that after ageing at 180 °C in red – the progressively warmer colours therefore correspond to increasing ageing temperature. For both conditions, the ageing duration was fixed at one hour, consistently with the thermal exposure time adopted during the subsequent PDIV measurements[3].

For the preparation of the aged samples, a small quantity of each oil was placed in the same pans used for TGA and maintained in the oven for one hour at the selected temperature – the oil analysed by FTIR was therefore not directly collected from the bottom of the 50 g oil volume contained in the test cells after the PDIV experiments because, within the comparatively large oil volume used in the test cell, thermal ageing and the release of volatile species may not occur uniformly in the entire liquid bulk, with the oil close to the free surface being expected to experience the most direct interaction with the surrounding gas phase. Conversely, the small amount of oil contained in the pans provides a larger exposed surface-to-volume ratio and a more uniform thermal exposure, thereby increasing the sensitivity of the FTIR comparison to possible temperature-induced modifications.

Something that must be mentioned regarding the four separate FTIR results for the mineral oils shown in figs. 3.5 to 3.8 is that, for each oil, the absorbance spectra were normalized with respect to the peak located at approximately 2921 cm^{-1} – the normalization is done in such a manner because this peak, which corresponds to the C–H asymmetric stretching vibration of methylene (–CH_2–) groups, exhibits exceptional stability and remains typically unaffected by thermal degradation [156][4]; acting as a constant internal spectral reference, this band allows for the reliable calculation of normalized absorbance ratios such as A_x/A_{2921} to quantitatively track other functional groups that dynamically alter as the oil degrades [156]. Furthermore, this normalization allows the relative evolution of the remaining spectral features to be compared while limiting differences associated with the absolute absorbance level of the individual measurements.

[2] although indeed the spectra obtained for each oil under the different ageing conditions appear largely overlapped when considered over the entire wavenumber range, small local variations can still be identified in specific spectral regions; these differences become more evident when the curves are examined in greater detail and are therefore highlighted through the enlarged views presented in the following

[3] no longer ageing treatments were therefore performed, since the purpose of the FTIR analysis was to investigate possible chemical modifications occurring under thermal conditions representative of the actual PDIV testing procedure rather than to reproduce long-term lubricant degradation

[4] to be more rigorous, the band at approximately 2921 cm^{-1} was selected as an internal normalization reference because it represents a dominant feature of the hydrocarbon backbone and is expected to remain comparatively stable under the moderate ageing conditions investigated here; this normalization does not imply that the absolute concentration of methylene groups is strictly invariant during thermal ageing, but it's expected to be quite stable in the considered conditions

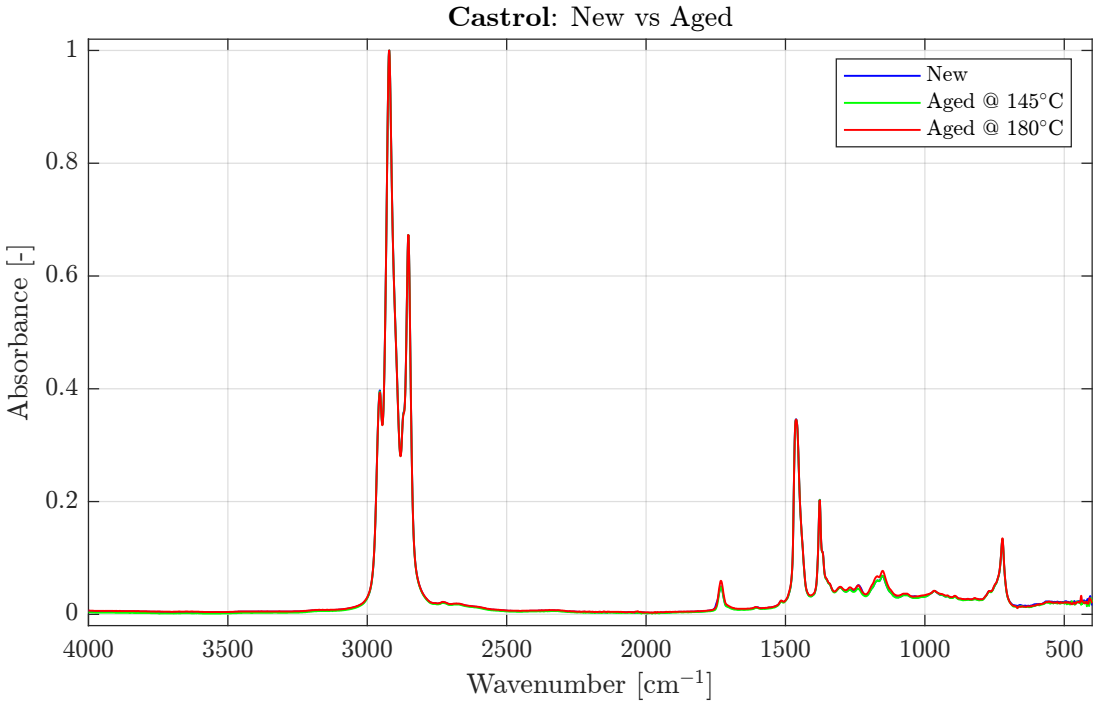


Figure 3.5. FTIR absorbance spectra of Castrol oil in new condition and after 1 h of thermal ageing at 145 °C and 180 °C

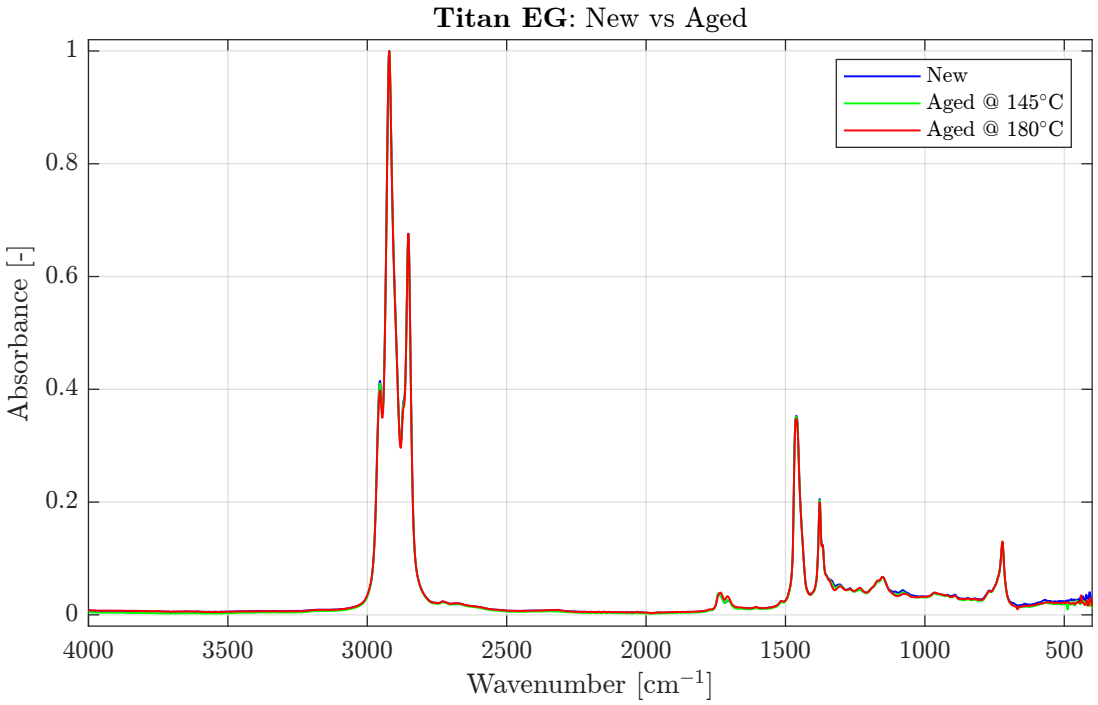


Figure 3.6. FTIR absorbance spectra of Titan EG oil in new condition and after 1 h of thermal ageing at 145 °C and 180 °C

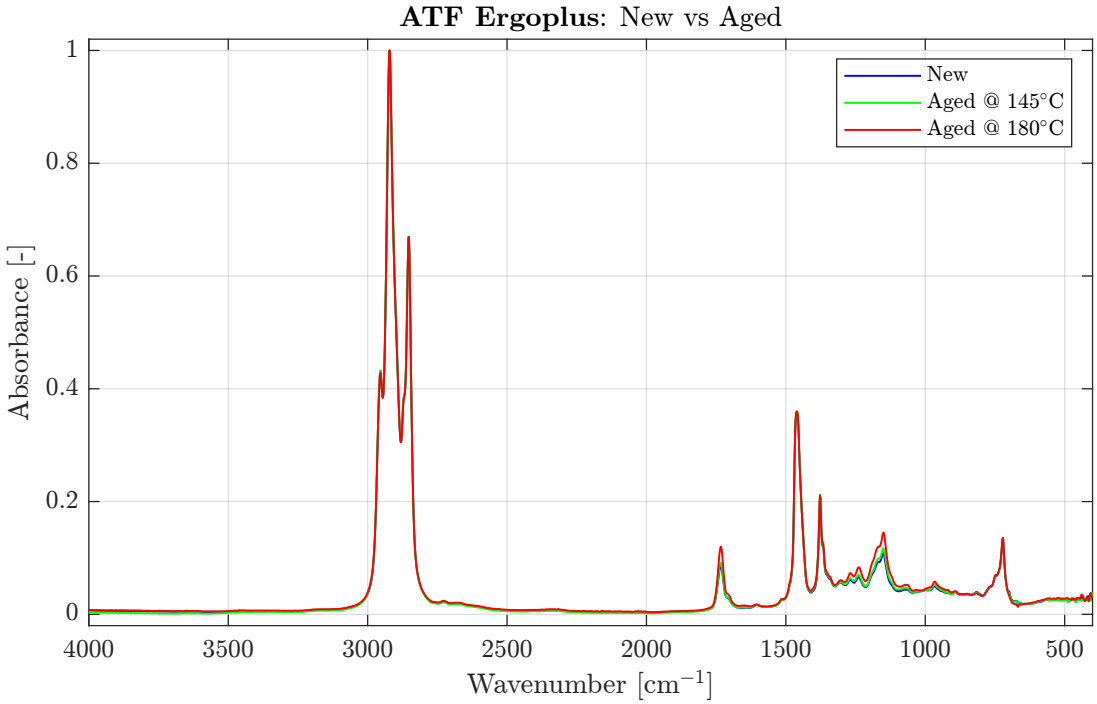


Figure 3.7. FTIR absorbance spectra of ATF Ergoplus oil in new condition and after 1 h of thermal ageing at 145 °C and 180 °C

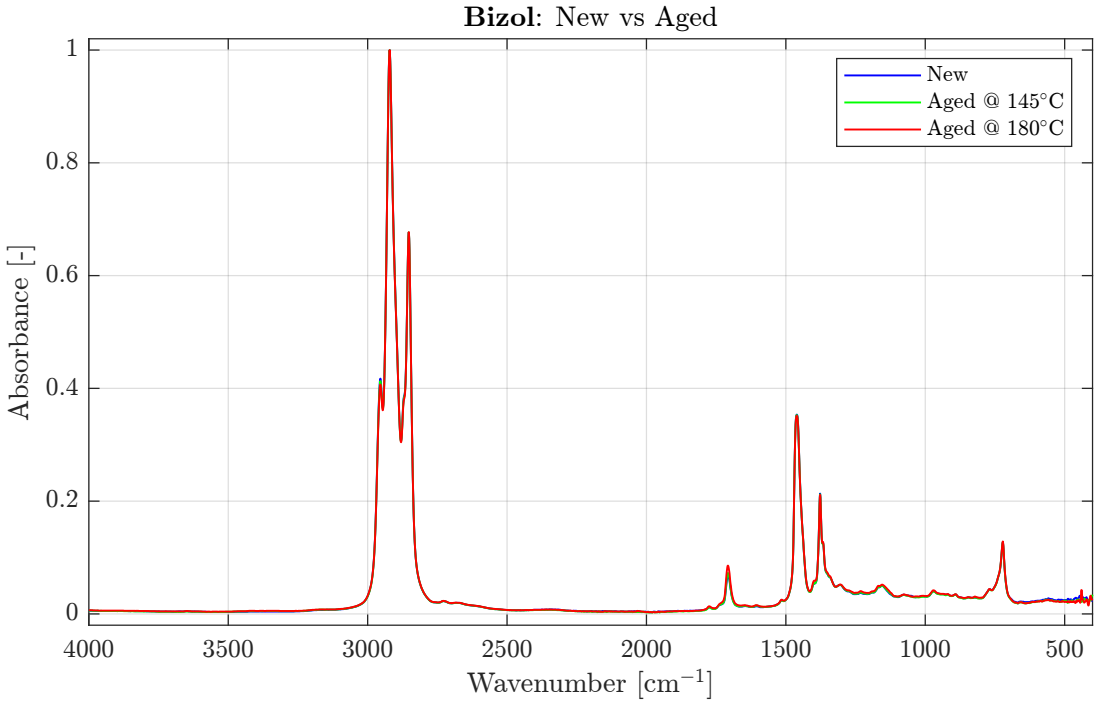


Figure 3.8. FTIR absorbance spectra of Bizol oil in new condition and after 1 h of thermal ageing at 145 °C and 180 °C

3.3 Choice of the test temperatures

The horizontal line visible in fig. 3.2a, corresponding to a normalized mass of 0.992, represents the threshold adopted for the selection of the oil test temperature, corresponding to a mass

loss of 0.8% with respect to the reference mass measured at 100 °C. Notice that this is the selection criterion adopted in this work, and not an universal threshold. For each mineral oil, the temperature at which this threshold was reached was identified and denoted as T_{min}, as reported in table 3.1; also their average is computed in the second-last row. A common upper temperature, denoted as T_{max}, was instead set to 180,° C for all the investigated oils, and it was selected on the basis of the maximum operating temperatures typically reported in the literature for electric traction motor applications. Eventually, for each oil, an intermediate temperature T_{avg} was then calculated as the arithmetic mean between the corresponding T_{min} and the common upper limit T_{max}, precisely as $T_{\text{avg}} = \frac{T_{\text{min}}+T_{\text{max}}}{2}$. On the basis of the average values for each column, three common temperatures were ultimately selected for the subsequent PDIV measurements: 145,° C, 160,° C, and 180,° C – the first two values were obtained by approximately rounding the average values associated with T_{min} and T_{avg}, respectively, while 180 °C was retained as the common upper test temperature. The adoption of the same three temperatures for all mineral oils provides a uniform basis for their comparison under equivalent thermal conditions. The oils reported in table 3.1 are the mineral oils, whereas Paryol, being an ester-based fluid with a markedly different chemical composition and thermal response, was treated separately: it was tested both at the three previously chosen common temperatures and at an additional oil-specific temperature of approximately 215 °C, corresponding to the same 0.8% mass-loss criterion adopted for the mineral oils, with Paryol being considered mainly as an ideal dielectric reference.

Table 3.1. Temperature initial data ranges used for selecting the proper test temperatures for PDIV tests of the investigated mineral oils

Oil	T_{min} [°C]	T_{avg} [°C]	T_{max} [°C]
Castrol	168	174	180
Titan EG	148	164	180
ATF Ergoplus	136	158	180
Bizol	144	162	180
Average	149	164.5	180
Chosen test temperature	145	160	180

3.4 Choice of the oils to be tested

As it will be clear from the results presented in section 3.5, the final PDIV experimental campaign was restricted to three representative lubricants: Castrol, Titan EG, and Paryol; indeed, if during the preliminary characterization phase, a broader set of five oils had initially been considered and investigated by means of TGA and FTIR analyses, following this preliminary screening, it was decided to reduce the number of fluids used for the complete PDIV measurement campaign and to retain the ester oil together with two representative mineral oils. Paryol was therefore selected as the ester-based reference, whereas Titan EG and Castrol were chosen among the mineral oils – this selection was intended to preserve the comparison between the two main lubricant families while keeping the experimental campaign sufficiently focused and manageable

and in order to focus on the actually mattering aspects; furthermore, ATF Ergoplus didn't behave in a performant manner from the thermal point of view and Bizol was resembling quite goodly the Titan EG in terms of their content from the FTIR analysis. Titan EG represents a traditional ICEV lubricant whereas Castrol oil, although not specifically developed exclusively for electric-vehicle applications, provides a mineral-oil reference with practical relevance due to its current use in electrified vehicle applications.

3.5 PDIV results under dielectric lubricant vapours exposure

For each specimen, the PDIV was first measured in air at ambient temperature and at the three selected temperatures of 145 °C, 160 °C and 180 °C; the same thermal conditions were subsequently investigated in the presence of oil by placing 50 g of each one of the different oils at the bottom of the stainless-steel test cell and keeping the jar closed during the measurements. In this first part, the specimens were dry, namely no wetting was performed.

All PDIV measurements were performed using the complete measurement circuit and acquisition system described in section 2.4.1. In particular, the PD signal was acquired using a central frequency of $f_m = 24\,\text{MHz}$ and a measurement bandwidth of $\Delta f = 600\,\text{kHz}$[5]. For each target temperature, two PDIV measurements were performed at times $t = 0$ and $t = 1\,\text{h}$ after the temperature settling: indeed, because of the finite thermal capacity of the test cell, the specimen and particularly the oil, a thermal transient occurred during the heating stage; the temperature measured by the thermocouple was therefore used as the reference for defining the beginning of each test condition. In particular, $t = 0$ identifies the measurement performed immediately after the thermocouple indicated that the prescribed temperature is reached; the temperature was then maintained constant for one additional hour, after which the second measurement as $t = 1\,\text{h}$ was performed under otherwise unchanged experimental conditions. This one-hour period was introduced to provide sufficient time for short-term thermal conditioning of the lubricant and for volatile species released from the heated oil to accumulate in the closed headspace of the jar. The comparison between the measurements at $t = 0$ and $t = 1\,\text{h}$ therefore allows the possible influence of the progressively established oil-vapour atmosphere on the PDIV to be evaluated, including additional reduction in inception voltage associated with the presence of thermally released volatile compounds.

As already mentioned, in addition to the measurements performed on initially dry specimens, a second experimental campaign was carried out after preliminary wetting of the back-to-back specimens with the corresponding lubricant: the oil was intentionally brought into direct contact with the active region of the specimen so that the influence of surface wetting could be investigated together with that of the oil-vapour atmosphere generated during heating; if the first campaign was intended primarily to investigate the effect associated with the progressively established oil-vapour atmosphere, the second campaign additionally accounts for the direct effect of preliminary oil wetting of the insulation surfaces. The same specimen was then subjected to the previously described thermal procedure and PDIV measurements performed at $t = 0$ and $t = 1\,\text{h}$ for each

[5] these parameters were selected experimentally since this combination provided the highest measurement sensitivity for the adopted setup, while the relatively narrow bandwidth allowed the contribution of background noise to be sufficiently limited, thereby improving the signal-to-noise ratio and the reliability of PD detection

selected temperature.

The raw PDIV values obtained during the experimental campaign are reported in tables B.1, B.3 and B.5 for the measurements performed on initially dry specimens and in tables B.2, B.4 and B.6 for the corresponding campaign performed after preliminary wetting of the specimens. The values reported in these tables represent the original experimental dataset from which all the subsequent processing and comparative analyses have been derived. Starting from these raw measurements, the results were subsequently normalized in order to provide an assessment of the effect produced by the different oil-vapour environments on PDIV regardless of the variability of the absolute value of PDIV due to the manufacturing differences of the different samples.

In each table, the four rows identified by the sample number correspond to four distinct specimens that were tested under nominally identical experimental conditions[6]. Reporting the absolute value of the measurements separately for each specimen makes it possible to retain the intrinsic specimen-to-specimen variability of the experimental results before any averaging or normalization procedure is applied. For the wetted-specimen campaign, the additional $T_{\mathrm{amb,wetted}}$ column reports the PDIV measured immediately after preliminary oil wetting and before the beginning of the heating cycle. The remaining values retain the same meaning adopted for the first campaign, with measurements acquired at $t = 0$ and $t = 1\,\mathrm{h}$ at each prescribed temperature. The two sets of raw data can therefore be directly compared while keeping the additional contribution associated with preliminary surface wetting clearly identifiable.

3.5.1 Dry specimens

The resulting comparison for the traditional testing, namely with no prior wetting of the specimens, is shown graphically in fig. 3.9[7]; here the normalized PDIV evolution is reported as a function of temperature for the different investigated oils. The normalization has this meaning: for every oil and temperature, the normalized quantity was first calculated independently for each of the four specimens as the ratio between the PDIV measured after 1 h of thermal exposure in the closed air-oil-vapour atmosphere and the corresponding PDIV measured for the same specimen in air at the same temperature; consequently, these normalized values were obtained at each experimental condition for every specimen and, eventually, the values were then averaged at each different test temperature; the resulting mean value is represented by the corresponding marker in the figure. The error bars were introduced to provide an immediate indication of the dispersion among the four specimens: rather than representing a statistical standard deviation, the upper and lower limits of the error bar correspond respectively to the maximum and minimum normalized values obtained within the four sample population.

One can briefly describe the results shown in fig. 3.9. At 145 °C Titan EG and Paryol

[6] yet, as mentioned, if the "external" conditions to the sample were kept as identical as possible, the sample themselves, being manufactured by hand and renewed for each one of the six series of tests that were performed, presented inevitable differences which are precisely visible from the raw data: the PDIV in air and at ambient temperature can vary quite a lot

[7] notice that the experimental information is represented exclusively by the discrete data points and their associated error bars, whereas the lines connecting them are included only as a visual guide; therefore, the actual PDIV evolution between two consecutive investigated temperatures is not known and may differ from the linear trend suggested by the connecting segments, since precisely no intermediate measurements were performed

exhibit very similar behaviour, with only a limited decrease with respect to the corresponding air measurements, while Castrol already shows a more pronounced reduction; at 160 °C the difference between the oils becomes clearer, with Castrol continuing to decrease more markedly, whereas Titan EG and Paryol remain comparatively close; at 180 °C, the trends diverge further: Castrol shows the largest PDIV reduction, Titan EG exhibits an intermediate behaviour, and Paryol maintains the highest normalized PDIV, therefore showing the most limited detrimental influence among the investigated oils.

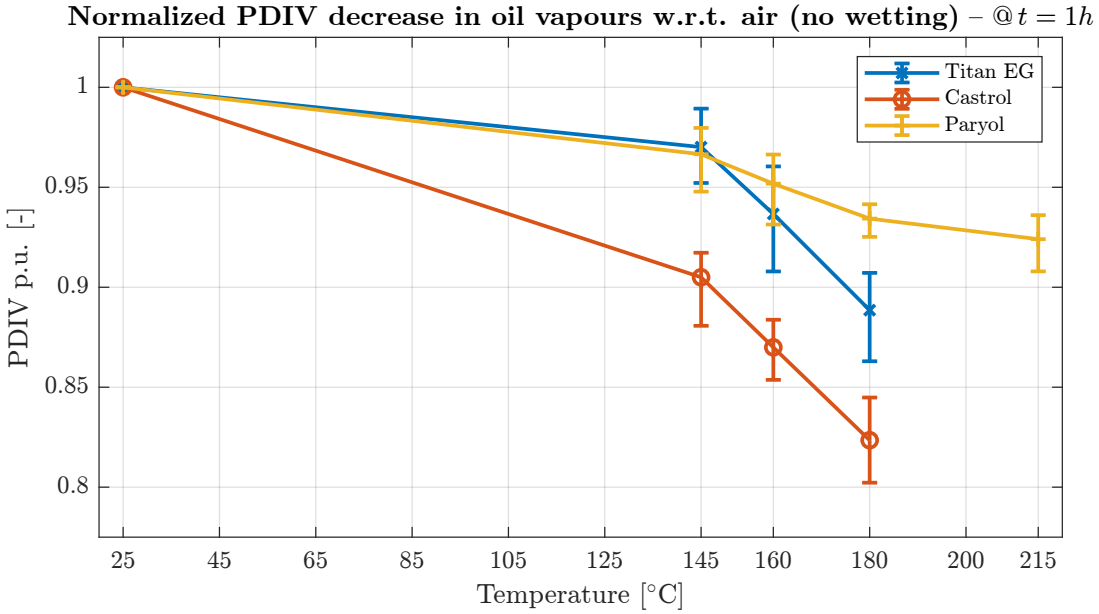


Figure 3.9. Normalized PDIV evolution as a function of temperature for the investigated oils, expressed in per-unit values with respect to the corresponding measurements in air – the comparison highlights the different influence of oil vapours on PDIV and their temperature-dependent effect

The normalized PDIV values measured at $t = 0$, namely immediately after reaching the target temperature, are reported in fig. 3.10 for the three investigated oils[8]. As noticeable precisely from fig. 3.10, at $t = 0$ the three lubricants already exhibit distinguishable effects on the normalized PDIV as the temperature increases: at 145 °C, the values remain relatively close to the air reference for all the investigated oils, with only a limited reduction being observed; at higher temperatures, the differences become more pronounced. Castrol shows the strongest decrease, reaching a normalized PDIV of approximately 0.85 at 180 °C, whereas Titan EG exhibits a more moderate reduction and Paryol maintains the highest normalized PDIV values over the investigated temperature range.

For comparison, fig. 3.11 superimposes these results on the corresponding measurements acquired after 1 h of isothermal exposure, allowing the evolution of the PDIV response with holding time to be directly assessed and compared. This comparison indicates that the relative ranking among the three oils is already substantially established at $t = 0$, although the magnitude of the PDIV reduction changes during the subsequent isothermal exposure. In particular, Castrol remains the lubricant associated with the largest PDIV decrease, while Paryol consistently shows the most limited influence even if at 145 °C Titan appears to perform better.

[8] the data acquired at $t = 0$ have been inserted after the ones at $t = 1$ h since they have been utilized only to try to give an explanation to the results shown in fig. 3.9, which is the actual interesting result of this thesis work

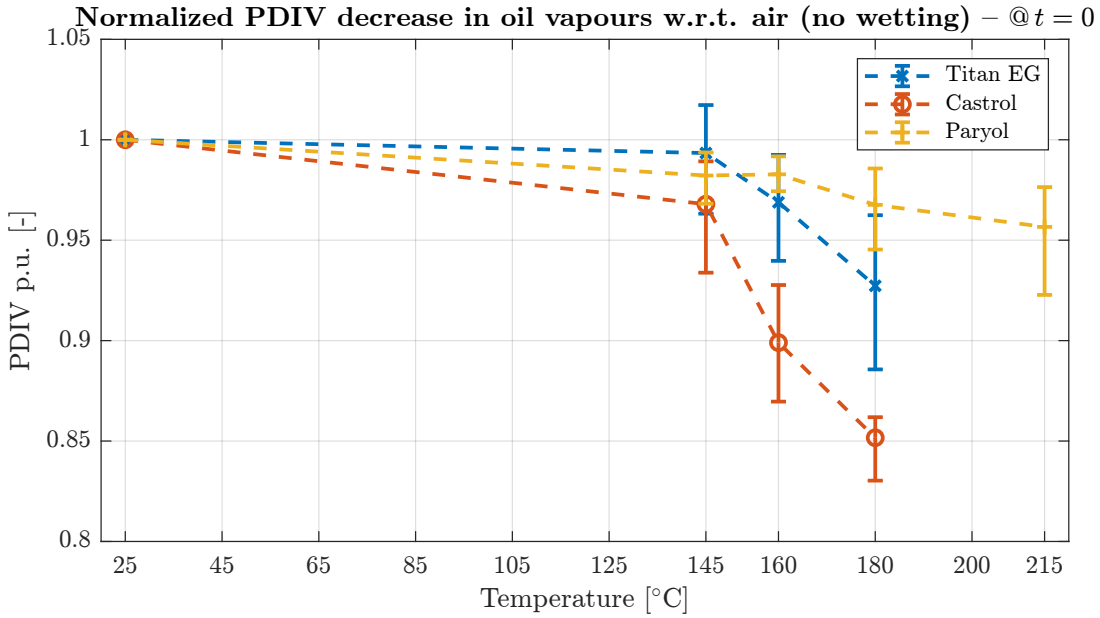


Figure 3.10. Normalized PDIV measured in the presence of oil vapours with respect to the corresponding value in air, for the investigated lubricants and test temperatures, considering the measurements acquired at $t = 0$, namely immediately after reaching the target temperature

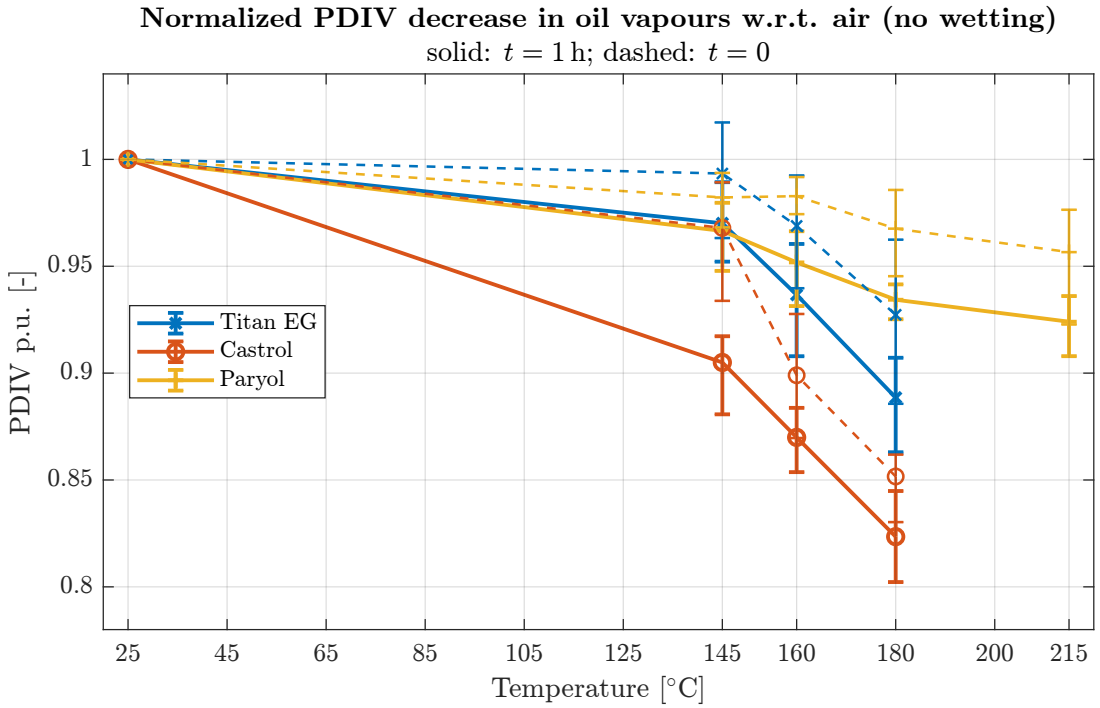


Figure 3.11. Comparison between the normalized PDIV measured at $t = 0$ and after 1 h at the target temperature in the presence of oil vapours, with respect to the corresponding measurements in air – dashed lines indicate the values obtained at $t = 0$, solid lines refer to the measurements acquired after 1 h

3.5.2 Wetted specimens

The same normalization procedure was subsequently applied to the measurements obtained from the preliminarily wetted specimens, and the resulting values are shown in figs. 3.12 and 3.13. Also in this case, the PDIV measured for each individual specimen in air at the same temperature

was used as the reference value. At ambient temperature, however, the numerator corresponds to the additional measurement performed immediately after wetting the specimen, $PDIV_{T_{\text{amb,wetted}}}$, so that the first point of each curve directly quantifies the effect produced by oil wetting before any thermal exposure. At the elevated temperatures, the normalized value was instead calculated using the PDIV measured after 1 h in the closed test cell, consistently with the procedure adopted for the non-wetted campaign. Four normalized values were therefore obtained for each oil and thermal condition, one for each specimen, and their arithmetic mean is represented by the corresponding marker. As for fig. 3.9, also in figs. 3.12 and 3.13 the error bars extend from the minimum to the maximum value obtained among the four specimens.

A particularly large increase in normalized PDIV is observed at ambient temperature immediately after wetting, with mean values considerably higher than the corresponding dry-air reference. Since this pronounced increase makes the subsequent high-temperature evolution difficult to distinguish on the same linear scale, fig. 3.13 provides an enlarged view of the high-temperature region[9]. Once the specimens are heated, the normalized PDIV rapidly falls to values close to unity. This is quite relevant, since this means that, even at higher temperatures, PDIV levels remain higher than the dry case, meaning either a small layer of wet oil remains long term or some surface modification of the insulation was induced.

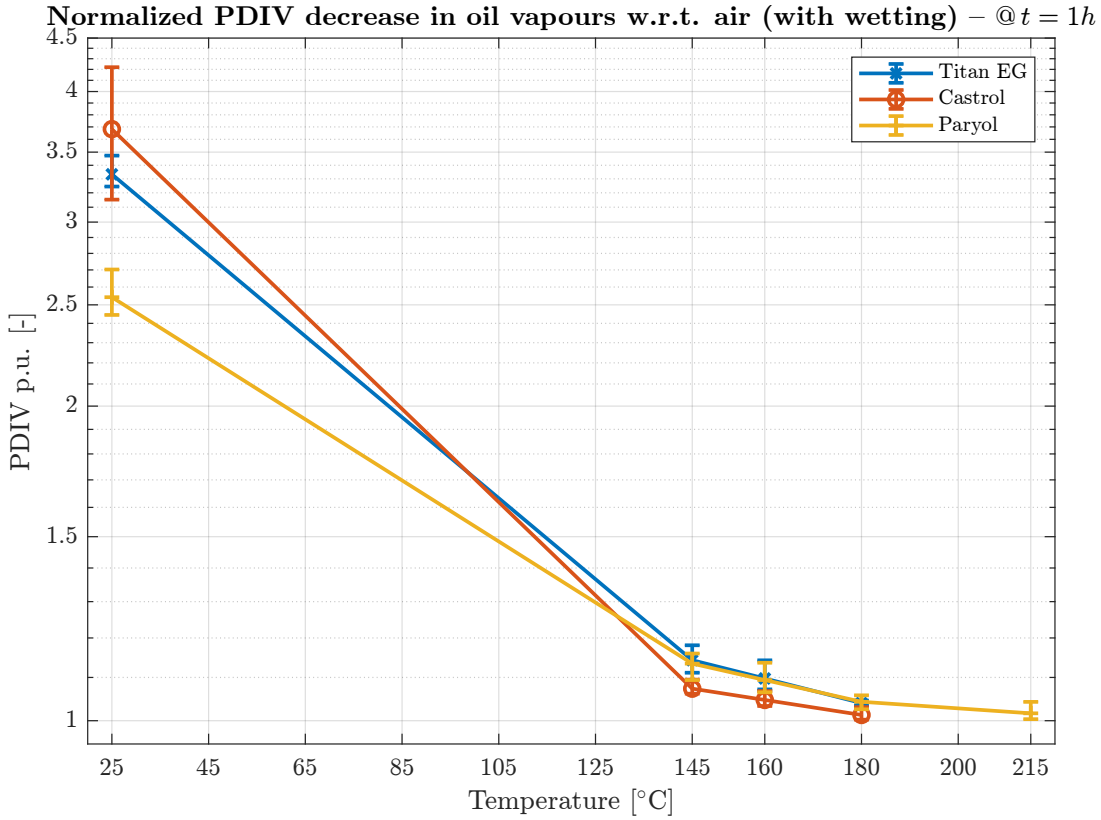


Figure 3.12. Normalized PDIV as a function of temperature for the investigated oils, expressed with respect to the corresponding measurements in air, with preliminary wetting of the back-to-back specimens – logarithmic scale on the y-axis is utilized

[9] the enlarged representation of fig. 3.13 therefore allows the behaviour in the points from 145 °C upwards to be more clearly appreciated without being dominated by the considerably larger values measured immediately after wetting at ambient temperature

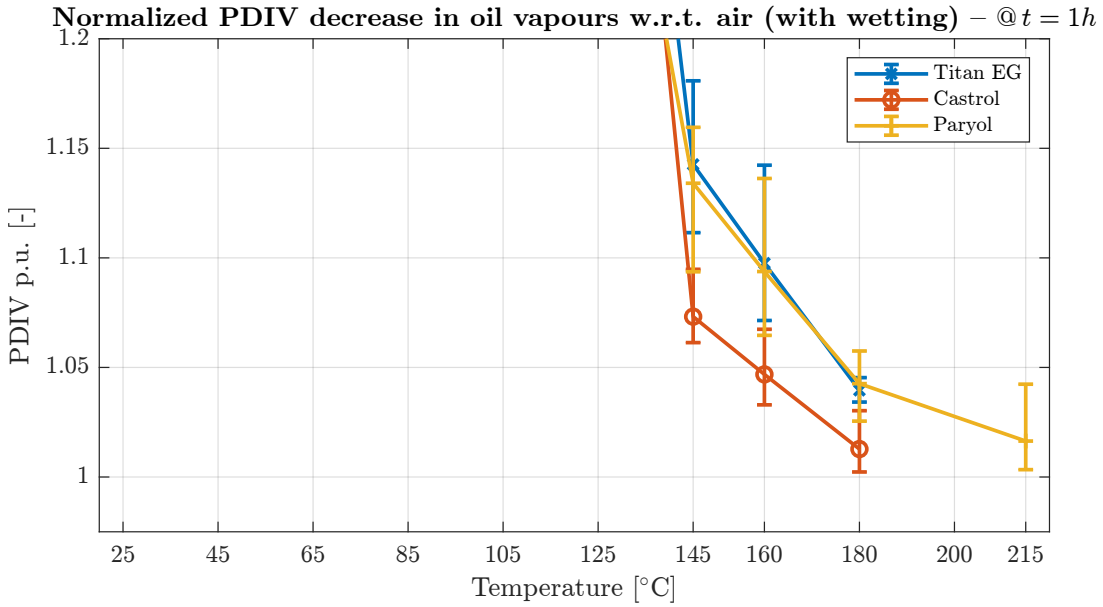


Figure 3.13. Enlarged view of the high-temperature region of fig. 3.12, shown with a linear y-axis to highlight the high-temperature differences among the investigated oils

3.6 PDIV vs. Temperature results, in air

Figure 3.14 compares the measured temperature dependence of the normalized PDIV behaviour in air only for non-wetted samples. The samples considered are the ones utilized also for the measurement with Castrol and Paryol oil-vapour atmosphere and utilized for the first set of measurements[10]. These trends are compared with the theoretical reference behaviour, obtained using the Dunbar and Peek temperature corrections which were introduced in section 1.5.3. The goal of the measurement of this section is to try to estimate the behaviour of the PDIV in pure air versus temperature for the given geometry with basic tools, and assess the goodness of this prediction[11].

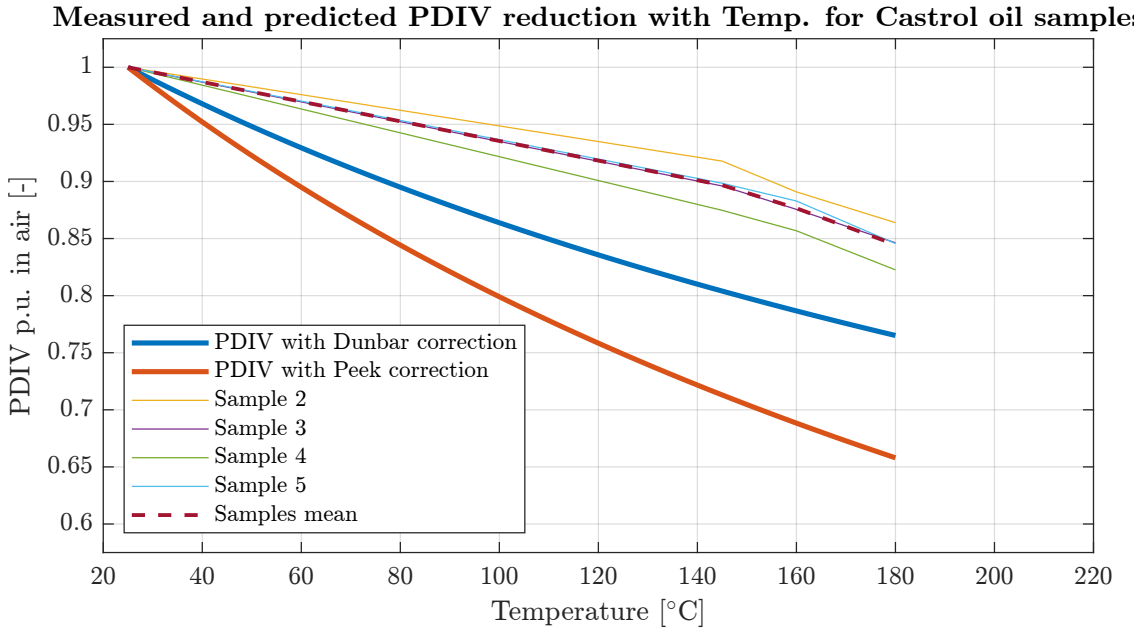
Although a progressive decrease in PDIV with increasing temperature is observed for both sets of samples, the experimental behaviour differs quantitatively from the predictions – in particular, considering fig. 3.14b[12] and the relative values, the measured reduction were:

- 8.25 % at 145 °C (theoretically should be 19.6 % with eq. (1.26))
- 11.04 % at 160 °C (theoretically should be 21.4 % with eq. (1.26))
- 14.86 % at 180 °C (theoretically should be 23.5 % with eq. (1.26))
- 23.18 % at 215 °C (theoretically should be 26.9 % with eq. (1.26))

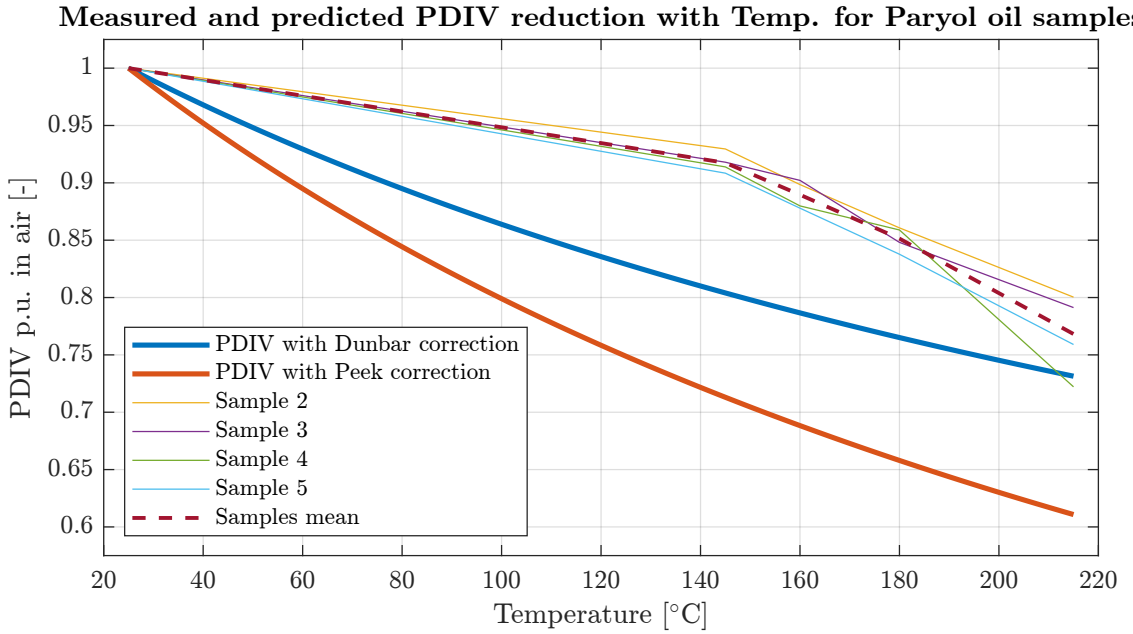
[10] they do not have any particular features; this identification is just precisely to identify which samples have been considered for this explanation

[11] however, as it will be highlighted with the discussion, there are some limitations of these very easy relations that have been implemented; if one wants to make a more accurate estimation of the actual PDIV behaviour, one has to use eq. (1.15) in a numerical way for the given geometry and for the actual gas mixture that is being considered (in this case it is quite simple, since it is pure air)

[12] also for all the other samples that were tested the results were in good agreement, namely the difference was always ~ 1 % or lower with the values here reported



(a) Normalized PDIV as a function of temperature for the four Castrol oil samples



(b) Normalized PDIV as a function of temperature for the four Paryol oil samples

Figure 3.14. Comparison between the measured and predicted temperature dependence of the normalized PDIV for Castrol and Paryol oil samples – figure, for what regards the analytical predictive models, is obtained with the same numerical value presented in section 1.5.3 apart from d which was considered $d = 150\,\mu$m (yet, even considering a different value of d doesn't allow the predicted value to match the mean samples value)

In particular, over the low-to-intermediate temperature range, the measured PDIV reduction is less pronounced than that predicted by either correction. A difference in the shape of the trends can also be observed: while the Dunbar and Peek curves exhibit an upward concavity, corresponding to a progressively decreasing sensitivity to temperature, the experimental results initially show the opposite tendency. This behavior becomes particularly evident for the the

specimens assigned to the Paryol test series, for which measurements were extended to higher temperatures: in this case, the PDIV reduction becomes progressively steeper at elevated temperature; therefore, the experimental results not only show a quantitative mismatch with the reference corrections, but also may suggest that the temperature dependence of the measured PDIV cannot be fully described by the curvature predicted by the Dunbar and Peek models.

Chapter 4

Discussion of results

4.1 Comparison between expected and experimental PDIV vs. temperature reduction

In section 3.6, with fig. 3.14, the experimentally measured temperature dependence of PDIV was compared with the trends predicted by the Dunbar and Peek temperature corrections; significant discrepancies were observed between the experimental results and both reference models. Here one can try to comment first and then give a possible explanation of that. As mentioned, the results confirm the expected decrease of PDIV with increasing temperature; however, the magnitude and shape of the measured reduction are not fully reproduced by either of the considered temperature corrections. In the low-to-intermediate temperature range, both Castrol and Paryol oil samples exhibit a noticeably weaker PDIV reduction than that predicted by the reference curves. A similar discrepancy is reported [84], who shows that the Peek's model predicts reductions of approximately 24 % at 120 °C and 37 % at 200 °C, whereas reductions of only about 10% at 120 °C and 14% at 200 °C were experimentally observed for non-impregnated twisted pairs (notice that this is a different geometry from the one considered in this work) – this indicates that the reduction in gas density alone with Peek's correction, or even considering the Dunbar's correction, cannot generally be translated into an equivalent proportional reduction of the inception voltage in an actual turn-to-turn insulation geometry: in fact, in geometries such as twisted pairs or B2B conductors, partial discharge inception is determined by the conditions established along the critical discharge path in a non-uniform electric field, rather than by the dielectric strength of a uniform gas gap alone.

In detail, the qualitative origin of this behaviour is consistent with what [84, 85] provide: increasing temperature reduces the air density and increases the mean free path of the electrons, thereby facilitating ionization and producing the expected overall decrease in PDIV; rigorously, given the fact that permittivity varies very little (indeed, the employed enamel has a glass transition temperature $T_g \approx 260\,°\mathrm{C}$) as well as the dielectric expands not in a considerable manner, what is more likely to happen is that the critical E-field line changes, since the lower gas density causes the discharge to occur across longer distances in a way to reach the critical number of charge carriers. Still, in a way, the inception condition remains dependent on the

actual field distribution and on the electrical and geometrical properties of the insulation system.

Consequently, the aforementioned Peek and Dunbar corrections, which were derived primarily from gas density considerations, should be regarded as reference trends rather than exact predictive laws for the present specimens, and the experimental results precisely agree with this kind of conclusion. In order to make a much better prediction, one should model with a FEM software the actual geometry and implement the Schumann's criterion, where the gas properties and the E-field distribution for the given geometry are modelled properly.

A further feature of the measurements is the different curvature of the experimental and predicted trends. The Dunbar's and Peek's reference profiles progressively flatten as temperature increases, whereas the experimental mean initially displays a comparatively mild reduction followed by a steeper decrease at the highest temperatures. Therefore, although the experimental PDIV remains above the values predicted by the corrections over most of the investigated range, its local temperature sensitivity increases at high temperature. This suggests that the mechanisms controlling inception cannot be represented by a single temperature-dependent air-density correction over the complete range, as precisely suggested by [84, 85]; rather, the increasing contribution of temperature-dependent modifications of the local inception conditions may become significant at elevated temperature. The available results do not allow these contributions to be separated quantitatively, and therefore the observed change in curvature should be interpreted as evidence of a limitation in the modelling capability of the simplified correction laws. Still, besides temperature dependency related to the air only, local field distribution and temperature-dependent dielectric properties must also be considered; more in detail, one should also consider not only the effect of air but include also the effect of dielectric oils and their behaviour versus temperature in terms of volatiles that are released – this is precisely the goal of the next section.

4.2 Comparative analysis of PDIV reduction for different oils

4.2.1 FTIR spectroscopic indices

The FTIR analysis was not intended to provide a complete chemical characterization of the investigated lubricants, but rather to identify spectral modifications induced by thermal exposure that could contribute to explaining the different effects observed on PDIV. In other words, instead of treating the dielectric degradation as an empirical mystery, FTIR spectroscopy can be used to quantitatively link the chemical degradation of the oil directly to the physical drop in electrical performance (PDIV mainly in this thesis work) – this is true volatiles aside, within limits of wavenumbers observed. For this purpose, the spectra of fresh and thermally aged oils have to be compared through selected spectroscopic indices associated with relevant changes in their chemical composition, namely [182, 183, 184]:

- Carbonyl Index (CI): describes the accumulation of polar traps;
- Aromatic/Aliphatic Index (AI): describes the loss of electron scavengers;
- Aliphatic Chain Index (I_{CH_2/CH_3}): describes changes in the relative abundance of methylene and methyl groups, providing an indication of aliphatic chain shortening during ageing;

- I_{C-O}: aims to track the formation of oxygen-containing degradation products.

The evolution of these indices has then to be compared with the PDIV behaviour observed for each lubricant, with the aim of identifying possible correlations between oil ageing, chemical composition and the influence exerted by the corresponding oil atmosphere on discharge inception.

Here the aforementioned indices are briefly described – one can always consider two typologies of indices: a robust version, which is an Integrated Band Area ratio, or a simpler version, which is a Peak Height ratio.

The **Carbonyl Index** is the primary metric used to monitor the oxidation level of the oil: under the combined action of high temperature and oxygen, the hydrocarbons in the oil decompose and oxidize, releasing a variety of carbonyl-containing by-products such as aldehydes, ketones and carboxylic acids, as already mentioned in section 2.2.3. This index is defined as[1] [2] [182]:

$$CI = \frac{\int_{1800}^{1650} A(\nu)\, d\nu}{\int_{1500}^{1420} A(\nu)\, d\nu} \quad \text{(robust)} \tag{4.1}$$

$$CI = \frac{A_{1710}}{A_{1460}} \text{ or also } CI = \frac{A_{1733}}{A_{1460}} \quad \text{(simplified)} \tag{4.2}$$

and it involves the carbonyl stretching region (C=O) around $1750 - 1680\,\mathrm{cm}^{-1}$ and a typically stable/reference band, namely the stable aliphatic CH_2 bending/scissoring around $1490 - 1430\,\mathrm{cm}^{-1}$. Another very similar index which can be calculated is the so-called oxidation index (OI), which is precisely calculated by integrating the absorbance area in the region between $1650\,\mathrm{cm}^{-1}$ and $1800\,\mathrm{cm}^{-1}$ (the difference with the CI is that the OI is not normalized to a reference/stable band) [185]:

$$OI = \int_{\nu_1}^{\nu_2} A(\nu)\, d\nu \tag{4.3}$$

where ν_1, ν_2 are to be defined as the boundaries of the carbonyl stretching region, and they can precisely be as in the CI definition equal to $1800 - 1650\,\mathrm{cm}^{-1}$. The carbonyl stretching band is considered in both indices since the accumulation of carbonyl products can be a critical driver behind the reduction of PDIV due to polar species generation, charge trapping and electric field distortion.

The **Aromatic/Aliphatic Index** measures the balance between the native aromatic

[1] to be clear, the robust one is calculated from the ratio between the integrated band absorbance of the carbonyl (C=O) peak from $1850\,\mathrm{cm}^{-1}$ to $1650\,\mathrm{cm}^{-1}$ and that of the methylene CH_2 scissoring peak from $1500\,\mathrm{cm}^{-1}$ to $1420\,\mathrm{cm}^{-1}$ as expressed by the following equation; the other two indices HI and AI have similar mining with reference to the respective bands

[2] since it is possible that some oils exhibit two distinct absorption features within the carbonyl region, approximately at 1733 cm^{-1} and 1710 cm^{-1}, the use of a single peak-based CI may not fully describe the spectral evolution induced by thermal ageing; the two bands can be associated with different carbonyl-containing chemical environments and may therefore evolve independently during ageing; thus, two separate peak-based indices $CI_{1733} = A_{1733}/A_{1460}$ and $CI_{1710} = A_{1710}/A_{1460}$ can be considered, using the relatively stable aliphatic CH_2 bending at 1460 cm^{-1} as reference, allowing to track the information about the two different absorption peaks

hydrocarbons and the aliphatic chains in the insulating oil; it is defined as:

$$AI = \frac{\int_{1610}^{1580} A(\nu)\, d\nu}{\int_{2970}^{2850} A(\nu)\, d\nu} \quad \text{(robust)} \tag{4.4}$$

$$AI = \frac{A_{1600}}{A_{2920}} \quad \text{(simplified)} \tag{4.5}$$

and it involves the aromatic ring stretching (C=C) band around 1600 cm^{-1} and the aliphatic stretching (C-H of CH_2 groups) around 2920 cm^{-1}. Aromatics provide an inherent "protective" mechanism in liquid dielectrics under high electric stress thanks to electron scavenging[3]; however, if these aromatic rings oxidize (for instance, forming phenols or aromatic ketones), they can give rise to volatile species which may reduce the PDIV. A kind of similar index can be introduced: the spectral region between 2800 and 3000 cm^{-1} represents the characteristic "fingerprint" of carbon-hydrogen (C-H) bonds in saturated, aliphatic hydrocarbons, which form the main chemical backbone of mineral oils [156]; within this region, the two most critical peaks are [156]:

- 2921 cm^{-1} peak corresponds to the asymmetric stretching vibration of C-H bonds in methylene ($-CH_2-$) groups;
- 2952 cm^{-1} peak corresponds to the asymmetric stretching vibration of C-H bonds in methyl ($-CH_3$) groups.

The ratio of their absorbance, namely[4]:

$$I_{CH_2/CH_3} = \frac{A_{2921}}{A_{2952}} \tag{4.6}$$

represents the **methylene-to-methyl ratio** CH_2/CH_3 **index** [156]. This indicates the average chain length: in long, unbroken aliphatic chains, there are thousands of internal $-CH_2-$ groups for every two terminal $-CH_3$ caps, resulting in a high A_{2921}/A_{2952} ratio [156]; if those same chains fragment into shorter pieces, the total number of internal $-CH_2-$ groups decreases relative to the newly formed terminal $-CH_3$ ends (indeed, as there is the chain scission, new $-CH_3$ ends are introduced, thus increasing the absorbance A_{2952}); this increases the 2952 cm^{-1} absorbance, causing the A_{2921}/A_{2952} ratio to decrease[5] [156]. Basically, longer chains means more methylene

[3] aromatic compounds have conjugated π-electron systems capable of absorbing the kinetic energy of accelerated free electrons, acting precisely as electron scavengers; this mechanism suppresses collisional ionization and partially inhibits streamer propagation

[4] the reason why 2921 cm^{-1} is in the numerator in the first case, but would act as a denominator in other normalization formulas, comes down to the difference between a structural chemical index and a mathematical normalization reference: in lubricant and polymer chemistry, the ratio A_{2921}/A_{2952} is traditionally defined as the methylene-to-methyl ratio, so that the value is directly proportional to the average chain length; if one flipped the ratio to A_{2952}/A_{2921}, namely by making the ratio to a quantity that is expected to be stable as for all the other indices, it would still be a valid number but it would represent instead the degree of branching/fragmentation of chain length

[5] one can here try also to give an explanation of why 2921 cm^{-1} was considered as an internal spectral reference for the normalization of the FTIR spectra: methylene groups ($-CH_2-$) make up the bulk "body" of the hydrocarbon chains in insulating or lubricating oils; under moderate thermal degradation or early-stage oxidation, while the highly reactive terminal sites, double bonds, or additive compounds might undergo chemical changes, the vast majority of the backbone methylene links remain intact; therefore, its absolute concentration in the bulk fluid changes negligibly, making it a stable spectroscopic anchor [156]

(larger numerator) relative to the ends hence higher ratio, while shorter/fragmented chains means fewer methylene segments relative to the newly created methyl ends (larger denominator) hence lower ratio. However, when an oil is thermally being aged, it is typically allowing some components of the oil to evaporate (usually the lighter molecules generally have lower boiling points and higher volatility). for instance, if some relatively methyl-rich species are preferentially lost from the liquid during heating since they are lighter, the residual oil may show a reduced relative contribution at 2952 cm^{-1} in terms of absorbance, thus causing an increase of the considered ratio. Thermal ageing can release lighter hydrocarbons and volatile degradation products, such as aldehydes, ketones, alcohols and organic acids, into the gas phase: their presence modifies the composition of the gaseous dielectric surrounding the insulation; this can alter electron–molecule collision and ionization processes and may cause the effective Townsend ionization coefficient to increase thus possibly resulting in a reduction of the PDIV.

The previous indices are the ones mostly reported in literature. However one can think to define an additional empirical spectral index here denoted as $\mathrm{C}-\mathrm{O}$ index, defined as:

$$I_{\mathrm{C-O}} = \frac{\int_{\nu_1}^{\nu_2} A(\nu)\, d\nu}{\int_{1490}^{1430} A(\nu)\, d\nu} \quad \text{(robust)} \tag{4.7}$$

$$I_{\mathrm{C-O}} = \frac{A_{1160}}{A_{1460}} \quad \text{(simplified)} \tag{4.8}$$

where ν_1 and ν_2 are to be defined around the central peak of $\approx 1160\,\mathrm{cm}^{-1}$ (it can be for instance chosen an interval of $1200 - 1100\,\mathrm{cm}^{-1}$). The goal is always the same: try to monitor how the $\nu_1 - \nu_2$ range varies given a reference/stable band – indeed, for mineral oils, which are predominantly composed of hydrocarbons, an increase in absorbance from the fresh to the aged condition in the $1000 - 1300$ cm^{-1} region may be associated with the formation of oxygen-containing degradation products during thermo-oxidative ageing; the oxidation of hydrocarbon chains can lead to the formation of hydroperoxides and, subsequently, alcohols, ethers, carbonyl compounds, and carboxylic acid: some of these species introduce C–O bonds, whose stretching vibrations contribute significantly to this fingerprint region. Such changes may also be relevant to the observed PDIV behaviour: oxygen-containing degradation products are generally more polar than the original hydrocarbon molecules and some low-molecular-weight products may volatilize at the investigated temperatures: their presence in the gaseous atmosphere can influence electron–molecule collision and ionization processes, thus also the PDIV.

It should nevertheless be emphasized that FTIR spectroscopy characterizes the chemical composition of the liquid phase and does not directly identify the volatile species released into the gaseous phase. Therefore, the FTIR results are used here as supporting evidence for interpreting the different PDIV trends rather than as direct proof of the chemical mechanisms governing discharge inception in the air–oil vapour mixture.

4.2.2 FTIR-based interpretation of PDIV behaviour – no wetting

Some of the spectroscopic indices introduced above are here applied to the fresh and thermally aged oil samples, not merely to quantify their chemical evolution, but primarily to investigate

whether the observed spectral modifications can provide a possible interpretation of the different PDIV trends exhibited by the investigated lubricants. Accordingly, the variations in the selected indices are going to be compared with the corresponding electrical results about the PDIV in order to identify exactly possible correlations between thermal-induced changes in oil composition and the effect of the resulting oil atmosphere on PDIV. The following comparison focuses initially on the PDIV measured in air and in the presence of oil vapours, namely on the results shown in fig. 3.9, without any preliminary wetting of the specimens, in order to isolate the effect of the gaseous environment generated by each lubricant.

The considerations that can be made about the results shown in fig. 3.9 are reported hereafter. At 145 °C, Titan EG and Paryol exhibit a very similar behaviour, with only a slight advantage for Titan EG in terms of the mean normalized PDIV value; however, as the temperature increases, the two oils progressively diverge. Titan EG shows a more pronounced deterioration in respect to Paryol, with the normalized PDIV decreasing significantly at 160 °C and especially at 180 °C, whereas Paryol maintains comparatively higher values and therefore exhibits a markedly less severe reduction. Castrol, on the other hand, shows the strongest detrimental effect over the entire investigated temperature range: its normalized PDIV is already substantially lower at 145 °C and continues to decrease with increasing temperature, reaching approximately 0.82 p.u. at 180 °C – this corresponds to a reduction of about 18% in PDIV in the presence of oil vapours with respect to the corresponding measurement in air at the same temperature, which is quite a remarkable negative effect of the oil presence. Overall, the results highlight a clear dependence of the vapour-induced PDIV reduction on both the lubricant type and the operating temperature, with Paryol showing the most stable behaviour at the highest temperatures and Castrol the most detrimental one given its largest PDIV reduction over the entire temperature range considered.

An additional observation is that the thermal stability of the lubricant does not necessarily correlate with its effect on PDIV. Although Castrol exhibits comparatively good thermal stability in TGA terms and relatively limited mass loss, its vapours produce the most pronounced reduction in PDIV among the investigated oils. To highlight quantitatively this consideration, one can consider the mass loss at the various test temperatures for the three investigated oils, reported in table 4.1: one can precisely see that, for the same applied temperature, the mass loss of Castrol oil is significantly lower compared to the one of Titan EG; furthermore, it can be seen also that the mass loss of Paryol is very small, which can be a partial explanation of the very good behaviour of the PDIV when it is involves as it's shown in fig. 3.9.

Table 4.1. Percentage mass loss of the investigated dielectric cooling oils at the temperatures selected for the PD tests; the values are referred to the mass measured at 100 °C, used as the reference mass for the normalization of the thermogravimetric curves of fig. 3.2a

Oil	**145 °C**	**160 °C**	**180 °C**
Paryol	≈ 0	0.0616 %	0.1805 %
Castrol	0.3186 %	0.5296 %	1.2254 %
Titan EG	1.2232 %	2.4135 %	5.0781 %

The behaviour in terms of mass loss of Castrol and Titan EG suggests that, despite the

relatively small amount of volatile species released, the chemical nature of the volatiles released by Castrol oil may be particularly detrimental from an electrical insulation perspective; in particular, the vapour composition may contain species with ionization characteristics that facilitate electron-avalanche development, thereby promoting partial discharge inception. Therefore, the amount of material volatilized alone cannot be regarded as a direct indicator of its influence on PDIV, since the chemical nature and ionization properties of the released species may play an equally, or even more, important role.

The contrasting behaviour observed for Castrol and Titan EG suggests precisely that the key aspect is not only the amount of material released upon heating, but also the chemical nature of the species generated. Therefore, a more detailed interpretation requires returning to the FTIR analysis and comparing how the characteristic absorption bands evolve with thermal ageing for the two oils. In particular, it is relevant to determine whether Titan EG exhibits changes in different spectral regions compared with Castrol, and/or whether the magnitude of these changes is lower despite its higher mass loss.

Another aspect that may help interpret the apparent discrepancy between the TGA and PDIV results is the time at which the electrical measurements are considered. Figure 3.9 is based on the PDIV values measured after one hour at the target temperature; it is therefore useful to perform the same comparison using the values measured at $t = 0$, namely immediately after the specimen reaches the prescribed temperature (see fig. 3.10). In fact, if the relative behaviour of Castrol and Titan EG were reversed at $t = 0$, this would indicate that the one-hour isothermal exposure plays a significant role in determining their final PDIV response. In that case, the larger mass loss of Titan EG observed by TGA could be interpreted as being associated with species that are comparatively less detrimental to the gaseous insulation, whereas Castrol, despite its lower overall volatilization, could progressively release or generate more electrically harmful species during the isothermal holding period. In this regard, one has to recall that the volatilization takes time, this in the one hour isothermal step some substances get released by the oil. Conversely, if the relative trend between Castrol and Titan EG remains unchanged also at t=0, then the explanation cannot primarily be attributed to the one-hour thermal exposure: in that case, the key issue would again be the chemical nature of the species released by the two oils, since Castrol would exhibit a poorer PDIV behaviour despite appearing thermally more stable than Titan EG from the TGA analysis, namely as shown in table 4.1 gives rise to a much lower mass reduction for the same temperature profile in the TGA. However, as visible from fig. 3.11, this comparison confirms that the relative behaviour of Castrol and Titan EG does not reverse when the measurements at t=0 are considered: indeed, as shown by figs. 3.9 and 3.10, Titan EG still exhibits a higher normalized PDIV than Castrol already at the beginning of the isothermal exposure. Therefore, the poorer PDIV performance of Castrol cannot be primarily attributed to a stronger degradation occurring during the subsequent one-hour holding period. This reinforces the need to identify a different explanation for the apparent discrepancy with the TGA results, since Castrol appears thermally more stable than Titan EG in terms of mass loss, while nevertheless producing a more detrimental effect on PDIV.

Thus, the usage of the following selected index is the adopted strategy, in order to eventually try to find a correlation with the PDIV behaviour. Their choice can be made starting from a

comparison between the FTIR spectra of the fresh and thermally aged oils, which reveals three most relevant temperature-dependent spectral regions where modifications are concentrated these regions are therefore selected as the main candidates for the subsequent quantitative analysis and thus they guide the choice of the indices. One can precisely consider figs. 3.5 and 3.6 and derive the following observations:

- A first variation occurs in the $3000 - 2800\,\mathrm{cm}^{-1}$ region: for both oils, the absorbance in this region decreases with increasing ageing temperature, particularly around $2955 - 2945\ \mathrm{cm}^{-1}$ and, to a lesser extent, around $2880 - 2870\ \mathrm{cm}^{-1}$; the change is especially noticeable when the ageing temperature is increased from 145 °C to 180°C; since this spectral region is directly related to the hydrocarbon backbone of the mineral oils, its evolution may indicate changes in the relative abundance or chemical environment of aliphatic groups caused by thermal treatment (in particular, this region is important because it may indicate modifications of the hydrocarbon chains, such as possible cracking, chain shortening, branching, or the selective loss of lighter fractions – from a PDIV perspective, this band can become particularly relevant if its variation is consistent with the TGA and PDIV results: lighter or more unsaturated species are generally more prone to volatilization and may therefore alter the composition of the gas phase): thus it's possible to use both the $I_{\mathrm{CH_2/CH_3}}$ and AI indices to evaluate possible influences of these volatile by-products.
- A second region of interest is located around $1733 - 1710\,\mathrm{cm}^{-1}$, where absorption is typically associated with carbonyl-containing species due to oil oxidation mainly (this is one of the most significant regions for interpreting oxidative ageing – it can be associated with aldehydes, ketones, carboxylic acids, and oxidized esters and, from an electrical perspective, these species may affect the PDIV not only because of their relatively low ionization potentials, but also because they can alter electron–molecule collision processes, collision cross-sections, ionization probability amd electron attachment); in Castrol, a clear increase in the peak around $1733\,\mathrm{cm}^{-1}$ becomes visible at the highest ageing temperature, whereas Titan EG exhibits a weaker modification, characterized by two nearby contributions around $1733\,\mathrm{cm}^{-1}$ and $1709\,\mathrm{cm}^{-1}$; the appearance or growth of absorption in this region is compatible with the formation or accumulation of oxygen-containing degradation products during thermal ageing, thus their chemical significance makes this band particularly useful for monitoring oxidation-related transformations: for this reason, the classic CI is employed to evaluate possible influences of the aforementioned volatile by-products.
- Finally, Castrol shows a further relevant modification in the $1170 - 1150\,\mathrm{cm}^{-1}$ region, where the corresponding absorption peaks become progressively more pronounced, especially after ageing at 180 °C; conversely, the Titan EG spectra remain comparatively flat and exhibit only limited temperature-dependent changes within the same wavenumber range (this different behaviour represents one of the clearest qualitative distinctions between the two oils); in this interval the self-defined I_{C-O} index can be employed (for mineral oils, an increase from the fresh to the aged condition may support the formation of oxygen-containing functional groups such as alcohols, ethers and esters – these species may influence PDIV mainly through polarity and electron–molecule collision kinetics: alcohols, ethers, and esters contain oxygen and are generally more polar than saturated hydrocarbons, which

can modify the electron energy distribution function and therefore the coefficients α, η and this may allow discharge inception at a lower electric field, thus possibly reducing PDIV).

A summary of what has just been mentioned is reported in table 4.2.

To investigate the possible chemical factors associated with the observed PDIV variations, four FTIR-based indices were selected: the I_{CH_2/CH_3} ratio, the Aromatic Index (AI), the Carbonyl Index (CI), and the I_{C-O} index – see respectively eq. (4.6), eq. (4.4), eq. (4.1) and eq. (4.7). The numerical values of AI, CI, and I_{C-O} were obtained by numerical integration of the corresponding spectral regions highlighted in fig. 4.1, whereas I_{CH_2/CH_3} was directly calculated as the ratio between the absorbance values of the selected CH_2 and CH_3 absorbance peaks, without any area integration. The resulting index values and their signed relative variations with respect to the 25 °C reference condition are summarized in Table 4.3.

The key result, that was already discussed, is that Titan exhibits a much greater mass loss than Castrol, while causing a smaller deterioration in PDIV; therefore, the total amount of volatilized material cannot, by itself, be considered the dominant parameter. Instead, the FTIR results suggest that the chemical nature of the species generated or released during ageing may be more important than the overall quantity of vapours produced. Considering precisely the values reported in table 4.3, one can mention that:

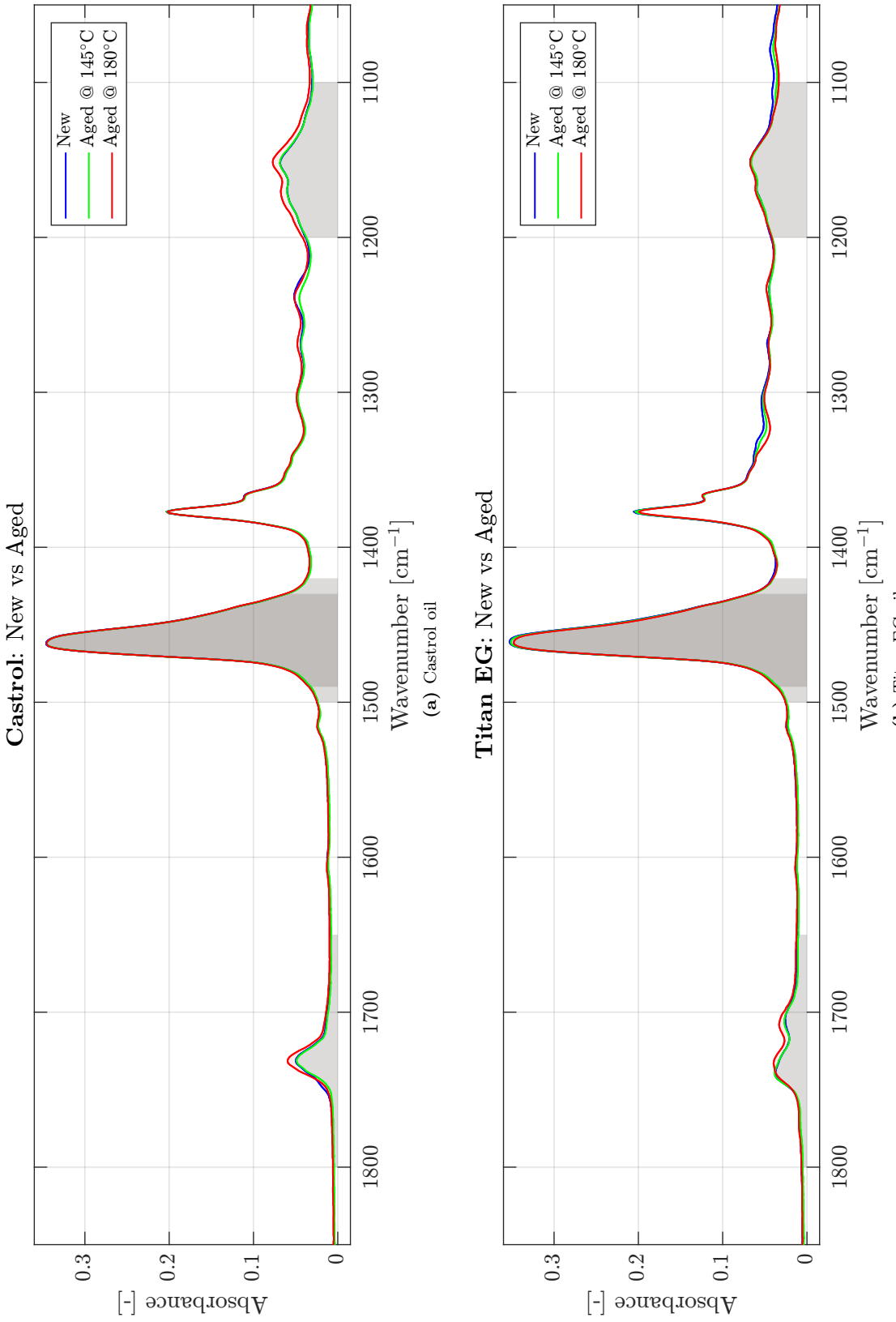
- I_{CH_2/CH_3} does not explain PDIV ranking: indeed this index changes in the opposite direction to what would be expected if hydrocarbon-chain fragmentation were the dominant mechanism; in fact, Titan exhibits a much larger variation of 4.36 % @180 °C compared with only 0.98 % @180 °C variation for Castrol oil, and yet Castrol causes a significantly larger reduction in PDIV $\Longrightarrow$ this suggests that simply modifying the aliphatic structure is not sufficient to explain the different electrical performance, namely although the aliphatic structure of Titan appears to undergo a larger relative modification this modification does not appear to be the dominant factor controlling PDIV.
- AI does not seem to be the discriminating parameter either: indeed, at 145 °C the relative variations of the AI index are almost identical while the corresponding PDIV reductions are very different, and at 180 °C Titan even shows a somewhat larger positive AI relative variation than Castrol but still performs better electrically.
- CI highlights that oxidation occurs, but does not uniquely explain PDIV ranking, and the same considerations done for I_{CH_2/CH_3} hold for CI as well, at least partially; indeed, at 180 °C it is $\Delta\text{CI}_{\text{Titan}} = 12.69\% > \Delta\text{CI}_{\text{Castrol}} = 10.60\%$ but it is also $\Delta\text{PDIV}_{\text{Castrol}} = 17.65\% > \Delta\text{PDIV}_{\text{Titan}} = 11.14\%$; therefore, not even "more carbonyls in the liquid implies greater PDIV deterioration" seems to be the dominant relationship; this is however a quite interesting result because CI confirms that both oils evolve chemically/oxidatively, but it does not discriminate well which atmosphere is electrically more detrimental (at least for the test conditions that have been considered in this thesis work).
- I_{C-O} can be regarded as the strongest discriminator between oils given that, among the four indices, it is the only one that clearly separates the two oils in a direction consistent with the electrical ranking, and it is the most interesting result since Castrol and Titan

Table 4.2. Qualitative interpretation of the selected FTIR indicators, with corresponding chemical changes, possible volatile species, and potential relevance to PDIV

FTIR indicator	**What it suggests**	**Possible volatile species associated with the same degradation pathway**	**Potential PDIV relevance**
$CI_{1710/1733}$	Oxidative carbonyl formation	Aldehydes, ketones, small organic acids, possibly esters	High
I_{CH_2/CH_3}	Modification/fragmentation of hydrocarbon chains	Lighter alkanes, alkenes, and secondary oxidation products	Medium – High
I_{C-O}	Evolution of oxygenated functionalities	Alcohols, ethers, and esters	Medium / supporting

Table 4.3. Absolute values and relative variations of the FTIR indices evaluated for Castrol and Titan oils at different aging temperatures, together with the corresponding variation in PDIV. Relative/percentage variations of indices are calculated with respect to the value measured at 25 °C.

Oil	T **[°C]**	I_{CH_2/CH_3}		**AI**		**CI**		$\mathbf{I_{C-O}}$		**ΔPDIV [%]**
		Value	$\Delta I_{CH_2/CH_3}$ **[%]**	**Value**	**ΔAI [%]**	**Value**	**ΔCI [%]**	**Value**	$\Delta \mathbf{I_{C-O}}$ **[%]**	
Castrol	25	2.5177	0	0.005718	0	0.2018	0	0.4762	0	0
	145	2.5301	0.4951	0.005153	−9.8810	0.1820	−9.8117	0.4772	0.2099	9.50
	180	2.5423	0.9796	0.005856	2.4134	0.2232	10.6045	0.5351	12.3687	17.65
Titan	25	2.4117	0	0.005903	0	0.2198	0	0.5005	0	0
	145	2.4377	1.0777	0.005315	−9.9610	0.2130	−3.0937	0.4881	−2.4775	2.99
	180	2.5167	4.3580	0.006168	4.4892	0.2477	12.6934	0.4905	−1.9980	11.14



(a) Castrol oil

(b) Titan EG oil

Figure 4.1. FTIR absorbance spectra of Castrol and Titan EG oils – shaded regions identify the spectral intervals considered for the calculation of the FTIR indices

show clearly different trends: for Castrol, the relative variation increases from +2.10% to +12.37% with temperature, whereas Titan shows a slight decrease, from −2.48% to −2.00% (this is a fundamentally different trend, since Castrol develops a strong positive increase in the C–O/C–O–C–related region at high temperature, while Titan EG slightly decreases); at the same time, Castrol consistently exhibits the larger PDIV deterioration. Among the considered indices, this therefore provides the strongest qualitative agreement with the electrical ranking, even if this does not imply a direct causal relationship of the form $I_{C-O} \uparrow \Longrightarrow PDIV \downarrow$, but it suggests that the evolution of the C–O/C–O–C spectral region may represent an important chemical difference between the two oils which can partially explain the PDIV trend[6].

Hence somehow a conclusion is that the indices $I_{\mathrm{CH_2/CH_3}}$, AI, and CI describe ageing but do not explain the oil ranking, whereas $I_{\mathrm{C–O}}$ appears to provide the clearest chemical discriminator between Castrol and Titan EG – this does not prove that C–O-containing compounds are responsible for the PDIV reduction, but it makes them the most interesting candidate family to investigate.

Thus it is worthwhile explaining why the information provided by I_{C-O} might represent a possible explanation of what has been seen: as it was described before, an increase[7] in the $1150 - 1170\,\mathrm{cm^{-1}}$ region in Castrol is compatible with a relative increase in oxygen-containing functionalities, associated for instance with alcohols, ethers, esters and other secondary oxygenated degradation products. From an electrical point of view, the possible release of oxygenated volatile compounds, associated with this degradation pathway, may precisely contribute to the reduction of PDIV by altering the electron-impact kinetics of the air–oil-vapour mixture. A first relevant mechanism is their comparatively low ionization energy: for instance, the ionization energies of ethanol and ethyl acetate, respectively belonging to the alcohols and esters classes, are approximately 10.48 eV and 10.01 eV respectively, whereas those of O_2 and N_2, so the main constituents of air, are approximately 12.07 eV and 15.58 eV [186, 187] – therefore, electrons that are not sufficiently energetic to ionize N_2 and O_2 may already access ionization channels of some organic vapours. However, ionization energy alone does not determine discharge inception

[6] to be rigorous, if the word "explain" might seen too strong, one can say that this result is qualitatively consistent with the observed PDIV trend and therefore represents a candidate chemical marker for further investigation.

[7] there is an apparent contradiction: the band around the $1150 - 1170\,\mathrm{cm^{-1}}$ peaks increases its absorbance while in this case we're saying that it's precisely the volatile compounds for that wavenumbers that might be responsible for the PDIV reduction: the increase in absorbance observed in the $1150 - 1170\,\mathrm{cm^{-1}}$ region can be associated with the evolution of oxygen-containing functionalities, mainly C–O and C–O–C bonds, formed during thermal and oxidative degradation of the oil; at first sight, this may appear contradictory with the hypothesis that volatile degradation products are released from the liquid and subsequently contribute to the reduction of PDIV; however, FTIR characterizes the chemical composition of the liquid phase remaining after ageing, not the species that have already migrated into the gaseous phase: during thermal ageing, the original hydrocarbon matrix can simultaneously generate degradation products with different molecular weights and volatilities, and smaller and lighter molecules may preferentially volatilize and enter the gaseous atmosphere, where they can modify electron–molecule collision processes and potentially affect discharge inception, whereas larger and less volatile oxygenated products can remain dissolved in the oil; if the formation of these C–O– and C–O–C-containing species is faster than their removal by volatilization, their concentration in the residual liquid increases, resulting in a higher absorbance in the $1150 - 1170\,\mathrm{cm^{-1}}$ region; therefore, the increase of $I_{\mathrm{C-O}}$ should not be interpreted as a direct measurement of the volatile species responsible for the PDIV variation, but rather as an indicator of a stronger evolution of oxygenated chemistry in the oil, and the same degradation pathway may simultaneously generate lighter volatile species capable of entering the gas phase and altering its electrical behaviour, which makes the evolution of this FTIR region particularly interesting when compared with the observed PDIV trend.

since each molecular species is characterized by energy-dependent electron-impact cross-sections for ionization, excitation, elastic scattering as well as electron attachment where relevant: the introduction of volatile compounds hence modifies the electron energy distribution function, which may end up in having a larger Townsend effective ionization coefficient α_{eff}, thus the discharge inception criterion can be reached at a lower electric field, thereby reducing the PDIV. The increase of the C–O-related FTIR index should therefore not be interpreted as direct proof of this mechanism, but as evidence of an ageing pathway potentially capable of producing oxygenated volatile species whose presence may modify the discharge kinetics of the gaseous phase.

Thus, to recall the difference between the electrical results of PDIV and TGA results, if a fraction of the responsible species is sufficiently small and volatile, the gas phase above Castrol could therefore contain a mixture of organic volatile compounds qualitatively different from the one produced by Titan, and here it's precisely where one can explain the apparent contradiction with the the results provided by the TGA:

$$\text{amount of vapour} \neq \text{electrical aggressiveness of vapour}$$

Indeed, Titan may volatilize significantly more material, but this material could consist mainly of species that are relatively less effective at modifying inception conditions; Castrol, on the other hand, might release less total mass, but a higher fraction of electrically more influential oxygenated/carbonyl-containing species. Indeed, the important parameter is not m_{vapour} for the PDIV variation, as it has been precisely explained for the two opposite trends of TGA and PDIV for Castrol and Titan EG, but rather the PDIV should therefore be regarded as depending on a combination of parameters that can be schematically represented as:

$$\text{PDIV} = f(x_i, \sigma_{\text{ion},i}, \sigma_{\text{att},i}, \sigma_{\text{exc},i}, E_{\text{ion},i}, E/N)$$

where x_i is the concentration of each volatile species and σ represent the different electron-molecule collision cross sections. So, eventually, even if from table 4.2 this supporting explanation was regarded as having medium relevance, still with the available data this represents a plausible interpretation consistent with the observed trends, although it cannot be uniquely demonstrated by the present measurements.

In synthesis, the comparison between the PDIV values at $t = 0$ and $t = 1\,\text{h}$ of fig. 3.11 suggests that larger time-dependent differences are not controlled by volatility alone. Indeed, TGA does not explain the ranking, as Titan shows much greater mass loss than Castrol, yet Castrol causes the larger PDIV deterioration. On the other hand, FTIR and its elaboration – especially CI and I_{C-O} – provides a more plausible qualitative correlation, indicating that the chemical nature of the oxygenated degradation products is more relevant than the overall amount of vapour released.

4.2.3 Interpretation of PDIV behaviour, with samples pre-wetting

The results obtained for the preliminarily wetted specimens, reported in figs. 3.12 and 3.13, show a temperature dependence broadly similar to that observed in the non-wetted configuration, although the normalized PDIV values remain systematically higher. Immediately after wetting,

at ambient temperature, a pronounced increase in PDIV is observed for all investigated lubricants. This behaviour can reasonably be attributed to the direct presence of a liquid oil layer within the inter-electrode region. In this condition, the geometry effectively experienced by the discharge is no longer the same as in the dry specimen: part of the air-filled gap is replaced or covered by the dielectric liquid, thereby modifying the local electric-field distribution and the discharge path.

As the temperature is increased, the normalized PDIV rapidly decreases and approaches values close to unity. This trend suggests that the initial effect produced by wetting becomes progressively less dominant during heating. A plausible explanation is that the oil initially present in the discharge region becomes less viscous with increasing temperature and tends to flow away from the critical interphase gap. At the same time, part of the liquid may evaporate. Consequently, the effective geometry progressively approaches that of the non-wetted specimen, and the influence of the liquid phase on the local electric field is reduced. Nevertheless, even at the highest investigated temperatures, the normalized PDIV values remain slightly higher than those measured in the non-wetted configuration. This residual difference may indicate that complete restoration of the original dry geometry is not achieved: a thin oil film may remain trapped on the insulation surfaces or within the narrow gap between the back-to-back conductors, even after prolonged thermal exposure. Alternatively, the preliminary wetting procedure may induce a persistent modification of the surface condition of the insulation. Both effects would alter the local electric-field distribution and the conditions for discharge initiation, explaining why the wetted specimens retain a modestly higher PDIV than the corresponding dry samples.

Overall, these results indicate that the very large PDIV increase observed immediately after wetting is mainly a geometrical and liquid-phase effect, rather than a consequence of a permanent improvement in the dielectric properties of the insulation system. As the temperature rises, drainage and evaporation progressively reduce the amount of liquid present in the critical region, weakening this effect and bringing the discharge behaviour closer to that observed under vapour-only exposure. The remaining difference at high temperature is therefore most likely associated with residual wetting or with a persistent surface modification induced by the lubricant.

Conclusion

The present thesis investigated the influence of dielectric cooling lubricants on the PDIV of hairpin-winding interphase insulation, with particular attention to the effects produced by oil-derived vapours and direct surface wetting under temperature conditions representative of electric traction applications. The experimental investigation combined PDIV measurements with thermogravimetric analysis (TGA) and Fourier Transform Infrared (FTIR) spectroscopy, with the main aim of identifying possible physical and chemical mechanisms responsible for the observed differences.

The electrical measurements clearly showed that the effect of the lubricant atmosphere is strongly dependent on both oil formulation and temperature; the dependence on temperature was also analysed without considering the oil's effect. Precisely considering a preliminary air only PDIV study versus temperature, the observed trends confirmed the expected reduction of inception voltage with increasing temperature. However, the experimentally observed behaviour could not be accurately reproduced by the presented Peek and Dunbar temperature corrections, either in magnitude or in the shape of the temperature dependence, since they appeared to be too much simplistic. This outcome highlights that, for the investigated back-to-back conductor geometry, partial discharge inception cannot be described solely through a correction of gas density. The non-uniform electric-field distribution and the geometry of the critical discharge path also play a fundamental role, suggesting that more accurate predictions would require a numerical description of the actual field distribution combined with an inception criterion such as the Schumann criterion.

Then, the effect of dielectric oil has been studied. Considering first the initially dry specimens, for which the influence of the oil was mainly associated with the air–oil-vapour atmosphere and measurements were considered at time $t = 1\,\mathrm{h}$ after the reaching of the desired temperature, Titan EG and Paryol exhibited very similar behaviour at 145 °C, with a slight advantage for Titan EG, whereas Castrol already produced a more pronounced PDIV reduction. As the temperature increased, the differences became progressively clearer: Paryol maintained the highest normalized PDIV, Titan EG showed an intermediate behaviour, and Castrol produced the largest deterioration. At 180 °C, Castrol resulted in a normalized PDIV of approximately 0.82 p.u., namely corresponding to a reduction of about 18% with respect to air at the same temperature. At the highest investigated temperatures, the overall ranking was Paryol as the best-performing lubricant, followed by Titan EG, with Castrol showing the most detrimental influence on PDIV. The comparison between measurements performed immediately after reaching the test temperature and after one hour of thermal exposure further showed that this relative ranking was already substantially established at $t = 0$, although the absolute magnitude of the reduction continued to evolve during the subsequent thermal exposure.

The physico-chemical characterization provided an important contribution to the interpretation of the different electrical behaviours. TGA initially suggested that Paryol was the most thermally stable fluid among the investigated lubricants, consistently with its limited influence on PDIV. Instead, the comparison between the two mineral oils revealed a particularly significant result: at 180 °C, Titan EG exhibited a mass loss of approximately 5.08%, compared with only 1.23% for Castrol, although Castrol produced a substantially larger PDIV deterioration. The same discrepancy was observed over the complete investigated temperature range. Consequently, it has been observed how the total amount of volatilized material cannot be regarded as the main parameter controlling PDIV degradation. Rather, the results indicate that the chemical nature of the released species is likely to be more relevant than the total vapour quantity. The fact that the Castrol–Titan ranking was already present at $t = 0$ further supports this interpretation, since the poorer behaviour of Castrol cannot simply be attributed to a greater accumulation of volatile products during the one-hour isothermal exposure.

To investigate this hypothesis, the FTIR spectra of Castrol and Titan EG were compared through four selected spectroscopic indicators: the $I_{\mathrm{CH_2/CH_3}}$ ratio, the Aromatic Index, the Carbonyl Index and the $I_{\mathrm{C-O}}$ index. The first three indices were able to describe different aspects of the chemical evolution of the oils, but did not reproduce the observed electrical ranking. In particular, the Carbonyl Index confirmed that oxidative modifications occurred in both oils, but Titan EG exhibited a larger relative variation at 180 °C despite maintaining a higher PDIV than Castrol. The $I_{\mathrm{C-O}}$ index instead provided the clearest qualitative distinction between the two fluids: at 180 °C, Castrol exhibited a strong positive variation of approximately +12.37%, whereas Titan EG remained slightly below its initial value, at approximately −2.00%. This evolution is consistent with a stronger development of C–O/C–O–C-related oxygenated functionalities in Castrol and, among the investigated indicators, represents the best qualitative correlation with the measured PDIV ranking. The resulting interpretation is therefore that thermal ageing may generate chemically different volatile fractions depending on the lubricant formulation. Oxygenated degradation pathways may produce alcohols, ethers, esters, carbonyl-containing species or other volatile organic compounds capable of modifying electron–molecule collision processes in the gaseous dielectric. Their presence may alter the electron energy distribution and the effective Townsend ionization coefficient, allowing the discharge inception condition to be reached at a lower applied electric field. From this perspective, an oil releasing a relatively small amount of electrically aggressive species may have a stronger influence on PDIV than another lubricant producing a considerably larger amount of less influential vapour. The central outcome of the comparison can therefore be summarized by the fact that vapour quantity does not necessarily correspond to vapour electrical aggressiveness. Nevertheless, since FTIR characterizes the residual liquid phase rather than directly identifying the species present in the headspace, the proposed mechanism should be regarded as a physically consistent interpretation supported by the experimental trends, rather than as direct proof of the chemical species responsible for the PDIV reduction.

The pre-wetted experiments provided an additional perspective on the role of the liquid phase. Immediately after wetting at ambient temperature, all lubricants produced a very large increase in PDIV, which can mainly be attributed to the direct presence of liquid oil in the critical

inter-conductor region and to the consequent modification of the local geometry and E-field distribution. With increasing temperature, this effect rapidly decreased and the normalized PDIV approached values close to unity, consistently with a progressive reduction in oil viscosity, drainage from the critical region and partial evaporation. Nevertheless, the PDIV remained slightly higher than in the corresponding non-wetted condition even at elevated temperature, suggesting that a residual oil film or a persistent modification of the insulation surface may remain after heating. The strong initial improvement associated with wetting should therefore be interpreted primarily as a geometrical and liquid-phase effect, rather than as a permanent improvement of the intrinsic dielectric properties of the insulation system. Furthermore, this improvement cannot be somehow exploited in the actual motor operation, given that, at the common operating temperatures of the motor, the temperature is such that the benefit observed at ambient temperature has already vanished.

Overall, the results of this work demonstrate that the introduction of dielectric cooling lubricants in the vicinity of hairpin-winding insulation cannot be evaluated exclusively from a thermal point of view, namely based on the temperature only. The lubricant formulation, its temperature-dependent chemical evolution, the composition of the resulting vapour phase and the actual wetting condition of the insulation can all significantly affect partial discharge inception. In particular, the comparison among the investigated fluids shows that thermal stability or total volatility alone are insufficient criteria for predicting electrical performance. Among the tested lubricants, Paryol provided the most favourable behaviour at high temperature, Titan EG represented an intermediate case, whereas Castrol exhibited the strongest detrimental effect on PDIV despite its comparatively lower mass loss.

Future developments

Characterization of oil vapours by Gas Chromatography

Gas Chromatography (GC) is a widely used analytical technique designed to separate, detect, and analyze volatile or semi-volatile compounds in a chemical mixture [188]. At its core, gas chromatography works by passing a vaporized sample through a tube, called a column, using a continuous flow of an inert gas, known as the mobile phase or carrier gas such as helium or nitrogen. Inside the column is a stationary phase, which is typically a microscopic layer of viscous liquid or solid polymer coated along the inner walls [188]. As the carrier gas pushes the vaporized mixture through the column, the individual molecules interact differently with the stationary phase depending on their physical properties, and these differences causes the mixture to separate into distinct "bands" of pure molecular components as it travels toward the exit of the column [189]. So basically the separation and identification of the different molecules present in the gases are obtained based on *when* the molecule exits the column rather than *where*: indeed, all molecules enter the column at the exact same physical starting point and exit at the exact same physical ending point, and the system identifies molecules based on the time it takes for them to travel through the entire column.

The previous one was a very generic description, but in our case what would have been really useful is not a generic gas chromatography on the liquid, but rather a Headspace Gas Chromatography, ideally coupled with mass spectrometry (HS-GC-MS) where the mass spectrum provides a sort of molecular fingerprint of the gas – it is almost perfectly complementary to FTIR, because FTIR tells how the oil changes chemically, whereas HS-GC-MS can tell which volatile molecules are actually present in the gas space above the oil: that exact gaseous space, in the experiment of this thesis work, occupies the gap between the two conductors representing the stator of the hairpin winding machine and can therefore modify the PDIV [190, 191]. Indeed, in our experiments we basically have a scheme like this one:

$$\text{oil} \xrightarrow{\text{heating}} \text{oil vapours} \xrightarrow{\text{gas mixture in the hairpin gap}} \text{PDIV}$$

and, with the headspace GC, instead of analyzing the entire liquid oil directly, it is placed in a sealed vial at a given temperature and the gas phase above the liquid is analyzed. Headspace GC-MS analysis of the gas phase above an oil is a well-established technique for identifying volatile oil degradation products: static headspace GC methods have been specifically developed to measure gases present in transformer oils [192].

A recent work adopted a very similar working strategy (see [191] for more): they applied the headspace GC on lubricant base oils during oxidation, identifying a large number of light degradation products; the same study also compared the chromatographic results with changes

observed in the FTIR of the oils, and this is particularly important because it shows that, combining FTIR spectroscopy and headspace GC, the two techniques provide complementary information for the investigation of lubricant oxidation and degradation. Indeed, the main difference between FTIR and HS-GC-MS lies in the level of chemical information that can be obtained from each technique:

- **FTIR spectroscopy** allows the evolution of specific absorption regions to be monitored, namely it mainly provides information about the presence and relative evolution of *functional groups*[8];
- **Headspace gas chromatography**, coupled with mass spectrometry, provides a much more molecule-specific characterization of the *individual* volatile fraction: instead of considering only changes in functional groups within the liquid oil, HS-GC-MS can identify individual volatile compounds present in the gas phase above the lubricant.

This distinction is particularly relevant for the interpretation of the PDIV results: FTIR can reveal that thermal ageing modifies the chemical structure of the oil and can indicate which functional groups are becoming more or less abundant; HS-GC-MS, on the other hand, can determine which specific volatile molecular species are actually transferred into the gaseous atmosphere above the oil. Combining the two techniques would therefore provide a more complete description of the relationship between oil degradation, vapour composition and the observed variation in PDIV.

However, this type of investigation could not be performed within the scope of the present work, since the equipment required for gas chromatographic analysis was not available in the university laboratory and it was not possible to carry out the measurements through external laboratories.

Experimental determination of Townsend ionization coefficient α

The material in this subsection is based on what is presented in [193, 194, 195, 196, 197]. For full details and proofs, one should refer to the original source.

The experimental determination of the first Townsend ionization coefficient α is particularly relevant in the context of the present work because this parameter enters directly into the physical description of electron-avalanche growth preceding partial-discharge inception. As discussed, the inception voltage can be estimated through the Schumann criterion by evaluating the cumulative ionization along the critical electric-field line (see eq. (1.15)). Given that the value of α represents the number of ionizing collisions produced by an electron per unit distance travelled in the direction of the field, its experimental characterization in air containing lubricant vapours could provide a more direct physical interpretation of the variations in PDIV observed for the different oils: a vapour composition promoting electron-impact ionization would increase the avalanche growth rate and could allow the critical Schumann condition to be reached at a lower applied voltage compared to pure air.

[8] for example, an increase in the carbonyl band may indicate that the concentration of C=O-containing species has increased, but FTIR alone generally cannot determine which specific molecular species are responsible for that increase

The classical experimental setup for measuring the first Townsend ionization coefficient α consists of a parallel-plate electrode system housed within a sealed gas/vacuum chamber, where typically the gas pressure and composition can be precisely regulated. The electrode assembly comprises a cathode and an anode designed to produce a highly uniform Laplacian electric field in the gap – they are the so-called *Rogowski electrodes*. The cathode is typically made of a photo-emissive material and is irradiated externally by a stable ultraviolet (UV) source, such as a mercury lamp or UV LED, through a quartz window to generate a continuous stream of initiatory "seed" electrons I_0 via photoelectric emission – to establish the baseline primary current I_0 before avalanche multiplication takes place, a very low DC voltage is initially applied across a small gap distance where ionizing collisions are negligible.

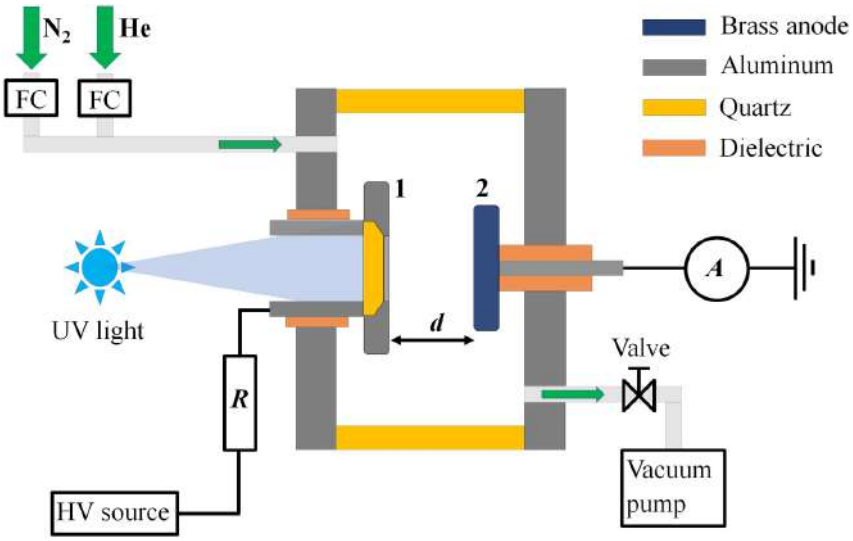


Figure 4.2. Schematic of the experimental set-up of the Townsend discharge chamber (adapted from [193])

In the classical distance-varying implementation, the gas pressure and reduced electric field are fixed while the electrode separation (d) is progressively varied. The applied DC voltage must therefore be adjusted proportionally to the gap according to (V=Ed), so that the electric field experienced by the electrons remains unchanged. This condition is essential because α is itself a strong function of the reduced electric field; keeping E/p, or equivalently E/N, constant ensures that the ionization probability per unit length remains approximately constant while only the available avalanche length is changed. Consequently, as the gap distance d between the electrodes is increased in precise, small increments using a high-precision micrometer, the applied DC voltage V must be increased proportionally to satisfy the relation $E = V/d$. For each step of distance d, the resulting amplified steady-state anode current (I) is measured using a highly sensitive electrometer or picoammeter. When secondary processes are negligible, namely under non-self-sustained discharge conditions and within a regime where secondary cathode ionization processes γ are insignificant, the current multiplication follows Townsend's exponential law:

$$I = I_0 \exp(\alpha d) \tag{4.9}$$

or, if secondary emission processes are not negligible, one can use the more complete eq. (1.9). Taking the natural logarithm of this expression yields a linear relationship: $\ln(I/I_0) = \alpha d$ and, by

plotting the calculated values of $\ln(I/I_0)$ on the y-axis against the electrode separation distance d on the x-axis, a straight line is obtained; the slope of the linear regression fit of this data directly corresponds to the value of the first Townsend ionization coefficient α at that specific reduced electric field. By repeating this entire distance-varying sweep at different values of E/p, the full functional dependence of the normalized ionization coefficient (α/p or α/N) on the reduced electric field can be mapped out by precisely associating the value of α as the slope of the line in the semi-log plane to the particular E-field value in correspondence of which that set of points have been obtained.

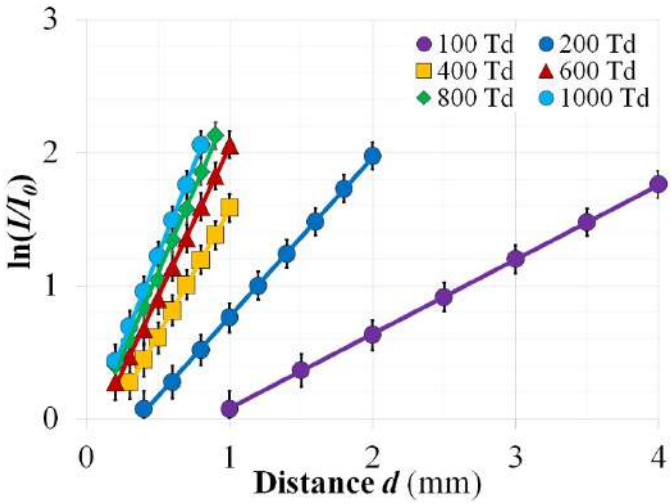


Figure 4.3. $\ln(I/I_0)$ as a function of electrode distance d for various reduced electric field values – solid lines show the linear fits used for the determination of α (adapted from [193])

A comparable procedure was used by [197], who measured the no-gain current plateau I_0, progressively increased the amplification field at fixed geometry, and obtained current-versus-voltage ionization curves from which the Townsend coefficient as a function of reduced field was determined – basically the amplification gap is fixed and the field/voltage is increased[9]; they first measure the gainless plateau I_0, then enter the multiplication region, calculate the gain, and derive α for the different fields. In terms of formulas it is:

$$I(V) = I_0 e^{\alpha(E)d} \tag{4.10}$$

where it is $E = \frac{V}{d}$ and the current as a function of the voltage curve can be thus expressed as:

$$I(V) = I_0 \exp\left[d\,\alpha\left(\frac{V}{d}\right)\right] \tag{4.11}$$

which allows eventually to compute/extract the first Townsend ionization coefficient for the

[9]From an implementation point of view, this fixed-gap configuration can be considered preferable: indeed, keeping the electrode separation constant considerably simplifies the mechanical design, since no precise movable electrode system is required, and eliminates the additional uncertainty associated with repeatedly setting and measuring the interelectrode distance – the experimental characterization could therefore be performed by varying only the applied DC voltage while maintaining a well-defined and reproducible electrode geometry

different field values as:

$$\alpha(E_i) = \frac{1}{d} \ln \frac{I_i}{I_0} \tag{4.12}$$

The upper part of the voltage sweep must, however, be treated carefully: as the field approaches breakdown, secondary mechanisms such as ion-induced electron emission from the cathode, photon feedback and space-charge effects become increasingly important, and the simple relation $I = I_0 e^{\alpha d}$ is no longer sufficient – experimentally, this transition is visible as an upward deviation from the primary Townsend amplification trend and eventually as the rapid current increase preceding breakdown. Consequently, only the portion of the characteristic for which the discharge remains non-self-sustaining should be used to determine the first Townsend coefficient; the onset of this deviation is itself physically relevant, since it identifies the region in which feedback mechanisms begin to contribute to the transition from an electron avalanche to a self-sustained discharge.

Although this experimental investigation was initially considered as a possible extension of the present work, the measurement of the first Townsend ionization coefficient was ultimately not performed because the required UV LED source, needed to generate the initial photoelectrons at the cathode, was not available within the experimental timeframe of the thesis.

Appendix A

Demonstrations on climate model parameters

A.1 TCRE and airborne fractions

In general, the global carbon–climate system exhibits several stable characteristics despite the strong anthropogenic disturbances that have occurred since the beginning of industrialization [198]. In particular, the airborne fraction of CO_2 has remained close to an average value of approximately 0.44 over the past 50 years[1] and, similarly, the ratio between global warming ΔT and cumulative CO_2 emissions Q_E (the ratio $\alpha = \frac{\Delta T}{Q_E}$ is the so-called *Transient Climate Response to cumulative carbon Emissions* (TCRE) and it is a metric that directly relates the total amount of carbon dioxide CO_2 humans have emitted over time, namely the cumulative historical anthropogenic emissions, to the resulting change in global mean surface temperature) has also remained relatively stable, not only in historical observations but also across many future climate projections [198]. In particular, the TCRE is a powerful tool for policymakers because it demonstrates that, to stabilize global temperatures at a certain level above the pre-industrialization level, there is a finite *carbon budget* that can be burned.

As shown in [198], it is possible to demonstrate that, if the system, namely is the coupled carbon–climate system, can be approximated as an assumption as a LinExp dynamical system in the shape of[2]:

$$\frac{\mathrm{d}x}{\mathrm{d}t} = f(t) - K\,x(t) \tag{A.1}$$

where $x(t)$ is the state vector of the carbon–climate system but in our case we consider it precisely equal to the net mass of current atmospheric CO_2, $f(t)$ is external forcing vector (mainly anthropogenic emissions, and in our case becomes precisely the annual emission rate

[1] the definition of airborne fraction will be given later

[2] Raupach basically relies on the fact that linear coupled systems can be decomposed into exponential eigenmodes, and the following one is the simplification where the justification is essentially that we are performing a projection of a high-dimensional dynamical system onto its dominant observable mode, because we are not trying to reproduce every internal process of the Earth system but only to explain the emergence of the near-linear relation between warming and CO_2 cumulative emissions

function), K is the response matrix describing sinks and climate adjustment processes that in our case becomes just a constant (this is the linear part), and then assuming the forcing to grow exponentially as (this is the exponential part):

$$f(t) = f_0 \cdot e^{rt} \tag{A.2}$$

where f_0 is the initial forcing/emission rate and r is the exponential growth rate of emissions, then the ratio $\alpha = \frac{\Delta T}{Q_{\mathrm{E}}}$, which is precisely the TCRE by definition, and $AF_{\mathrm{cumul}}(t) = \frac{x(t)}{Q_{\mathrm{E}}(t)} = \frac{x(t)}{\int f(\tau)\mathrm{d}\tau}$, which is the so-called cumulative airborne fraction (it is defined as the share of total human-induced CO_2 emissions that remains in the atmosphere compared to the total CO_2 emissions), as well as the instantaneous airborne fraction $AF(t) = \frac{\dot{x}(t)}{f(t)}$, which is a ratio of rates, are constant[3]. The key mathematical explanation comes from the fact that, for a linear system, exponentials are eigenfunctions thus the response also evolves exponentially with the same growth rate[4]:

$$x(t) \propto e^{rt} \quad \Longrightarrow \quad x(t) = Ae^{rt} \tag{A.3}$$

where A is an integration constant. Indeed, in order to prove the previous statement, it is possible to rewrite the TCRE as[5]:

$$\alpha = \frac{\Delta T}{Q_{\mathrm{E}}} = \frac{\Delta T}{\Delta C_{\mathrm{A}}} \cdot \frac{\Delta C_{\mathrm{A}}}{Q_{\mathrm{E}}} = \frac{\Delta T}{x(t)} \cdot AF_{\mathrm{cumul}} \tag{A.4}$$

where ΔC_{A} is the historical cumulative atmospheric carbon increase that is to say $x(t)$ with our previous symbol representation; $\frac{\Delta T}{\Delta C_{\mathrm{A}}}$ represents the climate sensitivity, namely how much the temperature increases per unit of CO_2 added to the atmosphere, and $\frac{\Delta C_{\mathrm{A}}}{Q_{\mathrm{E}}}$ represents the carbon sensitivity, namely the fraction of emitted CO_2 that actually remains in the atmosphere that is to say the cumulative airborne fraction AF_{cumul}. For reference, the TCRE metric gives that for every 1000 Gt of CO_2 emitted the global surface temperature rises by approximately 0.45 °C [6].

If all the previous assumptions hold, by plugging into eq. (A.1) the solution eq. (A.3) and calculating the integration constant that appears to be $A = \frac{f_0}{r+k}$ (one has in this manner determined the complete form of eq. (A.3), since r is a parameter and A is the only unknown), it is possible to calculate first the cumulative historical emissions as:

$$Q_{\mathrm{E}}(t) = \int_0^t f(\tau)\,\mathrm{d}\tau = \int_0^t f_0 e^{r\tau}\,\mathrm{d}\tau = \frac{f_0}{r}(e^{r\tau} - 1) \approx \frac{f_0}{r}e^{r\tau} \tag{A.5}$$

[3] notice that this statement is true only under our simplified assumptions of LinExp system with exponential forcing term, while in reality for instance the cumulative AF appears to be lower than the instantaneous AF [198]

[4] notice that for simplicity we considered only the steady-state particular solution, skipping the homogeneous solution which contains the transient terms which were instead maintained in [198] – this is reasonable because these terms have a time constant equal to $\tau = \frac{1}{r+k}$ such that, in the modern era and for actual values of r and k, they can be neglected – hence, somehow the core idea is that the reason the TCRE and other critical climate ratios have appeared nearly constant over historical modern history is precisely because the transient terms have died out, and the whole planetary system has settled into an exponential equilibrium

[5] because ΔC_{A} sits exactly in the middle as the state variable $x(t)$, it splits the problem into two distinct blocks:

- the carbon sensitivity ($\frac{\Delta C_{\mathrm{A}}}{Q_{\mathrm{E}}}$): how the input emissions update the state variable $x(t)$ (it's the cumulative airborne fraction AF_{cumul});
- the climate sensitivity ($\frac{\Delta T}{\Delta C_{\mathrm{A}}}$): how the state variable $x(t)$ drives the output warming.

Hence, by then exploiting the cancellation of exponentials, leads to the proof of the assertion:

$$AF_{\text{cumul}} = \frac{x(t)}{Q_{\text{E}}(t)} = \frac{\frac{f_0}{r+k}e^{r\tau}}{\frac{f_0}{r}e^{r\tau}} = \frac{r}{r+k} \tag{A.6}$$

namely we proved that the cumulative airborne fraction is constant, which in very simple terms means that the ratio between the net stock in the CO_2 tank and the total amount of historically poured CO_2 in the atmosphere remains completely constant, but more importantly that $x(t) \propto Q_{\text{E}}(t)$ under the aforementioned assumptions. Furthermore, again under these assumptions (otherwise this is not true anymore), also the instantaneous[6] airborne fraction appears to be constant and also equal to AF_{cumul}:

$$AF = \frac{\dot{x}(t)}{f(t)} = \frac{\frac{f_0 \cdot r}{r+k}e^{r\tau}}{f_0 e^{r\tau}} = \frac{r}{r+k} \tag{A.7}$$

Anyway we want to prove why actually the relation between cumulative historical emissions and temperature anomaly is linear by means of a constant. Up to now we proved with eq. (A.6) that the relation between $x(t)$ and $Q_{\text{E}}(t)$ is just a constant, and this is somehow a property of the LinExp systems. The missing part is that temperature responds approximately linearly to CO_2 perturbation for moderate changes, namely $\Delta T \propto x(t)$. In this regard, [199, 200, 201] show that the radiative forcing which affects Earth's energy balance, under the assumption of small CO_2 perturbation, can be approximated as linear. Hence eventually we reach the statement:

$$\Delta T \propto x(t) \propto Q_{\text{E}}(t) \quad \Longrightarrow \quad \Delta T \propto Q_{\text{E}} \;\text{ or }\; \Delta T = \alpha Q_{\text{E}} \tag{A.8}$$

where $\alpha = \text{TCRE}$ has the meaning of how many Kelvin of temperature increase we get per unit of carbon emission.

Furthermore, it has been mentioned in section 0.1.2 that *«if net zero greenhouse gas emissions are reached and sustained, the global surface temperature is projected to gradually decline after an earlier peak»* and this can be simply proved by using eq. (A.1). Indeed, if the yearly greenhouse gases emissions go to zero, namely $f(t) = 0$, then it is:

$$\frac{\mathrm{d}x}{\mathrm{d}t} = -Kx(t) < 0 \quad \Longrightarrow \quad x(t) \text{ decreases} \tag{A.9}$$

namely since it is $x(t) \propto Q_{\text{E}}(t)$ the cumulative historical emissions $Q_{\text{E}}(t)$ are decreasing and, since it is $\Delta T = \alpha Q_{\text{E}}$ then it comes that also the temperature anomaly should regress even with quite a large inertia.

In order to have an intuitive understanding about the meaning of airborne fraction, both in terms of cumulative and instantaneous terms, one can look at fig. A.1. This chart, titled *Carbon Dioxide Partitioning*, illustrates how human-emitted carbon dioxide has been distributed among Earth's natural reservoirs in years $1900 - 2020$, and it's based on a simple mass-balance principle:

- everything under the jagged filled areas represents where human-produced CO_2 goes,

[6] it would be better to call it as annual airborne fraction, since it's based on the ratio of the annual rates

namely it shows the three places that absorb this CO_2 emission:

  - the teal area represents the ocean sink, namely the amount of anthropogenic CO_2 dissolved into the world's oceans through air-sea gas exchange;
  - the light green area represents carbon absorbed by the terrestrial biosphere, primarily driven by enhanced plant growth and soil carbon storage;
  - the light blue area represents the remaining portion of human emissions which accumulates in the atmosphere, driving up parts-per-million;

- the pink solid line represents total CO_2 annual emissions including fossil fuel combustion, cement production, and land-use changes.

One can however notice that the stacked heights don't match the pink line, and this is the concept of the so-called *Carbon budget imbalance* (BIM): it is the gap between estimated total anthropogenic CO_2 emissions and the sum of the carbon stored in the atmosphere, ocean, and land reservoirs [202, 203]. While these should perfectly balance in the real world, mismatches occur because each component is estimated independently using different data and models [203]:

- the atmospheric growth is measured with absolute precision thanks to high-precision monitoring stations with physical sensors like the *Mauna Loa Observatory* in Hawaii [204];
- the fossil fuel emissions are calculated from highly accurate economic data, which gives as well very precise data;
- the sinks for CO_2, namely land and ocean, are estimated using complex models that are prone to specific errors.

Since the first two contributions can be obtained with quite large accuracy, they are treated as "ground truth" but when one tries to make the comparison between the two curves, namely the curve of total emissions from fossil fuels and land-change use and the curve resulting from the stack of the aforementioned 3 contributions, a mismatch precisely exists but this attributed to an inaccurate estimation of the natural sinks since they are based on complex models and sometimes they lack of extreme accuracy. This is also somehow useful because it tells researchers exactly which specific ecosystem models need optimization [202].

Furthermore, fig. A.1 allows to understand better the concepts and the differences between instantaneous Airborne Fraction $AF(t)$ and the cumulative airborne fraction AF_{cumul}:

- the *Instantaneous Airborne Fraction* $AF(t)$ is defined as the fraction of emissions that stayed in the atmosphere during one specific year, and it can be visualized as the thickness of the light blue band in that exact year divided by the total height of all three bands combined for that year;
- the *Cumulative Airborne Fraction* AF_{cumul} is defined as the fraction of all human emissions since the industrial revolution that is still in the atmosphere today, and it can be visualized as the total area of the light blue region from left to right, divided by the total combined area of all the coloured regions from left to right.

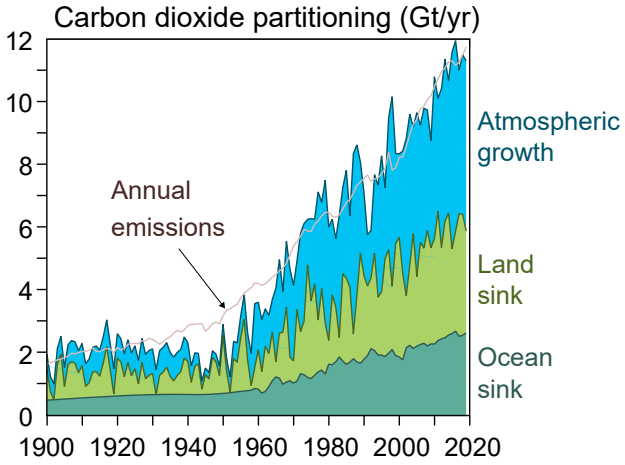


Figure A.1. The global carbon dioxide partitioning (atmospheric CO_2, land sink and ocean sink) averaged over the historical period 1900–2020 (adapted from [205])

A.2 Atmospheric CO_2 concentration

It is possible to explain why figs. 3 and 10 have the x-axis variable that is strongly connected: indeed atmospheric CO_2 concentration [ppm] and historical cumulative CO_2 emissions are strongly connected because cumulative emissions largely determine atmospheric concentration. Indeed, once we factor out from the annual emissions the portion of CO_2 absorbed by the environment through the cumulative airborne fraction, the remaining relationship is purely a function of the mass of the atmosphere (indeed one has to consider that historical cumulative emissions are different from total atmospheric accumulation, because not all emitted CO_2 remains in the atmosphere). If we look only at the CO_2 that actually stays in the air, namely precisely the airborne portion, the definition becomes just physical constant determined by the dry weight of Earth's atmosphere. The definition of 1 ppm is basically precisely one molecule of CO_2 per one million molecules of dry air in terms of molar ratio [206]. Thus it comes that:

$$C_{\mathrm{CO_2,atm}}(t) = C_0 + \left(\frac{\mu_{\mathrm{air}}}{\mu_{\mathrm{C}}} \cdot \frac{\mathrm{AF}_{\mathrm{cumul}}(t) \cdot Q_{\mathrm{E}}(t)}{M_{\mathrm{atm}}} \right) \cdot 10^6 \tag{A.10}$$

where:

- $C_{\mathrm{CO_2,atm}}(t)$ is the atmospheric CO_2 concentration at time t, in parts per million [ppm];
- C_0 is the the pre-industrial CO_2 baseline concentration;
- $AF_{\mathrm{cumul}}(t)$ is the Cumulative airborne fraction;
- $Q_{\mathrm{E}}(t)$ are the total cumulative human emissions measured as the mass of pure carbon (GtC) – this is done because, by tracking only the mass of the Carbon atom itself, scientists don't have to constantly add or subtract the weight of changing oxygen or hydrogen attachments as carbon morphs between gas, liquid, and plant matter during all the processes of partition that involve precisely carbon composites;
- M_{atm} is the the total dry mass of the Earth's atmosphere;

- μ_{C} is the atomic mass of Carbon;
- μ_{air} is the average molecular mass of dry air;
- eventually, 10^6 is the scaling factor needed to convert a raw mass ratio into parts per million (ppm).

Hence one can precisely see that, since as mentioned in section A.1 the appears to be practically constant, the relation between atmospheric CO_2 concentration and the historical cumulative emissions is just a matter of scaling. Indeed, eq. (A.10) can be rewritten as:

$$Q_{\mathrm{E}}(t) = \frac{C_{\mathrm{CO_2,atm}}(t) - C_0}{10^6} \cdot \frac{\mu_{\mathrm{C}}}{\mu_{\mathrm{air}}} \cdot \frac{M_{\mathrm{atm}}}{\mathrm{AF}_{\mathrm{cumul}}(t)} \tag{A.11}$$

The two eqs. (A.10) and (A.11) can be used in order to change the x-axes of figs. 3 and 10.

Appendix B

Experimental measured data

Hereafter, one can find reported the raw numerical data of the Partial Discharge Inception Voltage from which the elaboration of PDIV outcomes and comparisons have been performed throughout this thesis work in the previous chapters.

Table B.1. PDIV values measured for the investigated specimens in air and in the presence of Castrol oil. All voltage values are reported as $V_{\text{peak}}/\sqrt{2}$.

Sample No.	AIR				CASTROL oil					
	T_{amb}	145 °C	160 °C	180 °C	145 °C		160 °C		180 °C	
					$t = 0$	$t = 1\,\text{h}$	$t = 0$	$t = 1\,\text{h}$	$t = 0$	$t = 1\,\text{h}$
2	1521	1396	1355	1314	1381	1280	1257	1196	1091	1075
3	1366	1224	1196	1156	1143	1078	1053	1021	986	958
4	1285	1124	1101	1057	1079	1031	1011	973	911	893
5	1477	1327	1304	1249	1312	1201	1134	1121	1076	1002

Table B.2. PDIV values measured for the investigated pre-wetted specimens in air and in the presence of Castrol oil under different thermal conditions. All voltage values are reported as $V_{\text{peak}}/\sqrt{2}$.

Sample No.	AIR				CASTROL oil – wetted specimens						
	T_{amb}	145 °C	160 °C	180 °C	T_{amb}, wetted	145 °C		160 °C		180 °C	
						$t = 0$	$t = 1\,\text{h}$	$t = 0$	$t = 1\,\text{h}$	$t = 0$	$t = 1\,\text{h}$
2	1056	962	911	870	4113	1052	1021	967	941	893	872
3	1175	1108	1056	1011	3704	1244	1189	1158	1111	1102	1014
4	890	823	801	760	3756	991	901	897	855	847	783
5	1093	1023	1004	968	3782	1124	1088	1059	1039	1004	983

Table B.3. PDIV values measured for the investigated specimens in air and in the presence of Titan EG oil. All voltage values are reported as $V_{\text{peak}}/\sqrt{2}$

Sample No.	AIR				TITAN EG oil					
	T_{amb}	145 °C	160 °C	180 °C	145 °C		160 °C		180 °C	
					$t = 0$	$t = 1\,\text{h}$	$t = 0$	$t = 1\,\text{h}$	$t = 0$	$t = 1\,\text{h}$
2	1191	1099	1064	1012	1118	1074	1056	1019	974	918
3	1293	1173	1151	1102	1166	1128	1096	1045	976	951
4	1178	1087	1045	999	1047	1035	982	962	913	876
5	1162	1032	1011	1002	1031	1021	1002	971	949	909

Table B.4. PDIV values measured for the investigated pre-wetted specimens in air and in the presence of Titan EG oil under different thermal conditions. All voltage values are reported as $V_{\text{peak}}/\sqrt{2}$

Sample No.	AIR				TITAN EG oil – wetted specimens						
	T_{amb}	145 °C	160 °C	180 °C	T_{amb}, **wetted**	145 °C		160 °C		180 °C	
						$t = 0$	$t = 1\,\text{h}$	$t = 0$	$t = 1\,\text{h}$	$t = 0$	$t = 1\,\text{h}$
2	1276	1112	1078	1017	4432	1301	1236	1183	1155	1094	1057
3	1043	1001	942	904	3384	1187	1132	1079	1018	998	945
4	1217	1065	1012	964	4046	1277	1222	1182	1109	1056	1002
5	1151	1073	1026	965	3787	1312	1267	1191	1172	1045	998

Table B.5. PDIV values measured for the investigated specimens in air and in the presence of Paryol oil. All voltage values are reported as $V_{\text{peak}}/\sqrt{2}$

Sample No.	AIR					PARYOL oil							
	T_{amb}	145 °C	160 °C	180 °C	215 °C	145 °C		160 °C		180 °C		215 °C	
						$t = 0$	$t = 1\,\text{h}$	$t = 0$	$t = 1\,\text{h}$	$t = 0$	$t = 1\,\text{h}$	$t = 0$	$t = 1\,\text{h}$
2	1192	1108	1071	1026	954	1101	1077	1052	1035	997	966	926	893
3	1073	985	968	910	849	970	965	960	927	897	852	829	788
4	1382	1263	1216	1187	998	1407	1144	1062	1036	992	976	962	928
5	1245	1131	1093	1043	945	1095	1072	1065	1018	986	965	872	858

Table B.6. PDIV values measured for the investigated pre-wetted specimens in air and in the presence of Paroyl oil under different thermal conditions. All voltage values are reported as $V_{\text{peak}}/\sqrt{2}$

Sample No.	AIR					PAROYL oil – wetted specimens								
	T_{amb}	145 °C	160 °C	180 °C	215 °C	T_{amb}, wetted	145 °C		160 °C		180 °C		215 °C	
							$t = 0$	$t = 1\,\text{h}$	$t = 0$	$t = 1\,\text{h}$	$t = 0$	$t = 1\,\text{h}$	$t = 0$	$t = 1\,\text{h}$
2	1218	1128	1057	1026	968	2978	1373	1308	1254	1201	1157	1085	1034	1009
3	1183	1057	1021	943	894	3197	1269	1156	1107	1087	1032	984	916	897
4	1274	1176	1125	1115	1032	3243	1454	1339	1286	1243	1195	1164	1077	1048
5	1221	1108	1082	1059	912	3024	1348	1268	1204	1157	1106	1086	1015	916

References

Introduction

[1] United Nations Framework Convention on Climate Change. *Article 1: Definitions*. 1992. URL: https://unfccc.int/resource/ccsites/zimbab/conven/text/art01.htm (visited on 05/15/2026).

[2] António Guterres. *Secretary-General's Remarks on Climate Change*. URL: https://www.un.org/en/exhibits/page/un-remarks-5 (visited on 05/15/2026).

[3] Cynthia F Bearer et al. "Global climate change: the defining issue of our time for our children's health". In: *Pediatr. Res.* 98.4 (Oct. 2025), pp. 1170–1171. DOI: https://doi.org/10.1038/s41390-022-02290-7.

[4] United Nations General Assembly. *General Assembly Official Records, Seventy-Seventh Session: 4th Plenary Meeting*. A/77/PV.4. Sept. 2022. URL: https://digitallibrary.un.org/record/3996866 (visited on 05/15/2026).

[5] The Independent. *UN chief, speaking to leaders, doesn't mince words*. News article on António Guterres' remarks regarding Ukraine, climate, and global crises. 2022. URL: https://www.independent.co.uk/news/antonio-guterres-ap-ukraine-horn-of-africa-russia-b2171726.html (visited on 05/15/2026).

[6] Intergovernmental Panel on Climate Change (IPCC). "Weather and Climate Extreme Events in a Changing Climate". In: *Climate Change 2021 – The Physical Science Basis: Working Group I Contribution to the Sixth Assessment Report of the Intergovernmental Panel on Climate Change*. Cambridge University Press, 2021. URL: https://www.ipcc.ch/report/ar6/wg1/ (visited on 05/15/2026).

[7] Climate Council of Australia. *Report*. Climate Council of Australia, 2017. URL: https://www.climatecouncil.org.au/uploads/1b331044fb03fd0997c4a4946705606b.pdf (visited on 05/15/2026).

[8] UNESCO. *The United Nations World Water Development Report 2025 – Mountains and glaciers: Water towers*. United Nations Educational, Scientific and Cultural Organization, Mar. 2025. ISBN: 978-92-3-100743-9. DOI: https://doi.org/10.54679/LHPJ5153.

[9] World Meteorological Organization. *Record-breaking Heat Spreads Through Europe*. 2026. URL: https://wmo.int/media/news/record-breaking-heat-spreads-through-europe (visited on 07/06/2026).

[10] Ginevra Chelli. "La siccità del Po nel 2022 è stata la peggiore degli ultimi due secoli". In: *Nature Italy* (2023). DOI: 10.1038/d43978-023-00122-8. URL: https://www.nature.com/articles/d43978-023-00122-8 (visited on 05/22/2026).

[11] Il Fatto Quotidiano. *Fiume Po secca a Cremona, crisi idrica: agricoltura a rischio. Il direttore del Consorzio: "Situazione preoccupante"*. https://www.ilfattoquotidiano.it/2026/06/20/fiume-po-secca-cremona-crisi-idrica-agricoltura-a-rischio-direttore-consorzio-video/8424698/. Published: June 20, 2026; Accessed: 2026-07-06. 2026.

[12] La Stampa. *Così i giorni di caldo record stanno prosciugando il Po: la secca che allarma Torino*. https://www.lastampa.it/torino/2026/07/03/video/il_po_nella_morsa_della_siccita_la_secca_a_torino-15679425/. Published: July 3, 2026; Accessed: 2026-07-06. 2026.

[13] Il Giorno. *Dal Po in secca riemerge un antico ponte di barche a Pavia*. https://www.ilgiorno.it/pavia/cronaca/dal-po-in-secca-riemerge-d2416dcb. Published: 2026; Accessed: 2026-07-06. 2026.

[14] Fiona Charlson et al. "Climate Change and Mental Health: A Scoping Review". In: *International Journal of Environmental Research and Public Health* 18.9 (2021). ISSN: 1660-4601. DOI: 10.3390/ijerph18094486. URL: https://www.mdpi.com/1660-4601/18/9/4486.

[15] Achille Wilfred Ouambo Talla et al. "The heat, the heart and beyond: a narrative review of the many ways climate change impacts human health". In: *Front. Clim.* 7.1647942 (Oct. 2025). DOI: https://doi.org/10.3389/fclim.2025.1647942.

[16] Ruth M Doherty, Mathew R Heal, and Fiona M O'Connor. "Climate change impacts on human health over Europe through its effect on air quality". In: *Environ. Health* 16.Suppl 1 (Dec. 2017), p. 118. DOI: https://doi.org/10.1186/s12940-017-0325-2.

[17] Katherine G Arbuthnott and Shakoor Hajat. "The health effects of hotter summers and heat waves in the population of the United Kingdom: a review of the evidence". In: *Environ. Health* 16.Suppl 1 (Dec. 2017), p. 119. DOI: https://doi.org/10.1186/s12940-017-0322-5.

[18] Susan C Anenberg et al. "Synergistic health effects of air pollution, temperature, and pollen exposure: a systematic review of epidemiological evidence". In: *Environ. Health* 19.1 (Dec. 2020), p. 130. DOI: https://doi.org/10.1186/s12940-020-00681-z.

[19] Liheng Shan et al. "Global heatwaves: A scoping review on the trend, characteristics, impacts on air pollution and health". In: *Environ. Res.* 286.Pt 3 (Dec. 2025), p. 122976. DOI: 10.1016/j.envres.2025.122976.

[20] International Energy Agency (IEA). *Energy Technology Perspectives 2020*. Tech. rep. Paris: OECD Publishing, 2020. DOI: 10.1787/d07136f0-en. URL: https://doi.org/10.1787/d07136f0-en.

[21] Intergovernmental Panel on Climate Change. *Climate change 2014: Mitigation of climate change*. Accessed: 2026-07-06. Cambridge, England: Cambridge University Press, Jan. 2015. URL: https://www.ipcc.ch/site/assets/uploads/2018/02/ipcc_wg3_ar5_full.pdf.

[22] Will Steffen et al. "The anthropocene: from global change to planetary stewardship". In: *Ambio* 40.7 (Nov. 2011), pp. 739–761. DOI: 10.1007/s13280-011-0185-x.

[23] Will Steffen, Paul J. Crutzen, and John R. McNeill. "The Anthropocene: Are Humans Now Overwhelming the Great Forces of Nature?" In: *Ambio* 36.8 (2007), pp. 614–621. URL: http://www.jstor.org/stable/25547826 (visited on 05/22/2026).

[24] Katherine Calvin et al. *IPCC, 2023: Climate Change 2023: Synthesis Report. Contribution of Working Groups I, II and III to the Sixth Assessment Report of the Intergovernmental Panel on Climate Change [core writing team, H. lee and J. romero (eds.)]. IPCC, Geneva, Switzerland*. Tech. rep. Intergovernmental Panel on Climate Change, July 2023. DOI: 10.59327/IPCC/AR6-9789291691647.001.

[25] IPCC. *Climate Change 2021: The Physical Science Basis*. Assessment Report Sixth Assessment Report (AR6), Working Group I. Intergovernmental Panel on Climate Change, 2021. URL: https://www.ipcc.ch/report/ar6/wg1/downloads/report/IPCC_AR6_WGI_Full_Report.pdf (visited on 05/15/2026).

[26] Hannah Ritchie, Pablo Rosado, and Max Roser. "CO2 and Greenhouse Gas Emissions". In: *Our World in Data* (2023). URL: https://ourworldindata.org/co2-and-greenhouse-gas-emissions (visited on 05/14/2026).

[27] Hannah Ritchie, Pablo Rosado, and Veronika Samborska. *Climate Change: Annual concentration of atmospheric carbon dioxide*. Our World in Data. Data adapted from NOAA Global Monitoring Laboratory and United States Environmental Protection Agency. Retrieved from https://archive.ourworldindata.org/20260514-092120/grapher/co2-long-term-concentration.html. 2024. (Visited on 05/14/2026).

[28] A L Hirsch et al. "Can climate-effective land management reduce regional warming?" In: *J. Geophys. Res Atmos.* 122.4 (Feb. 2017), pp. 2269–2288. DOI: https://doi.org/10.1002/2016JD026125.

[29] NASA Global Climate Change. *Milankovitch (Orbital) Cycles and Their Role in Earth's Climate*. 2020. URL: https://climate.nasa.gov/news/2948/milankovitch-orbital-cycles-and-their-role-in-earths-climate/ (visited on 05/15/2026).

[30] NASA Global Climate Change. *Why Milankovitch (Orbital) Cycles Can't Explain Earth's Current Warming*. 2021. URL: https://climate.nasa.gov/explore/ask-nasa-climate/2949/why-milankovitch-orbital-cycles-cant-explain-earths-current-warming/ (visited on 05/15/2026).

[31] Claude Bardos and Olivier Pironneau. "The radiative transfer model for the greenhouse effect". In: *Bol. Soc. Esp. Mat. Apl. SeMA* 79.3 (Sept. 2022), pp. 489–525. DOI: https://doi.org/10.1007/s40324-021-00265-y.

[32] United States Environmental Protection Agency (EPA). *Overview of Greenhouse Gases*. https://www.epa.gov/ghgemissions/overview-greenhouse-gases. (Visited on 05/15/2026).

[33] United States Environmental Protection Agency. *Understanding Global Warming Potentials*. 2020. URL: https://www.epa.gov/ghgemissions/understanding-global-warming-potentials (visited on 05/15/2026).

[34] Intergovernmental Panel on Climate Change (IPCC). *History of the IPCC*. URL: https://www.ipcc.ch/about/history/ (visited on 05/16/2026).

[35] United Nations Framework Convention on Climate Change (UNFCCC). *History of the Convention*. URL: https://unfccc.int/process/the-convention/history-of-the-convention (visited on 05/16/2026).

[36] United Nations Framework Convention on Climate Change (UNFCCC). *The Kyoto Protocol*. URL: https://unfccc.int/process-and-meetings/the-kyoto-protocol (visited on 05/16/2026).

[37] European Commission. *The Kyoto Protocol*. URL: https://climate.ec.europa.eu/eu-action/international-action-climate-change/kyoto-protocol_en (visited on 05/16/2026).

[38] United Nations Framework Convention on Climate Change (UNFCCC). *The Paris Agreement*. URL: https://unfccc.int/process-and-meetings/the-paris-agreement (visited on 05/16/2026).

[39] European Commission. *Clean Energy for all Europeans Package (CEP)*. 2019. URL: https://commission.europa.eu/news-and-media/news/clean-energy-all-europeans-package-completed-good-consumers-good-growth-and-jobs-and-good-planet-2019-05-22_en (visited on 05/16/2026).

[40] European Commission. *The European Green Deal*. URL: https://commission.europa.eu/strategy-and-policy/priorities-2019-2024/european-green-deal_en (visited on 05/16/2026).

[41] United Nations. *COP26: Together for our planet*. 2021. URL: https://www.un.org/en/climatechange/cop26 (visited on 05/16/2026).

[42] UK Parliament House of Commons Library. *What were the outcomes of COP26?* 2022. URL: https://commonslibrary.parliament.uk/what-were-the-outcomes-of-cop26/ (visited on 05/16/2026).

[43] European Commission. *Fit for 55: Delivering on the Proposals*. URL: https://commission.europa.eu/topics/climate-action/delivering-european-green-deal/fit-55-delivering-proposals_en (visited on 05/16/2026).

[44] European Commission. *Delivering the European Green Deal*. URL: https://commission.europa.eu/topics/climate-action/delivering-european-green-deal_en (visited on 05/16/2026).

[45] COP28 UAE. *The UAE Consensus Negotiations Outcome*. 2023. URL: https://www.cop28.com/en/the-uae-consensus-negotiations-outcome (visited on 05/16/2026).

[46] United Nations Framework Convention on Climate Change. *COP 28: What Was Achieved and What Happens Next?* 2023. URL: https://unfccc.int/cop28/5-key-takeaways (visited on 05/16/2026).

[47] United Nations Framework Convention on Climate Change. *About COP 29*. 2024. URL: https://unfccc.int/cop29/about-cop29 (visited on 05/16/2026).

[48] United Nations Office of the High Representative for the Least Developed Countries, Landlocked Developing Countries and Small Island Developing States. *COP29 Outcomes – A Call to Action for the World's Most Vulnerable Nations*. 2024. URL: https://www.un.org/ohrlls/content/opinion-pieces/cop29-outcomes-%E2%80%93-call-action-world%E2%80%99s-most-vulnerable-nations (visited on 05/16/2026).

[49] UN Global Compact Network Italy. *COP30 in Belém: Main Outcomes and Climate Agreements*. 2025. URL: https://www.globalcompactnetwork.org/en/news/ungcn-italy-news/2639-cop30-in-belem-main-outcomes-and-climate-agreements.html (visited on 05/16/2026).

[50] European Commission. *What did COP30 achieve?* 2025. URL: https://climate.ec.europa.eu/news-other-reads/news/what-did-cop30-achieve-2025-12-01_en (visited on 05/16/2026).

[51] CNN. *COP30 agreement in Brazil and fossil fuels climate outcomes*. 2025. URL: https://edition.cnn.com/2025/11/22/climate/cop30-agreement-brazil-fossil-fuels-climate (visited on 05/16/2026).

[52] Matthew W. Jones et al. *National Contributions to Climate Change Due to Historical Emissions of Carbon Dioxide, Methane and Nitrous Oxide*. 2025. DOI: 10.5281/zenodo.16640595. URL: https://doi.org/10.5281/zenodo.16640595 (visited on 05/16/2026).

[53] United Nations Framework Convention on Climate Change (UNFCCC). *Nationally Determined Contributions (NDCs)*. URL: https://unfccc.int/process-and-meetings/the-paris-agreement/nationally-determined-contributions-ndcs (visited on 05/16/2026).

[54] Intergovernmental Panel on Climate Change. *Global Warming of 1.5°C. An IPCC Special Report on the impacts of global warming of 1.5°C above pre-industrial levels and related global greenhouse gas emission pathways, in the context of strengthening the global response to the threat of climate change, sustainable development, and efforts to eradicate poverty*. Cambridge, UK and New York, NY, USA, 2018. DOI: 10.1017/9781009157940.

[55] Glen P Peters et al. "The challenge to keep global warming below 2 °C". In: *Nat. Clim. Chang.* 3.1 (Jan. 2013), pp. 4–6. DOI: https://doi.org/10.1038/nclimate1783.

[56] Michael R. Raupach et al. "Sharing a quota on cumulative carbon emissions". In: *Nature Climate Change* 4.10 (2014), pp. 873–879. DOI: 10.1038/nclimate2384. URL: https://www.globalcarbonproject.org/global/pdf/Raupach_2014_Sharing%20a%20quota%20on%20cumulative%20carbon%20emissions.NatureCC.pdf (visited on 05/16/2026).

[57] Robbie Andrew. *It's Getting Harder and Harder to Limit Ourselves to 2°C*. 2020. URL: https://folk.universitetetioslo.no/roberan/t/global_mitigation_curves.shtml (visited on 05/17/2026).

[58] Hannah Ritchie. "Sector by sector: where do global greenhouse gas emissions come from?" In: *Our World in Data* (2020). URL: https://archive.ourworldindata.org/20251125-173858/ghg-emissions-by-sector.html (visited on 05/14/2026).

[59] Hannah Ritchie, Max Roser, and Pablo Rosado. "Energy Production and Consumption". In: *Our World in Data* (2020). URL: https://ourworldindata.org/energy-production-consumption (visited on 05/22/2026).

[60] Our World in Data. *Greenhouse Gas Emissions by Sector*. 2020. URL: https://ourworldindata.org/grapher/ghg-emissions-by-sector-stacked?time=earliest..2020&country=OWID_WRL~OWID_EUR (visited on 05/14/2026).

[61] European Patent Office. *Technologies to Enable a Sustainable Energy Transition*. 2022. URL: https://www.epo.org/en/news-events/in-focus/green-tech/energy-transition-technologies (visited on 05/22/2026).

[62] Asian Development Bank. *Six Technologies Powering the Clean Energy Transition*. 2024. URL: https://www.adb.org/news/features/six-technologies-powering-clean-energy-transition (visited on 05/22/2026).

[63] Joche Markard and Daniel Rosenbloom. "Phases of the net-zero energy transition and strategies to achieve it". In: (Nov. 2023). DOI: https://doi.org/10.48550/arXiv.2311.09472. arXiv: 2311.09472 [physics.soc-ph].

[64] Bhaskar Mitra et al. "Unveiling sectoral coupling for resilient electrification of the transportation sector". In: *NPJ Sustain. Mobil. Transp.* 2.1 (Jan. 2025). DOI: https://doi.org/10.1038/s44333-024-00019-z.

[65] International Transport Forum. *ITF Transport Outlook 2023*. Report. Paris: OECD Publishing, 2023. DOI: 10.1787/b6cc9ad5-en. URL: https://www.oecd.org/content/dam/oecd/en/publications/reports/2023/05/itf-transport-outlook-2023_4466cd78/b6cc9ad5-en.pdf (visited on 05/26/2026).

[66] Nicola Armaroli et al. "The Road Ahead: How to Reduce Emissions and Energy Use for Italy's Transport Sector". In: *Nature Italy* (2022). DOI: 10.1038/d43978-022-00098-x. URL: https://www.nature.com/articles/d43978-022-00098-x (visited on 05/25/2026).

[67] Karlo Hainsch. "Identifying policy areas for the transition of the transportation sector". In: *Energy Policy* 178.113591 (July 2023), p. 113591. DOI: https://doi.org/10.1016/j.enpol.2023.113591.

[68] U.S. Department of Energy and U.S. Environmental Protection Agency. *Electric Vehicle Benefits and Considerations*. 2026. URL: https://www.fueleconomy.gov/feg/evtech.shtml (visited on 05/25/2026).

[69] European Commission. *REPowerEU*. 2026. URL: https://commission.europa.eu/topics/energy/repowereu (visited on 05/25/2026).

[70] Meng Yuan et al. "The electrification of transportation in energy transition". In: *Energy (Oxf.)* 236.121564 (Dec. 2021), p. 121564. DOI: https://doi.org/10.1016/j.energy.2021.121564.

[71] Hannah Ritchie. "Cars, planes, trains: where do CO2 emissions from transport come from?" In: *Our World in Data* (2019). URL: https://archive.ourworldindata.org/20251125-173858/co2-emissions-from-transport.html (visited on 05/14/2026).

[72] International Energy Agency. *Transport sector CO2 emissions by mode in the Sustainable Development Scenario, 2000-2030*. IEA, Paris. 2022. URL: https://www.iea.org/data-and-statistics/charts/transport-sector-co2-emissions-by-mode-in-the-sustainable-development-scenario-2000-2030 (visited on 05/14/2026).

[73] International Energy Agency. *Introducing the Sustainable Development Scenario*. 2019. URL: https://www.iea.org/events/introducing-the-sustainable-development-scenario (visited on 05/26/2026).

[74] International Energy Agency. "Achieving Net-Zero Emissions by 2050". In: *World Energy Outlook 2020*. Paris: IEA, 2020. URL: https://www.iea.org/reports/world-energy-outlook-2020/achieving-net-zero-emissions-by-2050 (visited on 05/26/2026).

[75] International Energy Agency. *CO2 Emissions from Fuel Combustion 2019: Highlights*. Paris: IEA, 2019. URL: https://iea.blob.core.windows.net/assets/eb3b2e8d-28e0-47fd-a8ba-160f7ed42bc3/CO2_Emissions_from_Fuel_Combustion_2019_Highlights.pdf (visited on 05/25/2026).

[76] Georg Bieker. *A global comparison of the life-cycle greenhouse gas emissions of combustion engine and electric passenger cars*. White Paper. Washington, DC: International Council on Clean Transportation (ICCT), 2021. URL: https://theicct.org/publications/global-LCA-passenger-cars-jul2021 (visited on 05/26/2026).

[77] Giampaolo Buticchi, Pat Wheeler, and Dushan Boroyevich. "The More-Electric Aircraft and Beyond". In: *Proceedings of the IEEE* 111.4 (2023), pp. 356–370. DOI: 10.1109/JPROC.2022.3152995.

[78] Jaya Antony Perinba Selvin Raj et al. "Thermal management strategies and power ratings of electric vehicle motors". In: *Renewable and Sustainable Energy Reviews* 189 (2024), p. 113874. ISSN: 1364-0321. DOI: https://doi.org/10.1016/j.rser.2023.113874. URL: https://www.sciencedirect.com/science/article/pii/S1364032123007323.

[79] Anton Koshelev et al. "Effects of pulsed electric field accelerated aging on the properties of PAO cooling oil for electric motors". In: *Pulsed Power* 1.2 (2026), p. 100003. ISSN: 3117-5716. DOI: https://doi.org/10.1016/j.pup.2026.100003. URL: https://www.sciencedirect.com/science/article/pii/S3117571626000038.

[80] Hüseyi Tayyer Canseven. "Advanced direct cooling arrangements for machines with hairpin windings". In: *IEEE Access* 13 (2025), pp. 201711–201725. DOI: https://doi.org/10.1109/ACCESS.2025.3636754.

[81] Payam Shams Ghahfarokhi et al. "The oil spray cooling system of automotive traction motors: The state of the art". In: *IEEE Trans. Transp. Electrif.* 9.1 (Mar. 2023), pp. 428–451. DOI: https://doi.org/10.1109/TTE.2022.3189596.

[82] Hitoshi Okubo, Naoki Hayakawa, and Gian Carlo Montanari. "Technical Development on Partial Discharge Measurement and Electrical Insulation Techniques for Low Voltage Motors Driven by

Voltage Inverters". In: *IEEE Transactions on Dielectrics and Electrical Insulation* 14.6 (2007), pp. 1516–1530. DOI: 10.1109/TDEI.2007.4401236.

[98] Xueqiang Li et al. "Selecting cooling methods for electric motors". In: *Applied Thermal Engineering* 274 (2025), p. 126554. ISSN: 1359-4311. DOI: https://doi.org/10.1016/j.applthermaleng.2025.126554. URL: https://www.sciencedirect.com/science/article/pii/S1359431125011469.

[100] Edison Gundabattini et al. "A review on methods of finding losses and cooling methods to increase efficiency of electric machines". In: *Ain Shams Engineering Journal* 12.1 (2021), pp. 497–505. ISSN: 2090-4479. DOI: https://doi.org/10.1016/j.asej.2020.08.014. URL: https://www.sciencedirect.com/science/article/pii/S2090447920301854.

[112] Yinye Yang et al. "Thermal management of electric machines". In: *IET Electr. Syst. Transp.* 7.2 (June 2017), pp. 104–116. DOI: https://doi.org/10.1049/iet-est.2015.0050.

[126] Gamze Egin Martin, Mohamed El Baghdadi, and Omar Hegazy. "Advancements in thermal management for electric vehicles: Strategies, architectures, and power electronics cooling". In: *IEEE Access* 13 (2025), pp. 147511–147544.

Chapter 1: Theoretical background

[83] Berker Bilgin et al. "Making the case for electrified transportation". In: *IEEE Trans. Transp. Electrif.* 1.1 (June 2015), pp. 4–17. DOI: 10.1109/TTE.2015.2437338.

[84] Alberto Rumi. "Enhancing the Reliability of Electric Transportation Motors through Insulation Coordination and Improved Qualification". PhD thesis. Alma Mater Studiorum – University of Bologna, 2023. DOI: 10.48676/unibo/amsdottorato/10898.

[85] Alberto Rumi. "Enhancing the Reliability of Electric Transportation Motors through Insulation Coordination and Improved Qualification". PhD thesis. Alma Mater Studiorum – University of Bologna, 2023. URL: https://amsdottorato.unibo.it/id/eprint/9272/.

[86] Nursaid Polater, Tamer Kamel, and Pietro Tricoli. "Torque Comparison of Surface Mount and Interior Permanent Magnet Synchronous Motor for Railway Applications". In: *2021 IEEE 15th International Conference on Compatibility, Power Electronics and Power Engineering (CPE-POWERENG)*. 2021, pp. 1–6. DOI: 10.1109/CPE-POWERENG50821.2021.9501196.

[87] Leili Motor. *Surface-Mounted vs Interior Permanent Magnet Synchronous Motors: Key Differences*. https://www.leili-motor.net/surface-mounted-vs-interior-permanent-magnet-synchronous-motors-key-differences/. Accessed: 2026-08-06. 2025.

[88] TOPMAG. *Surface-Mounted vs. Interior Permanent Magnet Motors*. Feb. 24, 2026. URL: https://www.topmag.in/surface-permanent-magnet-motor-vs-interior-permanent-magnet-motor/ (visited on 08/07/2026).

[89] Rasul Hemmati, Fan Wu, and Ayman El-Refaie. "Survey of Insulation Systems in Electrical Machines". In: *2019 IEEE International Electric Machines and Drives Conference (IEMDC)*. 2019, pp. 2069–2076. DOI: 10.1109/IEMDC.2019.8785099.

[90] Mehmet Caglar Kulan, Samet Sahin, and Nick J Baker. "An overview of modern Thermo-conductive materials for heat extraction in electrical machines". In: *IEEE Access* 8 (2020), pp. 212114–212129. DOI: 10.1109/ACCESS.2020.3040045.

[91] Umair Paracha et al. “Next-generation electrical machine insulation systems: Materials, processing technologies, digitalization and circular-sustainability approaches – A critical review”. en. In: *Renew. Sustain. Energy Rev.* 242.117328 (Dec. 2026), p. 117328. DOI: https://doi.org/10.1016/j.rser.2026.117328.

[92] Xuanming Zhou et al. “Insulation for Rotating Low-Voltage Electrical Machines: Degradation, Lifetime Modeling, and Accelerated Aging Tests”. In: *Energies* 17.9 (2024). ISSN: 1996-1073. DOI: 10.3390/en17091987. URL: https://www.mdpi.com/1996-1073/17/9/1987.

[93] Greg C. Stone et al. *Electrical Insulation for Rotating Machines: Design, Evaluation, Aging, Testing, and Repair*. Hoboken, NJ, USA: John Wiley, Sons, and IEEE Press, 2004. ISBN: 9780471682899. DOI: 10.1002/047168290X.

[94] Chuxuan He, Chandra Prakash Beura, and Stefan Tenbohlen. “Investigation of Partial Discharge Activity in the Slot of a Hairpin-wound Stator”. In: *2020 International Symposium on Electrical Insulating Materials (ISEIM)*. 2020, pp. 565–568. URL: https://ieeexplore.ieee.org/document/9275693.

[96] Michael Chapman, Nancy Frost, and Rudolf Bruetsch. “Insulation Systems for Rotating Low-Voltage Machines”. In: *Conference Record of the 2008 IEEE International Symposium on Electrical Insulation*. 2008, pp. 257–260. DOI: 10.1109/ELINSL.2008.4570323.

[97] Paolo Mancinelli, Simone Stagnitta, and Andrea Cavallini. “Qualification of Hairpin Motors Insulation for Automotive Applications”. In: *IEEE Transactions on Industry Applications* 53.3 (2017), pp. 3110–3118. DOI: 10.1109/TIA.2016.2619670.

[99] Qingsong Wang et al. “Advances in thermal management technologies of electrical machines”. In: *Energies* 15.9 (Apr. 2022), p. 3249. DOI: https://doi.org/10.3390/en15093249.

[101] Taewook Ha et al. “Experimental study on behavior of coolants, particularly the oil-cooling method, in electric vehicle motors using hairpin winding”. In: *Energies* 14.4 (Feb. 2021), p. 956. DOI: https://doi.org/10.3390/en14040956.

[102] Payam Shams Ghahfarokhi et al. “Oil Spray Cooling with Hairpin Windings in High-Performance Electric Vehicle Motors”. In: *2021 28th International Workshop on Electric Drives: Improving Reliability of Electric Drives (IWED)*. 2021, pp. 1–5. DOI: 10.1109/IWED52055.2021.9376390.

[103] Jinchi Hou et al. “Study of the cooling performance of electric vehicle motors using a centripetal-inclined oil spray cooling system”. In: *Energies* 19.3 (Jan. 2026), p. 580. DOI: https://doi.org/10.3390/en19030580.

[104] Youngkyo Kim et al. “Study on oil cooling method for the powertrain of electric vehicles”. In: *Int. J. Heat Mass Transf.* 246.127073 (Aug. 2025), p. 127073. DOI: https://doi.org/10.1016/j.ijheatmasstransfer.2025.12707.

[105] Jesús Paredes et al. “New Oil-Flooded Direct Stator Cooling System for High Power Density Machines With Hairpin Windings”. In: *IEEE Access* 14 (2026), pp. 9838–9850. DOI: 10.1109/ACCESS.2026.3654831.

[106] Guillaume Bourhis et al. “Experimental Separation of No-Load Losses of an Electric Motor with Direct Oil Cooling”. In: *2022 International Conference on Electrical Machines (ICEM)*. 2022, pp. 1341–1347. DOI: 10.1109/ICEM51905.2022.9910757.

[107] Fulai Guo and Chengning Zhang. “Oil-cooling method of the permanent magnet synchronous motor for electric vehicle”. In: *Energies* 12.15 (Aug. 2019), p. 2984. DOI: http://dx.doi.org/10.3390/en12152984.

[108] Fengyu Zhang et al. “Improved Thermal Modeling and Experimental Validation of Oil-Flooded High-Performance Machines With Slot-Channel Cooling”. In: *IEEE Transactions on Transportation Electrification* 8.1 (2022), pp. 312–324. DOI: 10.1109/TTE.2021.3106819.

[109] Yuqing Liu et al. “Immersion evaporative cooling for high-power density motors in future aircraft”. In: *Appl. Therm. Eng.* 278.127036 (Nov. 2025), p. 127036. DOI: https://doi.org/10.1016/j.applthermaleng.2025.127036.

[110] P. Seri et al. “Influence of Automatic Transmission Fluid on Partial Discharge Inception Voltage in Hairpin Stators for Electric Vehicles”. In: *2025 IEEE Conference on Electrical Insulation and Dielectric Phenomena (CEIDP)*. 2025, pp. 756–759. DOI: 10.1109/CEIDP61707.2025.11218465.

[111] Haider Alam et al. “Impact of cooling oil on partial discharge and insulation reliability in inverter-fed EV motors”. In: *Cognizance Journal of Multidisciplinary Studies* 5.7 (July 2025), pp. 1–23. DOI: 10.47760/cognizance.2025.v05i07.001.

[113] Payam Shams Ghahfarokhi et al. “The Oil Spray Cooling System of Automotive Traction Motors: The State of the Art”. In: *IEEE Transactions on Transportation Electrification* 9.1 (2023), pp. 428–451. DOI: 10.1109/TTE.2022.3189596.

[114] Gabriele Puccio et al. “Development of Direct Oil Cooling Solutions for E-mobility Traction Motors : Part I: Stator Cooling Concept”. In: *2023 IEEE International Electric Machines and Drives Conference (IEMDC)*. 2023, pp. 1–7. DOI: 10.1109/IEMDC55163.2023.10238860.

[115] Tanguy Davin et al. “Experimental study of oil cooling systems for electric motors”. In: *Appl. Therm. Eng.* 75 (Jan. 2015), pp. 1–13. DOI: http://dx.doi.org/10.1016/j.applthermaleng.2014.10.060.

[116] Michele Merelli. “e-Motor cooling with oil jets: impact of flowrates and oil properties”. In: *2023 AEIT International Conference on Electrical and Electronic Technologies for Automotive (AEIT AUTOMOTIVE)*. 2023, pp. 1–5. DOI: 10.23919/AEITAUTOMOTIVE58986.2023.10217192.

[117] Myeong Hyeon Park and Sung Chul Kim. “Thermal characteristics and effects of oil spray cooling on in-wheel motors in electric vehicles”. en. In: *Appl. Therm. Eng.* 152 (Apr. 2019), pp. 582–593. DOI: https://doi.org/10.1016/j.applthermaleng.2019.02.119.

[118] P Alvarez et al. “Performance and testing of a helical winding for HTS electric machines for aircraft propulsion”. In: *IEEE Access* 13 (2025), pp. 1–1. DOI: 10.1109/ACCESS.2025.3612567.

[120] K H Nguyen et al. “Efficiency evaluation on cooling behavior of water-cooling jacket for synchronous reluctance motor”. In: *Journal of Research and Applications in Mechanical Engineering* (2024). DOI: 10.14456/jrame.2024.10.

[121] Chuan Liu et al. “Estimation of Oil Spray Cooling Heat Transfer Coefficients on Hairpin Windings With Reduced-Parameter Models”. In: *IEEE Transactions on Transportation Electrification* 7.2 (2021), pp. 793–803. DOI: 10.1109/TTE.2020.3031373.

[122] Taewook Ha and Dong Kyu Kim. “Study of injection method for maximizing oil-cooling performance of electric vehicle motor with hairpin winding”. In: *Energies* 14.3 (Feb. 2021), p. 747. DOI: https://doi.org/10.3390/en14030747.

[123] Alessandro Acquaviva et al. “Electromagnetic and calorimetric validation of a direct oil cooled tooth coil winding PM machine for traction application”. In: *Energies* 13.13 (June 2020), p. 3339. DOI: doi:10.3390/en13133339.

[124] Markus Schiefer and Martin Doppelbauer. “Indirect slot cooling for high-power-density machines with concentrated winding”. In: *2015 IEEE International Electric Machines and Drives Conference (IEMDC)*. 2015, pp. 1820–1825. DOI: 10.1109/IEMDC.2015.7409311.

[125] David Drexler. *Direct Cooling of the Stator Using Hollow Conductors – The Big Breakthrough in Downsizing Electric Drives?* LinkedIn post. July 2026. URL: https://www.linkedin.com/posts/david-drexler-915a72205_direct-cooling-of-the-stator-using-hollow-ugcPost-7426881194618884096-V0f-/ (visited on 08/09/2026).

[127] Andrea Cavallini. "Breakdown in gases". Lecture notes for the course "Predictive maintenance for electrical infrastructures", Alma Mater Studiorum - University of Bologna. 2025.

[128] Andrea Cavallini. "Partial discharge mechanisms". Lecture notes for the course "Predictive maintenance for electrical infrastructures", Alma Mater Studiorum - University of Bologna. 2025.

[129] Mohammed I. Elmezain, Mehmet Güleç, and Peter Sergeant. "Partial Discharge Prediction Model for Electric Motors With Enameled Flat Wire". In: *IEEE Transactions on Transportation Electrification* 12.3 (2026), pp. 4746–4755. DOI: 10.1109/TTE.2026.3663628.

[130] Leire Elorza Azpiazu et al. "Study of partial discharge inception voltage in inverter fed electric motor insulation systems". In: *Appl. Sci. (Basel)* 13.4 (Feb. 2023), p. 2417. DOI: https://doi.org/10.3390/app13042417.

[131] Toru Wakimoto, Hiroki Kojima, and Naoki Hayakawa. "Measurement and evaluation of partial discharge inception voltage for enameled rectangular wires under AC voltage". In: *IEEE Transactions on Dielectrics and Electrical Insulation* 23.6 (2016), pp. 3566–3574. DOI: 10.1109/TDEI.2016.005645.

[132] Pablo Alvarez et al. "Partial Discharge Assessment for High-Voltage Electric Machines for Aircraft Propulsion Applications". In: *IEEE Access* 13 (2025), pp. 152637–152650. DOI: 10.1109/ACCESS.2025.3603645.

[133] F. Pauli, N. Driendl, and K. Hameyer. "Study on Temperature Dependence of Partial Discharge in Low Voltage Traction Drives". In: *2019 IEEE Workshop on Electrical Machines Design, Control and Diagnosis (WEMDCD)*. Vol. 1. 2019, pp. 209–214. DOI: 10.1109/WEMDCD.2019.8887790.

[134] Giacomo Galli et al. "Paschen's Law in Extreme Pressure and Temperature Conditions". In: *IEEE Transactions on Plasma Science* 47.3 (2019), pp. 1641–1647. DOI: 10.1109/TPS.2019.2896352.

Chapter 2: Materials and methods

[135] SETARAM. *An Overview of Thermogravimetric Analysis and of Thermobalances*. URL: https://setaramsolutions.com/techniques/thermogravimetric-analysis-tga (visited on 08/09/2026).

[136] Austin J. Ryan. *Thermogravimetric Analysis (TGA): Theory and Applications*. Technical presentation. TA Instruments – Waters LLC. URL: https://www.tainstruments.com/wp-content/uploads/San-Jose-Thermal-TGA.pdf (visited on 08/09/2026).

[137] PerkinElmer. *Thermogravimetric Analysis (TGA): A Beginner's Guide*. Technical guide. PerkinElmer technical guide; Accessed: 2026-08-09. 2020. URL: https://www.researchgate.net/profile/Agustin-Forchetti-Casarino-2/post/Help_needed_in_TGA_analysis_analysis/attachment/65bbbcd353d234443fe15f05/AS%3A11431281221595450%401706802386707/download/faq_beginners-guide-to-thermogravimetric-analysis_009380c_01.pdf.

[138] Thomas Walker. "Unveiling the Secrets of Thermogravimetric Analysis: A Comprehensive Exploration". In: *Advanced Materials Science Research* 7.6 (2024), pp. 235–236. DOI: 10.37532/aaasmr.

2024.7(6).235-236. URL: https://www.openaccessjournals.com/articles/unveiling-the-secrets-of-thermogravimetric-analysis-a-comprehensive-exploration.pdf.

[139] yli325. "Thermogravimetric Analysis (TGA) for Polymer Characterization: Thermal Stability and Composition". In: *Advances in Polymer Science*. Ed. by Wendy Krause. Accessed: 2026-08-09. NC State University Pressbooks, 2026. Chap. 25. URL: https://ncstate.pressbooks.pub/advancesinpolymerscience/chapter/thermogravimetric-analysis-tga-for-polymer-characterization-thermal-stability-and-composition/.

[140] Zübeyde Bülbül and Birol Üner. "Thermogravimetric analysis (TGA) and determination of activation energies of waste paper products". In: *Bioresources* 18.4 (Aug. 2023), pp. 6944–6954. DOI: 10.15376/biores.18.4.6944-6954.

[141] Qiyuan Xie, Dandan Chen, and Yanwei Ding. "Thermogravimetric Analysis and Its Applications in Polymer Characterization". In: *Acta Polymerica Sinica* 53.2 (2022), pp. 193–214. DOI: 10.11777/j.issn1000-3304.2021.21210. URL: https://www.gfzxb.org/zh/article/doi/10.11777/j.issn1000-3304.2021.21210.

[142] Gunjan Navin Doshi. "Analysis and applications of FTIR systems". Accessed: 2026-08-10. Master's thesis. New Jersey Institute of Technology, 1998. URL: https://digitalcommons.njit.edu/theses/905/.

[143] Kazi Al-Amin et al. "Fourier transform infrared spectroscopic technique for analysis of inorganic materials: a review". In: *Nanoscale Adv.* 7.21 (Oct. 2025), pp. 6677–6702. DOI: https://doi.org/10.1039/d5na00522a.

[144] J.S. Held LLC. *Fourier Transform Infrared (FTIR) Technology Analysis*. May 4, 2022. URL: https://www.jsheld.com/insights/articles/fourier-transform-infrared-ftir-technology-analysis (visited on 08/10/2026).

[145] Robert M Silverstein et al. *Spectrometric identification of organic compounds*. 8th ed. Chichester, England: John Wiley and Sons, Sept. 2014. ISBN: 978-0-470-61637-6.

[146] Edith Michelle Maryse Joseph. "Application of FTIR microscopy to cultural heritage materials". PhD thesis. alma, 2009. URL: https://amsdottorato.unibo.it/id/eprint/1404/.

[147] Yahui Gong, Xuerong Chen, and Wei Wu. "Application of fourier transform infrared (FTIR) spectroscopy in sample preparation: Material characterization and mechanism investigation". In: *Advances in Sample Preparation* 11.100122 (Aug. 2024), p. 100122. DOI: https://doi.org/10.1016/j.sampre.2024.100122.

[148] Norman B. Colthup, Lawrence H. Daly, and Stephen E. Wiberley. *Introduction to Infrared and Raman Spectroscopy*. 2nd. New York, San Francisco, London: Academic Press, 1975. ISBN: 0-12-182552-3.

[149] Encyclopaedia Britannica. *Michelson Interferometer*. 2026. URL: https://www.britannica.com/technology/Michelson-interferometer (visited on 08/10/2026).

[150] IndiaMART. *PerkinElmer Spectrum Two N FT-NIR Spectrometer*. 2026. URL: https://www.indiamart.com/proddetail/perkinelmer-spectrum-two-n-ft-nir-spectrometer-2851537257448.html (visited on 08/10/2026).

[151] Ioana Stanciu. "Application of FTIR spectroscopy in the analysis and quality assessment of sunflower Oil". In: *J. Res. Chem.* 6.1 (Jan. 2025), pp. 113–117. DOI: https://www.doi.org/10.22271/reschem.2025.v6.i1b.178.

[152] V Macián et al. “Proposal of an FTIR methodology to monitor oxidation level in used engine oils: Effects of thermal degradation and fuel dilution”. In: *Tribol. Trans.* 55.6 (Nov. 2012), pp. 872–882. DOI: http://dx.doi.org/10.1080/10402004.2012.721921.

[153] Muhammad Ali Mehmood et al. “Comprehensive investigation on service aged power transformer insulating oil after decades of effective performance in field”. In: *Arab. J. Sci. Eng.* 45.8 (Aug. 2020), pp. 6517–6528. DOI: https://doi.org/10.1007/s13369-020-04559-7.

[154] Soumya Thakur, R Sarathi, and M G Danikas. “Investigation on thermal ageing impact on dielectric properties of natural ester oil”. In: *Electr. Eng. (Berl., Print)* 101.3 (Sept. 2019), pp. 1007–1018. DOI: https://doi.org/10.1007/s00202-019-00843-4.

[155] Qunfeng Zeng et al. “Performance deterioration analysis of the used gear oil”. In: *Adv. Chem. Eng. Sci.* 06.02 (2016), pp. 67–75. DOI: http://dx.doi.org/10.4236/aces.2016.62008.

[156] Andreea Mirela Teleașă et al. “Rheological study and FTIR analysis of thermally degraded mineral and biodegradable hydraulic fluids”. In: *Lubricants* 13.10 (Oct. 2025), p. 462. DOI: https://doi.org/10.3390/lubricants13100462.

[157] Ali Mazin Abdul-Munaim et al. “Absorption wavebands for discriminating oxidation time of engine oil as detected by FT-IR spectroscopy”. In: *Lubricants* 7.3 (Mar. 2019), p. 24. DOI: http://dx.doi.org/10.3390/lubricants7030024.

[158] Abi Munajad, Cahyo Subroto, and Suwarno. “Fourier transform infrared (FTIR) spectroscopy analysis of transformer paper in mineral oil-paper composite insulation under accelerated thermal aging”. In: *Energies* 11.2 (Feb. 2018), p. 364. DOI: http://dx.doi.org/10.3390/en11020364.

[159] Najmuddin Mohd Ramli et al. “Evaluation of oxidative and thermal stability of base oil for automotive application”. In: *Lecture Notes in Mechanical Engineering*. Lecture Notes in Mechanical Engineering. Singapore: Springer Nature Singapore, 2022, pp. 553–562. DOI: https://doi.org/10.1007/978-981-19-2890-1_52.

[160] Saliha Boudraa et al. “FTIR and FDS assessment of mineral oil under low electrical discharge”. In: *Diagnostyka* 23.2 (May 2022), pp. 1–7. DOI: https://doi.org/10.29354/diag/149994.

[161] Youssouf Brahami et al. “Thermal and electrical fault diagnosis in oil–paper insulation system: A comparative study of natural esters and mineral oil”. In: *Appl. Sci. (Basel)* 15.14 (July 2025), p. 7676. DOI: https://doi.org/10.3390/app15147676.

[162] A Rohman and Y B Che Man. “Application of FTIR spectroscopy for monitoring the stabilities of selected vegetable oils during thermal oxidation”. In: *Int. J. Food Prop.* 16.7 (Oct. 2013), pp. 1594–1603. DOI: https://doi.org/10.1080/10942912.2011.603874.

[163] Norhanifah Abdul Rahman, Matzaini Katon Katon, and Nurina Alya Zulkifli Zulkifli. “Analysis of Automatic Transmission using Fourier Transform Infrared (ftir) spectrocopy”. In: *e-AJ* 7.SI-TeMIC18 (Mar. 2019). DOI: https://doi.org/10.24191/e-aj.v7iSI-TeMIC18.5378.

[164] Qunfeng Zeng et al. “Performance deterioration analysis of the used gear oil”. In: *Adv. Chem. Eng. Sci.* 06.02 (2016), pp. 67–75. DOI: http://dx.doi.org/10.4236/aces.2016.62008.

[165] OMICRON electronics GmbH. *MPD 800: Universal Partial Discharge Measurement and Analysis System*. Product Information Brochure, Document L4215, Rev. 04/2022. Apr. 2022. URL: https://www.avalontest.com/images/uploaded/MPD-800-Product-Information-Brochure-ENU.pdf (visited on 08/11/2026).

[166] Manish Srivastava, Sunil Kumar Goyal, and Amit Saraswat. “Ester oil as an alternative to mineral transformer insulating liquid”. In: *Mater. Today* 43 (2021), pp. 2850–2854. DOI: https://doi.org/10.1016/j.matpr.2021.01.066.

[167] Jilani Rouabeh et al. “Studies of different types of insulating oils and their mixtures as an alternative to mineral oil for cooling power transformers”. In: *Heliyon* 5.3 (Mar. 2019), e01159. DOI: https://doi.org/10.1016/j.heliyon.2019.e01159.

[168] Samson Okikiola Oparanti, Ungarala Mohan Rao, and Issouf Fofana. “Natural esters for green transformers: Challenges and keys for improved serviceability”. In: *Energies* 16.1 (Dec. 2022), p. 61. DOI: https://doi.org/10.3390/en16010061.

[169] Pawel Rozga et al. “A review on synthetic ester liquids for transformer applications”. In: *Energies* 13.23 (Dec. 2020), p. 6429. DOI: http://dx.doi.org/10.3390/en13236429.

[170] Abderrahmane Beroual et al. “A Review on Electrical Breakdown of Natural Ester-Based Nanofluids Under Different Voltage Waveforms”. In: *IEEE Access* 12 (2024), pp. 75610–75624. DOI: 10.1109/ACCESS.2024.3400986.

[171] Ruijin Liao et al. “A comparative study of physicochemical, dielectric and thermal properties of pressboard insulation impregnated with natural ester and mineral oil”. In: *IEEE Transactions on Dielectrics and Electrical Insulation* 18.5 (2011), pp. 1626–1637. DOI: 10.1109/TDEI.2011.6032833.

[172] Wikipedia contributors. *Pour Point*. Wikipedia, The Free Encyclopedia. URL: https://en.wikipedia.org/wiki/Pour_point (visited on 08/14/2026).

[173] JR Reynolds. *Flash Point vs Fire Point: What's the Difference?* Pentyl Labs. Mar. 5, 2026. URL: https://www.pentyllabs.com/flash-point-vs-fire-point/ (visited on 08/15/2026).

[174] FUCHS Lubrificanti S.p.A. *TITAN ATF 6000 SL*. Technical Product Information, PI 2085 FLI, February 19, 2010. FUCHS Lubrificanti S.p.A. Feb. 2010. URL: https://valpetrol.com/wp-content/uploads/2015/07/ATF-6000-SL.pdf.

[175] BIZOL. *BIZOL Protect ATF D-VI synt*. URL: https://bizol.com/products/atf/protect-atf-d-vi-synt/ (visited on 08/15/2026).

[176] My Transfo Meeting. *A&A Fratelli Parodi Dielectric Esters: The Frontrunner of Sustainability*. URL: https://www.mytransfo.com/sponsorship/aa-fratelli-parodi-spa/ (visited on 08/15/2026).

[177] Andrea Cavallini. “Partial discharge measurement”. Lecture notes for the course ”Electrical assets management”, Alma Mater Studiorum - University of Bologna. 2025.

[178] OMICRON Energy. *MPD 800 – Universal Partial Discharge Measurement and Analysis System*. 2026. URL: https://www.omicronenergy.com/en/products/mpd-800/ (visited on 08/11/2026).

[179] DirectIndustry. *Partial Discharge Measuring System MPD 800 – OMICRON Electronics*. URL: https://www.directindustry.it/prod/omicron-electronics/product-13971-2265540.html (visited on 08/11/2026).

[180] OMICRON electronics GmbH. *MPD 800 Application Note*. Technical document. URL: https://www.omicronenergy.com/download/document/C3AEC48C-A9EC-4ABA-8757-4766B011CF54/ (visited on 08/11/2026).

[181] OMICRON Energy Solutions. *OMICRON MPD Suite: User Manual for Version 1.50*. Internal software documentation supplied with the OMICRON MPD Suite installation (Version 1.50), June 10, 2024. June 2024.

Chapter 4: Discussion of results

[182] Jasmine Almond et al. "Determination of the carbonyl index of polyethylene and polypropylene using specified area under band methodology with ATR-FTIR spectroscopy". In: *E-polymers* 20.1 (July 2020), pp. 369–381. DOI: https://doi.org/10.1515/epoly-2020-0041.

[183] Carbery Maddison et al. "An advanced analytical approach to assess the long-term degradation of microplastics in the marine environment". In: *Npj Mater. Degrad.* 7.1 (July 2023). DOI: https://doi.org/10.1038/s41529-023-00377-y.

[184] Claudia Campanale et al. "Fourier transform infrared spectroscopy to assess the degree of alteration of artificially aged and environmentally weathered microplastics". In: *Polymers (Basel)* 15.4 (Feb. 2023), p. 911. DOI: https://doi.org/10.3390/polym15040911.

[185] Homeyra Piri et al. "Biolubricant ageing analysis: Proposal for a real-engine test and chemical characterization". In: *J. Energy Inst.* 121.102121 (Aug. 2025), p. 102121. DOI: https://doi.org/10.1016/j.joei.2025.102121.

[186] National Institute of Standards and Technology. *Ethanol*. CAS Registry Number: 64-17-5. NIST Chemistry WebBook, NIST Standard Reference Database Number 69. URL: https://webbook.nist.gov/cgi/cbook.cgi?ID=C64175&Mask=27 (visited on 08/21/2026).

[187] National Institute of Standards and Technology. *Ethyl Acetate*. CAS Registry Number: 141-78-6. NIST Chemistry WebBook, NIST Standard Reference Database Number 69. URL: https://webbook.nist.gov/cgi/cbook.cgi?ID=C141786&Mask=E1 (visited on 08/21/2026).

Future developments

[188] ScienceDirect. *Gas Chromatography – An Overview*. Elsevier. URL: https://www.sciencedirect.com/topics/agricultural-and-biological-sciences/gas-chromatography (visited on 08/21/2026).

[189] Quality Analysis GmbH. *Gas Chromatography: How Does It Work?* Quality Analysis GmbH. URL: https://www.qa-group.com/en/glossary/gas-chromatography/ (visited on 08/21/2026).

[190] D M Levermore et al. "Headspace analysis of engine oil by gas chromatography/mass spectrometry". In: *Anal. Chem.* 73.6 (Mar. 2001), pp. 1361–1365. DOI: https://doi.org/10.1021/ac001157c.

[191] Carole Doncoeur et al. "Molecular characterization of lubricant base oil oxidation using *operando* headspace chromatography and rancimat". In: *Energy Fuels* acs.energyfuels.5c02751 (Aug. 2025). DOI: https://doi.org/10.1021/acs.energyfuels.5c02751.

[192] Yves Leblanc et al. "Static headspace gas chromatographic determination of fault gases dissolved in transformer insulating oils". In: *J. Chromatogr. A* 633.1-2 (Feb. 1993), pp. 185–193. DOI: https://doi.org/10.1016/0021-9673(93)83153-J.

[193] Rasmus Talviste et al. "Experimental determination of first Townsend ionization coefficient in mixtures of He and N $_2$". In: *J. Phys. D Appl. Phys.* 54.32 (Aug. 2021), p. 325202. DOI: https://doi.org/10.1088/1361-6463/ac0219.

[194] EEEGuide. *Experimental Arrangement to Measure Ionization Coefficients*. EEEGuide. URL: https://www.eeeguide.com/experimental-arrangement-to-measure-ionization-coefficients/ (visited on 08/21/2026).

[195] N. Crossette et al. "Determination of First Townsend Ionization Coefficient by Simulation". In: *2019 IEEE Pulsed Power & Plasma Science (PPPS)*. 2019, pp. 1–3. DOI: 10.1109/PPPS34859.2019.9009919.

[196] BrainKart. *Townsend's Criterion*. BrainKart. URL: https://www.brainkart.com/article/Townsend---s-Criterion_12886/ (visited on 08/21/2026).

[197] Archana Sharma and Fabio Sauli. "A Measurement of the First Townsend Coefficient in Argon Based Mixtures at High Fields". In: *Nuclear Instruments and Methods in Physics Research Section A: Accelerators, Spectrometers, Detectors and Associated Equipment* 323 (1992), pp. 280–283. DOI: 10.1016/0168-9002(92)90303-L.

Appendices

[198] M R Raupach. "The exponential eigenmodes of the carbon-climate system, and their implications for ratios of responses to forcings". In: *Earth Syst. Dyn.* 4.1 (Jan. 2013), pp. 31–49. DOI: doi:10.5194/esd-4-31-2013.

[199] Andrew H MacDougall. "The transient response to cumulative CO2 emissions: A review". In: *Curr. Clim. Change Rep.* 2.1 (Mar. 2016), pp. 39–47. DOI: https://doi.org/10.1007/s40641-015-0030-6.

[200] J. M. Gregory et al. "A new method for diagnosing radiative forcing and climate sensitivity". In: *Geophysical Research Letters* 31.3 (2004). DOI: https://doi.org/10.1029/2003GL018747.

[201] Intergovernmental Panel on Climate Change. "Climate Change 2001: The Scientific Basis". In: *Contribution of Working Group I to the Third Assessment Report of the Intergovernmental Panel on Climate Change*. Cambridge University Press, 2001. URL: https://archive.ipcc.ch/ipccreports/tar/wg1/222.htm (visited on 05/19/2026).

[202] Sudhanshu Pandey et al. "Reduction in Earth's carbon budget imbalance". In: *Nat. Commun.* 16.1 (July 2025), p. 6818. DOI: https://doi.org/10.1038/s41467-025-61588-2.

[203] Pierre Friedlingstein et al. "Global carbon budget 2024". In: *Earth Syst. Sci. Data* 17.3 (Mar. 2025), pp. 965–1039. DOI: https://doi.org/10.5194/essd-17-965-2025.

[204] Wikipedia contributors. *Mauna Loa Observatory*. 2026. URL: https://en.wikipedia.org/wiki/Mauna_Loa_Observatory (visited on 05/19/2026).

[205] Wikipedia contributors. *Airborne fraction*. 2026. URL: https://en.wikipedia.org/wiki/Airborne_fraction (visited on 05/18/2026).

[206] NOAA Global Monitoring Laboratory. *How We Measure Background CO2 Levels on Mauna Loa*. 2018. URL: https://gml.noaa.gov/ccgg/about/co2_measurements.html (visited on 05/19/2026).